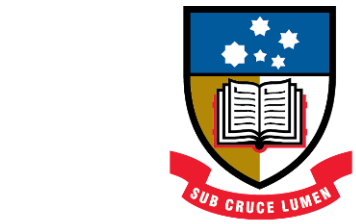

THE UNIVERSITY of ADELAIDE

NITROGEN OXIDES REDUCTION IN A POROUS BURNER

Shahrooz Afsharvahid

School of Mechanical Engineering

The University of Adelaide, South Australia 5005

A Thesis submitted in fulfilment of the requirements for the Degree of

Doctor of Philosophy

JULY 2016

STATEMENT OF ORIGINALITY

I certify that this work contains no material which has been accepted for the award of any other degree or diploma in my name in any university or other tertiary institution and, to the best of my knowledge and belief, contains no material previously published or written by another person, except where due reference has been made in the text. In addition, I certify that no part of this work will, in the future, be used in a submission in my name for any other degree or diploma in any university or other tertiary institution without the prior approval of the University of Adelaide and where applicable, any partner institution responsible for the joint award of this degree.

I give consent to this copy of my thesis, when deposited in the University Library, being made available for loan and photocopying, subject to the provisions of the Copyright Act 1968.

I also give permission for the digital version of my thesis to be made available on the web, via the University's digital research repository, the Library Search and also through web search engines, unless permission has been granted by the University to restrict access for a period of time.

ACKNOWLEDGMENTS

I would like to express my special appreciation and thanks to my one and only supervisor, *Professor Bassam Dally*. He did a remarkable job as a supervisor and mentor. I am especially thankful to his continuous encouragement, support and more importantly for his true friendship which allowed me to successfully finish this work. His advice, ideas and brilliant instructions have helped my scientific and personal development and have guided me both in my research and career life.

I would like to also thank the School of Mechanical Engineering management team (especially Professor Anthony Zander) for supporting and funding my study, the workshop and laboratory staff (especially Mr. Graham Kelly) who supported my experimental work even at times where I found it hard to keep going.

I would also like to specially thank *Professor Peter Ashman* for the great help with the few publications I had and also his remarkable knowledge of the chemical kinetics.

I like to express my special gratitude to *Professor Farid Christo* for his valuable help with the numerical modelling techniques and encouragement guided me into great world of CFD.

I need also to appreciate the patience and support from my work colleagues and the management team in *FCT Combustion*. *Constantine Manias* and *David Retallack*, are a great inspiration in terms of hardworking and going to great length to achieve desirable results. *Russell Jackson* well taught me that there is nothing wrong with being a professional and at the same time fun to work with. I found him to be an expert in transforming impossible obstacles to exciting challenges.

Special thanks go to *Ms. Alison-Jane Hunter* for her kind assistance with proofreading my thesis. Her skills and talent was instrumental in greatly improving the readability of this thesis. I appreciate her phenomenal attention to details.

Words cannot express my gratitude to my loving and caring *mother*, inspiring *father*, my two brothers, *Shahraam* and *Shahrokh*, and my beautiful newly engaged sister, *Sara*. I will always remember the huge sacrifices they made for me to give me the best possible chance in life which made me who I am today.

I would also like to thank my life friend, *Parto* for the unconditional support, love and friendship, believing in me, standing by my side and giving me the strength unconditionally. I also have been blessed to have many trustworthy and loyal friends particularly *Keivan* and *Eyad* who were always around when I needed help, encouragement or support.

Last but not least, I would like to express my deep love and gratitude to my beloved son, *Kian*. Your bright little smile has given me the motivation to keep going, from the second you opened your eyes to this world. I would like to thank you for being such a bundle of joy and laughter in my life and I feel that I am the luckiest father of all times, being able to call you my son.

ABSTRACT

Different aspects of porous burners have been studied in the past in terms of the bed material, design, heat transfer modes and flame characteristics. However, the application of porous burners to NOx reduction and the effect of the bed surface on the chemical reactions have not yet been explored. Hence, the objective of this study is to investigate the effect of the design and operating parameters on NOx reduction inside a porous burner.

To achieve this objective, a variety of flames, stabilised inside porous burners, were investigated experimentally, utilizing thermocouples, gas sampling and chromatography. Numerical tools were also used to understand the chemical pathways under different operating conditions better.

Premixed CNG-air and LPG-air flames at very low equivalence ratios were stabilised inside the porous bed. The relationship between the volumetric flow rate of the mixture and the minimum equivalence ratio was studied (experimentally and numerically) for equivalence ratios as low as φ=0.35 (equivalent to thermal power of 2kW). The maximum temperature observed to be consistent with super-adiabatic flame temperatures. The maximum measured NO_X and CO mole fractions at the burner exit were found to be in the order of few PPMs.

The conversion of NOx was then assessed. A mixture of CNG-air doped with NO was introduced into the burner inlet and the effects of the operating parameters on NOx reduction were assessed. It was found that NOx reduction is a function of the equivalence ratio, total flow rate and NO mole fraction at the inlet. Higher flow rates led to an increase in the conversion rate at higher equivalence ratios, due to shorter residence times, and the greater need for more flame radicals in the flame.

The numerical study revealed that different chemical pathways dominate at different equivalence ratios, which led to the production of other intermediates and stable radicals. The study showed that the Total Fixed Nitrogen, TFN, reduction followed a similar trend to the NOx reduction for moderately fuel-rich conditions ($\varphi \leq 1.2$) and opposite trends for higher equivalence ratios. For φ>1.2, most of the NO is converted to N-containing species such as N_2O, NH_3 and HCN and not to N_2. Analysis of the chemical pathways showed that the formation of nitrogen-containing species under very fuel rich conditions is due to the increased importance of the HCNO path, as compared with the HNO path. The best TFN conversion efficiency, 65%, was found at φ=1.1.

Intermediate radicals have different rates of destruction and production on the porous bed surface, especially for mixtures close to stoichiometric conditions. Under these conditions, the conversion of NO_X is strongly influenced by the concentration of H radicals. A collision probability of $\eta = 8\times10^{-4}$ was found to represent this radical loss effect and to help predict the destruction and production of intermediate terminals with a good level of accuracy.

This study also found that NOx reductions using porous burners are technically feasible and that the resulting CO in the exhaust, derived from the rich mixtures, can be burned outside the porous bed.

TABLE OF CONTENTS

LIST OF TABLES

LIST OF FIGURES

NOMENCLATURE

i. Roman Symbols

Symbol	Definition	Unit
a	Surface Area Density	m^{-1}
A	Arrhenius pre-exponential factor	s^{-1}
A_{up}	Burner Cross Sectional Area	M^2
C_m	Measured NO_x mole fraction	PPM
Cp	Specific Heat Capacity	$kJ.K^{-1}$
c_{pg}	Specific heat of gaseous species	$kJ.kg^{-1}.K^{-1}$
C_r	Reference NO_x mole fraction	PPM
ΔG_{ki}^*	The Gibbs free energy	$Kg.m^2.s^{-2}$
d_h	Hydraulic Diameter	M
D_i	Molecular diffusivity of the i^{th} species in Nitrogen	$m^2.s^{-1}$
d_p	Pore Diameter	M
E	Arrhenius activation energy	$J.mol^{-1}$
EI_i	Emission Index	-
$\mathrm{EI_i}$	Emission Index	-
F	Inertia coefficient	m^{-1}
f	Flame Location	m
h_v	Convective heat transfer coefficient for the porous medium	$W.m^{-2}.K^{-1}$
K	Permeability	m^2
K	Specific permeability of the porous medium	m^2/kg
k_{cj}	Diffusion rate of radical species, *i*, to the burner surface	s^{-1}
$k_{coll,i}$	Surface collision rate constant for species *i*	s^{-1}
k_{eff}	Effective rate of radical termination at the burner surface	s^{-1}
$k_{g,e}$	Effective thermal conductivity of the gas	$W.m^{-1}.K^{-1}$
k_j	First-order reaction rate constant for the j^{th} reaction	s^{-1}
kk	Total number of gaseous species	-
L	Bed length	m

m	Measured Oxygen concentration	Mole.m^{-3}
m''	Mass flow rate per unit area	kg.m^{-2}.s^{-1}
M_i	Molecular weight of the i^{th} species	g.mol^{-1}
Nu_d	Nusselt number based on the average particle diameter of the packed bed	-
P	Pressure	Pa
Pe	Péclet number	-
Pr	Prandtl number	-
R	Universal gas constant, 8.314	J/mol/K
R	Reference Oxygen concentration	-
Re	Reynolds number	-
S_p	Laminar Flame Speed	m.s^{-1}
T	Temperature	K
T_{amb}	Ambient temperature	K
T_g	Gas temperature	K
T_s	Solid temperature	K
u_p	Superficial velocity (cross sectional velocity)	m.s^{-1}
V_{bed}	Cross-sectional mean velocity (Darcian velocity)	m.s^{-1}
V_p	Total Volume of Pebbles	m^3
V_{pm}	Volume of Porous Media	m^3
$\overline{C}_i$	Mean gas speed of species *i*	m.s^{-1}

ii. Greek Symbols

Symbol	Definition	Unit
Φ	Equivalence ratio	-
γ	Radical recombination efficiency = k_{eff} / k_{coll}	-
η	Relative rate of radical termination = k_{eff} / k_{ci}	-
μ	Dynamic viscosity	$kg.s.m^{-1}$
n	Arrhenius temperature coefficient	-
θ	Burner surface-to-volume ratio ($6400m^{-1}$, for this burner)	m^{-1}
ρ	Gas density	$Kg.m^{-3}$
σ	Stefan-Boltzmann constant	$W.m.K^{-4}$
$\overline{\sigma}$	Average Reaction Rate	$Mol.s^{-1}$
Δ	Packed Bed Sphere Diameter	m
Ɛ	Porosity	-
Λ	Coefficient of Thermal Conductivity	-
v	Kinematic viscosity	$m^2.s^{-1}$
σ(x)	Net Reaction Rate	Mol/cm^3s
τ_{eff}	Effective Residence Time	s
$\overline{\Phi}$	GER, Global equivalence ratio	-

iii. Acronyms and Abbreviations

Acronym	Definition
CNG	Compressed Natural Gas
FLOX	Flameless Oxidation
HVR	High Velocity Regime
LPG	Liquefied Petroleum Gas
LVD	Low Velocity Detonation
LVR	Low Velocity Regime
MILD	Moderate or Intense Low oxygen Dilution
ND	Normal Detonation
NOx	Nitrogen Oxides
PB	Porous Burner
PBM	Porous Burner Model
PPB	Part Per Billion
PPM	Part Per Million
PRB	Porous Radiant Burner
RCR	Rapid Combustion Regime
SCW	Super-adiabatic Combustion Wave
SVR	Sound Velocity Regime
TFN	Total Fixed Nitrogen

INTRODUCTION

1.1 Importance of combustion

Combustion has played a major role in human existence throughout history, improving the quality of life throughout history. Mankind has used it for cooking, warming up, refining and treating metals for making tools and armaments, for example. A quick glance around our local environment shows that combustion is still an essential element that contributes to our current life-style. The majority of our transport systems rely on burning fuel, as is the case in cars, trains, airplanes and ships. The heat for our houses, offices, shops and the like comes either directly from gas-based or oil-based furnaces or indirectly through electricity that is generated by burning different types of fossil fuels. As a result, most of the world's energy (power and heat) needs for thermal power generation is produced from the combustion of fossil fuels. As a consequence, two major issues have become essential to balance the sustainability of energy resources and economic growth: improving thermal efficiency and lowering pollutant emissions.

1.2 Environmental pollution

Emission of pollutants has put human health in danger in different ways. This includes both types of primary pollutants (those emitted from combustion systems) and secondary air pollutants (those produced by the post reactions of primary pollutants in the atmosphere). Major pollutants include carbon dioxide (CO_2), water vapour (H_2O) and nitric oxide (NO) which is the main component that causes acid rain and results in plant damage [1]. Other pollutants include nitrogen dioxide (NO_2), carbon monoxide (CO), a variety of hydrocarbons (HC), sulphur oxides, soot and other particulates. For example the emission of NO_X produced in the stratosphere (mostly produced by jet engines), although contributing less than 2% of global pollution [2], is the major cause of the destruction of the ozone layer in the atmosphere. The destruction of stratospheric ozone allows more harmful ultraviolet solar radiation to reach the earth's surface.

The effects of the emission of pollutants attract intense political and community pressures, resulting in stringent emission reduction regulations (e.g. the Montreal Protocol in 1987 focusing on stratospheric ozone destruction, the 1990 clean air act amendments discussing air toxic and hazardous air pollutants, the Kyoto protocol in 1997 concerned with the greenhouse effect and global warming and the 2015 Paris agreement to mitigate emissions to reduce their effects in terms of climate change).

On the other hand, fossil fuel reserves are becoming depleted and more expensive to recover. These depletions are encouraging the development of new combustion technologies to utilise alternative sources and improve the thermal efficiency in existing ones. To achieve these aims, scientific communities worldwide have been engaged in research programs aiming at developing technologies to minimise the emission of hazardous pollutants and reduce fuel consumption, which will improve the thermal efficiency of existing and new combustion systems [3-5].

Nitrogen oxides (NO_X) are an example of these major pollutants. They are formed in combustion processes as a result of:

- Thermal or Zel'dovich mechanism which dominates in high-temperature combustion over a wide range of equivalence ratios. The mechanism consists of three chain reactions:

$$O + N2 \Leftrightarrow NO + N$$

$$N + O2 \Leftrightarrow NO + O$$

$$N + OH \Leftrightarrow NO + H$$

- Fenimore or prompt mechanism formation, which is particularly important in fuel rich zones within the flames, i.e. by high temperature combination of free nitrogen and oxygen. Prompt NO_X refers to those oxides of nitrogen that are formed early in the flame and do not result from the Zel'dovich mechanism. Prompt NO_X formation is caused by the interaction between certain hydrocarbon and nitrogen components and/or an excess of oxygen atoms that lead to early NO_X formation;

- N_2O-intermediate mechanism, which is important in lean ($\varphi < 0.8$) and low temperature, premixed combustion;

- Fuel nitrogen mechanism, in which fuel-bound nitrogen is converted to NO. The fuel-N mechanism is not generally important in premixed combustion systems since most fuels used in premixed combustion contain little or no bound nitrogen. But in non-premixed combustion applications, some fuels, such as coal and heavy distillates, carry significant amounts of fuel-bound nitrogen.

For natural gas firing, virtually all of the NO_X emissions result from thermal fixation, which is commonly referred to as thermal NO_X, or from prompt NO_X. The formation rate is strongly temperature dependent and generally occurs at temperatures in excess of 1800 K and generally is more favoured in the presence of excess oxygen. At these temperatures, the usually stable nitrogen molecule dissociates to form nitrogen atoms, which then react with oxygen atoms and hydroxyl radicals to form NO, primarily.

In general, NO_X formation can be retarded by abatement techniques. The underlying principles of most of these techniques involve reducing the concentrations of oxygen atoms at the peak combustion temperature, by reducing the peak flame temperature and the residence time in the combustion zone. For example in industrial burners and spark-ignition engines, this can be achieved by mixing flue or exhaust gases with fresh air or fuel. Another strategy to reduce NO_X levels is to use multi-stage

combustion, in which combustion occurs in a lean stage followed by a rich stage or vice versa. Catalytic converters are also employed in automotive applications to reduce NO_X emissions from combustion systems. Reburning, is another method of NO_X control, where some of the fuel is introduced downstream of the main combustion zone to convert NO_x back into N_2.

1.3 Alternative combustion systems

Different combustion systems have been designed and brought to practice during the last few decades in order to reduce emissions and decrease fuel consumption at the same time. Such systems include lean premixed gas turbines, MILD combustion or flameless oxidation (FLOX®) and porous burners (PB). This thesis is concerned with the principles of operation of porous burners' technology and its potential to be utilised widely in low NO_X combustion processes.

1.4 Porous Media Combustion

In conventional burners (i.e. open flame burners) the premixed air and fuel chemically reacts (burns) in a self-sustaining flame, which is stabilised at the burner exit via fluidic or mechanical means. The burning of premixed (sometimes partially premixed) air and fuel in such flames occurs in a narrow combustion zone, which is usually called a flame front. A flame front is usually only few millimetres thick.

In porous burners, combustion takes place inside cavities and pores of a porous matrix, as shown in Figure 1.1. The porous matrix mostly consists of ceramic-based foams or discrete materials packed in an 'enclosure', forming a porous bed. The flame stabilises inside the porous bed, or close to the exit surface for porous radiant burners, which are described later. Heat is recirculated upstream, mainly by radiation, from a high temperature zone to incoming reactants. Reactants are preheated without being diluted with exhaust gases, unlike some other regenerative or recuperative systems. The preheated fuel/oxidiser mixture enters the reaction zone, releases energy and either heats up the rest of the bed using convection or transfers heat to a local heat exchanger. The exchange with the bed creates an excess enthalpy regime in the reaction zone, which results in stretching the flame front, a

higher flame speed and stable combustion under leaner fuel/oxidiser mixture conditions. The stabilisation mechanism described above is mostly similar in all kinds of porous burners.

The two most developed porous burners are:

- Porous Burners (PB): Porous beds are reasonably thick (more than a few centimetres) and the flame stabilises inside the porous matrix exhibiting a wider flammability limit [6-9]. In the next few chapters, porous burners are studied and their physical and chemical properties are investigated in detail via numerical modelling or laboratory experiments.

- Porous Radiant Burners (PRBs): These burners are also known as surface flame burners, surface combustion burners or as a "Flat Porous Inert Surface" [10]. In porous radiant burners, the flame stabilises very close to the surface of the porous matrix, usually operating at nearly stoichiometric conditions and radiation is the dominant heat transfer mechanism [11-15] (see Figure 1.1). As an example, "radiant tube burners" have radiation units inside, in which a radiating surface is placed between a flame and a load. Another variation is the Super-adiabatic Radiant Porous Burner developed by Vandadi et al. [16, 17]. They used radiation rods to preheat the incoming air/fuel mixture and enhance the burner thermal or combustion efficiency. Another type is termed surface combustion [18-21] infrared burners. They incorporate a radiating surface with a porous refractory through which a combustion mixture is passed and then burned above the surface to heat the surface by conductive heat transfer. Gas-fired infrared generators also have a burner with a radiating refractory surface that is heated directly with a gas flame [22].

The porous matrix in each category can appear as an inert medium [9, 23-25] or as a catalytic supporter [26-29].

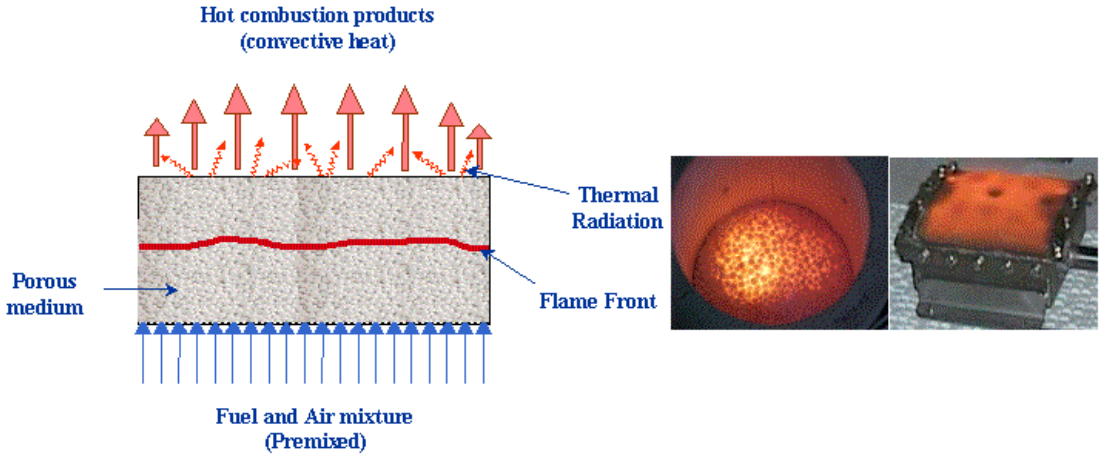

Figure 1.1: Porous burner schematic (left), Regular porous burner (middle) [30], and Porous radiant burner (right) [31].

1.4.1 Advantages of porous burners

Porous burners (PB) have so far been proven to have many environmental advantages over conventional burners, with respect to reduced emissions of NO_X and CO. Furthermore, these burners have several operational advantages including high radiant heat outputs, wider dynamic power ranges (about 1:20 [32]), wider flammability limits, increased thermal efficiency, fast heat-up times and uniform heat distribution [13]. As an example, the wider flammability limits of porous burners could be utilised to burn fugitive methane gases emitted from mines, landfill gases, and the combustion of gaseous fuels derived from the gasification of solid biomass. These types of gases are usually diluted by a large amount of air and/or inert gases with a heating value smaller than 250 kJ/m^3, which is equivalent to a flame temperature increase of about 200 K [33]. Usually, in conventional burners, a large amount of fuel is needed to enrich these low-heating value gas mixtures and burn them in a cost effective and safe manner. Using the right porous burner technology, feeding these gases into a PB can establish a self-sustaining flame, while the released energy can be utilised in some other applications.

To summarise the above mentioned characteristics of porous burners, one can conclude that porous burners using high radiation characteristics employ high thermal efficiency and low emissions of most harmful pollutants such as NO_X and CO [34]. Wider flammability limits and higher power density result in a smaller volume combustion zone and hence smaller burner dimensions (about 10 times [32]);

flexibility in the adaptation of the combustion chamber geometry of the burner, and high flame speeds are some of other attractive characteristics of these burners. These advantages over conventional burners make the PB applicable to a wide range of applications.

1.4.2 Applications of porous burners

The thermal output of PBs is mostly based on radiation, so they can be employed by the many industries using infrared heating. What follows is a list of applications and industries to which PBs directly contribute. Many of them are described in detail by Mößbauer [35] and Rumminger [36]:

- Catalytic assisted combustors and Porous reactors [32]
- Gas turbine combustion chambers
- Thermal regeneration and thermal efficiency improvement in diesel engines [37-40]
- Radiant heaters: commercial and residential space heating [41], chemical & metal processing, glass annealing, coatings & paint drying, food processing, pulp and paper drying, independent vehicle heaters for automobiles
- Combustion of liquid fuel (such as oil and kerosene) [42]
- Heat generator for chemical reactors
- Steam generation [43]
- Dual-fuel burner (gas- and liquid-fuels)
- Burner for the power generation from mineral oil, liquid, pyrolysis or coking plant gas
- Burner for the regenerative energy sources, such as gasified biomass, hydrogen (from solar energy), wood gas, biogas [44], dump or sewer gas and low-calorific value fuels [45-47]
- Ultra-lean combustion in which the fuel concentration is well below the flammability limit when compared with conventional flames (see a detailed review by Wood et al. [45])

- Thermal exhaust cleaning: by using this burner it is possible to reduce the levels of H-C and NO_x and utilise the energy produced [48, 49]

- Syngas production for fuel cell applications [50-53]

1.4.3 Limitations of porous burners

Durability of the ceramic-based materials of the main body or the porous matrix is still a challenge for manufacturers of such materials. Although the temperature is relatively low through lean and ultra-lean combustion, it is still high enough to causes cracks and degradation due to thermal cycling [54]. Metal-based porous materials can be utilized as an alternative substitute for ceramic-based materials. Metal-based porous materials (i.e. austenitic and ferritic stainless steels [55]) have a better resistance to thermal shock and are more robust when compared with ceramic-based porous materials. However, at temperatures higher than 1200 K [55], oxidation-induced corrosion can result and this limits the functional lifetime of such materials. Hence, porous burners are preferred in moderate temperature conditions, especially in ultra-lean or ultra-rich combustion regimes.

Another common problem with porous burners is flame stability inside the porous matrix for a wide range of firing rates and equivalence ratios. This is especially important to avoid the risk of flashback and blow-out phenomena. This implies a certain limited range of stable flames for a particular porous burner design and geometry.

Apart from the physical limitations of a porous matrix, limited fundamental knowledge of heat transfer and fluid mechanics during the combustion process within the bed have kept the modelling efforts relatively immature. Modelling full combustion without making certain common assumptions and simplifications is still very difficult. Researchers in this field face different challenges in modelling the combustion process, which involves solving simultaneously the energy and mass conservation equations and the chemical kinetics in the porous matrix. Energy equations should be solved individually for both solids (as schematically shown in Figure 1.2) and gas within the porous media, considering conduction, convection and radiation. Oliveira et al. [56] and Ziauddin et al. [24] focused their modelling on ignition temperature over a wide range of parameters. They provided a

comprehensive review of all modelling challenges and proposed a simplified approach to fully explain both surface and homogenous reactions.

It is worth noting that chemical kinetics is usually considered for the gas phase only when inert porous media is used. However, inert porous media could also affect the chemical kinetics in the gas phase within the porous media, as will be discussed later in this study.

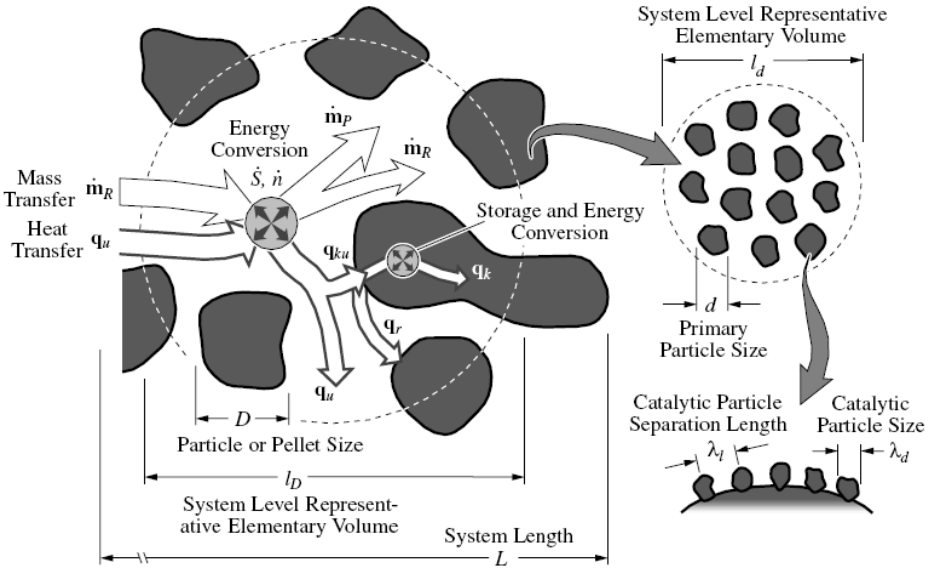

Figure 1.2: Heat and mass transfer in a schematic porous medium, formed by a continuous gas phase and dispersed solid phase [56].

It is worth noting that in the last decade, researchers and scientists from both the academic and industry sectors have made great progress in eliminating most of the problems and limitations mentioned earlier. Hence, as described earlier in section 1.4.2 “Applications of porous burners”, porous burners are being utilized extensively in niche applications in a wide range of industries.

1.5 Motivation for the research

The concept of porous burners has been known for some time and the technology is relatively mature, although some of the fundamentals are yet to be fully explored.

For example, little is known about the efficacy of introducing the fuel into the porous bed (as compared with premixing it with the air *a priori*) of flames’ stability and emissions in a porous media. Consideration of the nature of porous media, which

restricts easy access to the internal parts of the porous media, has played a major role in shifting most studies and applications towards a premixed (or partially remixed) air fuel mixture within porous media.

Another area which has not yet been extensively studied is the detailed understanding of pollutants' (in specific NO_X) formation and destruction mechanisms within the porous media. This includes both catalytic and inert porous media, where the effect of the surface reaction is usually excluded from modelling studies.

These issues form the basis of the present study, which is aimed at furthering understanding of flame stability and heat transfer mechanisms over different operating ranges.

Also, this study investigates the effects of surface chemistry on NOx formation, within porous media, when inert materials have been used as the porous matrix.

Designing and developing modular porous burners and then investigating flame stability under different conditions, i.e. premixed air and fuel, non-premixed air and fuel, lean and ultra-lean combustion regimes and rich and ultra-rich combustion regimes are the foci of this study. Once the stabilisation mechanisms are known, CO and NO_X emissions can be quantified. The results of these findings are then used to study NO_X formation and reduction mechanisms when a PB is used as a post processor for existing combustion systems. Later, findings from those studies will be compared to a numerical model in order to extend the scope of this project beyond its experimental limitations.

1.6 Scope

This research aims to advance our knowledge and understanding of heat transfer characteristics and chemical kinetics inside porous burners in lean and rich combustion regimes. In particular this experimental and numerical study will address the following objectives:

- Investigate the effects of different operating parameters including; the firing rate (flow rate), equivalence ratio and fuel type on the stability and the location of the flame inside porous burners;

- Investigate the PB flame structure, temperature and exhaust gas emission as a function of the operating parameters;
- Investigate the NOx and Total Fixed Nitrogen reduction mechanisms inside a PB and the role of the surface reactions of their conversions.

To achieve the above, different modular porous burners have been designed and built in the School of Mechanical Engineering at the University of Adelaide. A variety of flames were stabilised and studied in these burners, using various experimental and numerical techniques.

1.7 Thesis structure

Following this chapter (Chapter 1), which has provided a general introduction and presented the research topic, the thesis is structured as follows:

Chapter 2: In this chapter, the background literature is presented and discussed. It covers research into combustion within porous burners, as well as NO_X reduction mechanisms in different combustion systems.

Chapter 3: In this chapter, different fuel injection designs to achieve stabilised flames inside the PB are presented and discussed. The chapter covers the advantages and challenges in introducing the air and fuel separately and the physical difficulties to create a homogenous air-fuel mixture, resulting in a uniform flame inside the PB.

Chapter 4: In this chapter, experimental and numerical investigations of flames stabilised in a PB are presented and the behaviour of premixed flames and their pollutant emissions under different firing rates, equivalence ratios and fuel types are investigated. Effects of super-adiabatic flame temperatures and excess enthalpy are also studied and discussed.

Chapter 5: In this chapter, the findings and results from previous chapters are used to develop a porous burner in which the reduction of initial NO_X in an experimental and modular PB is investigated and the results are then simulated using a numerical model.

Chapter 6: In this chapter, the effects of the surface reaction on NO_X reduction mechanisms are investigated and discussed. These effects are a consequence of the

high surface to volume ratio, despite the inert nature of the porous bed material (i.e. silicon carbide and aluminium oxide).

Chapter 7: In this chapter, a summary of all the findings from this research are provided. This is followed by a list of conclusions from this work and latter some recommendations for future work which this study could be a useful base.

BACKGROUND

2.1 Porous Burners: Principles of operation

The most basic configuration of a porous burner consists of an organic-, metallic- or ceramic-based porous matrix within a high temperature resistant structure. The premixed air and fuel mixture (from low-pressure gases to liquid macromolecules [56]) enters the porous matrix where it is preheated by recirculating heat, mainly radiation, from the high temperature zone to upstream parts of a porous matrix, as schematically shown in Figure 2.1. As the preheated mixture gets close to the flame front location, the temperature rises to that required for ignition; reactions then occur and energy is released. One part of the released energy convectively heats up the porous matrix downstream as hot products flow through the pore structure of the matrix to the exit. The rest of the flame released energy is radiated back to the porous matrix upstream and heats the incoming unburned gas, keeping this cycle running and helping to stabilise the flame within the bed. The flame location is controlled by the balance between the flow speed and the laminar flame speed, with a major role undertaken by the heat transfer. When the flow speed is lower than the laminar flame speed, flashback occurs. To deal with this problem and extend the stability range, a different porous matrix (shape, size or material) can be used at the PB inlet [54, 57].

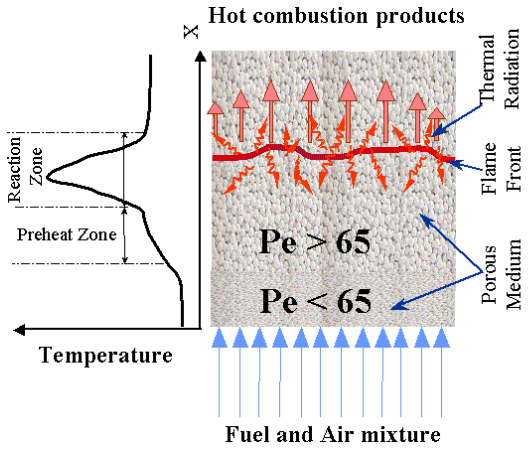

Figure 2.1: Schematic of a porous burner and its principles of operation

Many researchers have investigated flame propagation and stabilisation inside the porous matrix in the last three decades [35, 57-59]. Babkin et al. [60] showed experimentally that the propagation is completely dependent on the modified Péclet number:

$$Pe = \frac{S_p d c_P \rho}{\lambda} \qquad (2.1)$$

Where λ, S_P, c_p, and ρ are the coefficient of thermal conductivity, laminar flame speed, specific heat capacity and density of the unburned gas mixture, respectively. Here d is the equivalent porous diameter, which differs for different geometries and calculations. For some fluid mechanics calculations, the hydraulic diameter d_h is used. For porous burners with sphere packed beds, the bead diameter (d_m) is used and the pore diameter (d_p) will give the best results for calculating the Péclet number. Lyamin and Pinaev [61] proposed a formula for determining d_m, instead of using the hydraulic diameter for a cylindrical tube, where the porous medium works as a flame arrestor;

$$d_m \approx \frac{\delta}{2.77} \qquad (2.2)$$

where d_m is the equivalent porous diameter for a sphere packed bed and δ is the diameter of the spheres.

Babkin et al. [60] showed that for values of Péclet numbers greater than 65, flame propagation happens. For values less than 65, the heat release to the porous media is

less than the heat production and the flame will be extinguished. This outcome later became a major consideration in the design and testing of several bi-layered porous burners [62]. Porous burners have thicker flame fronts when compared with free flame burners. For example a Bunsen burner has a flame thickness of ~1 mm in the case of methane/air under atmospheric conditions [63], while in porous burners it can be in the scale of several centimetres [64].

2.2 Porous medium materials and shapes

Compared with conventional burners, porous burners are exposed to lower temperatures because of the different heat transfer mechanisms, predominantly radiation heat transfer. But these temperatures are still high enough to cause severe thermal and chemical stresses. These stresses, over time, downgrade most of the porous metal structures and are the major reason for cracks developing in porous burners [65]. Recent progress in the production of ceramic-based materials has allowed the use of more durable materials with a variety of geometrical, physical and chemical characteristics. The pores and the vigorous shapes of the packing material impose large vortex structures and large friction coefficients, resulting in an extensive momentum and interphase energy exchange between the solid and the gas phase. Porosity (void fraction) is one of the most important parameters of the porous medium, which significantly impacts on flow velocity, momentum and even the stability of the flame. It is defined as:

$$\varepsilon = \frac{V_{PM} - V_P}{V_{PM}} \qquad (2.3)$$

where ε is the porosity, V_{PM} is the porous media volume and V_P is the total volume of pebbles; such as spherical balls or saddles.

Mößbauer et al. [25] reviewed metal-based and ceramic-based materials used in porous burners. They compared aluminium oxide, silicon carbide, metal alloys and solid zirconia with respect to temperature resistance, conduction heat transport, start-up phase, radiation heat transport, dispersion and pressure drop. The effect of the presence of an $LaMnO_3$ (Pervoskite-type catalyst) deposited over a FeCrAlloy fiber

panel on the porous burner's performance has been investigated by Cerri [66]. The results were then compared with a non-catalytic burner. Catalytic porous burners showed significantly lower concentrations of CO and HC but the NO_X levels were remarkably similar to those from the non-catalytic burner when operated below 800 kW/m^2.

There have been many different studies using different materials and different porosities [67], but generally, the most common materials used in porous media can be classified into three major groups; porous foams/fibres, wire meshes and discrete elements.

2.2.1 Porous foams/fibres

Ceramic foam is a porous material with open cavities within a continuous ceramic matrix, usually processed by a polymeric-sponge replication technique [68]. Ceramic foams are available in a variety of materials. The composition is specified as a base material stabilised by another material used as a binder. Base materials include: silicon carbide, silicon nitride, mullite, cordierite (a bicolour mineral silicate of magnesium, aluminum, and sometimes iron), alumina and zirconia. Some materials, including magnesia and yttrium, are used as a binder i.e. to make Y_2O_3-stabilized ZrO_2 known as YSZ [69]. The rigid structure of foams allows them to be operated at any angle, which makes them easier and more practical to use. On the other hand, the lower resistance of the ceramic foams to thermal shocks and cracking limits the use of porous foams in some applications.

Trimis [32] and Mößbauer et al. [35] reviewed the use of SiC foams, mixer-like structures made of Al_2O_3 fibres (Figure 2.2a), C/SiC^{TM} (Figure 2.2b) and ZrO_2 (Figure 2.2c) foams in different applications.

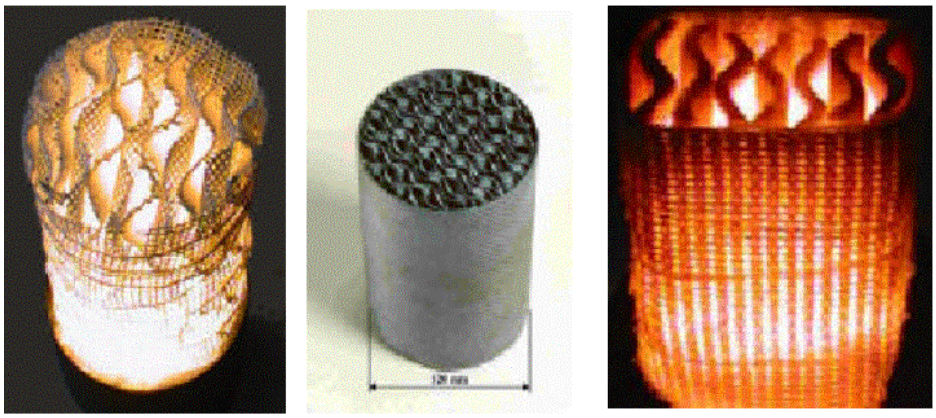

Figure 2.2: Different ceramic porous foams: (a) Al_2O_3 fibres, (b) C/SiC™ structure and (c) static mixer made of ZrO_2 foams [32]

They compared the above-mentioned materials in terms of the high temperatures, thermal expansion coefficient, thermal conductivity, specific thermal capacity, thermal stress resistance parameter and thermal emissivity. They related the applications of this technology to a variety of applications and the type of material that can be utilized in each one of them. Such applications include:

- Household and air heating systems
- Light oil burners
- Gas turbine combustion chambers
- Independent vehicle heating systems
- Steam generators
- Oxy-fuel combustion
- Other special applications [32, 35].

The above list highlights the applicability of PB technology to a wide range of applications due to the benefits mentioned earlier, namely; small and compact designs, large turndown ratios and low pollutant emissions.

2.2.2 Metallic wire meshes and foils

Wire meshes used as a porous matrix have a short start up time, high thermal capacity per unit volume, high radiation heat characteristics and an excellent low

pressure drop. The constraints of using metals as a porous matrix lie in the limited temperature range they can allow. For nickel-based and Fe-Cr-Al-alloys the maximum use temperature is about 1300 °C, while for porous foams typical maximum temperatures can be more than 1600 °C. At the same time, due to the high porosity, they have poor conduction heat transport and dispersion properties. Figure 2.3 shows a picture of a Fe-Cr-Al-alloy wire mesh.

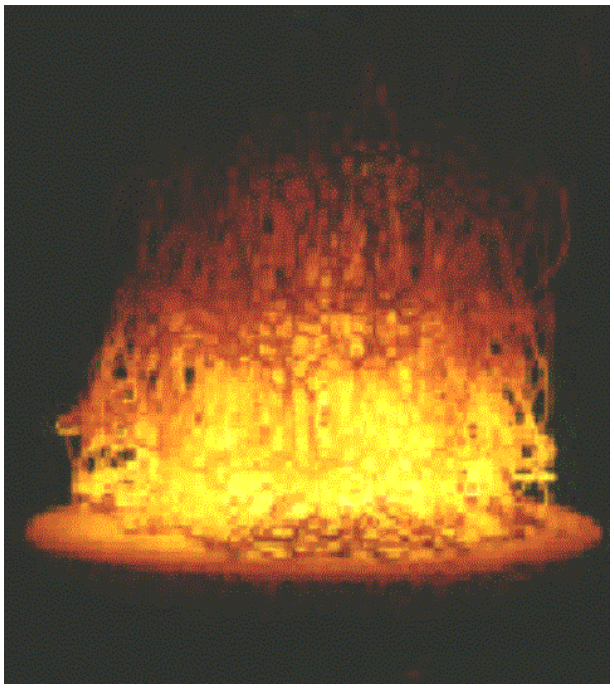

Figure 2.3: Fe-Cr-Al-alloy wire mesh[32]

2.2.3 Discrete materials

Discrete ceramic elements are mostly made of alumina in a ball or saddle shape. A saddle has an elongated concave shape, like a horse saddle. Their sturdy shape and the fact that they are not constrained in a rigid matrix, makes them less subjected to stress. A packed bed of sphere balls has a porosity of 0.36 to 0.43 [70], while porosity will be increased for the irregularly shaped saddles to around 0.9 [71]. Availability of different sizes of discrete materials makes them easier to fit and pack as a matrix in any shape of container. The specific surface 'a' (the surface area density) for a packed bed, formed with ceramic spherical beads with a diameter of δ, can be calculated as:

$$a = \frac{6(1-\varepsilon)}{\delta} \qquad (2.4)$$

The surface area density '*a'* of the porous media is generally quite large, compared with conventional burners.

2.3 Flow inside porous medium

Materials which are used as porous media have relatively high porosity. Hence pressure drops within the porous medium are mostly low and pore Reynolds numbers of less than 300 have been reported in the past. The pore Reynolds number [72] can be defined as:

$$\mathrm{Re} = \frac{\rho d u_p}{\mu} \qquad (2.5)$$

Where u_p is the superficial velocity (cross-sectional mean velocity), μ is the fluid viscosity and d is the characteristic length of the porous media. For example, for a packed bed of spherical beads, d is the beads' diameter, or mean pore diameter, when porous foams are used.

In most modelling cases or applications and where the flow velocity is low using porous burners, the particle or pore size of the porous matrix is small when compared with the hydrodynamic length scales. So, the inertial forces are small and negligible and the flow velocity u is a function of the applied pressure differential,

$$u = \frac{K}{\mu}\frac{\partial P}{\partial x} \qquad (2.6)$$

where μ is the fluid viscosity, P is pressure and K is the specific permeability of the porous medium for low velocity flow and steady conditions.

2.4 Combustion within porous media

Combustion in porous media is different in nature from that of conventional combustion or free flames. There are phenomena which make the combustion in porous burners either advantageous or challenging in some other respects. The efficient heat transfer between the gas and the solid phases, caused by the high

surface area of the porous media, is the main factor in achieving uniform temperatures across the porous medium. Also, heat transfer from the flame zone through radiation and conduction via a solid medium heats the porous solid and, subsequently, the incoming reactants by convection. This heat recirculation process results in higher burning speeds, excess enthalpy combustion, lower pollutant emissions and the ability to stabilise leaner flames. Below, some of the main characteristics of porous burners are explained and discussed.

2.4.1 Ignition, heat-up process and stabilisation in PB

Stabilisation in porous burners can be defined as having a steady combustion within the porous media. The reaction zone does propagate neither upstream nor downstream unless conditions change. Changing the equivalence ratio or firing rate shifts the reaction zone, but establishing the original configurations brings the flame back to the original, stable location. Reaching a stable combustion in porous media results in a wider reaction zone and higher heat transfer between the gas-phase and the porous medium, and subsequently a more uniform temperature within the bed. Kennedy et al. [6, 7] investigated flame stability and ways to identify the controlling parameters in a PB. They classified the stability of the combustion, on what they called ‘filtration combustion’, in terms of super-adiabatic combustion waves (SCWs). The propagation of the SCW was related to the thermal wave within a porous matrix. A correlation was also developed which identified the regimes of decaying and stable waves. The stability of the flame was then conditioned on the filtration velocity and fuel concentration (related to adiabatic temperature). In order to utilise this wave and extract the energy produced under these conditions, a reciprocal flow burner, operated by a periodic flow reversal, was devised [73].

Cerri et al. [28] showed different combustion regimes and performances for various porous matrices, including catalysed materials. As shown in Figure 2.4, the catalyst caused a reduction of the radiant regime area and an enlargement of the blue-flame regime. On the other hand, the catalyst affected both porosity and the tortuosity of the foam matrix, which caused an increase in the pressure drop across the foam, as well as the local momentum of the gas phase.

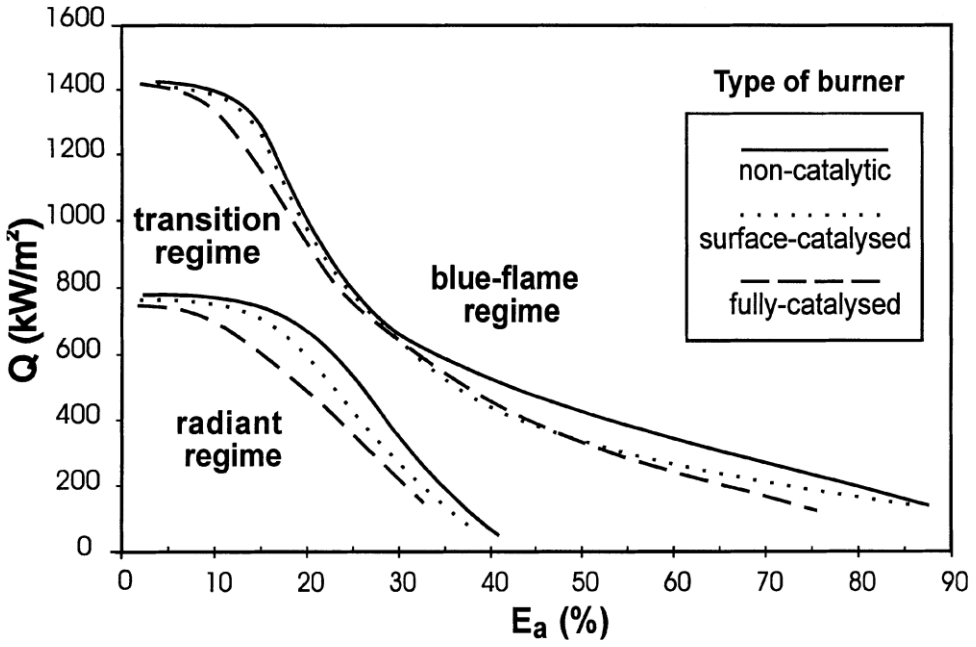

Figure 2.4: various combustion regimes as a function of excess air E_a and firing rate Q for three different types of burners: non-catalytic, surface catalysed and the fully catalysed structures [28].

2.4.2 Propagation speed

Flame propagation in porous media has been of interest for many years. The majority of the studies have been performed in tubes containing porous materials. Premixed air/fuel enters the system and ignites at one end or somewhere inside the bed. The flame front starts moving (propagating) and stabilises at a certain location if the flow rate, equivalence ratio and Péclet number are within the range of stabilisation. Otherwise, the flame will blow off and extinguish or flashback upstream which could be a major safety concern. Lammers et al. [74] studied the flashback and stabilisation phenomena for both porous burners and porous radiant burners. The study investigated different parameters, including equivalence ratios, porous medium physical characteristics, environment temperature and radiation to the environment. They proved numerically that the volumetric heat transfer coefficient and the porous medium material effective conductivity are the parameters which affect the flash-back limits the most, as they have the largest impact on the effective burning velocity inside the porous medium.

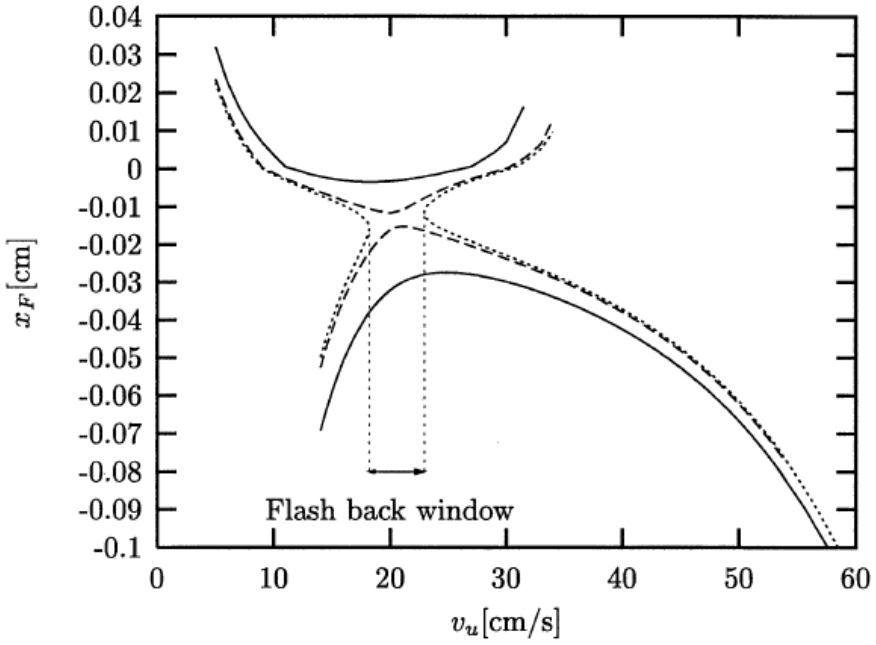

Figure 2.5: Stabilisation diagram for flames stabilised inside and outside a porous burner in ambient temperatures and in hot environments (T_{env}= 750 K, dashed line, T_{env}=775 K, dotted line) for Φ= 0.9 [74].

Their findings showed numerically the stabilisation window for an environment temperature (as they phrased it) of 775 K (as shown in Figure 2.5).

Similarly, Akbari et al. [75], in a parametric numerical study, determined the flashback, stable combustion and blow-out regions in PBs. The variant parameters included porosity, equivalence ratios and firing rates. The results are shown in Figure 2.6 and Figure 2.7.

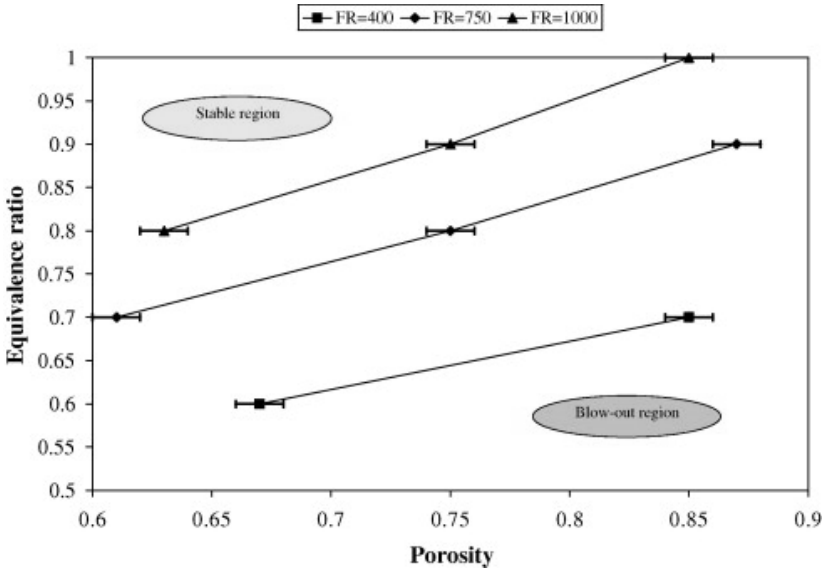

Figure 2.6: Stability diagram with respect to the lower flammability limit and the matrix porosity for three distinct values of firing rate [75]

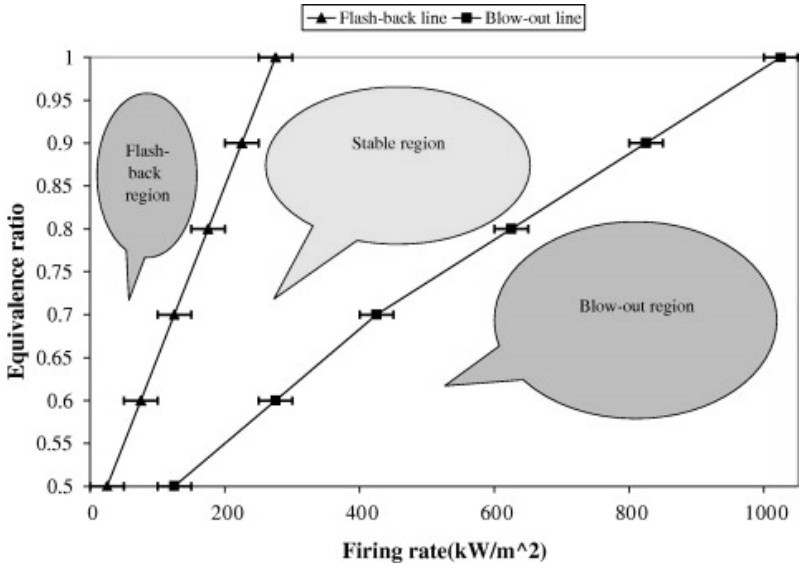

Figure 2.7: Stability diagram with respect to flammability limits and turn–down ratio [75]

Lyamin and Pinaev [61] and Babkin et al. [60] defined different flame propagation regimes in porous media as a parameter of the flame wave velocity. They performed several experiments on methane/air and propane/air mixtures and measured flame propagation velocities for a wide range of pressures, equivalence ratios and characteristic sizes of cavity space. They showed that in porous media the flames accelerate and attain high velocities as effectively in rough tubes as in tubes containing obstacles. They believed that the most important factor for this

acceleration is a positive feedback between the velocities of flame propagation and fresh gas movement. Based on the study performed by Lyamin and Pinaev [61] and Babkin et al. [60], six regimes were observed, which are listed in Table 2.1:. The low velocity regime (LVR) includes an intense interphase heat exchange in the zone of chemical transformation and normally combustion velocity is less than 10^{-4} m/sec. The factors that define the wave velocity are the thermal structure and propagation limits. Convective gas movement mechanisms under uniform pressure are an example of high velocity regime HVRs, where a typical velocity lies between 0.1 m/sec and 10 m/sec. Smooth changes in pressure will push the velocity to higher values, defined as a rapid combustion regime (RCR). Further increases in the pressure gradient lead to a sound velocity regime (SVR), which is defined as falling between 100 m/sec to 300 m/sec. Detonation is defined for velocities of more than 500 m/sec and can be caused by self-ignition under shock wave interactions in low velocity detonation (LVD), or in normal detonation regimes under heat and pulse losses.

Regime	Wave velocity (m/s)	Flame propagation mechanism
Low velocities (LVR)	0- 1 x 10^{-4}	Heat conductivity, interphase heat exchange
High velocities (HVR)	0.1-10	Convective, uniform pressure
Rapid combustion (RCR)	10-100	Convective, smooth pressure gradient
Sound velocities (SVR)	100-300	Convective, pressure gradient
Low velocity detonation (LVD)	500-1000	Self-ignition under shock wave interaction
Normal detonation (ND)	1500-2000	Detonation under heat and pulse losses

Table 2.1: Steady-state regimes and reaction transfer mechanisms for gas combustion in inert porous media [60, 61]

2.5 Super-adiabatic flame temperature (excess enthalpy combustion)

One of the interesting features of PB is the ability to extend the flammability limit and to achieve high reaction rates, leading to effective flame speeds, in excess of the laminar flame speed of the inlet mixture. Recirculation or recuperation of heat from the combustion products to the air/fuel mixture upstream of the reaction zone is one of the mechanisms that contribute to this phenomenon. The peak temperature can be higher when compared with the adiabatic flame temperature, for a range of equivalence ratios.

Many applications use preheated incoming reactants in order to obtain higher flame temperatures and thus higher efficiency. Weinberg [76] first studied the idea of borrowing energy from a premixed flame to preheat the incoming mixture of air and fuel. Enthalpy is transferred from products to reactants, which helps achieving higher temperatures in excess of the adiabatic flame temperature for a certain equivalence ratio. Hardesty and Weinberg [77] later showed theoretically that the flammability limit for what they called excess enthalpy flames, is beyond that for free propagating flames. They believed that the backward radiation from solids within the reaction zone is the main cause of the heat up of the porous medium upstream of the reaction zone. The second most effective heat transfer mechanism was found to be the transferred heat via conduction by the porous medium itself. Heat transfer via radiation (from hot gas to the incoming reactants) was found to be almost negligible. Hanamura et al. [33] investigated the super-adiabatic temperature phenomena in a reciprocating heat engine using a one-dimensional numerical model. Their system included a thin porous medium inside a cylinder and one piston in each side of the porous matrix. They concluded that super-adiabatic temperature would increase the thermal efficiency when compared with other engines like Otto and diesel. Their results also confirmed that using a porous medium with a large conduction-radiation parameter would increase the maximum temperature, resulting in the extension of the flammability limit.

2.6 Multi stage combustion in porous burners

Several researchers have investigated multi stage combustion [22, 46-52] in which the air/fuel mixture is combusted in at least two successive combustion regions within a porous matrix. The products of the first stage mix with the unburned fuel/air mixture and this mixture acts as a reactant in the next stage of the porous matrix. This method enables the minimising of pollutant emissions by controlling the maximum temperature, temperature distribution and equivalence ratios in each individual stage. As the first stage combustion is happening in a lean or ultra-lean fuel/air mixture, the combustion gases from the first stage still contain enough oxygen to burn more fuel in the second stage. Chaffin [78] reported an experimental investigation in a cylindrical quartz-tube porous burner and showed that the NO_X concentration was higher than in a regular single-stage porous burner when the system is fed with a rich fuel/air mixture in the first stage and a lean mixture in the second stage. On the other hand, the NO_X concentrations decreased while the system was working with a lean first stage and rich second stage for the same overall equivalence ratio as for regular single stage burners. Bell et al. [79-81], in two sets of experiments, showed that using both methods (rich first stage and lean second stage and vice versa) decreases the thermal and prompt NO_X concentrations. Their best result was a 50% reduction of NO_X in the case of lean combustion at the primary stage, followed by the addition of a rich fuel mixture in the second stage. Khinkis et al. [82] performed experiments on staged combustion by removing the heat directly from the porous matrix. This keeps the combustion temperature generally below the temperature required for substantial NO_X formation. They embedded heat exchanger tubes directly inside the porous matrix and reported NO_X concentration levels of less than 10 ppm. They believed that intense heat transfers between the porous bed and the heat exchanger results in high combustion intensity, high efficiency, ultra low, NO_X generation, creating opportunities to design smaller combustors and lower operating costs. Maruko [29] performed similar experiments on multistage catalytic combustion using noble metal catalysts at conditions under 1000 °C and using silica at conditions up to 1400 °C. Pickenäcker et al. [51, 52] designed a multi stage porous medium burner according to the criterion presented by Babkin et al. [60] and measured NO_X and CO concentrations simultaneously. Their results showed that while other pollutants like CO and unburned hydrocarbons can be kept below the

limits of environmental standards, NO_X emissions could be decreased by 30% compared with the most efficient single stage porous medium burner.

Although multistage combustion in porous burners contributed to decreasing NO_X emissions, some aspects of this approach are yet to be explored. Several researchers published different results. Some believed using rich-lean stages will increase the NO_X emissions and some found that multi staging in either rich-lean or lean-rich would decrease the pollutant emissions significantly. How the lean-rich or rich-lean multi staging in porous burners contributes in the combustion process and the effect of thickness and material on each stage of stabilising of the flame are some of the unsolved issues in this field.

2.7 Liquid fuels

Combustion of liquid fuels in conventional burners, which employ a spray nozzle (or swirl spray [83]) to atomise and mix the fuel with air, faces many problems. Because of poor spray qualities and difficulties in flame stabilisation, due to the influence of the aerodynamic behaviour of air and fuel droplets, conventional liquid fuel burners show a low power modulation. The vaporizing and combustion zones are not completely separated, so the system is sensitive to changes in the temperature and flow field, which arise with power rate modulations [42]. Hence, burners that make stable continuous combustion possible for a wide range of heat loads for liquid fuels are required. PB is one of the most successful systems in achieving this. Using porous burners with liquid fuels will extend the flammability limit against the input load of liquid fuels as a result of the contribution of the porous matrix as a fuel distributor, a flame holder and a medium to absorb the imposed radiation. PB also enhances the evaporation rate of the liquid fuel, obtaining help from the significant radiation heat from the solid phase [84-88]. Once the liquid fuel vaporises, the combustion of the vapour-air takes place using a similar mechanism to that of gaseous fuels, described before in detail. Of interest in liquid fuels is the auto-restart phenomenon. It implies that when a flame within the porous medium extinguishes due to a momentary interruption of the fuel or oxidiser, combustion will immediately restart after restoring missing fuel or oxidisers. This parameter will increase the safety factor for industrial applications. Incineration of liquid hazardous waste [53,

89] is one of the most useful applications of porous liquid burners. Due to the low energy content of liquid hazardous waste, incineration in conventional burners is quite difficult. On the other hand the soot formed in conventional incinerators often acts as a local condensation site for hazardous materials, becoming hazardous itself when emitted to the atmosphere. Vaporization of liquid fuels before combustion can prevent this problem.

Jugjai et al. [87] and Takami et al. [90] investigated the flammability limit of kerosene in a porous burner and quantified the NO_X emission from the liquid fuel stabilised in the porous burner. Jugjai et al. [87] successfully stabilised a flame within a limited range of equivalence ratios of $\varphi = 0.37$ to $\varphi = 0.55$ for a firing rate of 520 kW/m^2 to 700 kW/m^2. Takami et al. [90] performed similar experiments within the range of firing rates falling between 674 kW/m^2 and 3879 kW/m^2. Their apparatus, which had a relatively high turndown ratio, (more than 7) could operate within equivalence ratios of 0.9 down to 0.1. Their experimental results showed that the temperature profile for kerosene-air flames is very similar to methane-air flames. They also measured the NO_X emission behaviour within their experiments in 5 different axial positions along the bed. The measurements showed NO_X emissions of less than 60 ppm for most experiments, except under extreme conditions. These values showed a good improvement when compared with NO_X emissions from the combustion of kerosene in conventional open-spray liquid burners. Korzhavin et al. [91] investigated the propagation characteristics of flame inside a porous medium wetted with n-octane as fuel. The whole porous matrix was restricted in a closed vessel. For each individual test case, the tube was charged with air up to a particular pressure and then sealed. Measurements were taken for a wide range of initial temperatures, from 18 °C to 39 °C and initial pressures from 70 kPa to 700 kPa. The pressure rise showed a bigger value for porous mediums wetted with liquid hydrocarbon, when compared with a dry, porous medium. They observed two different combustion regimes inside the porous medium: a high velocity regime and an evaporative-diffusion regime. The evaporative-diffusion regime showed greater sensitivity to porous media heat capacity variations. Fuse et al. [84] developed a fuel-vaporizing combustor equipped with a porous burner made of Al_2O_3 and 1.7 MHz-ultrasonic oscillator using ethanol as fuel. Stable and complete combustion was achieved within a range of equivalence ratios between 0.63 and 0.8, similar to a

premixed combustion. Compared with premixed combustion in porous burners, the NO_X concentration was higher (59 ppm to 97 ppm on a 0% oxygen base) due to an increase in the heat value per surface area of the flame, caused by a shorter flame.

Applications of liquid fuel in PB show a promising future for this industry. Low emissions of pollutants, high combustion intensity with moderate turndown ratios and compactness have made PBs more advantageous when compared with conventional liquid fuel burners. On the other hand, liquid fuels, compared with gaseous fuels, have a higher energy rate and less pressure drop due to the increase in their mole number.

2.8 Pollutant emissions

Beginning in the 1960s, increasing levels of smog and toxic pollutants became the major environmental problem. Hence, one of the major concerns of any newly-designed combustion system is to minimise and control pollutant emissions.

Combustion processes occur in the gas phase (as the interacting medium) without any significant contribution to and from other phases. This will make the temperature rise steeply in the vicinity of the flame. The combustion process has small radiation and conduction characteristics, which result in high local temperatures. These high local temperatures help in the formation of large quantities of pollutant emissions, especially nitrogen oxides. In PB, the flame propagates in cavities of an inert or catalytic porous medium [63]. The intensive heat transfer between the gas- and solid-phase makes the local temperature relatively low and prevents the high temperature regions that cause the production of nitrogen oxides. Hence, it has been found that PB is one of the most successful combustion systems to achieve this goal.

Most experiments performed by researchers on different types of PBs have quantified major pollutants, like NO_X and CO. Bingue et al. [92] experimentally investigated NO_X and CO emissions from a porous burner operating under lean and ultra-lean conditions. Within the ultra-lean region ($\varphi < 0.5$) they measured NO_X concentrations of less than 4 ppm and CO concentrations of less than 10 ppm. They also found that although faster filtration velocities and higher combustion temperatures correspond to higher NO_X concentrations, the emission index is more dependent on the equivalence ratio than any other parameter. The emission index is a

dimensionless quantity and for species *i* can be defined as the ratio of the mass of species *i* to the mass of fuel burned by the combustion process:

$$EI_i = \frac{m_i}{m_F} \qquad (2.7)$$

Mößbauer [25] investigated steady combustion within the range of 0.53 to 0.91 for methane/air. They reported NO_X concentrations of less than 25 mg/kWh and CO concentrations of less than 7 mg/kWh over the complete range of dynamic power (about 1:20). They showed that porous burner emissions are significantly lower than the European standards, as shown in Figure 2.8. These results were in the same order of magnitude for NO_X measurements on a radiant porous burner developed by Bouma et al. [93].

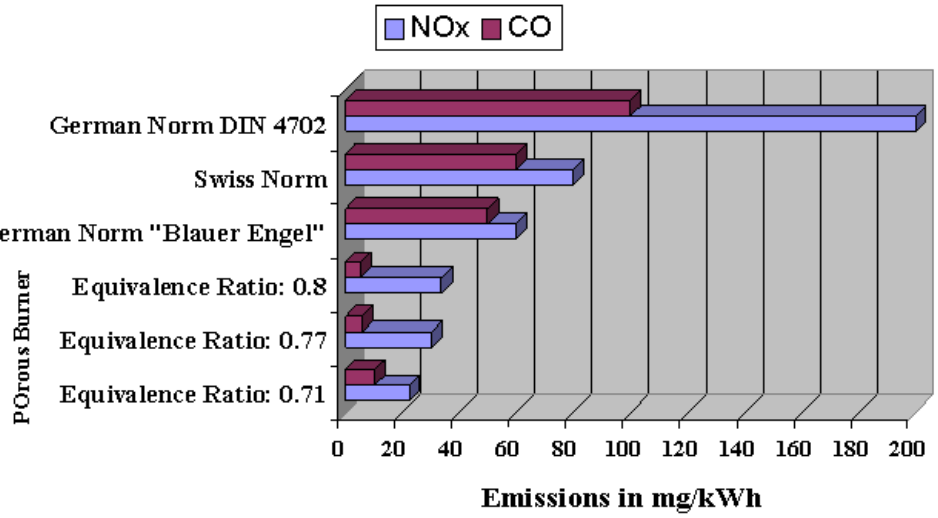

Figure 2.8: NO_X and CO emissions of a 30 kW porous media burner in comparison with stringent European standards [25]

Cerri et al. [28] investigated NO_X and CO production in porous media for non-catalysed, surface-catalysed and fully-catalysed ceramic foams. Figure 2.9 shows that the NO_X emissions for three different types of porous matrices are not very different. Although for higher excess air values, the fully-catalysed burner yields NO_X concentrations higher than those for non-catalysed and surface-catalysed burners. Figure 2.10 shows CO concentrations for non-catalysed burners at power densities less than 300 kW/m^2 and at excess air values less than 10% or bigger than 80%, were higher than for the two other types of burners. Under these conditions, the

catalyst promoted a significant reduction of the CO levels. Such a reduction was more pronounced for the surface catalysed than for the fully-catalysed burner. Presumably, the higher local momentum in the fully catalysed foam resulted in a lower residence time for the reacting gases in the catalytic burner.

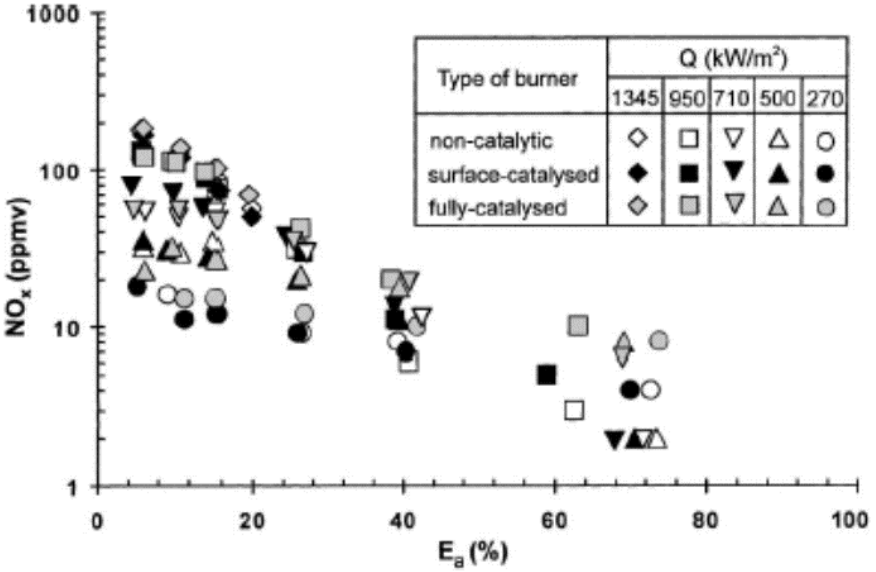

Figure 2.9: NO_X emissions as a function of excess air E_a for different firing rates Q for three ceramic burners: non-catalytic, surface-catalysed and the fully-catalysed burners [28].

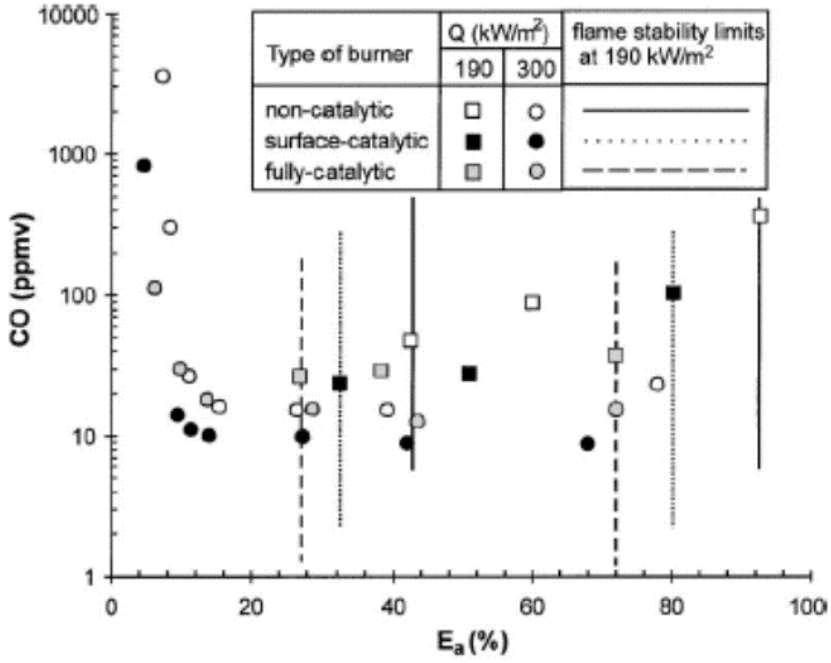

Figure 2.10: CO emissions as a function of excess air Ea for two different firing rates Q=190 and 300kW/m2 for the three ceramic burners: non-catalytic, surface-catalysed and the fully-catalysed burners [28].

2.9 NO_X reduction mechanisms

New combustion technologies with low NO_X emissions have been developed and utilised. The lifetime of most stationary combustion systems is decades long. Hence, the treatment of exhaust gases to decrease the emissions of NO_X becomes more viable. Different NO_X reduction mechanisms have been developed in the past. These mechanisms include burner replacement, fuel staging, fuel reburning, steam or water injection, selective catalytic reduction and selective non-catalytic reduction [94]. In many instances this has led to a reduction in combustion efficiency and has required expensive retrofits [95]. Among the aforementioned NO_X reduction techniques [95], reburning [96] is a cost effective technology [97] in which nitric oxide is consumed using fuel as a reducing agent. This method was developed in the early 50s and was termed "reburning" by Wendt et al. [96]. An NO_X reduction of 50%-70% [98] is achievable using such an approach. The process involves partial oxidation of the reburning fuel, under fuel-rich conditions, followed by the reaction of hydrocarbon radicals (CH_X) and NO. This results in the formation of intermediate nitrogen species such as HCN and their subsequent conversion to N_2. More recently, detailed analysis of the reburning chemistry, by Dagaut et al. [99] along with an earlier study by Kilpinen et al. [100], has revealed the important role of the HCCO radical which reacts with NO to produce either HCNO or HCN, both of which are then subsequently reduced to N_2. In general, reburning happens when gaseous, liquid or solid hydrocarbon fuels are injected downstream of the main combustion zone. Further reductions of NO_X species, through advanced reburning and second generation advance reburning, are also possible via the addition of agents such as ammonia [101], urea or similar substances [102]. NO_X reductions of up to 90% are achievable using advanced reburning technologies, which invariably involve catalytic surfaces. Such successful results have encouraged researchers to conduct bench-scale and pilot-scale reburning experiments in order to develop the technology to a mature stage where it can be implemented in existing combustion systems.

One of the earliest industrial scale systems for NO_X reburning was performed in Japan. Their system was capable of reburning 50% of the NO_X in a full-scale boiler by Mitsubishi in the early 1980s. Later, the Babcock & Wilcox [103] company in Japan successfully applied the technology to a few wall-fired utility burners. Ever

since, the reburning process has been investigated in many different combustion systems, such as flow reactors [104] and jet stirred reactors [105, 106].

Despite the successful progress achieved, reburning is still considered a very complex process, which relies on several parameters which influence its performance. It also involves a number of interrelations among these parameters, which make it very difficult to study the influence of each variable individually. The most important parameters which control reburning efficiency are finite-rate mixing, equivalence ratios and reaction zone temperatures [100, 107, 108].

NO_X reburning has been analysed extensively for a wide range of temperatures. Maintaining a uniform constant temperature over the experimental domain has made the experiments a real challenge. Bilbao et al. [109] have conducted a range of experiments in a 1500 mm long quartz-tube, which has a diameter of 23 mm. Observing a longitudinal temperature profile they assumed that the temperature is almost constant in a 600 mm zone in the middle of the tube. They used this zone to determine the gas residence time. Their results showed that for moderately low temperatures (between 600 °C and 1100 °C) NO_X reduction efficiency increases as the temperature increases. It was found that at a given temperature, the fuel effectiveness in NO_X reduction follows the sequence: acetylene, ethylene, ethane, natural gas and methane. It is also found that natural gas and methane are of greater interest for high temperature applications, while acetylene is more suitable for low temperature cases. Dagaut et al. [105] explained this sequence through the importance of the HCCO intermediate for the production of HCN and extended the list to include propene. They noted that more HCCO is produced from acetylene fuels than the other reburning fuels, especially at lower temperatures.

Using similar experimental techniques, Dagaut and Ali [110] extended this study to include a Liquefied Petroleum Gas (LPG) blend for a range of equivalence ratios and a temperature range of 950 K to 1450 K. They found that using LPG as a reburning fuel follows the same general oxidation path already delineated for simple alkanes.

Williams and Pasternack [111] used a McKenna flat flame burner to investigate the intermediates of premixed flames for a variety of fuels doped with NO. They showed that for a fixed temperature of ~1800 K the methane, ethane and ethylene flames all have similar re-burning chemical pathways, whilst acetylene flames are quite

different. They noted that acetylene produces about three times as much CN and NCO as other fuels.

A few studies also examined the controlling parameters and the type of fuel that can be used for the reburning process. Ditaranto et al. [16] investigated the influences of oxygen concentration, temperature, steam concentration, and mixing conditions in a laboratory scale experimental set-up, representing a 5 kW methane jet flame burning in the turbine exhaust gas of a virtual 10 kWh gas turbine, containing up to 50 ppm NO_X. The NO_X reduction was successfully reproduced, showing reduction efficiencies as high as 30%. It has been found that reburning is best achieved at conditions with low oxygen, low temperature and high steam concentration. Others [112-114] examined the influence of a variety of gaseous, liquid and solid fuels on the reburning efficiency of NO_X, while others again concentrated on reducing NO_X from the recirculated exhaust gas from oxy-fuel combustion systems [115, 116].

It is clear from the above that moderately low temperatures, fuel rich conditions and sufficiently high residence times are required to achieve the reduction of NO_X using hydrocarbon fuels. It is also apparent that well controlled conditions are required in order to optimize the conversion efficiency better.

In summary, it can be concluded that porous burners [32, 54, 62, 117-121] were found to be a suitable medium to achieve such controlled conditions. The large inner surface area of the porous bed ensures an efficient heat transfer [117] between the solid and gas phases. Although in most porous burners, overall flow is calculated in the laminar range; in the vicinity of the small pores within the porous media there is a likelihood of a turbulent gas flow. This effect, locally, increases the effective diffusion and heat transfer within the gas phase. These phenomena result in a different temperature pattern from the adiabatic flame temperature for different equivalence ratios. The maximum temperature in porous media for a range of equivalence ratios between 1 and 2 are considerably below the adiabatic flame temperature. This great advantage results in better NO_X conversion and makes porous burners a suitable post processor for NO_X reburning.

2.10 Surface reactions

The highly developed inner surface of the porous bed ensures an efficient heat transfer between the solid and gas phases. While the overall flow is laminar, in the vicinity of the small pores within the porous media, the local gas flow is turbulent. As a result, modelling the combustion process in porous burners is very challenging due to the requirement for the simultaneous solution of mass and energy balances for a large range of geometric length scales, coupled with the estimation of the thermo-physical and thermo-chemical properties. This is further complicated by the requirement for large chemical kinetic mechanisms in order to describe pollutant formation and other kinetically-controlled phenomena, adequately. Porous media also embrace a wide range of pore sizes, porosities, pore connectivity and specific interfacial areas between phases. Porous matrices use different organic-, ceramic- or metallic-based materials and the fluid-phase properties may range from low-pressure gases to liquid macromolecules. Convection, conduction and radiation between the gas- and solid-phase, and energy release due to chemical reactions, must also be included [56].

Many researchers have modelled porous burners treating the non-catalytic porous media as being chemically inert [23-25, 54, 61, 64, 78, 91, 92, 118-122]. However, it is known that the presence of surfaces can strongly influence gas-phase reaction systems (e.g. the oxidation of hydrogen and carbon monoxide [123]). This effect arises as a result of heterogeneous reactions between gas-phase radicals and surfaces. The rate of radical termination at a surface is strongly influenced by both the nature of the surface and the conditions, if any, under which the surface has been pre-treated. Given the large surface-to-volume ratios that are characteristic of porous burners, it seems imperative that these surface reactions, leading to termination of the gas-phase radicals, be considered when modelling combustion, and the formation of minor species, in porous burners. To the author's knowledge, no previous studies have considered the impact of surface reactions on NO_X conversion in porous burners.

In the absence of detailed information about the surface or an elementary heterogeneous gas-solid reaction mechanism, it is possible to use a short-cut approach to estimate the impact of surface reactions for a gas-phase system. One

such approach is to estimate the maximum possible rate of radical termination as the mass-transfer-limited rate [124-126]. In this case, the diffusion-limited reaction rate may be calculated following the method of Thomas et al. [124], based on a cylindrical channel model, assuming laminar flow. Another related approach is to assume that only a certain fraction of radicals that diffuse to the surface are consumed, as defined by a sticking coefficient or collision probability.

2.11 Modelling

Modelling the combustion process in porous burners has been the most challenging task in their development. Simultaneous solving of mass and energy transfers under the influence of a large range of geometric length scales, thermo-physical and thermo-chemical properties, besides the chemical kinetics for both solid- and gas-phases, has retained the modelling stage as quite immature. Porous media embrace a wide range of pore sizes, porosities, pore connectivities and specific interfacial areas between phases. The prediction of pollutant formation requires the use of detailed simulations and chemistry. Convection, conduction from gas to a solid medium and chemical energy release from reactants must be included in the gas-phase equation, while conduction, radiation and convection from solid to gas should be considered in the solid phase equation. Using a catalytic porous matrix will also increase the non-equilibrium even further [56].

Several researchers have modelled the combustion process in porous burners in the last few decades. Based on chemical kinetics, models are classified as one-step reaction [127-129], multi-step reactions or complete reaction sets [36, 118, 130]. Among those multi-step reaction modelling studies, Mishra et al. provided the most complete calculations, accounting for energy equations for the solid and the gas phases (non-local thermal equilibrium) and multi-step chemical kinetics. Mishra et al.'s [130] calculations also included the issue of radiation from the solid porous matrix, by considering the porous medium to be absorbing, emitting and also scattering.

The one-step reaction mechanism assumes that all of the heat releases in a thin flame front but the multi-step reaction mechanism considers a wider reaction zone. Hsu and Matthews [131] studied one-step and multi-step kinetic models and differences in

their performance. They found that one-step kinetic models are not accurate enough to predict the peak flame temperatures, but they can be used for prediction of exit temperatures and flame speeds with a reasonable accuracy. While the one-step reaction simplifies the numerical modelling, a multi-step reaction is more representative of the actual combustion process. Furthermore, incomplete combustion, where reactants are not completely converted to their final products, can only be modelled with multi-step reaction mechanisms. For either case, the resulting equation set is extremely stiff and it is difficult to achieve a converged solution. Even successful standard techniques (such as the PREMIX code [132]) often fail and must be modified when applied to porous media.

Shardlow [133] developed a one-dimensional numerical model which has the capacity to model both homogeneous and heterogeneous reactions in multi-layered porous burners. The numerical model represents the conservation of energy equations for both gas and solid phases. Those energy equations include the convective heat transfer between the gas and solid phases. The radiative heat transfer is considered only in the solid phase energy equation. Although he showed a good agreement between his model and some experimental data, the code is still incapable of predicting flame properties using catalytic porous media. Rumminger et al. [14] used another one-dimensional model to analyse a radiant surface burner and to investigate the influence of placing a porous medium close to the burner exit on radiant efficiency, NO_X and CO production.

Predictions of super-adiabatic flame temperatures within the porous matrix have been reported by many researchers. Min and Shin [8] showed the excess enthalpy phenomena inside a ceramic honeycomb. Their model showed a good reproduction of temperature profiles and flame behaviours. On the other hand the model predicted a stable flame downstream of the combustor, which was not the case in the experiment. This instability can be blamed on the two-dimensional effects of heat loss, while the analysis was based on a one-dimensional representation of heat loss. Hackert et al. [129] developed another model and examined a honeycomb burner and a geometry consisting of many parallel plates. The two-dimensional model was capable of predicting the peak burning rate for insulated burners, the downstream radiant output and their behaviour as a function of the equivalence ratio.

Other researchers modelled flame stabilization, heat transport mechanisms, and chemical kinetics in porous burners. Early work on surface-stabilized burners was performed by Yoshizawa et al. [134], who applied a one-dimensional two-phase model with one-step kinetics to investigate the effects of heat transport parameters on flame structures and burning velocities. Later on, Martynenko [23], in a similar experiment, showed that the most important parameters for self-sustaining combustion in an inert porous medium, under a fixed thickness of porous medium, are:

- the superficial velocity of the gaseous phase
- the thermal conductivity of the solid and
- the convective heat transfer coefficients across different phases.

Neef et al. [120], using a one-dimensional model, showed that a minimal mass flow rate is required to establish steady combustion inside a porous inert media. They defined their model based on a multi-layer porous burner, which was constructed by Trimis and Durst [135]. They found that full combustion, including flames, exists for a Péclet number within the range of 800 to 3000. For Péclet values between 350 and 800, when more than 75% of reactants are consumed, the combustion was not complete and for values less than 350, no combustion existed. They compared their results with a numerical solution of a two-dimensional problem and observed that there is a good agreement in the cases of temperature and mass fraction distribution along the cooling boundary. Like most of the models, radial temperature distribution across the bed was non-uniform and the agreement between solutions of one-dimensional and two-dimensional models was not completely satisfactory.

Sathe et al. [127] and Rumminger [36] employed models to analyse flame behaviour in a porous radiant burner PRB. Sathe et al. [127] using a one-dimensional, one-reaction model, showed that stable combustion could be maintained in two spatial domains: one in the upstream half of the porous bed and another in a thin layer close to the exit plane. In the upstream zone, the flame front moved downstream as the flame speed increased. Tong et al. [136] using a one-dimensional model with spatially dependent heat generation carried out an analysis to determine the performance of PRB as a function of fibre size. Silica and alumina fibres were considered for use as porous materials. They found that a smaller fibre diameter

results in a smaller, single scattering albedo and a higher radiant output for both types of fibres. They obtained an increase of 63% and 109% respectively for the silica and alumina fibres for a characteristic temperature of 1000 °C and 72% and 150% for a characteristic temperature of 1500 °C.

Certain common assumptions have been made for all models of combustion within porous media. Although those assumptions helped scientists to simplify the modelling and improve the knowledge of combustion within the porous bed, still, some of them led to inaccurate solutions. Most of the researchers assume that the fuel and oxidiser are completely premixed and have certain initial conditions when they enter the system. Radiation heat transfer to/from the gas-phase has been neglected in most models and it has been assumed that the gas within the pores works as non-participating medium. In all cylindrical models, it has been assumed that there is no radial heat loss to the surrounding environment and these assumptions have led to a relatively high level of inaccuracy in the models to date.

2.12 Research Objectives and Gap

It is clear from the above literature review that, despite many years of research on the different aspects of porous burners' design, operation and characteristics, there are very few studies that address the issue of NOx and TFN (Total Fixed Nitrogen) reduction using PBs. While different aspects of porous burners have been studied at length, their application to NOx and TFN reduction and the effect of surface reactions are yet to be explored.

BED FUEL INJECTION IN A POROUS BURNER

3.1 Introduction

Due to physical limitations, and in particular air and fuel mixing problems, few studies have been conducted on the injection of fuel at different positions in the bed instead of premixing it with the air externally. An extensive search in the literature resulted in very few studies, some in non-peer reviewed publications [137, 138].

One of the major problems with premixed porous burners is flashback. Hall [139] reported that flashback problems could be eliminated by altering the fuel and air injection positions but CO emissions were considerably higher than those from premixed air/fuel mixtures. He also showed that the turn-down ratio range in 'non-premixed' PBs is wider when compared with the equivalent fuel to air ratios in premixed PBs.

Kamal and Mohamad [140] used a vane-rotary burner to stabilise non-premixed flames and found that the radiation flux was improved. They also measured the CO and NO_X emissions from their high swirl burner and reported very low values of pollutant emissions from their non-premixed porous burner.

The following chapter explores the challenges associated with injecting the fuel into the porous bed and its impact on mixing and stabilisation of a flame in the porous burner. The data will be used to develop an understanding of the flame behaviour and pollutant emissions in a porous burner when the air and fuel streams are introduced to the porous burner at different locations. Later on, these data will be compared with a premixed air and fuel mixture inside a porous burner in order to explore optimum ways to operate porous burners safely.

3.2 Experimental setup

An experimental system was designed and built for this study. The system was designed in such a way that it allows the user to investigate the effects of different parameters on chemical and physical flame properties in a porous burner. These parameters include the flow velocity (flow rate or firing rate), equivalence ratio (excess air) and chemical kinetics (different fuels). The maximum flame temperature, flame location and flame thickness were some of flame properties investigated in this study. Access to a multi-component gas analyser system allowed for the accurate measurement of O_2, NO_X, CO and CO_2. The burner was designed in such a way as to make the radial and axial gas sampling in the porous bed possible. The modular design allowed for fast and easy assembly and the flexibility to test different configurations. The burner system consists of three sections: namely, a swirl-burner, a heat exchanger and a porous bed. The components are connected to a control system to allow full control of the burner.

3.2.1 Swirl-burner

The swirl-burner has two roles: to preheat the porous medium and supply hot exhaust gases to the PB. It consists of a central jet with an 8mm inner diameter surrounded by a bluff-body with a diameter of 50 mm. The use of a bluff body ensures a shorter and more stable flame. The annulus has an inner diameter of 100 mm and extends to 290 mm. A combustion chamber is attached to the annulus and extends for 190 mm. It has a 50 mm side opening for ignition and a 25 mm hole for a flame detector. Different fuel mixtures can be supplied through the central jet (Figure 3.1 and Figure 3.2).

Air is sourced from a compressor through an adjustable regulator and pressure gauge. It is supplied through three tangential inlets on the sides and two radial inlets further upstream. Tangential air inlets were chosen to create a swirling flow, which creates better mixing and shorter flames through a recirculation zone stabilised on the bluff-body. The relative air mass ratio supplied to the tangential and radial air inlets controls the swirl number and the upward swirling motion. The current design ensures a stable, short flame for a wide range of conditions.

To meet safety concerns a UV flame detector (Landis and Staefa, QRA10.c) is installed in the 25 mm opening in the combustion chamber. It reports the presence of the flame inside the combustion chamber to a solenoid, which controls the fuel supply. If the flame blows off, the fuel flow will automatically shut down. A quartz plate is placed in front of the detector. The plate allows the transmission of the UV light to the detector and prevents damage of the detector by the hot gases.

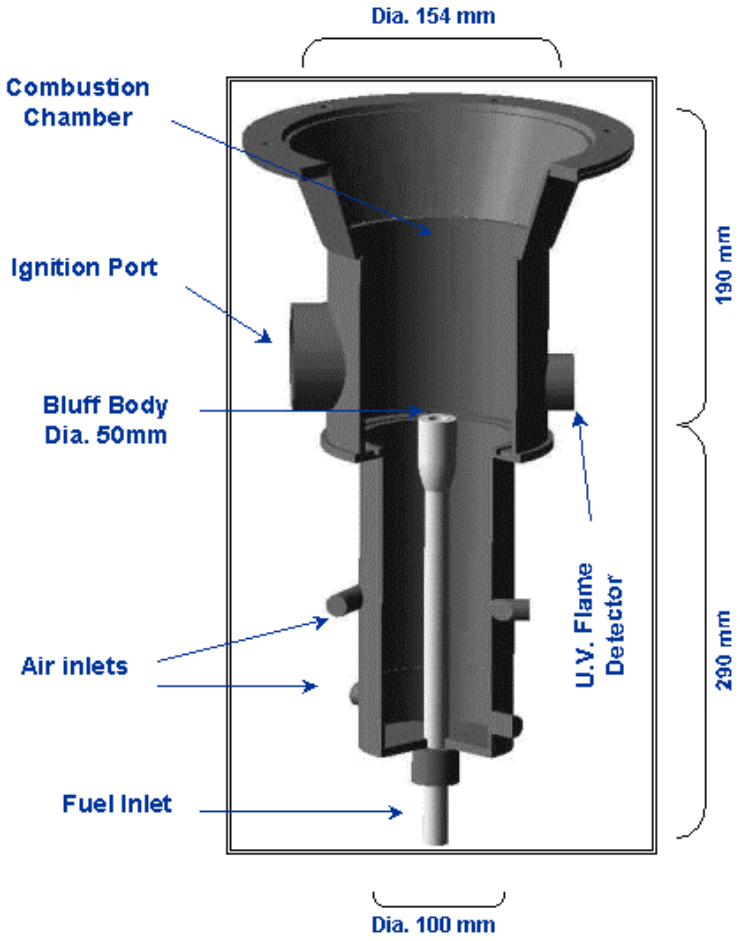

Figure 3.1: Schematic description of swirl burner

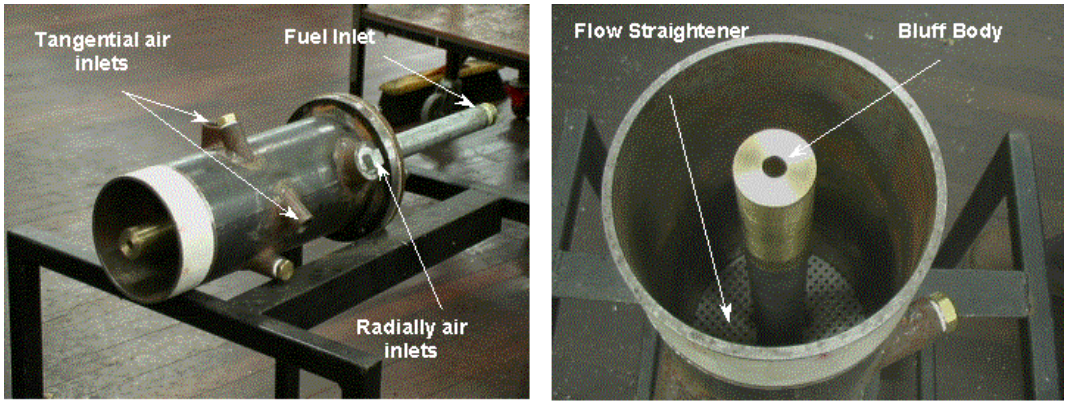

Figure 3.2: Manufactured swirl burner, air and fuel inlets (left), bluff body and flow straightener (right)

3.2.2 Heat exchanger

Controlling the temperature inside the PB was essential in order to conduct different experiments and test different configurations. In particular it allows the de-coupling of the reactants' temperature and the equivalence ratio. A heat exchanger is used to control the temperature of the exhaust gases before entering the porous burner. The heat exchanger extends for 400 mm and is made of ¼" copper tube. The outer annulus has an inner diameter of 154 mm. A fibre blanket, 25 mm in thickness, is used to insulate the heat exchanger to minimise heat losses to the surroundings. Water is used as the coolant. The heat exchanger also enhances the mixing of the hot products and excess air, which improves the uniformity of the flow properties at the inlet to the PB.

The heat exchanger was designed to reduce the temperature of the swirl-burner exhaust gases from 2000 K to 800 K. This was a challenging task due to the space limitations and the low heat transfer capacity of air. A heat transfer analysis was performed, resulting in the design of a heat exchanger unit, as shown in Figure 3.3.

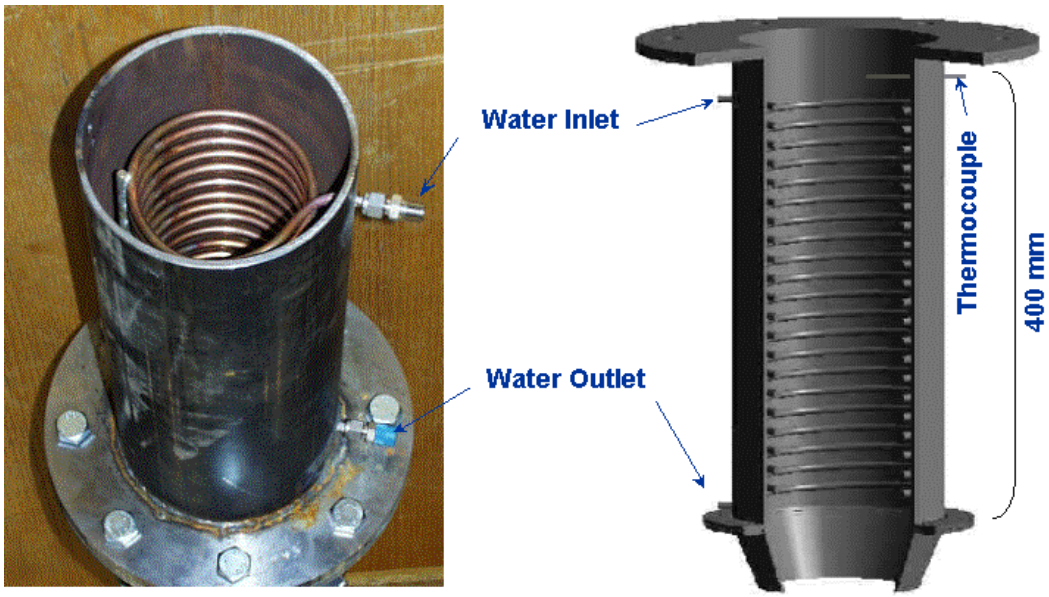

Figure 3.3: Manufactured (left) and schematic view of heat exchanger (Right)

3.2.3 Porous burner

A circular geometry for the porous burner was selected to match the swirl-burner and the heat exchanger. This symmetrical geometry also helps to make the radial heat distribution across the surface more uniform, resulting in less complexity in modelling. The modular porous burner consists of a main ceramic tube, insulation and fuel distribution system: each one is described in detail, below. Insulation for the porous burner is necessary to minimise heat losses through its walls and also to achieve a better heat uniformity. A number of holes circumferentially drilled along the main ceramic tube can be used as inlets for the temperature probes, sampling gas probes and as ports to introduce extra fuel or air. The main ceramic tube can be filled with different porous materials and shapes in different experiments.

3.2.3.1 Main tube

The main tube is made of ceramic (99% Alumina) with an inner diameter of 154 mm, an outer diameter of 214 mm and is 600 mm long (Figure 3.4). It is attached to the heat exchanger via a thick flange and is sealed using a high temperature resistant gasket. The ceramic tube has 22 multi-purpose holes (circumferentially), with 7 mm diameter, spaced at 25 mm and staggered at 90º. The holes in the casing of the ceramic tube are used for inserting N-type thermocouples. They can be positioned at

the centre of the cylinder or can be moved across the ceramic tube. This allows for the measuring of radial temperature profiles in different levels of the porous medium. The holes can also be used for inserting the fuel distributor in any level. A perforated plate is used upstream of the ceramic tube to hold the porous medium and make the incoming gases more uniform. A sampling probe can also be inserted in any of the side holes.

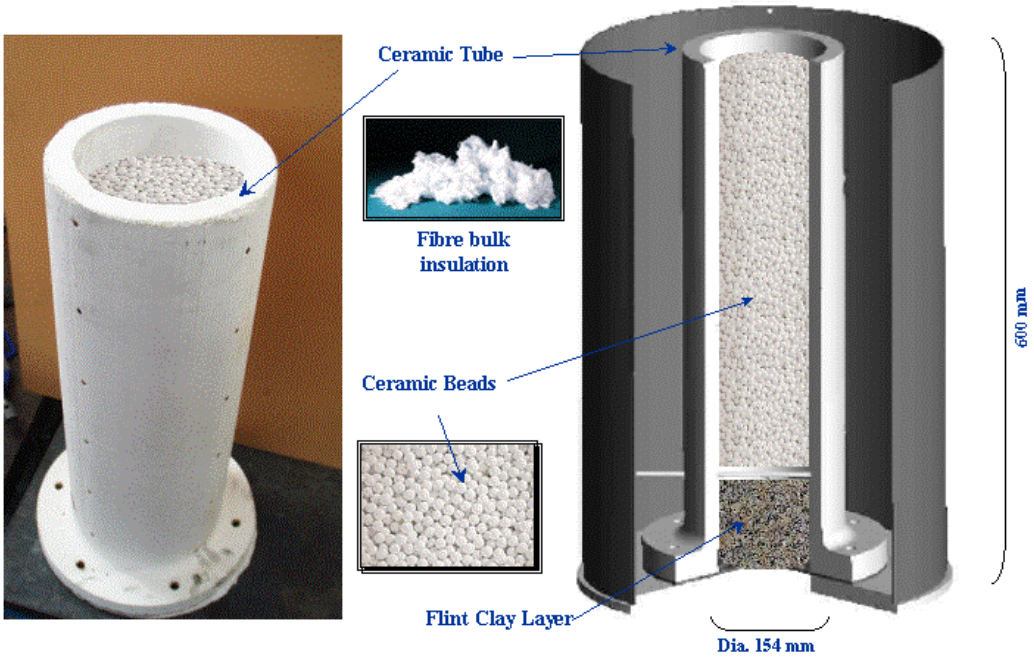

Figure 3.4: A view of the manufactured (left) and designed (right) ceramic tube

3.2.3.2 Insulation

The ceramic tube is insulated using fibre bulk to minimise heat losses to the surroundings. A 2mm thick perforated sheet is rolled to create a cylinder with 450 mm diameter. The fibre bulk is then inserted between the ceramic tube and the perforated plate. The use of the perforated plate allows for the easy insertion of the thermocouples, fuel distributor and gas sampling probe through the fibre bulk and the holes in the ceramic tube. Minimising the heat losses through the outer surface of the ceramic tube is essential to achieve a quasi-adiabatic condition, which is easier to model and to control. The selection of the insulation material and thickness was calculated analytically as a one-dimensional convective-conductive heat process across a multiple layer cylinder. The total thickness of the insulation material was

selected such that the outer surface temperature of the perforated cylinder is less than 50 °C at all times. Such a low temperature satisfies key safety requirements.

3.2.3.3 Temperature measurements

Due to the high radiation characteristics of the porous materials and continuous heat transfer between the gas and solid phases, solid phase temperatures could differ from the gas temperature along the porous medium [141-144]. The dominant heat transfer mechanisms include but are not limited to conductive heat transfer in solid phase, convection from incoming gas and radiation from solid to gas phase. There are also other parameters that could affect the temperature measurements (in this study, using thermocouples inside the porous medium). These parameters include the temperature range, thermocouples' response time, thermocouples' junction diameter and emissivity [145].

Temperature measurements, and hence errors, associated with temperature measurements could also be a function of time. Depending on the response time of the thermocouples' junction, readings of the same point could change slightly as time passes.

Considering the expected temperature range to which the thermocouples will be exposed, N-Type thermocouples were selected for all subsequent experiments. All the thermocouples were similar and they were all calibrated before the experiments. The thermocouple's shield is made of Inconel alloy 600, which has an emissivity of 0.19 - 0.21. For temperatures between 293 °C and 1250 °C, thermocouples could have a maximum ± 9 °C inaccuracy in addition to those above-mentioned parameters.

These errors have been minimized for the temperature measurements by waiting long enough for each condition to let thermocouples' reading be stabilised and get to a quasi-equilibrium state before changing the conditions further.

3.2.3.4 Material selection

Figure 3.5 a, b and c show different materials and shapes that can be used as the porous matrix. The modular design of the porous burner allows for the use of a variety of materials, shapes or layers (bilayered or multi-layered). Most experiments

are accomplished using alumina-based flint clay (Figure 3.5 a) as flame arrestor in the first region and alumina ceramic beads (Figure 3.5 b) in the combustion region as an inert porous matrix. A layer of flint clay is set on top of the perforated plate. The flint clay has low thermal conductivity, which helps in minimising backward radiation and flashback into the lower sections. It consists of fine materials (2 mm to 3 mm in diameter for some experiments and 2 mm to 5 mm for others) that work as a flame arrestor because of the narrow passageways. Alumina ceramic beads of a 6mm nominal diameter are then added on top of the flint clay.

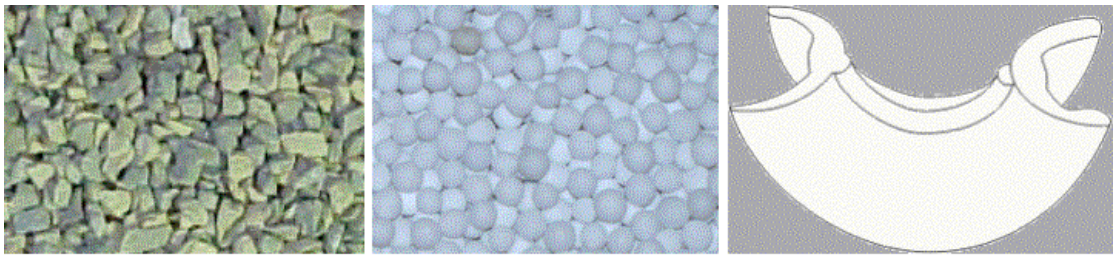

Figure 3.5: Varity of material used as packed bed: (a) Calcinated flint clay, (b) Alumina ceramic beads and (c) alumina saddles as an alternative for ceramic beads

3.2.4 Fuel distribution system

For those experiments where the fuel should be fed into the PB independently from incoming gases to the PB, the fuel can be introduced via a fuel distributor through one of the circumferentially distributed holes around the ceramic tube. Different shapes of fuel distributors were made and tested. The effects of each fuel distributor on flame uniformity, flame thickness and location were investigated and are described hereafter.

3.2.5 Control system and Data collection

All the thermocouples are attached to a 16-channel data logger (DATA SCAN 7220 RS 629-415), which is used to send all the measured temperatures, at fixed time intervals, to a PC and store them in an ASCII file.

The gas sampling tube takes the exhaust gases to the gas analyser unit (Figure 3.6) where all the data are analysed and recorded in a file. The gas analyser system consists of a FUJI ELECTRIC ZRH CO_2 and CH_4 analyser, Thermo Environmental

42H Chemiluminescence NO_X analyser, ECOTECH ML®9830B CO analyser and ECOTECH 9400 Data acquisition system. Table 3.1 shows the technical specification of the gas analyser components used in the gas sample recordings.

The data acquisition system used the data control software AQMS, version 5.00.3, to interpret and store data in an ASCII file. Further details can also be found in Section 3.2.

Apparatus	Range	Accuracy	Zero drift	Span drift
Thermo Environmental 42H Chemiluminescence NO_X analyser	0-10, 20, 50, 100, 200, 500, 100, 2000, 5000 PPM	50 PPB	50 PPB	± 1% Full scale
FUJI ELECTRIC ZRH CO_2 and CH_4 analyser	0-0.05, 0.1, 0.2, 0.5, 1, 2, 5, 10, 20, 50	± 0.5% Full scale (for low range) ± 1% Full scale (for high range)	±2% of full scale/week	± 2% of full scale/week
ECOTECH ML®9830B CO analyser	0-200 PPM	0.1 PPM or 1% of reading, whichever is greater	0.01 ppm per °C	0.05 per °C

Table 3.1: Technical specification of gas analyser as per calibration certificates

Figure 3.6: Gas analyser system showing the different analysers and data acquisition system

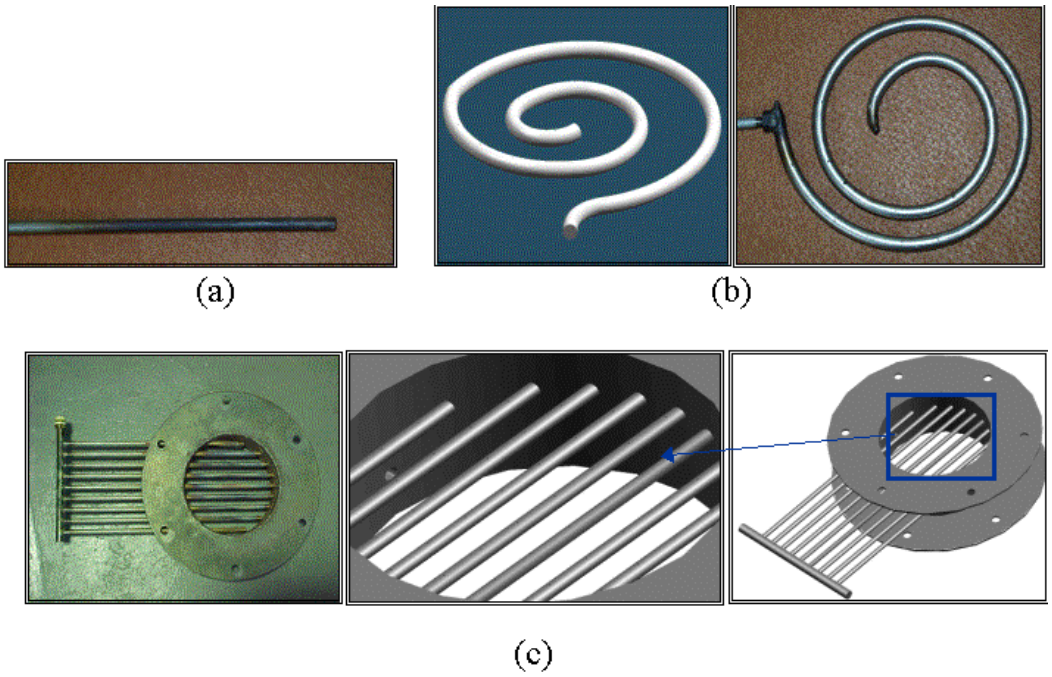

Figure 3.7: Different fuel distributor designs used in the experimental study: (a) single-tube, (b) spiral-tube and (c) multi-tubes

3.2.5.1 Single-tube fuel distributor

The fuel distributor (single-tube) was made of a 6mm stainless steel tube. It was blocked at the end and had two rows of 0.6 mm holes drilled in the horizontal sides along the tube (Figure 3.7 a). The insulated ceramic cylinder was filled with a 75 mm layer of flint clay, followed by a 350 mm layer of Alumina ceramic beads. The fuel (CNG – see Table 3.2) in the porous burner is supplied via a radially inserted tube mounted at the top of the flint clay layer. To do the experiments with a single-tube fuel distributor, the system was assembled as shown schematically in Figure 3.8 (right) and practically in the laboratory as shown in Figure 3.8 (left). For clarity, the assembled porous burner system is shown without the fibre bulk insulation layer.

	Mass fraction (Y)	Lower heating value	Molecular weight (W)	Mole fraction (X)
	(%)	(MJ/kg)	(kg/kmol)	(%)
Methane	90.9	50.016	16.043	95.3
Ethane	6.1	47.489	30.069	3.4
Nitrogen	0.9	0.000	28.013	0.5
Carbon dioxide	2.1	0.000	44.011	0.8
CNG	**100.0**	**48.391**	**16.807**	**100**

Table 3.2: CNG composition and physical properties.

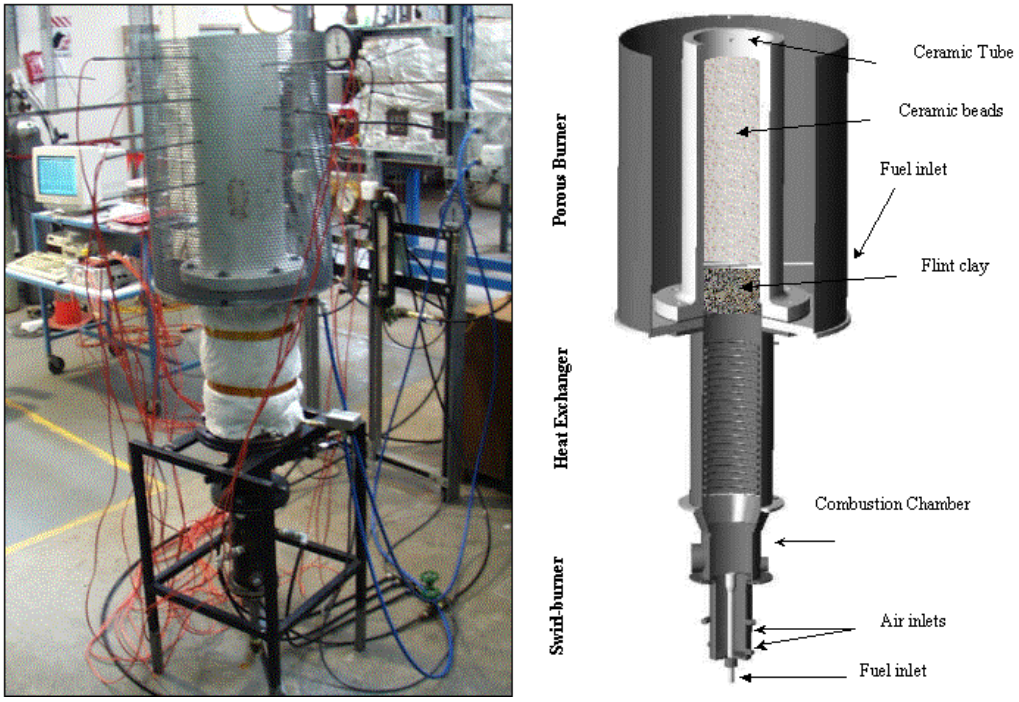

Figure 3.8: The porous burner assembly: schematically (right), and as assembled in the laboratory (left).

3.2.5.2 Spiral-tube fuel distributor

After completing the first set of experiments with a single-tube fuel distributor, a second fuel inlet (a spiral-tube) was manufactured to enable a better understanding of the fuel distribution effects across the ceramic tube in terms of the stability and location of the flame. The spiral-tube fuel distributor was also made of a 6 mm stainless steel tube rolled into a spiral shape with 0.6 mm holes in the horizontal sides and at the bottom (Figure 3.7 b). Similar experiments to those performed for

the single-tube fuel distributor were then repeated with the newly designed fuel distributor. The ceramic tube was filled with 75 mm of flint clay as a flame arrestor and 350 mm of 6 mm nominal size ceramic beads. The spiral-tube fuel distributor (Figure 3.7 b) was inserted through the second hole downstream of the ceramic tube. The porous bed was heated up to ~500 °C and the fuel in the swirl burner was turned off. The premixed and heated mixture was ignited on the top of the beads. After a while, the surface started glowing and the flame slowly propagated upstream. A stable flame was first established inside the porous bed and the equivalent ratio was adjusted by varying the air and/or fuel flow rates. The system was then operated for a sufficiently long time before recording the temperatures to ensure steady state conditions prevailed.

3.2.5.3 Multi-tube fuel distributor

A multi-tube fuel distributor consists of a series of stainless steel tubes (Figure 3.7 C), all inserted horizontally in a short steel cylinder (a mixing chamber). To make sure that the fuel distribution is as uniform as is physically possible, a code (Appendix B) was developed which calculates the distance between the steel tubes, holes on each tube and also the diameter of the holes.

The distance between the tubes and holes in each row is calculated using the results of the experiments on a single-hole tube and simple pressure drop calculations (Figure 3.7c). The experiments started by taking the swirl burner and heat exchanger off and installing an electrical heater to heat up the porous bed (Figure 3.10). The electrical heater helped heat up the bed more quickly and eliminated the need for the swirl burner's operation.

Figure 3.9: Leister electrical air heater 10000 S used in the 'porous bed fuel injection' experiments

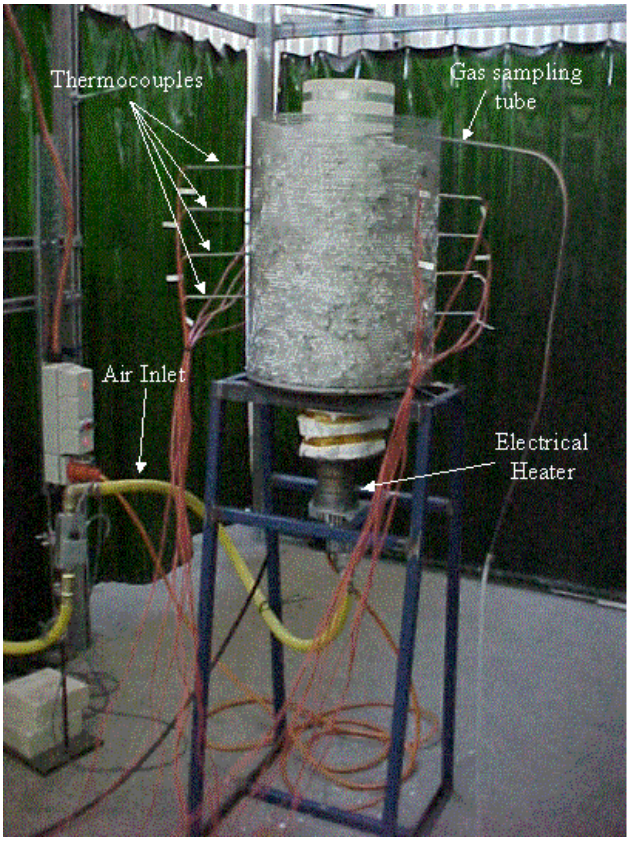

Figure 3.10: Porous burner assembly with electrical heater

Similar to other experiments, the ceramic tube was filled with 75 mm of flint clay as a flame arrestor and 350 mm of 6 mm nominal size ceramic beads. The porous bed was heated up to ~ 800 K and then the heater was turned off and a mixture of air/fuel was ignited on the top. After a while, the top surface started glowing and then the flame propagated upstream and stabilisation happened somewhere within the porous bed.

3.3 Results and discussion

One thing which was common across all the 'non-premixed' experiments was that the air and fuel mixing was a challenge, in terms of the need to inject the fuel into the incoming air and accommodate the residence time before reaching the flame front and impacting on the porous medium. In all the experiments, the Global Equivalence Ratio (GER) was used, which is simply an indication of the mass ratio between the total incoming air and total injected fuel. In the following sections, $\overline{\Phi}$ is used to indicate the global equivalence ratio.

In the following section, the experimental results from different fuel distribution designs are discussed and compared. Depending on the various set-ups, different parameters were considered in the experiments, i.e. flow velocities, mixture flow rates, equivalence ratios or thermal powers. Two tables have prepared in Appendices E1 and E2 which lists and translates different flow rates to different flow velocities and also thermal powers for both CNG and LPG fuel/air mixtures.

3.3.1 Single-tube fuel distributor

The porous burner was heated up using the swirl-burner until the temperature in the bed reached ~ 500 °C. The swirl-burner was then switched off, but the air flowrate was kept constant at 230 l/m. The fuel (CNG) supply to the porous burner was turned on and a mixture with a global equivalence ratio of $\overline{\Phi}$ = 0.4 was established.

The premixed and heated mixture at the top of the porous burner was then ignited. Initially, the flame moved rapidly to a location about 225 mm above the perforated plate, as shown in Figure 3.11. With the flame radiating backwards, the flame front gradually shifted upstream (this took around 9 minutes) and stabilised at a location 175 mm above the plate. The temperature profiles presented in Figure 3.11 were measured axially at the centreline of the ceramic tube. The inlet temperature to the burner was measured at 37°C. The sharp increase in the temperature between locations 150 mm to 175 mm, indicate the existence of a flame. The temperature profile can be regarded as in a quasi-steady state, as a minor variation in the temperature was still recorded at the end of the experiment. The temperature variation at the end of experiment was recorded to be less than 1°C /min (and continuously decreasing) versus tens of degrees per minute at the start of the experiment (depending on the thermocouple position). The exact location of the flame front cannot be accurately determined, however it is believed that the flame front would have stabilised closer to the 150mm location.

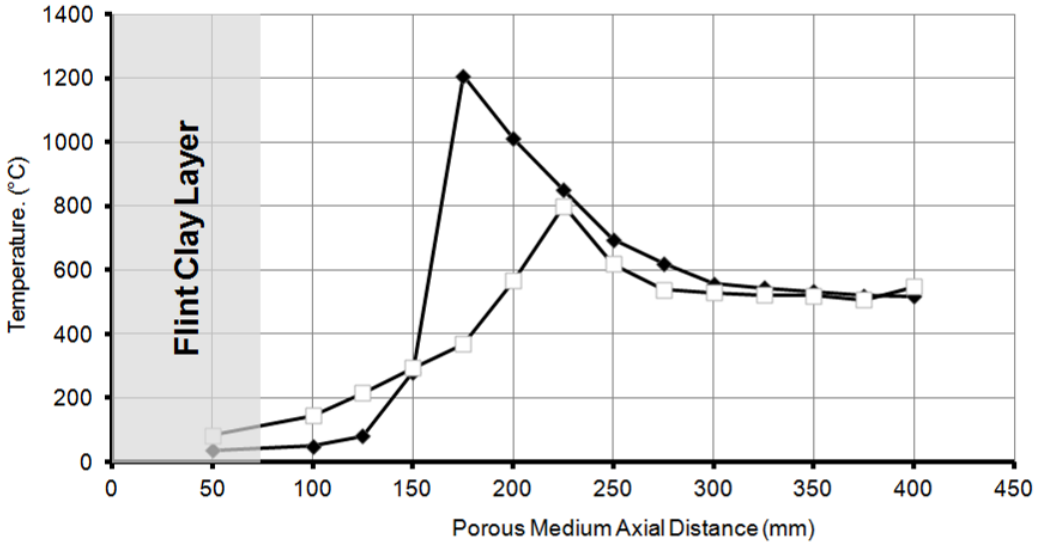

Figure 3.11: Temperature profiles along the centreline of the ceramic tube. □ Initial position of the flame in the bed; ◆ final position of the flame in the bed. A single-tube is used as fuel distributor.

Despite being successful in securing a stable flame at $\overline{\Phi}$ = 0.4, the results of the temperature uniformity in the radial direction were not adequate and the flame was propagating in a non-uniform fashion, as shown schematically in Figure 3.12. The fuel was burning in two rectangular regions off the centreline. The presence of the flame in those two regions showed that the fuel has been burnt in a non-uniform area across the ceramic tube. Also, the radial temperature measurements at different levels were further evidence of temperature non-uniformity across the porous burner. A temperature difference of 180ºC was observed between various radial parts of the porous medium for a certain height in the burner, as shown in Figure 3.13.

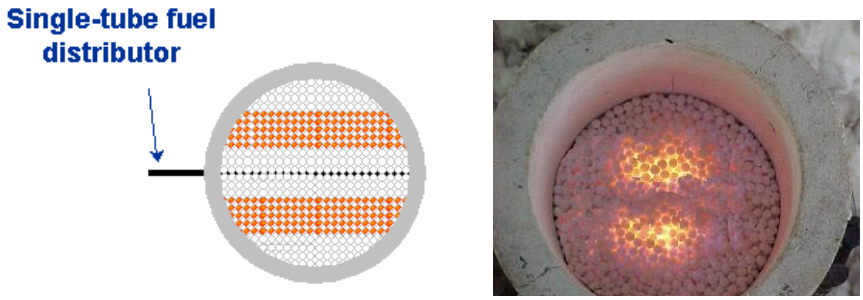

Figure 3.12: Top view picture of the PB using a single-tube fuel distributor. Schematic view and fuel distributor insertion (left)

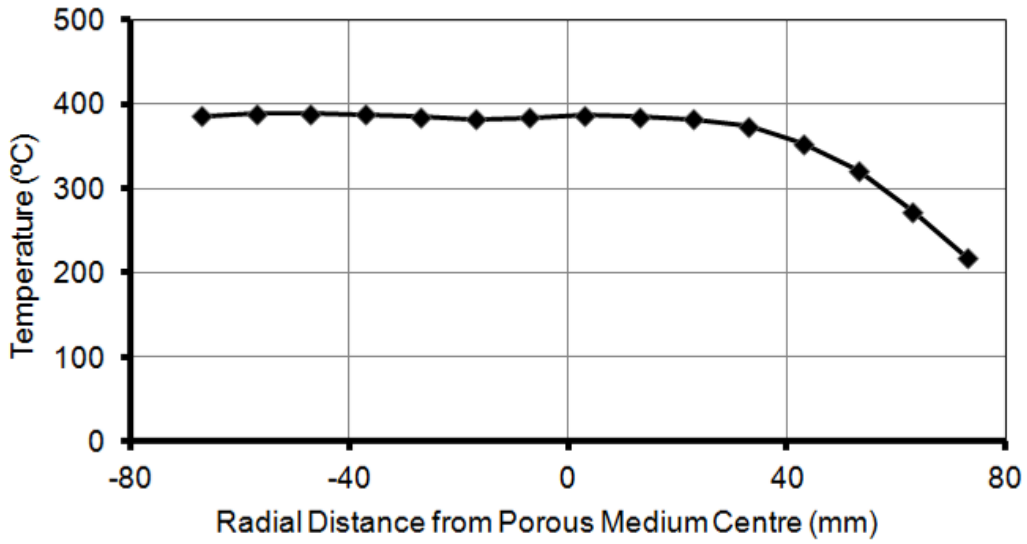

Figure 3.13: The radial flame temperature gradient in a single fuel distributor. Measurements were from a +125mm axial location of the porous bed.

It is worth noting that different ultra-lean air/fuel mixtures ($\overline{\Phi}$ < 0.4) were tried, with no success in stabilising the flame in the porous bed. This lack of success is caused by the significantly different temperatures in the bed, due to a non-uniformed fuel distribution across it, hence the difficulty in establishing flame stabilisation at any given location. It is worth noting that having forward and backward radiation resulting in uniform heat distribution and the presence of a reasonably hot solid bed in the vicinity of the flame zone are known to play a major role in stabilising the flame in porous burners.

3.3.2 Spiral-tube fuel distributor

Figure 3.14 shows the measured temperature profiles for different global equivalence ratios and thus different thermal powers for a fixed air flow rate of 265 lit/min. For $\overline{\Phi}$ = 0.7 (which corresponds to a total thermal power of 10.62 kW), the flame is located ~150 mm downstream of the burner inlet. The Figure 3.14 also shows that the fuel is not consumed completely in the first region and that a proportion of the fuel is burning at locations 275 mm and 400 mm downstream of the burner inlet, which shows the existence of two flame fronts. Decreasing the global equivalence ratio to $\overline{\Phi}$ = 0.5 did not change the flame locations. The temperature within the bed and at the exit, however, dropped to values lower than those for $\overline{\Phi}$ = 0.7. Further

decreases in the global equivalence ratio to $\overline{\Phi}$ = 0.4 made a significant change to the flame location within the bed. The flame moved downstream to 275 mm downstream of the burner inlet. As most of the fuel was burning in this region, the temperature was relatively high but the exit temperature was lower than before.

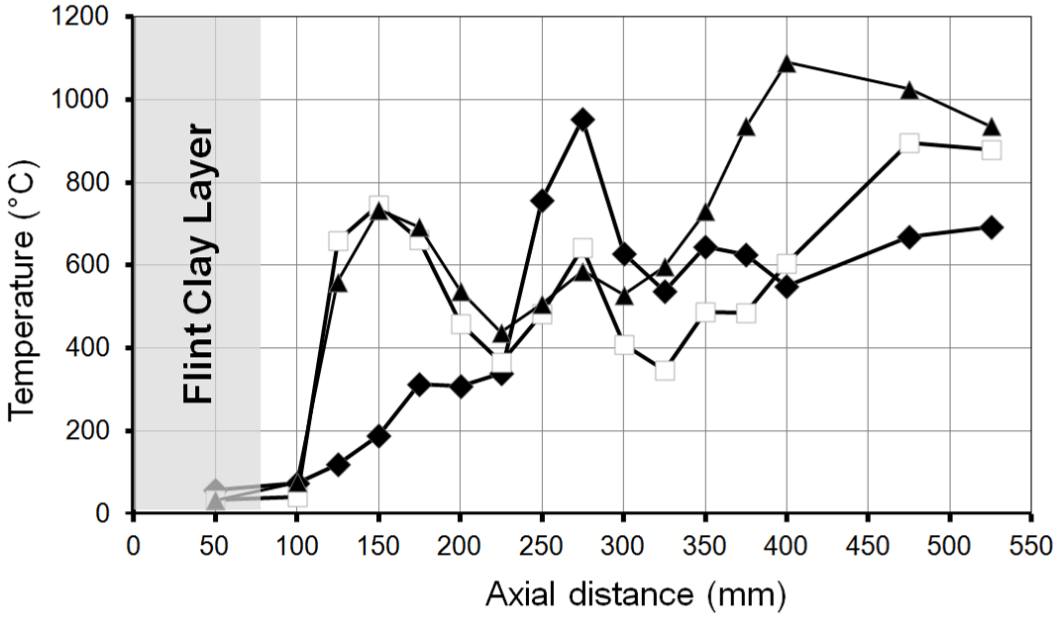

Figure 3.14: Temperature profiles along the centreline of the ceramic tube when a spiral-tube is used as a fuel distributor. ◆, □ and ▲show a fuel/air mixture with a total flow rate of 265 lit/min and GER of 0.4, 0.5 and 0.7 respectively.

Figure 3.15 shows the temperature profiles along the centreline of the ceramic tube for different global equivalence ratios 0.15, 0.2 and 0.3, corresponding to air flow rates of 200 lit/min, 150 lit/min and 100 lit/min, respectively. The total thermal power is fixed at 1.72 kW for all cases, by fixing the fuel flow rate and varying the air flow rate to change the $\overline{\Phi}$.

Experiments were started by reducing GER to $\overline{\Phi}$ = 0.3 (by reducing the fuel flow rate). The flame position moved upstream to ~ 475 mm, which is close to the burner exit. Further reduction of GER to $\overline{\Phi}$ = 0.2 and then to $\overline{\Phi}$ = 0.15 (by increasing the air flow rate), moved the flame further downstream towards the burner exit. As shown in Figure 3.15, the temperature along the porous bed is reduced significantly as the incoming fuel/air mixture velocity exceeded the flame speed for a particular

air/fuel mixture. At the same time, the temperature downstream of the flame was dropping, caused by convective and radiative heat transfer mechanisms.

The other phenomenon observed during the experiments was that of multiple flame fronts along the burner. This could be an indication of non-uniform mixing of fuel and air. It is believed that part of the fuel was burning in an ultra-rich combustion zone in some areas within the bed and some fuel mixed with the air further downstream and was burning closer to the surface.

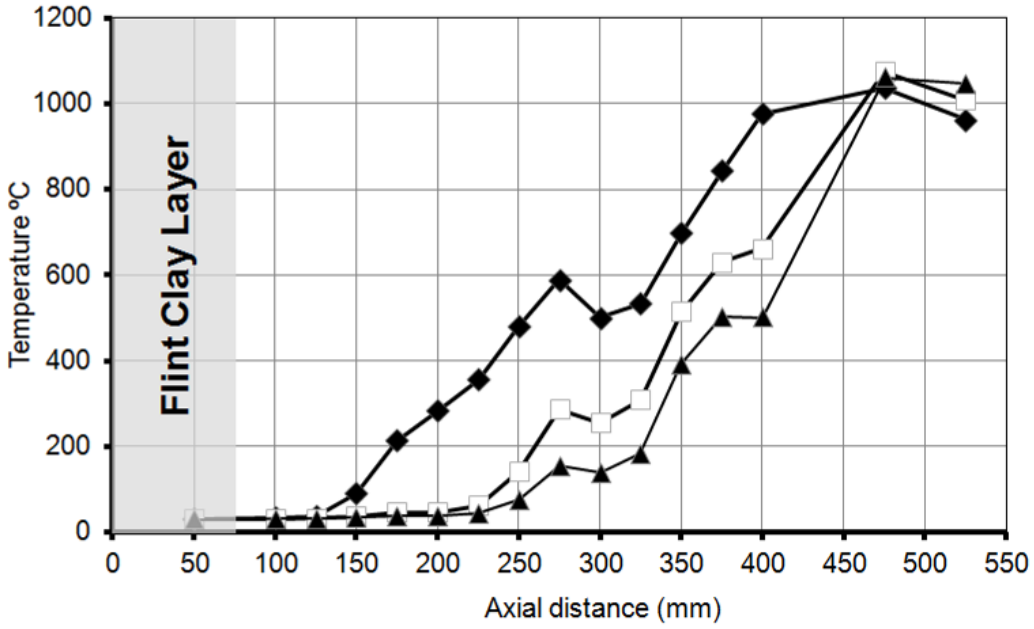

Figure 3.15: Temperature profiles along the centreline of the ceramic tube for different GERs. ▲, □ and ◆ show a global equivalence ratio of 0.15, 0.2, and 0.3 and a flow rate of 200, 150 and 100lit/min respectively. The firing rate is fixed at 92kW/m^2 for all cases. A spiral-tube is used as a fuel distributor.

The results in Figure 3.14 and Figure 3.15 show that it is possible to burn lean air/methane mixtures ($\overline{\Phi}$ = 0.5 and $\overline{\Phi}$ = 0.4) within the bed and also ultra-lean mixtures ($\overline{\Phi}$ = 0.3, 0.2, and 0.15) close to the surface, while maintaining a stable flame with an average temperature between 950 °C – 1050 °C. However, considering the uniformity of fuel/air mixing was still in doubt, further experiments were needed to confirm the results.

It is worth mentioning that stabilising a flame of a mixture with $\overline{\Phi} < 0.6$, using conventional free flame burners, is extremely difficult, while burning ultra-lean mixtures ($\overline{\Phi} < 0.5$) is nearly impossible under atmospheric pressure.

Figure 3.16 shows top view photographs of the burner during the start-up and flame propagation processes. The flame distribution across the surface and thus temperature uniformity are improved, compared with a single-tube fuel distributor, but it is still not uniform, as seen in Figure 3.16 (c).

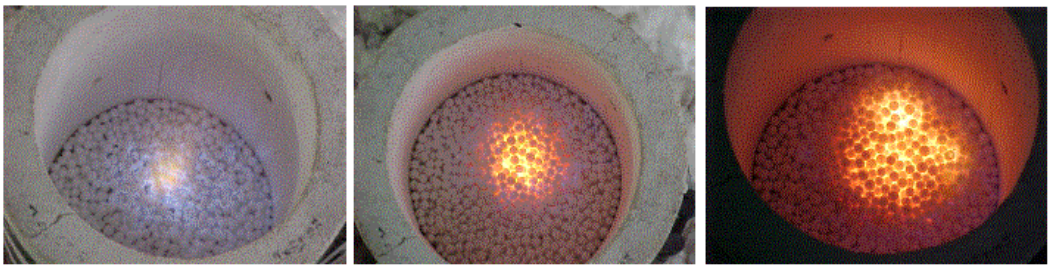

Figure 3.16: Top view pictures of PB using spiral-tube fuel distributor: (a) igniting on the top surface, (b) glowing and start propagating and (c) propagation upstream and stabilisation.

Unfortunately, the radial temperature distribution was not measured for the flames with a spiral fuel distribution. Instead, a non-reacting experiment was conducted to measure the distribution of the fuel within the porous bed. In this experiment, pure oxygen was fed through a spiral-tube fuel distributor while air was fed in the same way as for the reacting case. The oxygen concentration was then sampled at different radial locations to evaluate the uniformity of the distribution. The results are presented in Figure 3.17. It is clear that the results show a marked improvement in uniformity distribution. However, the distribution was not uniform enough to result in a uniform temperature across the porous bed, as is evident in the Figure above. It is worth noting that while this is an improvement in comparison with the measured temperature profiles for a single-tube fuel distributor, it was not yet sufficient to provide the uniformity required.

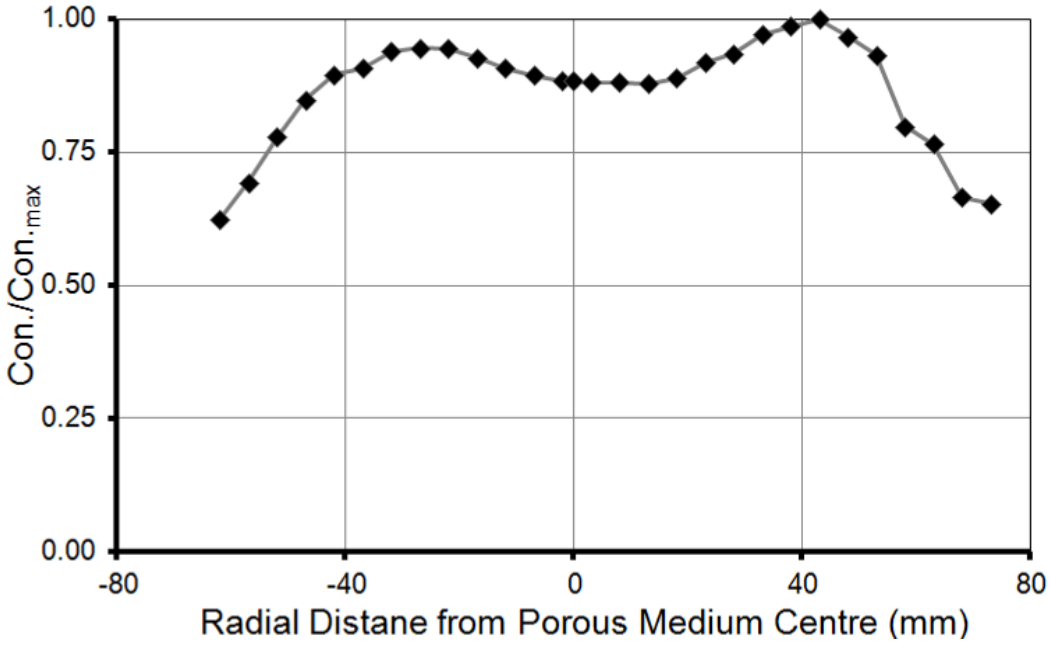

Figure 3.17: Testing of gas distribution uniformity in a spiral-tube fuel distribution system. Oxygen was used (no combustion) in the fuel distributor and the concentration of oxygen was measured at different radial locations at 125mm downstream of the fuel distributor.

3.3.3 Multi-tube fuel distributor

In order to improve the temperature uniformity within the porous burner, a multi-tube fuel distributor was installed in the porous burner and the effects of GER and the flow rate on the flame location and stability of the flame were studied. Figure 3.18 illustrates the temperature profiles along the centreline of the ceramic tube for different airflow rates (300 lit/min, 400 lit/min, 500 lit/min and 600 lit/min) and for $\overline{\Phi}$ = 0.3. For the first case, the flame was sustained for a flow rate of 300 lit/min and GER of $\overline{\Phi}$ = 0.3. The sharp increase in the temperature (from 236 °C at 75 mm to 1023 °C at 100 mm downstream of the burner inlet) shows that the reaction is happening somewhere close to 100 mm downstream of the burner inlet. It was observed that increasing the flow rate to 400, 500 and 600 lit/min does not change the flame location but increases the flame temperature to 1088 °C, 1203 °C and 1274°C, respectively. This increase is believed to be due to increasing firing rate for higher flow rates. Meanwhile, the radiative heat loss from the porous medium was almost the same, increasing the firing rate, while keeping the GER the same, was releasing more heat within the bed and hence increasing the temperature.

It was also observed that the temperature profiles for different total flow rates of 300, 400 and 500 lit/min are consistent. The discrepancy with the profile at 600 lit/min is believed to be related to an experimental error induced by not reaching sufficiently steady state conditions. More time was required for the porous bed to reach a thermal steady state. Nonetheless, the profiles are consistent and show a similar pattern.

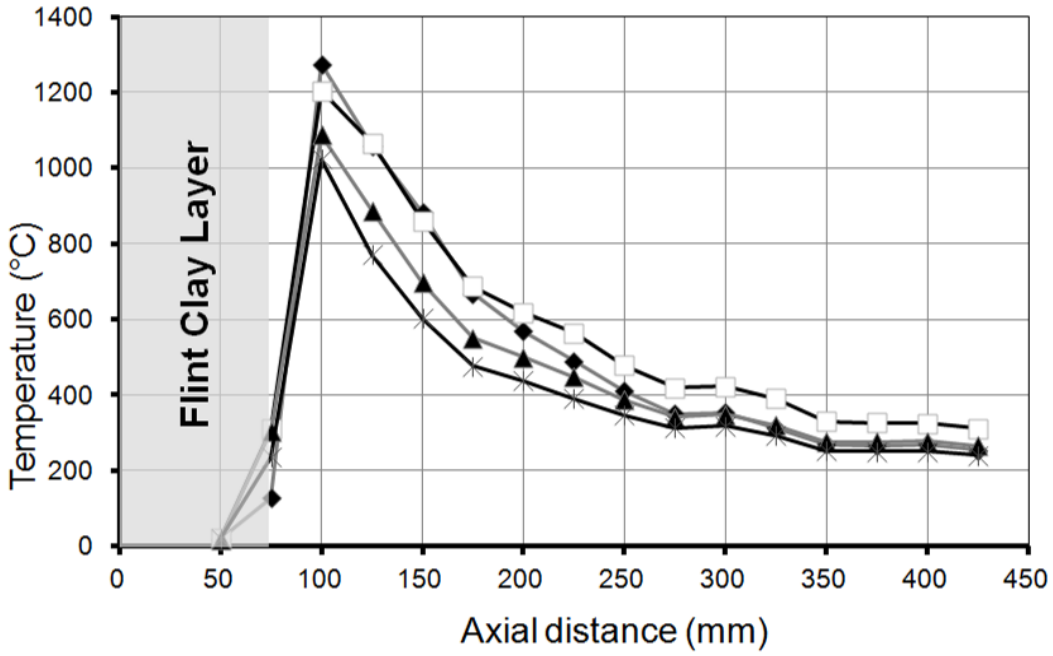

Figure 3.18: Measured temperature profiles along the centreline of the ceramic tube for flow rates of 300 (✳), 400 (▲), 500 (□) and 600 (◆) lit/min and a global equivalence ratio of $\overline{\Phi}$ =0.3.

Further experiments were conducted using the same configuration to investigate the effects of different $\overline{\Phi}$s while the total flow rate was kept constant. Hence, after fixing the airflow rate at 500 lit/min, different $\overline{\Phi}$s (0.3 down to 0.15) were tried, as presented in Figure 3.19. For $\overline{\Phi}$ = 0.3, the maximum flame temperature reached 1162 °C and stabilised 100 mm above the flint clay layer. Decreasing $\overline{\Phi}$ to 0.25 changed the flame temperature to 998°C, but did not change the flame location. A further decrease of the $\overline{\Phi}$ to 0.15 moved the flame zone upstream and caused more reductions in the flame temperature to 939 °C and 603 °C, respectively. It is worth noting that flames with $\overline{\Phi}$ < 0.2 were unstable and blew out easily.

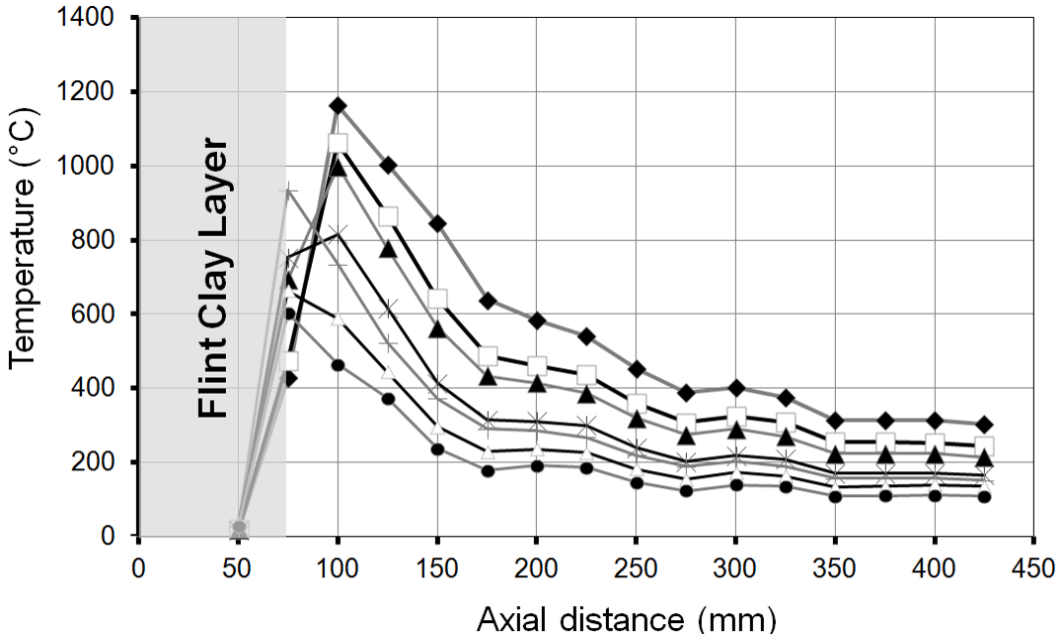

Figure 3.19: Measured temperature profiles along the centreline of the ceramic tube for global equivalence ratio of flow rates of $\overline{\Phi}$ = 0.3 (◆), $\overline{\Phi}$ = 0.275 (□), $\overline{\Phi}$ = 0.25 (▲), $\overline{\Phi}$ = 0.225 (✳), $\overline{\Phi}$ = 0.2 (+), $\overline{\Phi}$ = 0.175 (△) and $\overline{\Phi}$ = 0.15 (●) and a flow rate of 500 lit/min. A multi-tube is used as a fuel distributor.

Figure 3.20 shows a comparison between the measured and calculated $\overline{\Phi}$ equilibrium temperatures, as well as the NO_X concentration for different $\overline{\Phi}$s. Both temperature profiles exhibit a linear behaviour but the measured temperature profile inside the porous media has a steeper slope. From the Figure 3.20, one could conclude that for $\overline{\Phi}$ > 0.15, the measured temperatures exceed the equilibrium temperatures and the difference increases as $\overline{\Phi}$ increases. These higher flame temperatures are related to the excess enthalpy phenomenon previously described in the literature.

Also shown in Figure 3.20, is the measured NO_X concentration for 0.15 < $\overline{\Phi}$ < 0.3, both as absolute values and at reference 3% oxygen concentration. The reference NO_X values were calculated using measured oxygen concentrations during the experiments and based on:

$$C_r = C_m \frac{20.9 - r}{20.9 - m} \qquad (3.1)$$

In which C_r, C_m, r and m are the reference NO_X concentrations, measured NO_X concentrations, reference oxygen concentrations (please note, industry references are different from industry to industry and usually fall between 3% and 10%) and measured oxygen concentrations.

As expected, the NO_X levels are quite low for $\overline{\Phi}$ < 0.2 and the NO_X increases as $\overline{\Phi}$ increases. However, the NO_X emissions are still fairly low when compared with conventional flames.

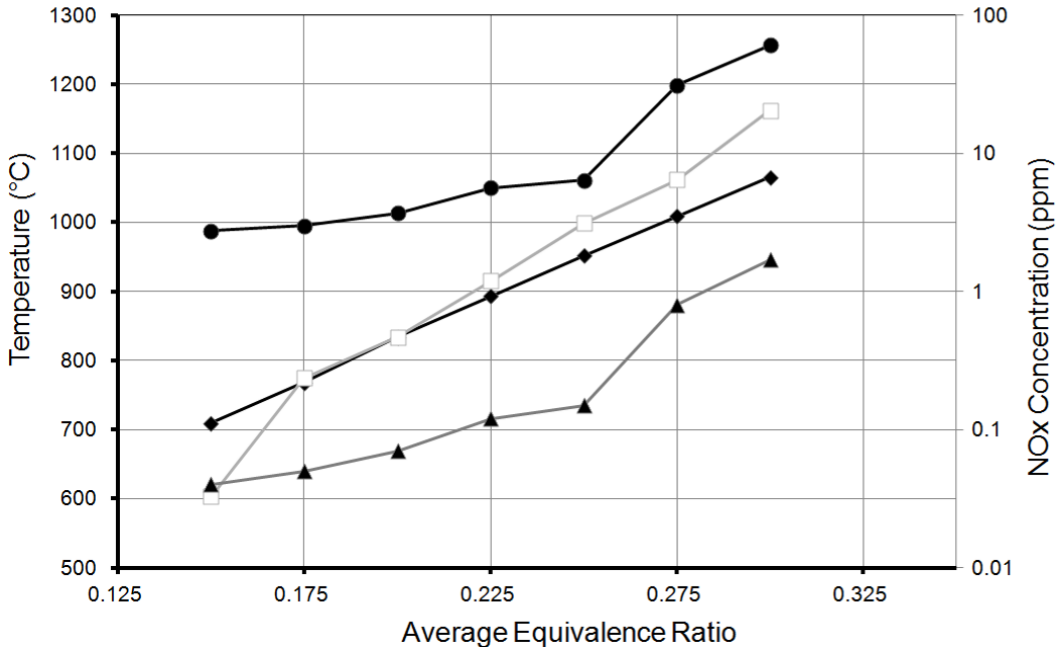

Figure 3.20: Comparison of experimental and equilibrium temperatures and measured NO_X for ($\overline{\Phi}$ = 0.15 to $\overline{\Phi}$ = 0.3) and atotal flow rate of 500 lit/min. ◆ and □ adiabatic flame temperatures and measured flame temperatures respectively. ▲ and ● measured NO_X concentrations (absolute values and at 3% oxygen respectively. A multi-tube fuel distributor is used.

Figure 3.21 shows photographs of the flame/heat distribution on the top of the porous bed. It is clear that heat is more uniformly distributed and that the multi-tube fuel distributor works better than in the two earlier designs. Air and fuel are mixed better in the mixing chamber and hence the temperature profile is more radially uniform.

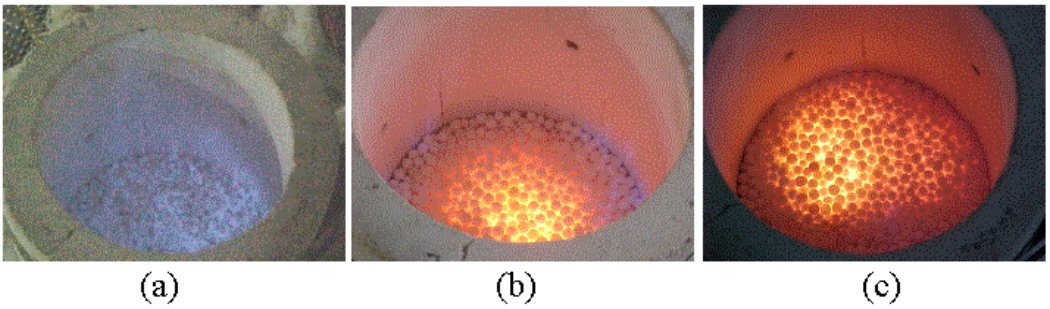

Figure 3.21: Top view of the PB using a multi-tube fuel distributor: (a) igniting on the top surface, (b) glowing and starting to propagate and (c) propagation upstream and stabilisation inside the porous medium.

A repeat of the non-reacting experiments of pure O_2 in the fuel stream show a more uniform mixture distribution (see Figure 3-21), which is consistent with the uniform temperature observed visually in Figure 3-20 (C).

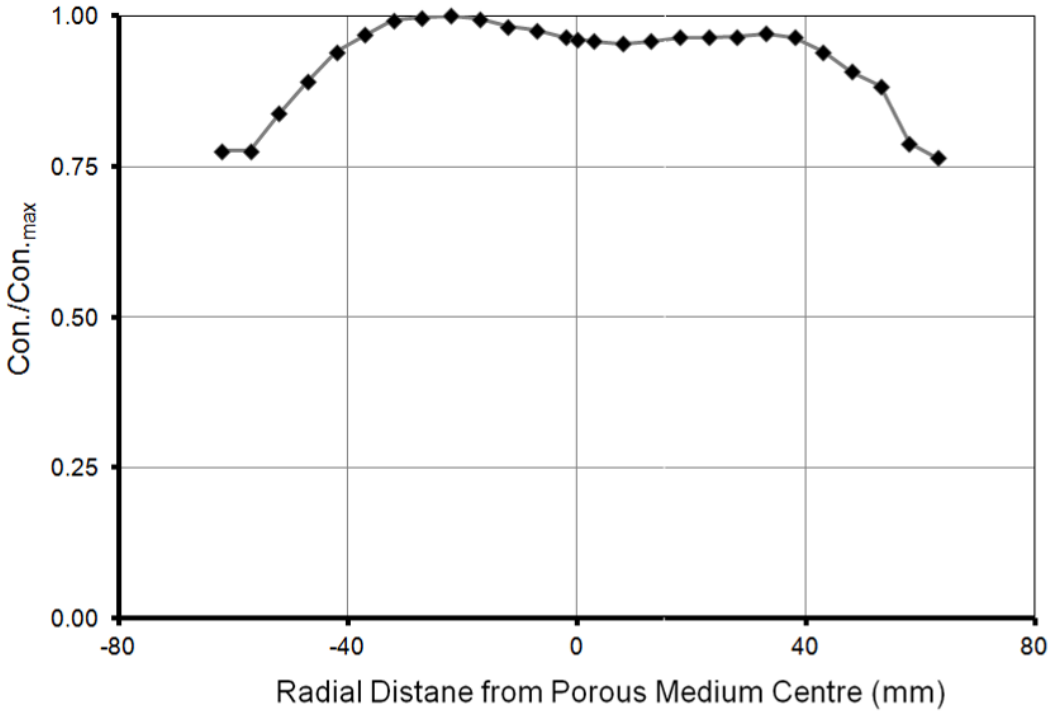

Figure 3.22: Fuel distribution uniformity in a multi-tube fuel distribution system. Oxygen was used (no combustion) in the fuel distributor and the concentration of oxygen was measured in different radial locations at 225 mm downstream of the fuel distributor.

3.4 Summary and Conclusions

Injecting the fuel into the porous bed is fraught with many challenges, mostly due to the difficulty of ensuring good homogeneous air and fuel mixtures. Non-uniform mixtures influence flame stability differently at different mixture strengths.

Despite known difficulties associated with the stabilisation of 'non-premixed' flames in a porous burner, the proposed experimental setup succeeded in the stabilisation of lean flames of CNG/air. Different avenues for introducing the fuel into the air stream were trialled and the impact on flame uniformity, stability and emissions was measured. The following conclusions can be drawn from the bed fuel injection experiments:

- Uniformity of fuel distribution, and hence radial heat distribution, plays a major role in the stabilisation of the flame within the bed. A stable flame inside the porous bed with a global equivalence ratio of $\overline{\Phi}$ = 0.4 was achieved when using a single-tube fuel distributor. The flame appeared in two distinct zones associated with the two rows of holes in the tube. The flames stabilised close to the exit plane and exhibited great sensitivity to minor variations in the inlet flow rates;

- The spiral-tube fuel distributor improved the fuel distribution radially when compared with a single-tube fuel distributor. Using a spiral-tube, it was possible to stabilise the flames with $\overline{\Phi}$ = 0.4 within the porous bed and as low as $\overline{\Phi}$ = 0.15 close to the porous bed exit plane. Flow rates of 200 lit/min and 500 lit/min were possible for similar fuel mixture strengths;

- The multi-tube fuel distributor produced the most radially uniform fuel/air mixture. Studying the central part of the burner (away from the walls – central area with a radius of 40 mm), it can be concluded that the fuel concentration and hence heat distribution is quite uniform. Flames with 600 lit/min were stabilised in the bed and with $\overline{\Phi}$ = 0.15. The NO_X levels are less than 1 ppm for $\overline{\Phi}$ < 0.275 and slowly increase when $\overline{\Phi}$ increases.

PREMIXED AIR/FUEL IN A POROUS BURNER

4.1 Introduction

The experiments performed with different fuel distributors, as discussed in the previous chapter, flame distribution and improved temperature uniformity can be seen in Figure 3.12, Figure 3.16 and Figure 3.21. Yet there is still considerable non-uniformity in terms of the air/fuel mixture, leading to high levels of inaccuracy when modelling optimisation processes, as there is much remaining assumed about uniform radial distribution and treatment of the system as one-dimensional, axially along the bed. Although premixed air/fuel mixtures impose a higher risk of flashback, few strategies have been utilized which minimize this risk and prevent the flame from propagating upstream of the bed inlet section. The majority of these strategies relied on controlled heat transfer and, in particular heat extraction from the porous layers in the vicinity of mixing chamber. In this chapter, a new set of experiments were conducted using premixed air/fuel mixtures and the results are compared with those from Chapter 3.

4.2 Experimental setup

A new configuration for the PB system, to supply premixed air/fuel, was assembled, as shown in Figure 4.1 (left). Fuel is introduced through a T-piece connection to the air supply line (see Figure 4.1, right). A partially mixed air/fuel mixture is then completely mixed inside a mixing chamber upstream of the porous bed. To avoid any risk of explosion and flashback, a non-return valve is installed on the fuel supply line (see Figure 4.1, right).

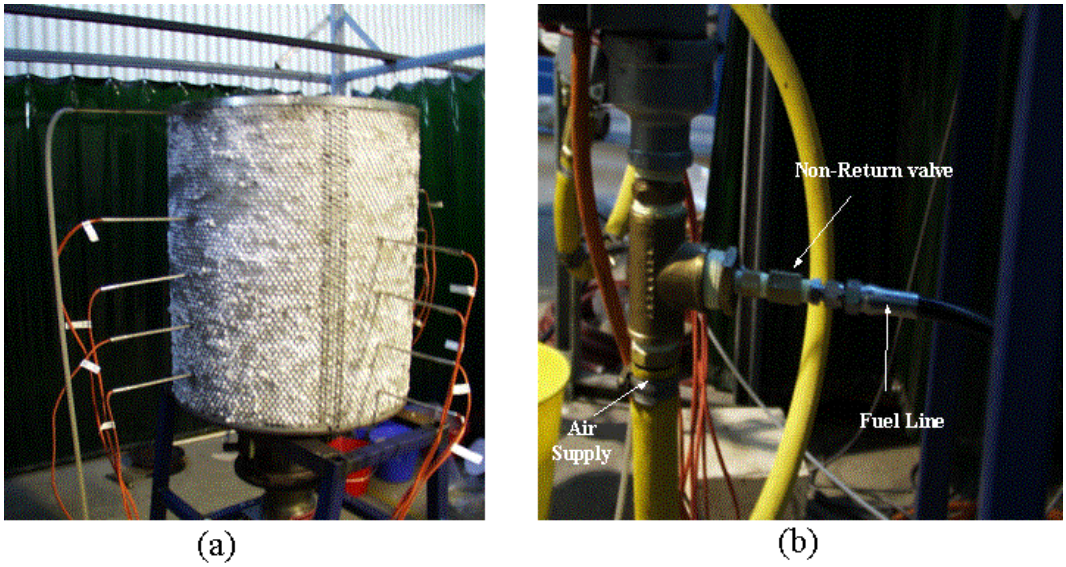

Figure 4.1: Assembly for feeding premixed air/fuel (left), a close view of the air and fuel supply lines (right)

4.2.1 Electrical heater

To accelerate the porous medium heating up process, and hence the stabilisation of the flame, a Leister electrical air heater 10000 S was used upstream of the porous medium.

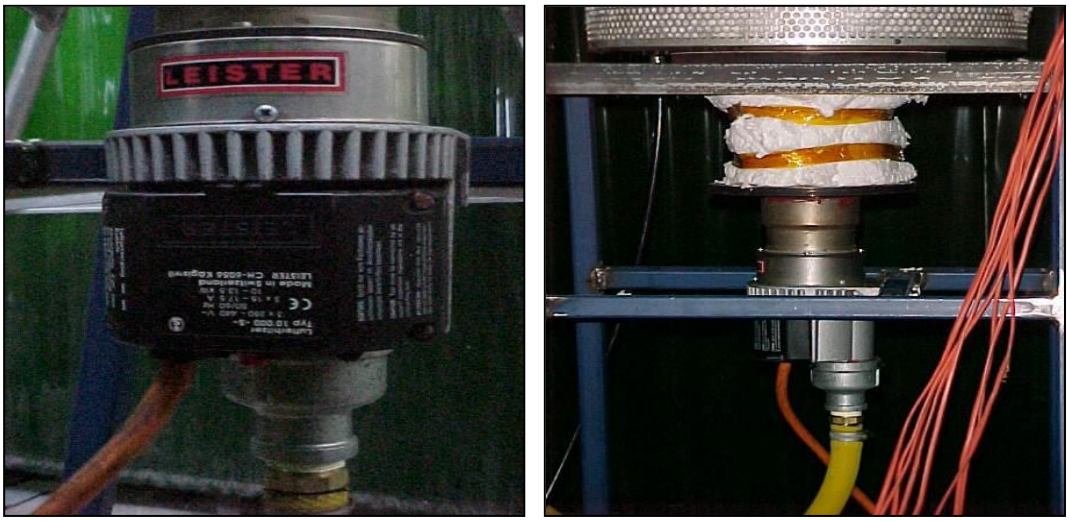

Figure 4.2: Leister electric air heater 1000 S (left), Air heater assembled upstream of the porous medium (right)

The electric heater had the capacity to handle a maximum of 650 lit/min of ambient air when used upstream of the porous bed. The total flow rate, at elevated temperatures of ~750 K, decreased to 430 lit/min due to the increase in air viscosity.

4.2.2 Porous medium and temperature measurement

The bi-layered PB is filled with 75 mm of flint clay, sized between 2 mm and 3 mm, followed by 345 mm of ceramic beads with a nominal diameter of 6.35 mm. The ceramic tube is insulated by 125 mm of fibreglass bulk. A set of 16 N-Type thermocouples are inserted circumferentially around the ceramic tube every 25 mm in order to measure the temperature at the centreline. The thermocouples were staggered such that they were inserted from four different directions so as not to obstruct the flow on one side. Thermocouple no. 15 is located at the top surface of the ceramic beads and was measuring and reporting the bed surface temperature. The exhaust gas temperature is measured by thermocouple no.16. For safety reasons, the first thermocouple is inserted in the flint clay layer to measure the incoming air and fuel mixture temperature and prevent any un-expected situation where the temperature increased sufficiently to cause ignition and/or flashback. Temperature measurement uncertainty was discussed earlier in Section 3.2.3.3.

4.2.3 Start-up

The porous bed is first preheated to around 800 K using a Leister electrical air heater 10000 S. The electric heater is then turned off. Air and fuel valves are subsequently opened and the required air and fuel are supplied to the porous bed through gas flowmeters. Fuel entrains into the air stream via a T-piece connection and mixes with the incoming air before reaching the porous bed. The air/fuel mixture is then ignited on the top surface of the bed with a close to stoichiometric mixture, using a hand held torch. The bed, which has been preheated with the electric air heater, is then heated up through radiation and conduction heat transfer from the flame that had propagated upstream through the bed. When the local temperature exceeded 850 K, it was possible to operate the burner under lean or ultra-lean flame conditions.

4.3 Numerical modelling

Combustion processes inside porous media include many physical and chemical phenomena, which need detailed consideration. These include chemical reactions, mass and heat transfers, including conduction, convection and radiation. Hence, numerical investigations of combustion processes have always been a challenging task. In this section a numerical method has been selected to represent these processes in a porous burner (PB). The porous burner model (PBM) which was developed by Shardlow [133] is used in this study. It is based on the original Sandia Premix model [132].

The computational model presented assumes a one-dimensional, laminar and adiabatic flow. The code utilises the core routines of the chemical kinetics package, CHEMKIN [132, 146-148]. The code was used previously by Christo et al. [11, 31, 149] and showed a reasonable agreement with their experimental results, mostly when applied to porous radiant burners. In this section, the PBM code is used to predict combustion characteristics in porous burners for a wider range of conditions inside PBs. A full description of the PBM model and governing equations are included in Appendix C.

4.3.1 Model description

PBM includes a separate energy equation for the gas and the solid-phase accounting for conduction, convection and radiation heat transfer mechanisms in both phases. The model allows detailed chemistry of gaseous species and surface reactions to be incorporated. The model is capable of handling single-layer or multi-layer porous burners and is suitable for planar, cylindrical or spherical geometry. A schematic description of the model is shown in Figure 4.3.

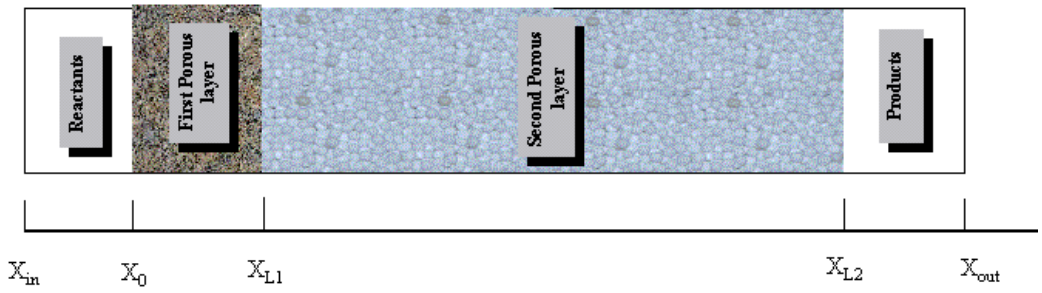

Figure 4.3: Schematic description of the computational domain for the porous burner model.

4.4 Results and discussion

4.4.1 Validating of the 1-D assumption

Figure 4.4 shows radial profiles of the temperatures of liquefied petroleum gas (LPG)/air flames (see Table 4.1 for the composition of LPG). The measurements were taken at locations 175 mm, 225 mm, and 275 mm above the flint clay layer. While the temperature profiles at each location show an almost linear decline from one side to another radially, the temperature around the centreline is consistent within ±20 °C. The slope radially is not well-understood, especially as to how it changes from one axial location to another. As the experimental measurements are all done on the centreline of the burner, the variations in temperature radially are assumed to be related to heat transfer, flame response and stability. Worth noting is the large cylinder diameter used for this burner, which is designed to isolate the centreline flame properties from the wall effects, which will make it more suitable for 1-D representation at the centreline, especially when using numerical techniques.

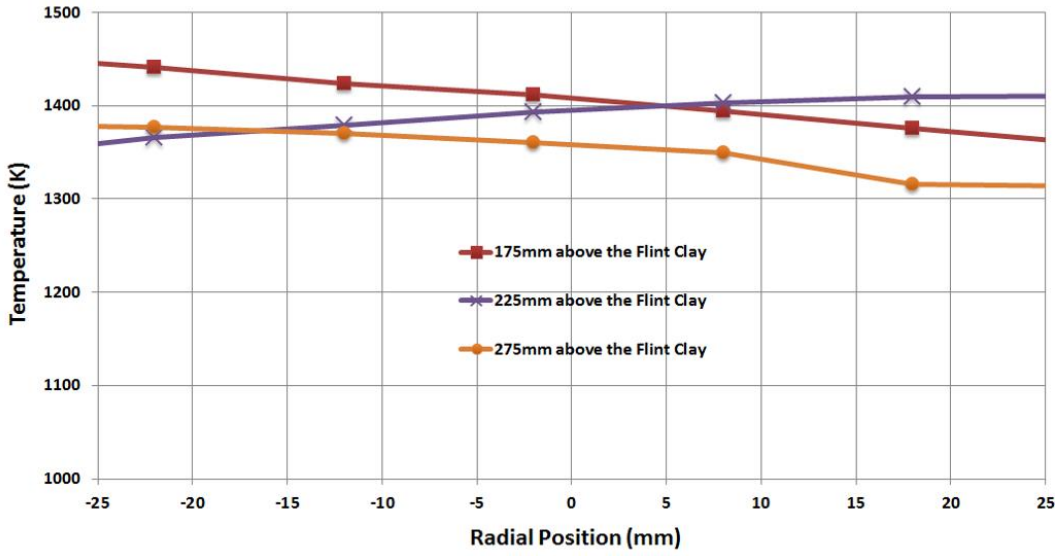

Figure 4.4: Measured Temperature radial profiles at different axial locations for LPG/Air flames with φ = 0.39.

4.4.2 Heating up process and propagation speed

Pre-heating of the porous bed before starting the flame is one way to speed up the attainment of flame stabilisation and achieve a steady state more quickly. This preheating is achieved either with a swirl-burner, an electrical heater or by using the heat transfer characteristics of the flame itself. Once the bed is hot and a stoichiometric flame is stabilised inside it, lean and ultra-lean flames can be stabilised. Figure 4.5 illustrates the heating up process using the swirl-burner upstream. It has been observed that the temperature increase happens in three different stages. At the first stage, all thermocouples reach a temporary equilibrium temperature of ~ 63 °C in a short time of less than three minutes. The bed is gradually heated until the temperatures of all the thermocouples reach the maximum value, which is a function of the incoming gas temperature. It is believed that water vapour in combustion products from swirl-burners cause this step temperature increase.

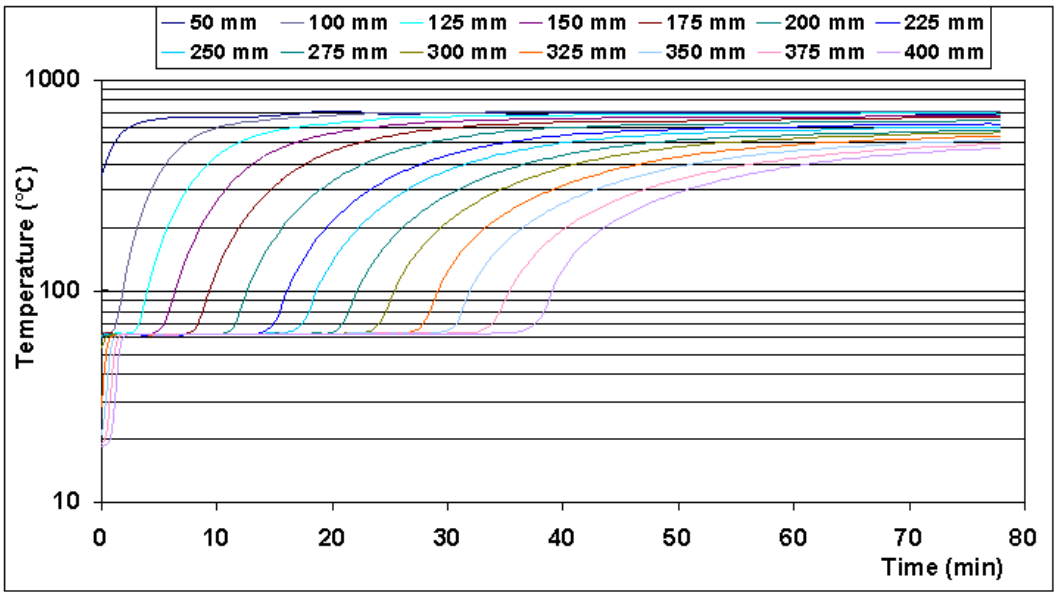

Figure 4.5: Measured centerline temperatures at different axial locations inside the porous bed during the heat up process, using an external swirl-burner

The heating up process using the electrical heater is presented in Figure 4.6. Unlike the swirl-burner, the electrical heater produces no water vapour and the heat will be consumed proportionally to heat up the whole bed at the same time. Upstream of the porous matrix was more affected by heat released from the electrical heater and hence it reaches the maximum temperature in a shorter time. It is worth noting that the maximum operating temperature for the heater was 650 °C.

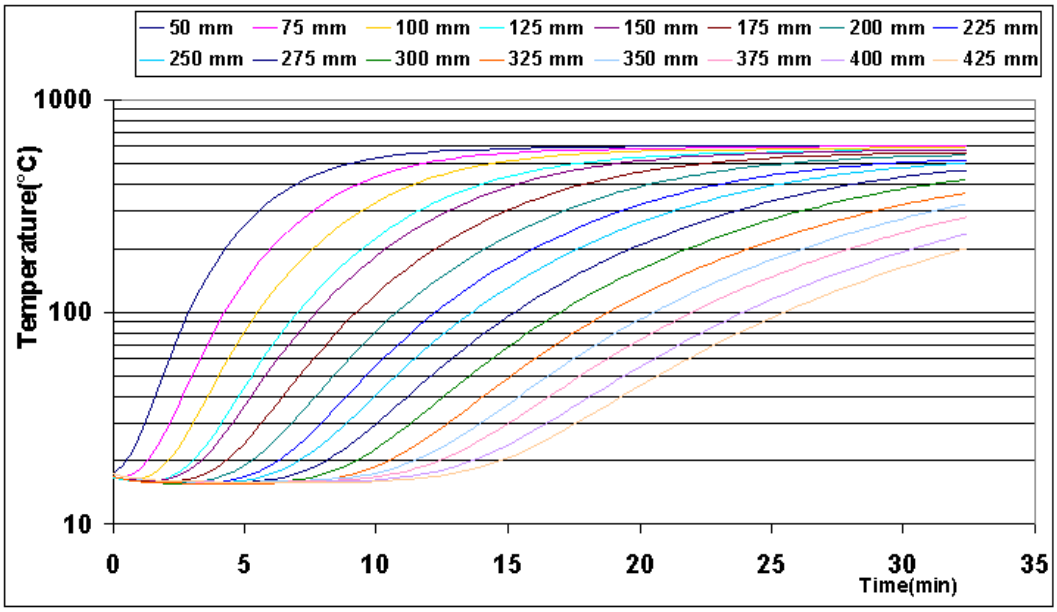

Figure 4.6: Measured centerline temperatures at different axial locations inside the porous bed during the heat up process, using an electrical heater

Figure 4.7 shows a different method for heating up the bed from the two previously described methods. Unlike those two methods, no external heat source was used. The air/fuel mixture was ignited on the top surface of the beads with an equivalence ratio ($0.6 < \varphi < 0.9$) within the flammability limit. Through radiation and conduction processes of the porous matrix the flame propagates upstream and heats up the bed gradually. After the whole bed reaches the required temperature, it is possible to reduce the equivalence ratio to lower values and stabilise a flame with a lean or ultra-lean regime.

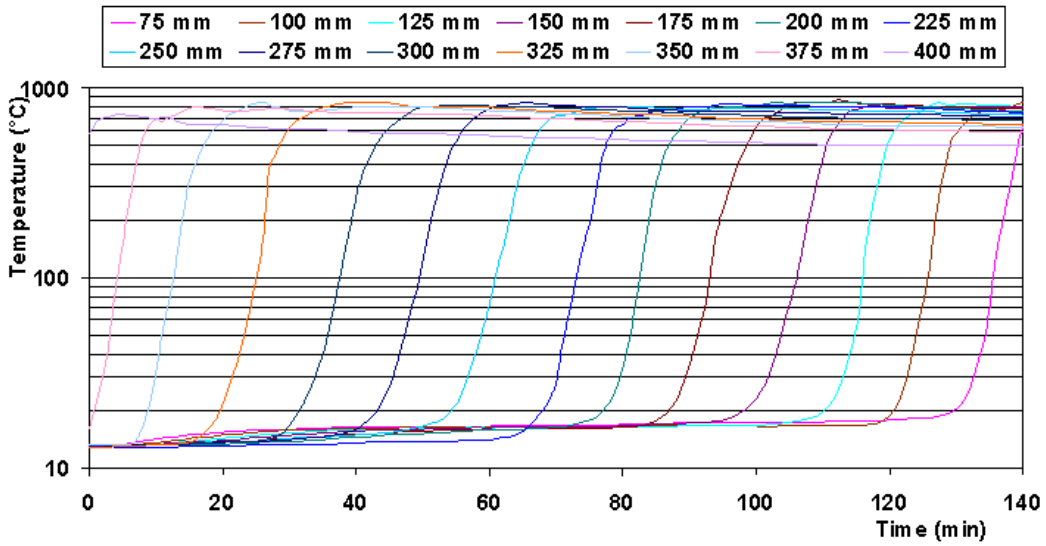

Figure 4.7: Measured centerline temperatures at different axial locations inside the porous bed during the heating up process, using combustion in the porous bed (recuperating)

It is clear from the information above that the use of an external heat source to heat up the bed (an electrical heater and/or a swirl burner upstream) is a quicker method to heat up the porous matrix. However, heating up the bed by initiating a flame on top of the bed and allowing it to propagate upstream is proven to be more effective, especially given that the total time from cold start to a stable flame was shorter. It was found that once the porous medium is heated by the internal flame, decreasing the equivalence ratio to lower values will result in quick stabilisation of the flame not far from the current flame front.

4.4.3 Effect of flow velocity on flame stabilisation and the location of the flame

In the following subsections, results from both experiments and numerical modelling of premixed air/fuel flames, stabilized in the porous bed, are presented and discussed. Figure 4.8 to Figure 4.17 show a parametric study aimed at identifying the effects of flow velocity, equivalence ratio and fuel type on a flame's physical characteristics.

Compressed Natural Gas (CNG) and Liquefied Petroleum Gas (LPG) have been selected as fuels for these experiments. Each fuel mixture was introduced into the PB and results have been recorded after stabilisation of the flame inside the matrix. Fuels' contents and their physical properties are presented in Table 3.2 and Table

4.1. Methane (CH4) is used as a fuel in the numerical modelling and is compared with experimental results from CNG fuel (~ 90.9% CH4).

	Mass fraction (Y)	Lower heating value	Molecular weight (W)	Mole fraction (X)
	(%)	(MJ/kg)	(kg/kmol)	(%)
Propane	95.250	46.357	44.090	94.2
Ethane	3.250	47.489	30.069	4.70
Butane	1.500	45.742	58.120	1.10
LPG	**100.0**	**46.385**	**43.587**	**100.0**

Table 4.1: LPG composition and physical properties.

Figure 4.8 shows measured centreline temperature profiles for CNG/air flames. The equivalence ratio was fixed at $\varphi = 0.4$ and the flow velocity was varied between 9 and 28 cm/sec. These velocities represent the operating envelope for this fuel mixture and burner geometry. For the 9 cm/sec flow velocity, the flame front, identified at the location of the highest measured temperature, stabilises at the top of the flint clay layer. This lower threshold is determined by heat loss from the flame, which still sustains the bed at above ignition temperature, and allows the flame to propagate. Simultaneously, the momentum balance at the flame front determines the higher flow velocity limit. At flow velocities much higher than the local flame speed, the flame front propagates downstream and the flame extinguishes. It is worth noting that the maximum flame temperature is almost the same for all flow velocities. Also noticeable is that increasing the flow velocity results in a shift in the location of the flame front further downstream. This can be attributed to the increase in flow momentum and changes in the preheating rate of the incoming gases. There is a smooth temperature gradient in all cases, starting from the flame front location, which has the maximum temperature and extends 375 mm downstream of the burner inlet. This gradient is caused by heat losses through sidewalls and insulation to the surroundings. The radiation heat losses to the surroundings make the temperature gradient steeper between 375 mm and 425 mm downstream of the burner inlet.

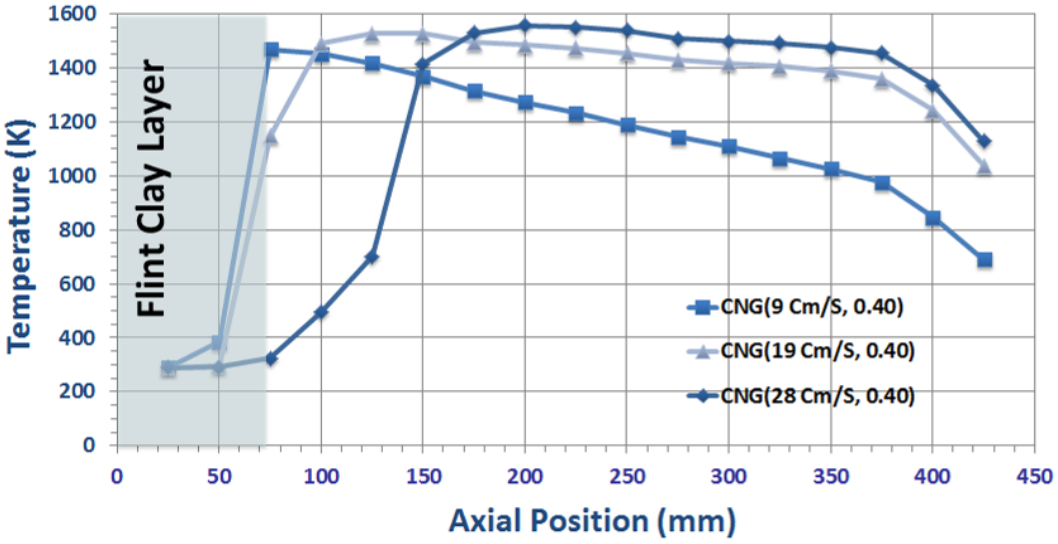

Figure 4.8: Measured centreline temperature profiles for CNG/air flame at φ = 0.4 and for different flow velocities.

Similarly, temperature profiles for LPG/air flames at φ = 0.4 and different flow velocities are shown in Figure 4.9. The results are similar to those of the CNG/air flames (Figure 4.8), albeit for the 28 cm/sec velocity case, with a slight decrease in the maximum flame temperature and a further downstream shift in flame position becoming more noticeable.

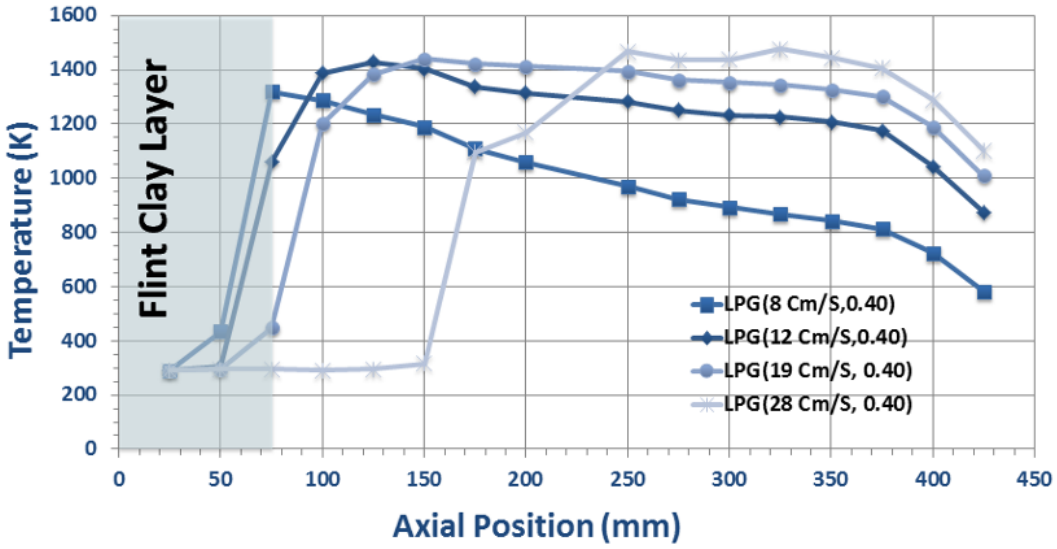

Figure 4.9: Measured centreline temperature profiles for LPG/air flame at φ=0.4 and different flow velocities.

Figure 4.10 and Figure 4.11 show the numerical modelling results for methane fuel at two different flow velocities (9 & 19 cm/s) and different equivalence ratios (φ = 0.35

& φ = 0.4). The experimental results (dashed lines with symbol) for equivalent cases are also plotted in these Figures. The dotted lines represent the calculated gas temperature and the solid lines represent the calculated solid temperature profiles for a range of 0 – 425 mm of the porous layers.

The temperature peak, shown in Figure 4.10, moved from 75 mm to 82 mm downstream of the burner inlet as the flow velocity increased from 9cm/sec to 19cm/sec. This flame behaviour is consistent (although the shift in the experimental results is much higher than for the numerical results) with results achieved experimentally and can be attributed to the difference in flow momentum and the preheating rate. Further increases in flow velocity to 29 cm/sec for equivalence ratio φ = 0.35, move the flame front out of the porous bed. The stability limit, established experimentally, was also found numerically, where blow off occurred at an equivalence ratio φ = 0.35 and a flow velocity of 29 cm/sec. This phenomenon was described before, in Section 2.5, as excess enthalpy or a super-adiabatic flame temperature.

The maximum flame temperatures in the numerical results show a good agreement with the experimental results (the difference was observed to be less than 10% or between 50 K to 100 K for all cases). The modelled flame front results show a very sharp and thin behaviour (in the order of 2-3 mm), while experimentally the temperature profile peak appears wider. This can be attributed to spatial resolution where the thermocouples used in the experiments are 6 mm in diameter and distributed at 25 mm intervals.

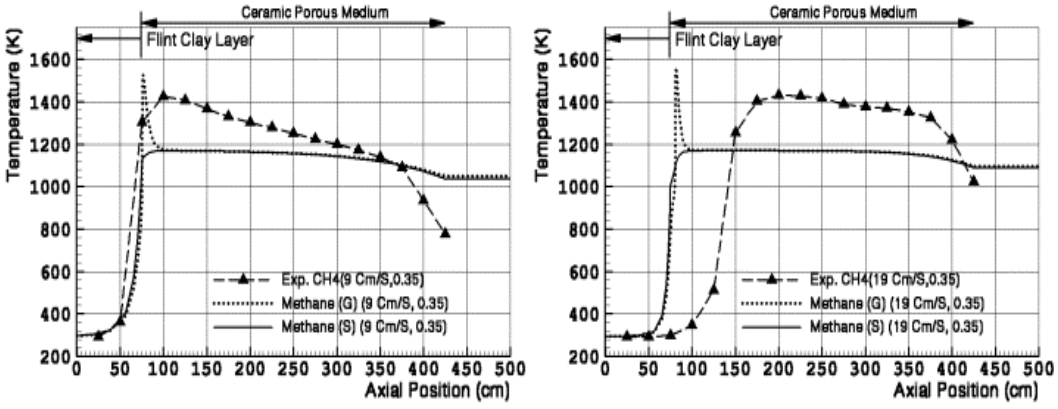

Figure 4.10: Comparison of measured and calculated centerline temperatures for initial velocities of 9 cm/sec and 19 cm/sec and an equivalence ratio of φ = 0.35.

A large discrepancy was observed between the calculations and experimental results in the post flame front region. Few parameters could cause higher temperatures in the experimental results, as compared with the calculations. One larger inaccuracy in the temperature measurement is due to the different radiation characteristics of the thermocouple and the porous medium. The thermocouple's shield is made of Inconel alloy 600 which has an emissivity of 0.19 - 0.21, while the ceramic beads have a higher emissivity of 0.45 to 0.69. Probes inserted into a hot medium can be influenced by conduction if the temperature difference across the medium is not uniform. In the experiments, it was assumed that the temperature is uniform and hence was no conduction from other parts of the bed. A full description of thermocouple inaccuracies can be found in Section 3.2.3.3. One smaller effect that may contribute to the discrepancy here is the failure of the PBM model to account for the radiation heat transfer from the gas phase to the solid phase. This may have had the effect of decreasing the gas temperature and increasing the solid phase temperature, which would bring the results (for both the gas and solid phases) closer to the experimental results.

Steeper temperature gradients in the same region were observed for the experimental results, which are believed to have been caused by heat losses to the surrounding areas, through the sidewalls. Compared with the porous burner power of ~5 kW, heat losses to the surroundings through the sidewalls and insulation were measured to be between 0.5% and 1% per centimetre for most cases. More accurate results may be achieved by modelling the PB in a 2-D code, which would account for both the radial and the axial heat transfers.

At the burner exit, while the temperature gradient for the numerical model is very small, the experimental results showed a sudden decrease at the burner exit. This is attributed to the larger heat loss to the surroundings from the radiation. This effect is not considered in the numerical model.

Similar results to those for equivalence ratio $\varphi = 0.35$ were observed for equivalence ratio $\varphi = 0.40$, as shown in Figure 4.11. At these conditions, the flame front showed less sensitivity to the increase in flow rate. The flame front shifted from 74 mm to 78 mm downstream of the burner inlet as the flow velocity increased from 9 cm/sec to 19 cm/sec. At the same time, the maximum flame temperature rose from 1520 K to 1620 K, which resulted in a 50 K higher temperature at the burner exit.

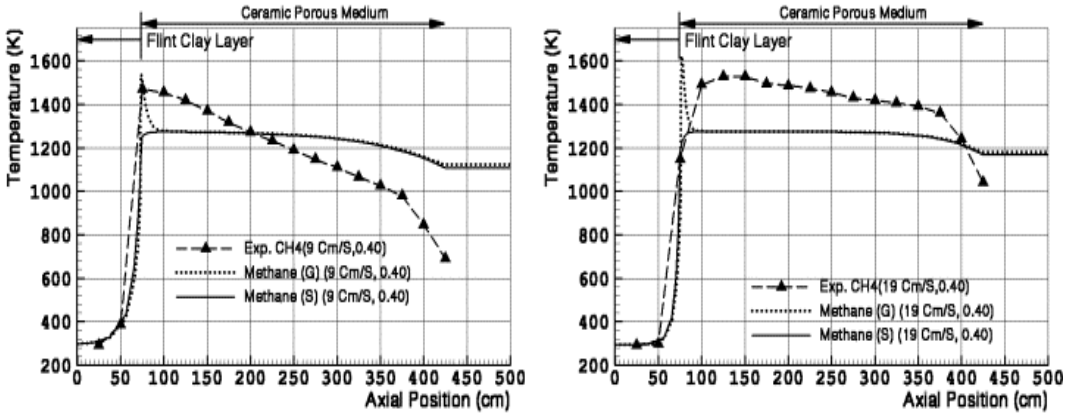

Figure 4.11: : Comparison of measured and calculated centerline temperatures for initial velocities of 9 cm/sec and 19 cm/sec and an equivalence ratio of φ = 0.40.

The influence of the inlet flow velocity on the flame temperature at a fixed equivalence ratio of φ = 0.40 is shown in Figure 4.12. The numerical data for the inlet flow velocities of 19 cm/s, 38 cm/s and 56 cm/s show the expansion of the preheating zone and the increase in flow temperature at the exit, with the increase in the flow velocity. These results are consistent with observations made earlier from the experimental results.

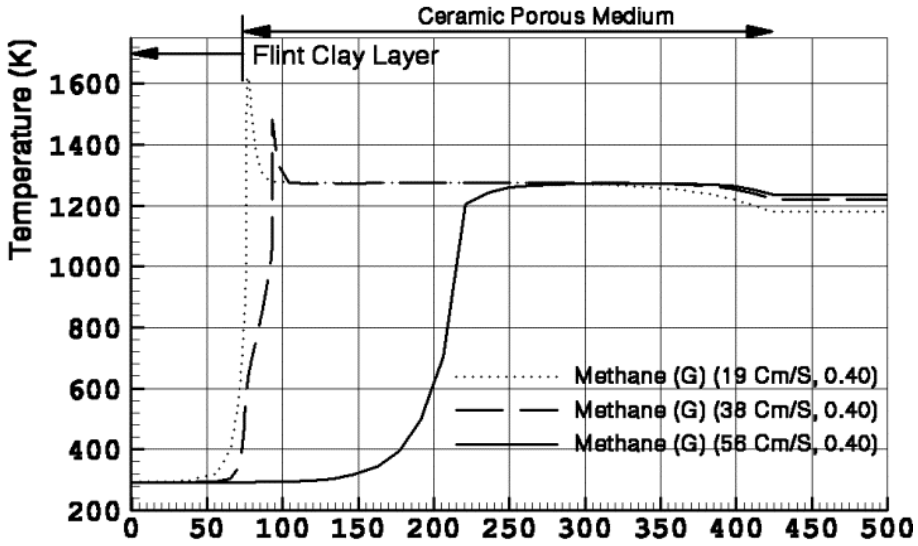

Figure 4.12: Comparison of calculated flame temperatures for cases with inlet flow velocities of 19 cm/s, 38 cm/sec and 56 cm/sec and an equivalence ratio of φ = 0.40

4.4.4 The effect of equivalence ratios on flame front locations

Figure 4.13 and Figure 4.14 show, respectively, centreline temperature profiles of CNG/air and LPG/air flames for an inlet flow velocity of 19 cm/sec and equivalence ratios of φ = 0.35 and φ = 0.4. It is clear that, for both mixtures, decreasing the equivalence ratio causes the flame to stabilise at a location further downstream from the burner entrance.

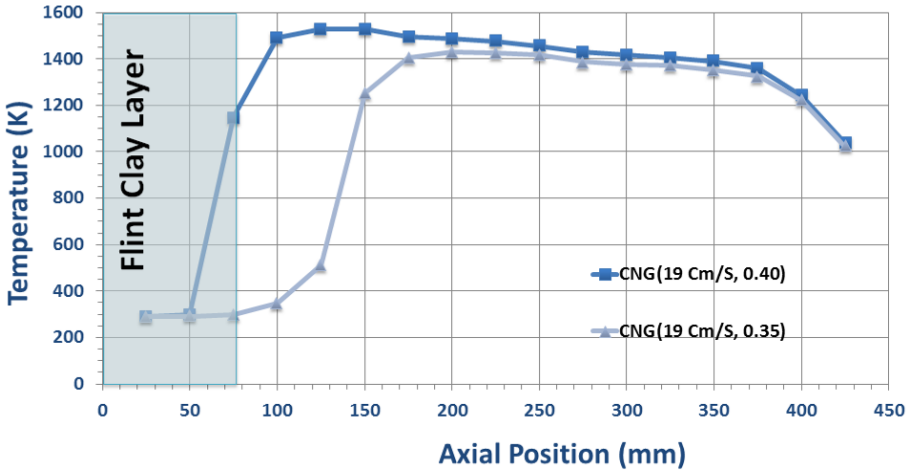

Figure 4.13: Temperature profiles for an inlet flow velocity of 19 cm/sec and different equivalence ratios for CNG/air flames.

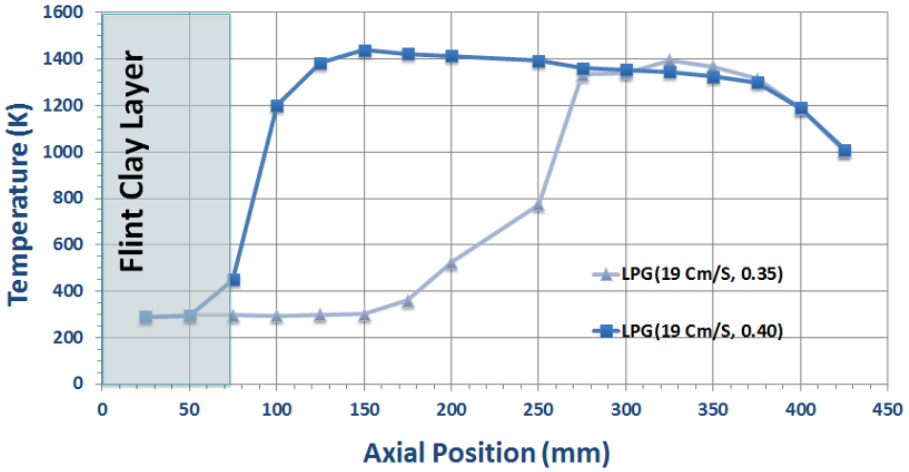

Figure 4.14: Temperature profiles for an inlet flow velocity of 19 cm/sec and different equivalence ratios for LPG/air flames.

The magnitude of the shift in flame position differs between the CNG/air and LPG/air flames, which are, in turn, also influenced by the equivalence ratio. This is attributed to the reduction in the flame speed and slight decrease in the flame

temperature. A smaller effect could be due to mixture momentum as the LPG mixture has a higher density compared with the CNG mixture. Figure 4.15 represents the numerical results of two different equivalence ratios, φ = 0.35 and φ = 0.40, for a flow velocity of 19 cm/sec. The effect of the change in equivalence ratio on both the flame location and the maximum flame temperature is highlighted. To compare the numerical and experimental results, solid and gas temperature profiles (solid and dotted lines) from the numerical models and the measured temperature profiles (dashed lines) are plotted simultaneously in Figure 4.15 a and Figure 4.15 b. For the flow velocity of 19 cm/sec and equivalence ratio φ = 0.35, it is clear that the flame front is established at 82 mm downstream of the burner inlet. Increasing the equivalence ratio to φ = 0.4, increases the flame speed and hence shifts the flame slightly upstream to 78 mm. Because of the low radiation characteristics of the first layer, the incoming fuel/air mixture is not preheated and the temperature gradient is very sharp. Further increases in the equivalence ratio do not change the flame location, even though the flame temperature increases to higher values. This scenario is consistent with the experimental results as shown in Figure 4.15 (a) and Figure 4.15 (b) (dashed lines).

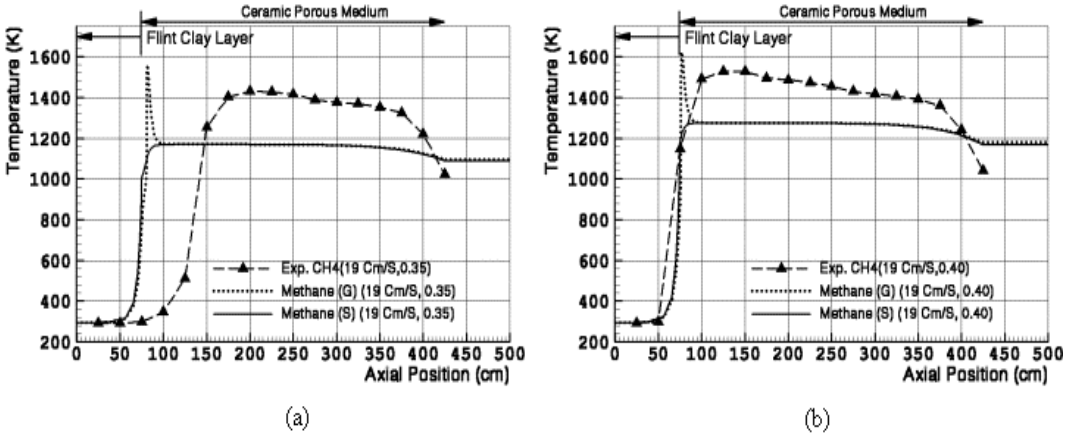

Figure 4.15: Comparison of measured and calculated centerline temperatures for a flame with an inlet flow velocity of 19cm/sec and for φ = 0.35 (a) and φ = 0.40 (b). The solid lines are the calculated bed temperature; the dashed lines are the calculated gas temperature and the symbols are the measured gas temperature.

4.4.5 Effect of fuel type on the flame front location

Figure 4.16 shows a comparison between the CNG/air and LPG/air flames for similar conditions (flow velocity of 19 cm/sec and φ = 0.40). For both cases, the flame front is located between 100 mm and 150 mm downstream of the burner's inlet. Increasing the flow velocity by almost 50% moved the flame front downstream by a distance of Δx_1= 62 mm for the CNG/air flame and a distance of Δx_2= 75 mm for the LPG/air flame. The shift in flame front Δx_2 is always larger than Δx_1, which indicates that LPG flames are more sensitive to an increase in flow velocity than CNG flames. It is also shown that although LPG has a higher firing rate under similar operating conditions (4.67 kW LPG flames versus 4.58 kW CNG flames), higher temperatures are achieved for CNG/air flames.

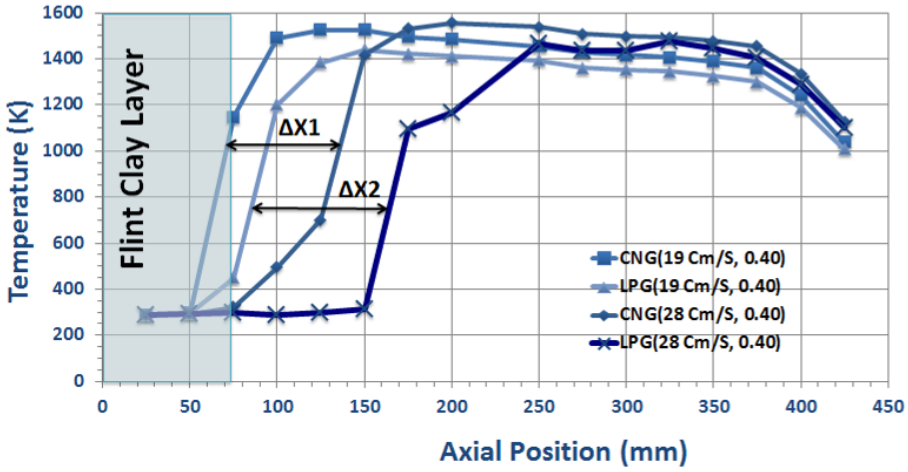

Figure 4.16: Comparison of CNG/air and LPG/air flames for similar equivalence ratios and different flow velocities

Figure 4.17 shows the results for an equivalence ratio of φ = 0.35 and different flow velocities for CNG/air and LPG/air fuel mixtures. The flame front for the 19 cm/sec velocity case and φ = 0.35 is located between 75 mm and 100 mm downstream of the burner's inlet. As in the φ = 0.4 case (Figure 4.16), doubling the flow velocity causes the flame front for both flames to move downstream, respectively by Δx_1= 68 mm for a methane/air and Δx_2= 170 mm for a propane/air flame. In this case too, the shift in the flame front Δx_2 is larger than Δx_1. Furthermore the change in the magnitude of Δx_2 for φ = 0.35 is much larger than that observed for φ = 0.4. This indicates that the sensitivity of LPG/air flames to an increase in flow velocity becomes much higher at lower equivalence ratios. The results in Figure 4.16 and

Figure 4.17 also show that methane/air flames produce a slightly higher flame temperature than propane/air flames.

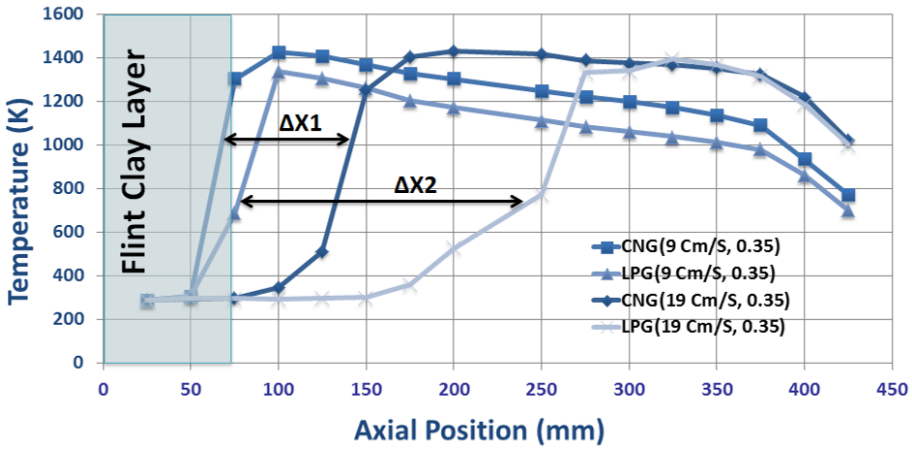

Figure 4.17: Comparison of CNG/air and LPG/air flames for similar equivalence ratios and flow velocities

Understanding the above phenomenon is quite complex, taking most of the available data to show that the opposite trend is expected. For example, the laminar flame speed for propane at Φ=0.6 is 0.13 m/s [150, 151] while for methane at φ = 0.6 is 0.08 m/s [150, 151]. The heat capacity for propane is 1.67 kJ/kg.K while it is 2.2 kJ/kg.K for methane. The auto-ignition temperature for propane is 470ºC while it is 580ºC for methane. The flow momentum of the propane mixture is almost the same as the methane mixture (2% less). Putting aside the fact that we are dealing with a mixture of fuel and air at a low equivalence ratio (the air constitutes more than 95% of the volume of the mixture) the above differences do not seem to lead to more stable propane flames, as compared with the case for methane flame.

Nonetheless, it is clear from the temperature axial profiles that an increase in flow velocity affects the mixture's heating rate and impacts on the ignition delay. The profiles also show a gradual increase up to auto-ignition temperatures before the flame seems to propagate at a higher rate. This seems to be true for the higher velocity cases and for both fuels. The difference between CNG and LPG is not fully understood and may be related to the location of the flame front and the heat transfer upstream, which is also coupled with the ignition delay phenomenon. Resolving this issue will require more detailed modelling, which is beyond the scope of the current study.

4.4.6 Super-adiabatic flame temperature and excess enthalpy

Figure 4.18 and Figure 4.19 show the comparison of calculated, adiabatic, and measured maximum flame temperatures for both CNG/air and LPG/air flames at different equivalence ratios and flow velocities. It is clear that the peak temperatures in all the experiments are higher than the adiabatic flame temperatures by at least 200°C for CNG/air flames and 150°C for the LPG/air flames. This is attributed to the enhanced heat transfer between the gas and the solid in the bed and has been described before as excess enthalpy in Section 2.5. It is worth noting that the diameter of the shielded thermocouples is similar to that of the ceramic beads. Heat conduction and radiation from the beads to the shield might introduce inaccuracies in the measurements. These inaccuracies, however, are expected to be negligible. On the other hand, the maximum calculated flame temperature, as shown in Figure 4.18, is ~100 K higher than the equivalent experimental flame temperature. Differences in temperature are blamed on heat loss to the surroundings through the ceramic tube walls and the insulation. This heat loss is not accounted for in the numerical modelling, which treats the porous burner as a 1-D adiabatic system. Closer results can be achieved by modelling the porous burner in a 2-D model, which would account for both radial and axial heat transfer. It is worth noting that it was not possible to conduct modelling in the LPG case due to numerical convergence issues, which appear to be associated with a lack of suitable chemical kinetics data at reduced temperatures.

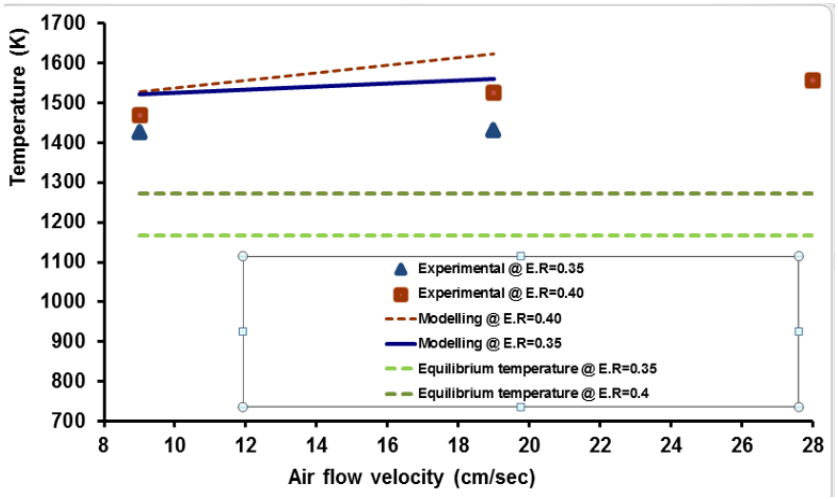

Figure 4.18: Comparison of measured and calcuated maximum flame temperatures for CNG flames with equivalnce ratios of φ = 0.35 and φ = 0.4. Also plotted are the equilibrium flame temperatures for two equivalence ratios.

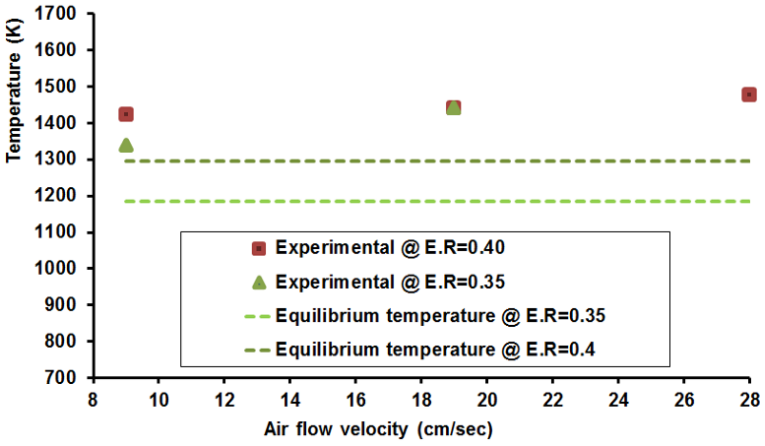

Figure 4.19: Comparison of measured maximum flame temperature for LPG flames with equivalnce raios of φ = 0.35 and φ = 0.4. Also plotted are the equilibrium flame temperature for two equivalence ratios.

4.4.7 Pollutants Emission

Table 4.2 and Table 4.3 show NO_X and CO mole fractions for all cases of interest in this study. Measurements of less than 4 ppm and 6 ppm, respectively, for NO_X and CO were recorded in most cases. The measured NO_X mole fraction is significantly smaller than the equivalent condition for premixed, freely propagating flames [152]. This is attributed to lower temperatures and the longer residence time in the porous bed. Although the measured CO mole fraction showed higher values when compared with the numerical modelling, it is still very low and classifies the porous burners in

the range of low-CO emission technologies. The low mole fraction of CO in the exhaust is attributed to lean combustion in the porous burners and sufficient residence times to convert CO to CO_2.

		φ = 0.35			Φ = 0.40		
		T (K)	NO_X (ppm)	CO (ppm)	T (K)	NO_X (ppm)	CO (ppm)
Adiabatic free flame (CH_4)		1166	~130	~0.001	1272	~268	~0.01
Experimental	9 cm/sec (CNG)	1425	0.17	2.99	1469	1.35	5.23
	19 cm/sec (CNG)	1430	1.3	2.77	1526	1.77	2.4
	28 cm/sec (CNG)	Blow Off	N/A	N/A	1557	2.52	1.38
Modelling	9 cm/sec (CH_4)	1522	N/A	0.15	1529	N/A	0.006
	19 cm/sec (CH_4)	1560	N/A	0.72	1624	N/A	0.04
	28 cm/sec (CH_4)	Blow Off	N/A	N/A	Blow Off	N/A	N/A

Table 4.2: Comparison of equilibrium and measured flame temperatures and relevant measured NO_X and CO mole fractions, in the exhaust, for CNG/air flames.

		φ = 0.35			φ = 0.40		
		T (K)	NO_X (ppm)	CO (ppm)	T (K)	NO_X (ppm)	CO (ppm)
Adiabatic free flame (C_3H_8)		1186	~153	~0.001	1295	~315	0.02
Experimental	9 cm/sec (LPG)	1339	1.2	2.89	1424	1.46	0.18
	19 cm/sec (LPG)	1441	1.36	6.68	1440	1.38	3.45
	28 cm/sec (LPG)	Blow Off	N/A	N/A	1476	1.37	0.03

Table 4.3: Comparison of equilibrium and measured flame temperatures and relevant measured NO_X and CO mole fractions, in the exhaust, for LPG/air flames.

The results, above, show that the experimental porous burner is capable of stabilising flames down to φ = 0.35 for both CNG/air and LPG/air flames. This is an encouraging result, which is in line with previous studies. The findings in these experiments helped with the understanding of the flame stabilisation process and also NOx formation in porous burners. These findings were later used as a solid base in the NOx reduction studies, which will be discussed in the next two chapters.

Also, the extension of this range to lower equivalence ratios will require further optimisation of the burner geometry and fuel feed-in mechanism. This can be

achieved by further analysis of the current data and trends and sampling inside the bed.

4.5 Summary and Conclusions

In this chapter, the stability and characteristics of lean premixed flames stabilised in a porous burner were measured and reported for fuel mixtures of CNG/air and LPG/air. Few parameters were found to be of higher importance in regards to flame stability in the porous burners. The key parameters include the flow velocity, equivalence ratio and fuel types. Using an experimental porous burner, these parameters were investigated individually and the following conclusions can be drawn:

1. It is possible to stabilise CNG/air flames in porous media within a range of flow velocities between 9 and 28 cm/sec and equivalence ratios down to 0.35. It is worth noting that the minimum equivalence ratio for igniting a CNG/air flame, under atmospheric conditions, in conventional burners, is slightly less than 0.5 [153].
2. The maximum measured NO_X and CO mole fractions at the burner exit, for CNG/air flames, were 1.3 ppm and 2.77 ppm, respectively. The maximum temperature achieved at an equivalence ratio of 0.35 was 1430 K, which is 264 K higher than the equilibrium temperature for the same equivalence ratio.
3. An LPG/air flame was stabilised in the porous burner within a range of flow velocities between 9 and 28 cm/sec and equivalence ratios down to 0.35. The maximum measured NO_X and CO at the burner exit was 1.36 ppm and 6.68 ppm, respectively. The maximum temperature achieved at equivalence ratios of 0.35 was 1395 K, which is 209 K higher than the equilibrium temperature for the same equivalence ratio.
4. For both fuels, it was found that increasing the flow velocity for low equivalence ratio mixtures has a noticeable effect on the distance to which the flame front shifts downstream. Under similar conditions, propane/air flames showed more sensitivity in terms of flame stability and location in comparison with methane/air flames.

5. Calculation results showed consistent trends with experimental results. Differences in the maximum flame temperatures between the calculation and the experimental results were observed to be less than 10%. The model is also capable of predicting the extinction limit and preheat region quite well. More work is needed to understand the discrepancy between the calculated temperature distribution and that measured in the experiments. A more sophisticated model needs to be considered, which is capable of accounting for the three dimensions as well as the physical and chemical interactions in the burner.

POROUS BURNER AS A POST-COMBUSTION MEDIUM

5.1 Introduction

NO_X Re-burning is a term first used by Wendt et al. [96] back in 1973, and describes a proven technology [97] in which nitric oxide is consumed using fuel as a reducing agent. The process involves partial oxidation of the re-burning fuel, under fuel-rich conditions, followed by the reaction of hydrocarbon radicals (CH_X) and NO. This results in the formation of intermediate nitrogen species such as HCN and subsequent conversion to N_2. In general, re-burning happens when gaseous, liquid or solid hydrocarbon fuels are injected downstream of the main combustion zone.

NO_X re-burning has been extensively analysed for a wide range of temperatures using different burners. Maintaining a uniform constant temperature over the experimental domain has made the experiments a real challenge. Bilbao et al. [109] have conducted a range of experiments in a 1500 mm-long quartz-tube which had a diameter of 23 mm. Observing a longitudinal temperature profile, they assumed that

the temperature is almost constant in a 600 mm zone in the middle of the tube. They used this zone to determine the gas residence time. Their results showed that for moderately low temperatures (between 600 °C and 1100 °C), the NO_X reduction efficiency increases as the temperature increases. It was found that at a given temperature, the fuel effectiveness in NO_X reduction follows the sequence: acetylene, ethylene, ethane, natural gas and methane. It is also found that natural gas and methane are of greater interest for high temperature applications while acetylene is more suitable for low temperature cases. Dagaut et al. [105] explained this sequence through the importance of HCCO intermediates for the production of HCN and extended the list to include propene. They noted that more HCCO is produced from acetylene fuels than the other re-burning fuels, especially at lower temperatures.

Using similar experimental techniques, Dagaut and Ali [110] extended this study to include a Liquefied Petroleum Gas (LPG) blend for a range of equivalence ratios and a temperature range from 950 K to 1450 K. They found that LPG, as a reburning fuel, follows the same general oxidation path already delineated for simple alkanes.

Williams and Pasternack [111] used a McKenna flat flame burner to investigate the intermediates of premixed flames for a variety of fuels doped with NO. They showed that for a fixed temperature of ~1800 K, the methane, ethane and ethylene flames all have similar reburning chemical pathways, while acetylene flames are quite different. They noted that acetylene produces about three times as much CN and NCO, compared with other fuels.

It is clear from the discoveries above that moderately low temperatures, fuel rich conditions and sufficiently high residence times are required to achieve reductions of NO_X, using hydrocarbon fuels. It is also apparent that well controlled conditions are required in order to better optimize the conversion efficiency.

Porous burners are known to have well-controlled bed temperatures and residence times over a wide range of operating conditions. Porous burners also have reasonably uniform temperature profiles radially, and lack steep temperature gradients and hence hot spots (refer to section 4.4.1 and later in Figure 5.7).

These characteristics are indications of a promising and desirable medium for the NO_X conversion process. Furthermore, relatively low operating temperatures lead to lower CO concentrations for fuel rich conditions [154].

Despite an extensive literature search, there seems to be little previous research on NO_X reduction using porous burners. Beside the experimental study by this author, in 2005 [49], which reported on the effects of equivalence ratios, flow velocities and input NO levels on NO_X reburning efficiencies, Binguea et al. [155] were the only group who studied the effect of the equivalence ratio on NO reburning in porous burners experimentally. They reviewed the effect of the equivalence ratio on NOx destruction and achieved NOx reburning in excess of 60% when their porous media was running with very rich fuel combustion regimes, up to equivalence ratios of 3. What were missing from those experiments were the attempts at co-investigating the other parameters that affect reburning efficiencies, such as the bed temperature and firing rate (inlet flow rate).

The effect of the presence of a $LaMnO_3$ (Pervoskite-type catalyst) deposited over a FeCrAlloy fiber panel on the porous burner performance has been investigated by Cerri [66]. The results were then compared with a non-catalytic burner. Catalytic porous burners showed significantly lower concentrations of CO and HC but the NO_X levels in the exhaust were similar to those in non-catalytic burners, when operated below 800 kW/m^2.

In this chapter, flame stabilisation over a wide range of flow velocities and rich equivalence ratios in a porous burner is investigated. The study also focuses on the parameters that control NO_X conversion inside a porous burner, both experimentally and numerically, including; the equivalence ratio, temperature, residence time and input NO level.

5.2 Experimental setup

A new experimental porous burner was developed and manufactured in the school of Mechanical Engineering at the University of Adelaide. Figure 5.1 shows a sketch of the new porous burner, which mainly consists of a mixing chamber followed by a heat exchanger and an insulated ceramic porous bed.

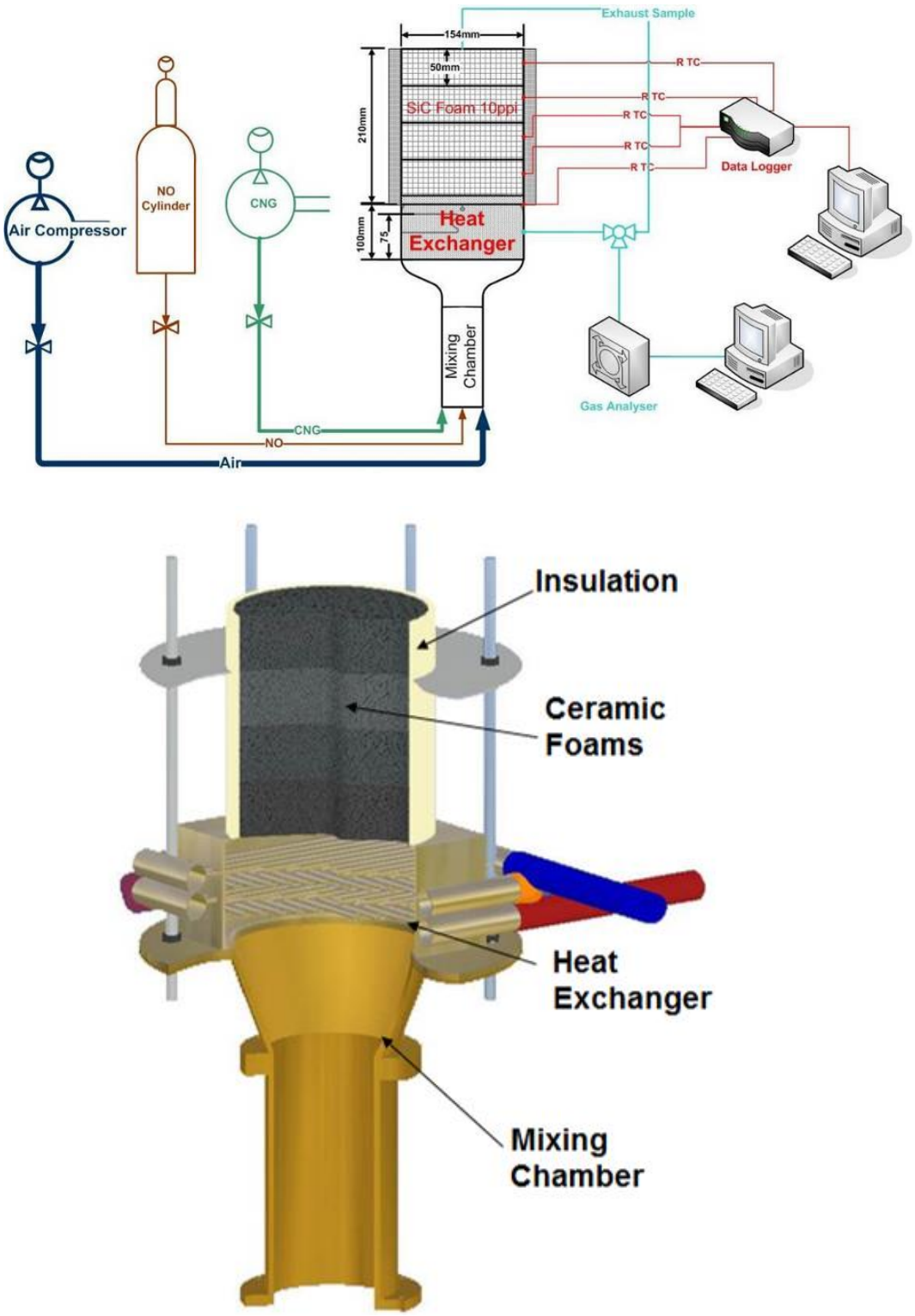

Figure 5.1: New porous burner setup and schematic

The mixing chamber has a relatively large volume (3,521 cm^3), which helps to achieve complete mixing of the inlet gases. The inlet gases can include air,

Compressed Natural Gas (CNG), NO and diluents such as nitrogen or carbon dioxide which could vary in ratio for different cases.

The porous bed is securely placed and sealed on the top of a heat exchanger (see 5.2.1 for details) and consists of 4 silicon carbide disks stacked on top of each other. Each disk is 50 mm thick, has a diameter of 150 mm, a porosity of ~ 90%, and has 10 pores per inch (ppi). The porous bed is insulated using Kaowool paper (2600 grade) followed by Kaofil Pumpable. R-type thermocouples are inserted circumferentially inside the porous bed through pre-manufactured grooves, at 25 mm intervals (staggered at 90°). The thermocouples' bodies are insulated using 710 ceramic (aluminium oxide with an emissivity of around 0.5, at temperatures above 1000 °C). While it is known that solid and gas temperatures could be different due to the high emissivity of porous materials [144, 156] and also many other parameters (i.e. the diffusivity of the gases, the surface temperature, the surface reaction etc. [157]). To minimize the temperature difference between the gas and solid phases, thereby minimising the results' inaccuracies, all the temperature measurements were taken after the temperature had become steady in the porous burner. Also, to ensure that the stabilisation of the temperatures in the bed occurs in a consistent rate, the temperatures were collected along the centreline of the burner at 5 second intervals. Once the temperature readings in all the thermocouples were stabilised (less than half a degree temperature difference per minute), the flow conditions were changed to another case.

Gas samples were withdrawn from both the mixing chamber and the exhaust gases using stainless steel tubes. The gas samples were analysed using a Chemiluminescent NO_X analyser (ML® 9841B) for NO and NO_X (with NO_2 determined by difference). The NO_X analyser has a range of 0-20 ppm with a resolution of 0.001 ppm. For NO and NO_X concentrations in excess of 20 ppm, the sample gases were diluted with N_2, using a dual channel sample diluter (ECOTECH 1412PD). The sample diluter was equipped with two individual dilution channels (ratios of 5:1 and 8.9:1), enabling the analysis of NO and NO_X concentrations up to 890 ppm.

The air and fuel are fed through the mixing chamber, wherein NO and other diluents such as nitrogen and carbon dioxide could be added to the mixture. The mixture was ignited on the top, and the flame propagated upstream along the porous bed. For

most cases, flames were stabilised at a location very close to the top of the heat exchanger. The effects of different equivalence ratios, flow velocity and initial NO_X levels in the inlet gas mixture on flame stabilisation, NO_X and TFN (Total Fixed Nitrogen) conversion efficiency were investigated.

Here, the NO_X conversion is defined as the ratio of the outlet NO_X concentration to the inlet NO_X concentration. Similarly, the TFN conversion ratio is calculated as:

TFN conversion ratio = $1- [TFN] / [NO_{in}] \times 100$

Where;

$[TFN] = [NO] + [NO_2] + [HCN] + [NH_3] + 2 \times [N_2O]$

Note that [TFN] corresponds to the overall concentration of nitrogen compounds except N_2, and is a reliable indicator of the efficiency of the reburning process. It is also worth mentioning that NO_{in} accounts for externally introduced NOx, in addition to flame produced NOx.

5.2.1 Heat exchanger

Flashback is a common problem when using porous burners. This implies a certain limited range of stable flames for a porous burner with a specific geometry. Hence, there is a need to extend the safe and stable operating conditions, including blow off and flashback, of the porous burner. To deal with this problem and extend the stability range, a different porous matrix (shape, size or material) can be used at the PB inlet [54, 57].

The heat exchanger is made of four rows of longitudinal and lateral ¼" copper tubes which use water as the coolant. The tubes are fitted in a copper box (150 mm x 150 mm x 100 mm) which is filled with calcined flint clay particles with a diameter less than 2mm. Calcined Flint clay has a low thermal conductivity ($K = 0.03\ W.m^{-1}.K^{-1}$) and during the experiments was always kept below 200 °C by the cooling coils. This flint clay section prevents flame flashback and hence extends the operating envelope of the porous burner. The small layer of flint clay between the cooling coils and porous bed is added to provide preheating of the fresh reactants.

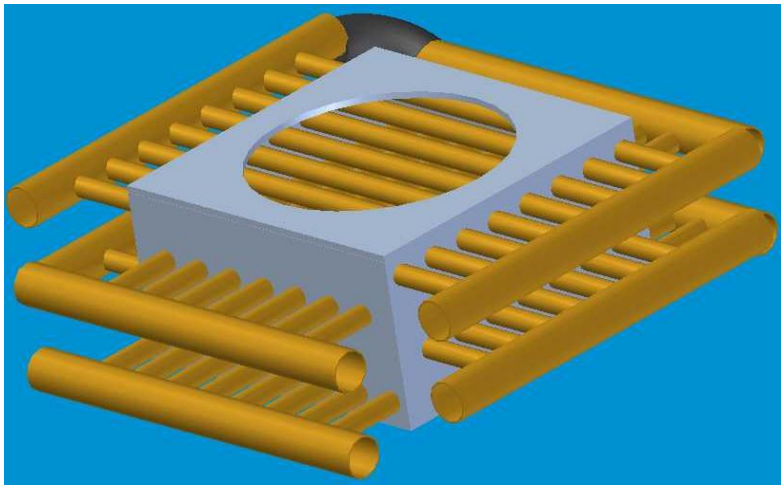

Figure 5.2: Sketch of the heat exchanger design

Figure 5.3: Photograph of the heat exchanger assembly

5.2.2 Control systems and measuring devices

Fischer & Porter calibrated volumetric flowmeters were used to control the fuel and air flow rates and a mass flowmeter was used to control the NO_X flowrate. More details can be found in Section 4.2.3.

The data from the thermocouples were fed into a data acquisition system, which ran the data control software AQMS version 5.00.3 to interpret and store data in an ASCII file. A flame detector is used to report the flame presence to a solenoid that can shut down the fuel supply in case the flame blows off.

5.3 Numerical modelling

The objective of the numerical calculations is to provide an insight into the chemical kinetics and NO_X conversion chemistry for the different experimental conditions considered in this study.

The PLUG simulator from the CHEMKIN [158] package was used in this study. PLUG is designed to model the non-dispersive and one-dimensional chemically reacting ideal gas mixture flowing in a channel of arbitrary geometry. The code incorporates the CHEMKIN [158] and SURFACE CHEMKIN software packages to interpret problems involving the gas-phase, elementary heterogeneous chemical kinetics in the presence of a solid surface and also the thermodynamic properties.

The porous burner was designed to have a uniform radial temperature profile. In addition, the tubular burner shape, very high porosity of the foams, and the relatively large burner diameter result in the flow being similar to that of a plug flow reactor. In the model, the reactor temperatures were set to values equal to those measured experimentally. Other assumptions that the model uses were also achieved experimentally, including: fully mixed inlet gases, uniform gas concentrations across the burner, and a small pressure drop along the burner. The GRI-Mech 3.0 chemical kinetic mechanism [159] was used for all kinetic modelling calculations. Some other assumptions were also made, and are discussed below.

The pressure drop across the porous media [160-162] is calculated as:

$$\Delta P = L V_{bed} \left(\frac{\mu_f}{K} + \frac{\rho F}{\sqrt{K}} V_{bed} \right) \tag{5.1}$$

In the above equation V_{bed}, μ_f, K, ρ, F and L are the actual bed flow velocity, dynamic viscosity, permeability, gas density, inertia coefficient and bed length, respectively.

For the conditions used in the experiments, it was found that the maximum calculated pressure drop along the porous foam is 243 Pa. With such a small pressure drop, the assumption of isobaric conditions is valid. Hence, atmospheric pressure was assumed for all the numerical calculations.

The fuel used in the experiments was CNG which comprised methane, ethane, propane, butane, nitrogen and carbon dioxide with volume fractions as given in Table 3.2

Since GRI-Mech 3.0 does not include C4H10 in its list of species and associated reactions the 0.3% of C4H10 in the CNG was substituted with the same amount of C3H8 in the numerical study.

5.4 Results and Discussion

In the following section, the flames' characteristics at different operating conditions are discussed. In addition, the experimental results are presented, which validate and clarify those assumptions made earlier in the numerical model. Finally, the results from the experiments are presented, along with the numerical calculations.

Both experiments and modelling were performed for air flow rates ranging from 50 slpm to 200 slpm, the equivalence ratios range from 1.0 to 2.0, for different inlet NO mole fractions of up to 1800 ppm. The effect of the critical parameters on NO_X and TFN conversion efficiencies such as flow rates (residence times), equivalence ratios and initial NO_X mole fractions are also presented and discussed.

5.4.1 Flame temperature and heat loss

For conventional open flames, the maximum flame temperature occurs at an equivalence ratio slightly larger than unity. Figure 5.4 shows the maximum measured temperature in this porous burner plotted against the equivalence ratio for a CNG flame with an air flow rate of 150 slpm. It is clear that the temperature increases with the equivalence ratio until it becomes constant at ~1600 K, prior to the flame becoming unstable and blowing off. The equivalence ratio at which the flame blows out was found to be different for different flow rates. For example, flames with flow rates of 50 slpm, 100 slpm and 150 slpm are found to be stable up to equivalence ratios of 2.1, 2.0 and 1.9, respectively. As a result, lower flow rates have a wider range of flame stability for this porous burner.

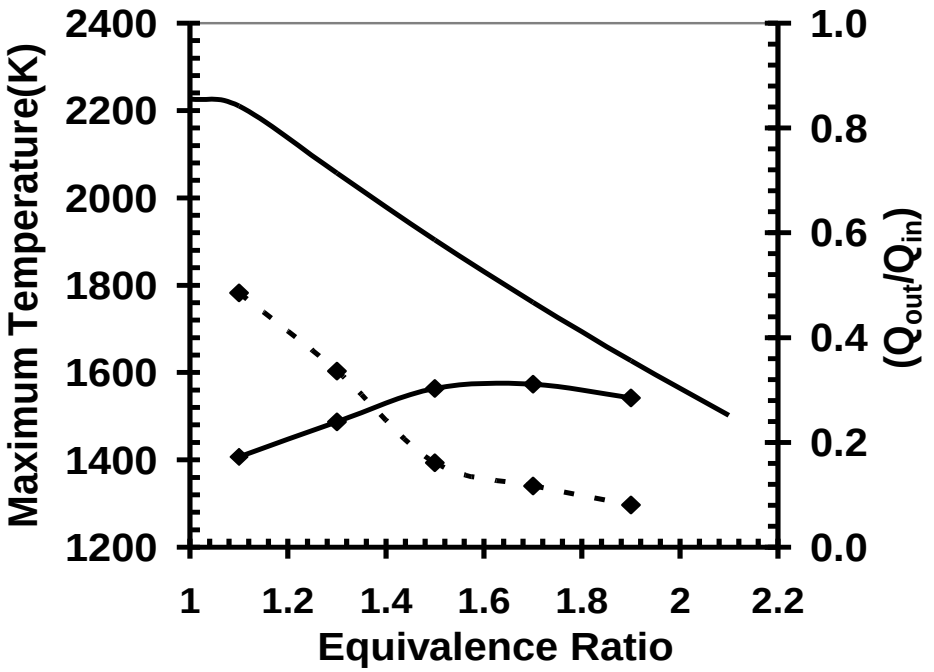

Figure 5.4: Measured maximum flame temperatures in the porous burner, along with the adiabatic flame temperature for fixed air flow rates of 150 slpm versus the equivalence ratios. The solid line represents the adiabatic flame temperature, (Solid line,♦) represents the measured maximum temperature and (dashed line,♦) represents the ratio of heat extracted by the heat exchanger to the firing rate.

Figure 5.4 also shows the adiabatic flame temperature and the ratio of heat extraction. The Heat extraction values are calculated by conducting an energy balance over the heat exchanger by measuring the water flow rate and inlet and exit temperature of the water. This heat loss is then normalized by the total heat input into the burner by the fuel.

It is clear that the measured temperature is much lower than the adiabatic flame temperature at lower equivalence ratios and this difference decreases close to blow out. This trend is consistent with that observed for the heat extraction ratio. It is found that flames with higher equivalence ratios stabilise further downstream from the heat exchanger and hence the ratio is lower. These trends are found to be consistent with other trends reported in the literature, e.g. Binguea et al. [51].

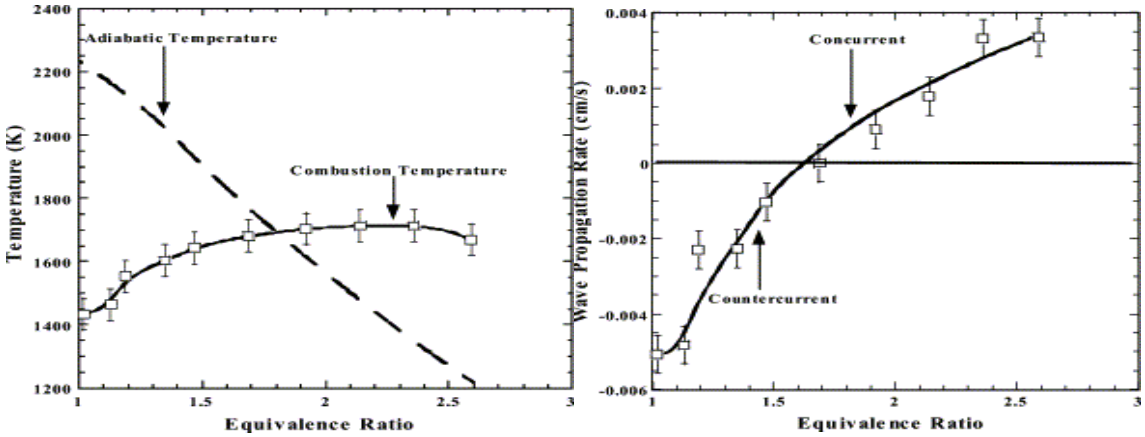

Figure 5.5: Temperature versus equivalence ratios for a flow velocity of 25 cm/sec (left) from another porous burner using Methane as fuel [51]. Propagation wave velocity plotted versus different equivalence ratios (right) [51].

Figure 5.5 (left) shows the measured flame temperature as well as the calculated adiabatic flame temperature, plotted against the equivalence ratio for a similar burner [51]. It is clear that the difference between the measured flame temperature and the adiabatic flame temperature decreases with the increase in equivalence ratio. Also apparent from the Figure is the semi-uniform temperature achieved at higher equivalence ratios, as observed earlier. Nonetheless, the difference between the adiabatic flame temperature and the maximum measured temperature is very different close to blow off, which is contradictory to other findings. Also plotted in Figure 5.5 (right), is the wave propagation rate for the same equivalence ratio, showing the flame propagation rate and direction as a function of the equivalence ratio. Flames with fuel-air mixtures closer to stoichiometric tend to propagate upstream, while flames with richer mixtures, >1.6, propagate downstream. This Figure highlights the sensitivity of these to the equivalence ratio.

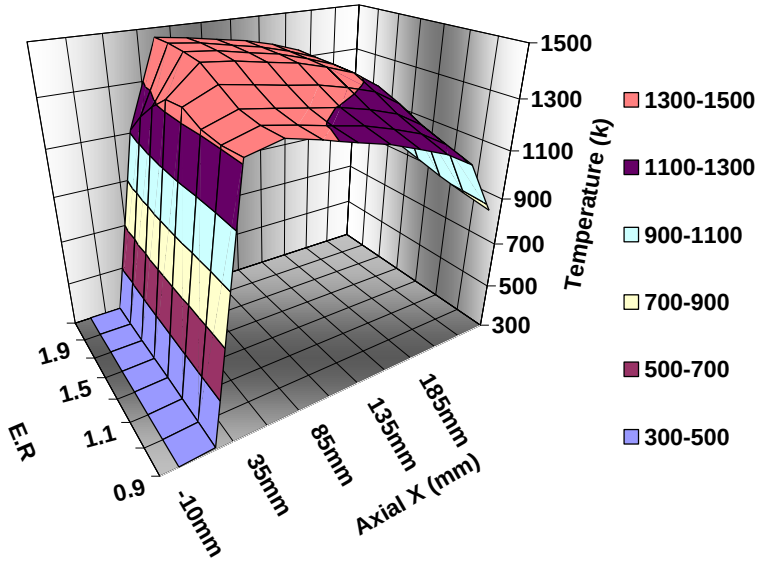

Figure 5.6: 3D contour presenting the measured centreline axial temperature for different equivalence ratios and a fixed inlet air flow rate of 100 slpm.

Figure 5.6 shows the measured temperature profiles along the centreline of the burner for flames with different equivalence ratios. The profiles exhibit a sharp increase from the ambient temperature very close to the heat exchanger (x = 0), which points to the ignition of the mixture and the axial location of the flame front. It is clear from this Figure that, with an increase in equivalence ratio, the location of the peak shifts downstream and away from the heat exchanger. Further downstream the temperature drops slightly because of the heat loss through the burner walls, until a large drop occurs close to the burner exit. This drop is believed to be caused by radiation to the surroundings. From the Figure it is clear that for lower equivalence ratios the flame front is narrower and the high temperature region is smaller (see range of 1300-1500 K). As the mixture becomes richer it appears that the front is much wider and this zone extends to a larger area within the bed.

Figure 5.7 shows the measured radial temperature profiles at two axial locations along the burner. These temperature profiles were measured using thermocouples located at 85 mm and 135 mm above the heat exchanger. These temperatures were measured in flames with an air flow rate of 50 slpm, an equivalence ratio of 1.5, and after stabilisation of the temperature readings.

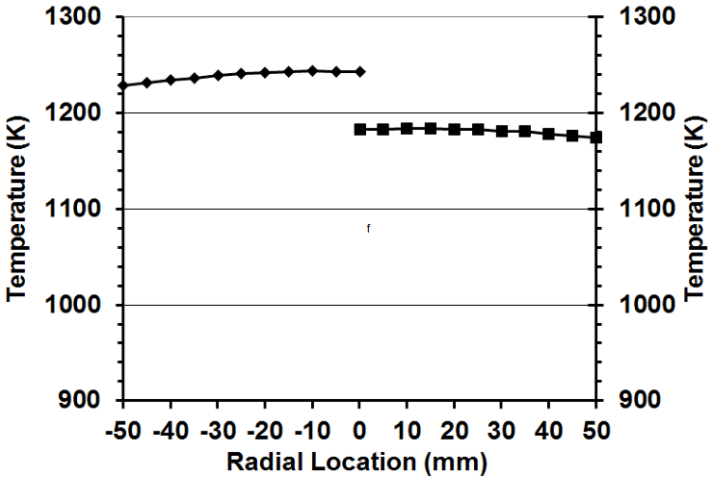

Figure 5.7: Measured radial temperature profiles for an air flow rate of 50 slpm and equivalence ratio of 1.5. (Solid line,♦) and (solid line,■) show radial temperatures at 85 mm and 135mm above the heat exchanger, respectively.

It is clear that in the region around the centre, with a diameter of at least 60 mm, the temperature varies by less than 5 K, while at the burner edge the drop is in the order of 20 K. This shows that temperature measurements in the middle are not affected by heat losses to the surroundings through side-wall heat loss.

As a result, reasonably uniform axial temperatures, as shown in Figure 5.6 (between x = 50 mm to x = 150 mm), in addition to a uniform radial temperature, as shown in Figure 5.7 ($0 \leq r \leq 30$), make this porous burner a suitable media for the NO_X and TFN conversion process. These measurements also vindicate our assumption for the numerical calculations, especially the one-dimensional flow and the use of the centreline profile as a representative of the temperature profile along the burner.

5.4.2 CO emission

The mechanism of NOx and TFN reduction relies on the supply of free radicals in the flame, which are being facilitated through the fuel rich flames. As a consequence, a substantial amount of CO is emitted from the burner, especially for a mixture with a high equivalence ratio. Figure 5.8 present the calculated CO mole fractions versus the equivalence ratio for a CNG-air mixture. It is noteworthy that it was not possible to measure the amount of CO in the exhaust due to the limited range of the gas analysis system that was available at the time. A simple chamber was built and mounted on top of the porous burner to investigate the possibility of CO burning in

the exhaust. This chamber had a central bluff body and three tangential air jets, which mixed the ambient air with the hot exhaust mixture in order to oxidise the CO to CO_2. It was found that almost the entire CO was converted to CO2 in this chamber, without the need for any additional heat input. Following this discovery, the issue of CO in the exhaust was ignored and not considered further in this study.

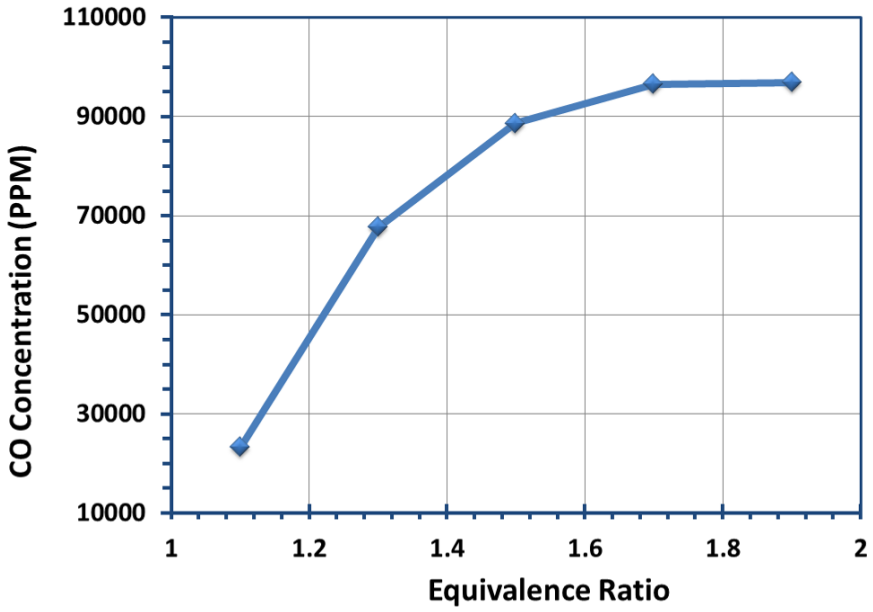

Figure 5.8: Calculated CO mole fractions at the exit of the porous burner for an air flow rate of 100 slpm and input NO of 100 ml plotted versus the equivbalence ratio.

5.4.3 Effect of Equivalence Ratios on NOx and TFN

Figure 5.9 shows the NO_X and TFN conversion efficiency plotted versus the equivalence ratios for an air flow rate of 100 slpm. For all cases, 100 ml of NO was added to the mixture.

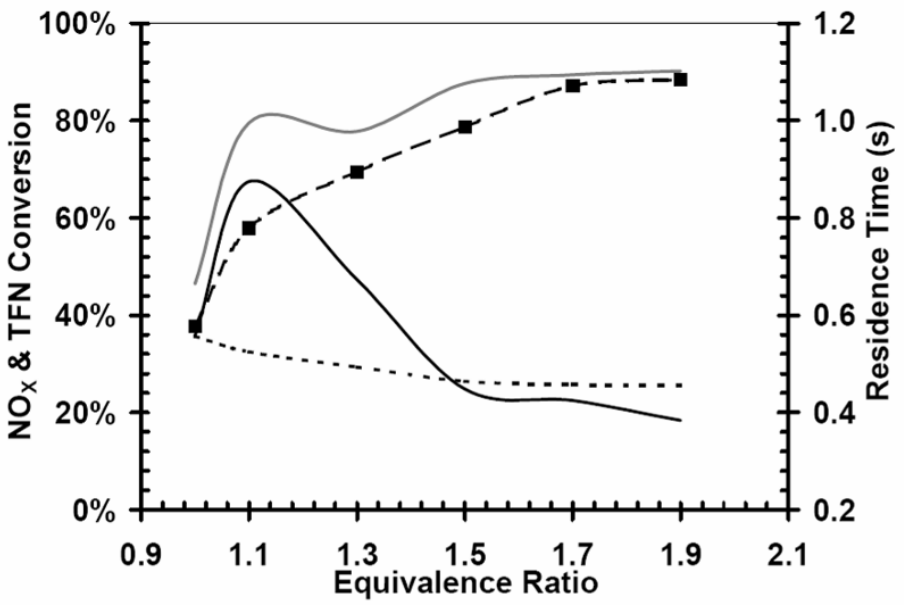

Figure 5.9: Measured NO_X conversion ratios and calculated NO_X and TFN conversion ratios plotted versus the equivalence ratio for an air flow rate of 100 slpm and initial NO level of 100 ml. The black solid line, grey solid line and (dashed line,■) represent the calculated TFN conversion, calculated NO_X conversion and experimental NO_X conversion, respectively. The dotted line shows the calculated residence time for different equivalence ratios.

It is clear that NO_X conversion increases with the increase in the equivalence ratio, and the available free HC radicals in the flame. The NO_X conversion starts at φ = 0.93, increases sharply up to φ = 1.2 and plateaus at φ > 1.5. It was found that the maximum NO_X conversion is reached at an equivalence ratio of φ = 1.5 for 50 slpm, 1.7 for 100 slpm and 1.9 for 150 slpm (not shown). By increasing the fuel/air ratio beyond these values, the NO_X conversion efficiency remains the same for a small range and eventually starts to drop. At the same time, increasing the equivalence ratio far beyond these values makes the flame unstable and blows it out of the burner.

It is clear from this Figure that the NO_X and TFN conversion profiles exhibit different behaviours at different equivalence ratios. While NO_X shows a better conversion when increasing the equivalence ratio, the predicted TFN concentration at the output revealed different results. The analysis showed that NO does not necessarily convert to N_2 for all conditions. For equivalence ratios close to unity, most of the NO is predicted to be converted to N_2 with low concentrations of HCN, NH_3 and N_2O. As the fuel concentration in the mixture increases, the TFN conversion follows a similar trend to the NO_X conversion for moderately fuel-rich conditions ($\varphi \leq 1.2$) and opposite trends for higher equivalence ratios. For φ > 1.2

most of the NO is converted to N-containing species such as N_2O, NH_3 and HCN and not to N_2.

In comparing the experimental and numerical results, see Figure 5.9, it is observable that the measured and predicted NO_X conversions agree better at higher equivalence ratios ($\varphi > 1.5$) and there is an inconsistency in the profile for moderately fuel rich flames ($1 < \varphi < 1.5$). Nonetheless, the trend of increased NO_X conversion with the increase in the equivalence ratio was captured well. However, the inconsistency is believed to be caused by the physical location of the flame front. Having equivalence ratios close to unity results in higher propagation waves upstream, as presented in Figure 5.5 (bottom). This causes the flame to move upstream close to the heat exchanger, as shown in Figure 5.10 and makes temperature measurement rather difficult. It is worth noting that only the temperature at 25 mm above the heat exchanger was recorded in the experiments. These values were then fed into the PLUG flow reactor. In the lower equivalence ratio cases, the flame front is likely to have been closer to the heat exchanger with a higher temperature than the one recorded at 25 mm. This will lead to the lower measured NO_X conversion rates, as seen in Figure 6.

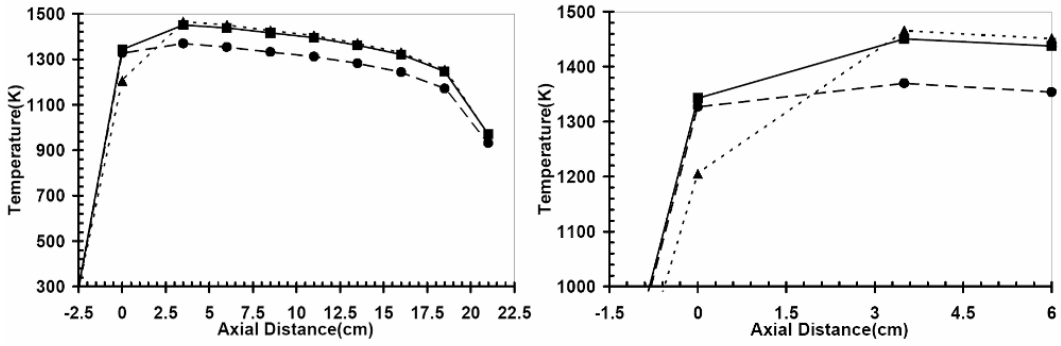

Figure 5.10: Axial temperature profiles for different equivalence ratios and inlet air flow rates of 100 slpm (left). Zoomed-in profiles close to the flame front (right). (Dashed line,●), (solid line,■) and (Dotted line,▲) represent equivalence ratios of 1.1, 1.5 and 1.9, respectively.

In order to understand the contribution of the various N-containing species on the predicted NO_X and TFN conversion efficiencies, an analysis of the chemical pathway was conducted for two equivalence ratios. Figure 5.11 presents species mole fractions along the reactor for a case with an equivalence ratio of 1.1, air flow rate of 100 slpm and 100 ml of NO in the mixture. Under these conditions (i.e. $\varphi = 1.1$), the

inlet NO (896 ppm) is reduced predominantly to molecular N_2 at the burner exit. The extent of NO conversion to N_2 is calculated to be 67%, based on the conservation of atomic nitrogen. Some NO is also converted to NH_3 (42 ppm), N_2O (30 ppm) and HCN (5 ppm) but in much smaller amounts (see Figure 5.11). The outlet concentration of TFN is 291 ppm.

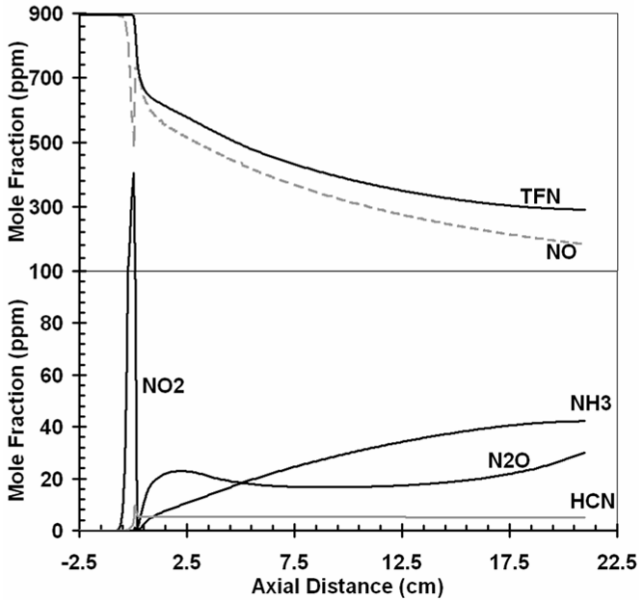

Figure 5.11: Calculated mole frcation of major N containing species for an air flow rate of 100 slpm, an equivalence ratio of 1.1 and 100 ml of NO at the inlet. Note the different scales in upper and lower graphs.

The mechanism of NO reduction under these conditions, which has been elucidated by analyzing the rates of progress for each species, is shown schematically in Figure 5.12. While reactions R212 and R214 form a cycle, with the NO reduced to HNO and back again, there remains a net flux of NO to HNO. The reverse of reactions R197 and R280 accounts for the reduction of HNO to NH. The larger flux of NH is reduced to N_2O (R199) and subsequently to N_2 (R183, R185), while a smaller flux is reduced directly to N_2 (R198). A small amount of NH is also reduced via NH_2 (-R202) to NH_3 (-R277 & -R278).

$H + NO + M \rightarrow HNO + M$	R212
$HNO + H \rightarrow H_2 + NO$	R214
$HNO + H_2 \rightarrow NH + H_2O$	–R197
$HNO + CO \rightarrow NH + CO_2$	–R280
$NH + NO \rightarrow N_2O + H$	R199
$N_2O + H \rightarrow N_2 + OH$	R183
$N_2O (+ M) \rightarrow N_2 + O (+M)$	R185

$NH + NO \rightarrow N_2 + OH$ R198
$NH + H_2 \rightarrow NH_2 + H$ –R202
$NH_2 + H_2 \rightarrow NH_3 + H$ –R277
$NH_2 + H_2O \rightarrow NH_3 + OH$ –R278

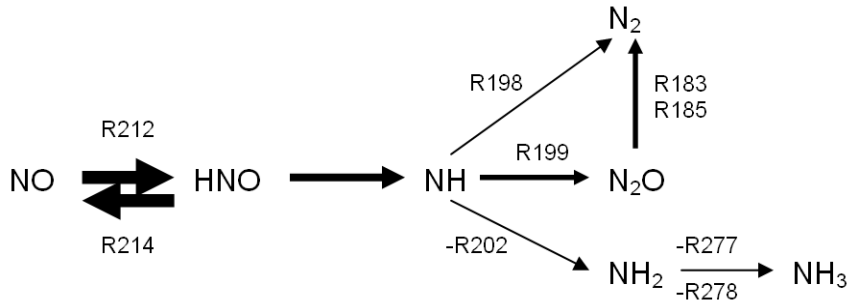

Figure 5.12: Mechanism of NO reduction for an air flow rate of 100 slpm, an equivalence ratio of 1.1, and 100 ml of input NO. The thickness of the arrows is indicative only and is not scaled accurately.

Under very fuel-rich conditions (i.e. $\varphi = 1.7$), the mechanism is different and the inlet NO (848 ppm) is reduced predominantly to NH_3 at the burner exit, with smaller amounts of NO reductions to N_2 and HCN, as shown in Figure 5.13. The extent of NO conversion to NH_3 is 43% with an NH_3 outlet concentration of 487 ppm. Smaller amounts of NO are converted to N_2 (92 ppm) and HCN (80 ppm). Under these conditions, the outlet concentration of N_2O is negligible. The outlet concentration of TFN is 658 ppm and thus only 22% of the inlet NO is converted to N_2.

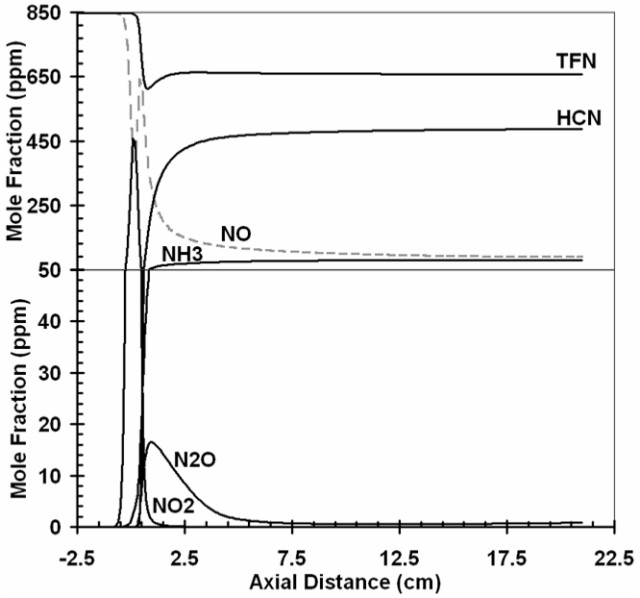

Figure 5.13: Calculated mole fractrions of major N containing species for an air flow rate of 100 slpm, an equivalence ratio of φ = 1.7 and 100 ml of input NO. Note the different scales in upper and lower graphs.

Here the NO reduction is initiated by reaction with HCCO (R274) to form HCNO. HCNO is then reduced via three separate channels (Figure 5.14): the major channel is via reaction R270 to form HNCO. The minor channels are via R271 forming HCN as a stable product and via R272 forming NH_2 as an intermediate product. HNCO is reduced directly to NH_2 (R265), which then reacts with either H_2 (-R277) or H_2O (-R278) forming NH_3 as the major stable product. A minor reaction sequence exists in which NO is reduced firstly to HNO via reaction R212. HNO then reacts with either CO (-R280) or H_2 (-R197) to form NH which then reacts with NO to form either N_2 (R198) as a stable product or N_2O (R199) as an intermediate; N_2O reacts directly with H (R183) to form stable N_2.

$HCCO + NO \rightarrow HCNO + CO$	R274
$HCNO + H \rightarrow H + HNCO$	R270
$HCNO + H \rightarrow OH + HCN$	R271
$HCNO + H \rightarrow NH_2 + CO$	R272
$HNCO + H \rightarrow NH_2 + CO$	R265
$NH_2 + H_2 \rightarrow NH_3 + H$	–R277
$NH_2 + H_2O \rightarrow NH_3 + OH$	–R278
$H + NO + M \rightarrow HNO + M$	R212
$HNO + CO \rightarrow NH + CO_2$	–R280
$HNO + H_2 \rightarrow NH + H_2O$	–R197
$NH + NO \rightarrow N_2 + OH$	R198
$NH + NO \rightarrow N_2O + H$	R199
$N_2O + H \rightarrow N_2 + OH$	R183

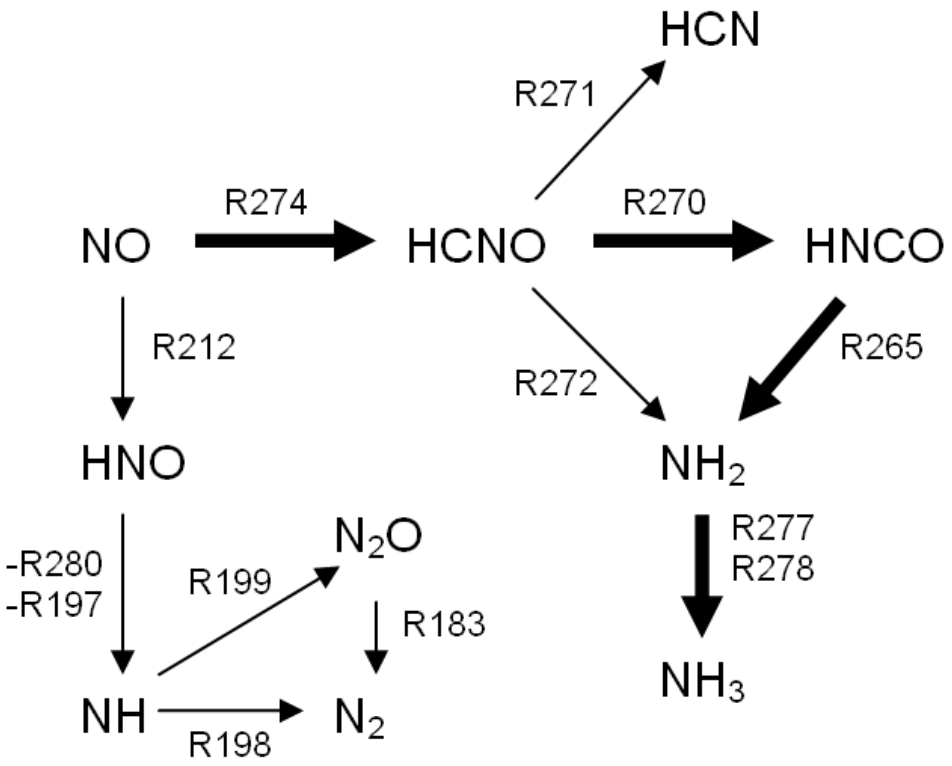

Figure 5.14: Mechanism of NO reduction for an air flow rate of 100 slpm, an φ = 1.7, and 100 ml of input NO. Note that the arrows' thicknesses are indicative and are not scaled accurately.

It is clear from the above results that different chemical paths dominate at the different equivalence ratios, which lead to the production of other intermediates such as NH_3.

The predictions reported in Figure 5.14 are broadly consistent with the modelling results of Dagaut et al. [99] for similar fuels and at similar equivalence ratios. Some differences are apparent, which are to be expected given the different kinetic mechanisms employed. Notably, the GRI-Mech 3.0 mechanism does not include the important channel: HCCO + NO → HCN + CO_2 and so this is missing from Figure 5.14. Thus the current calculations are likely to under-predict the formation of HCN [99]. This, of course, cannot be verified in the present experiments since [HCN] was not measured.

5.4.4 Effects of Flow Velocity (residence time) on NOx and TFN

The flame front location in porous burners is a function of the flow velocity (flow rate), the equivalence ratio and the rate of heat extraction from the system. The residence time is not only related to the flow velocity but to the other parameters too; i.e. for similar equivalence ratios, increasing the flow velocity results in higher flame temperatures, as seen in Figure 5.15, and a decrease in the residence time.

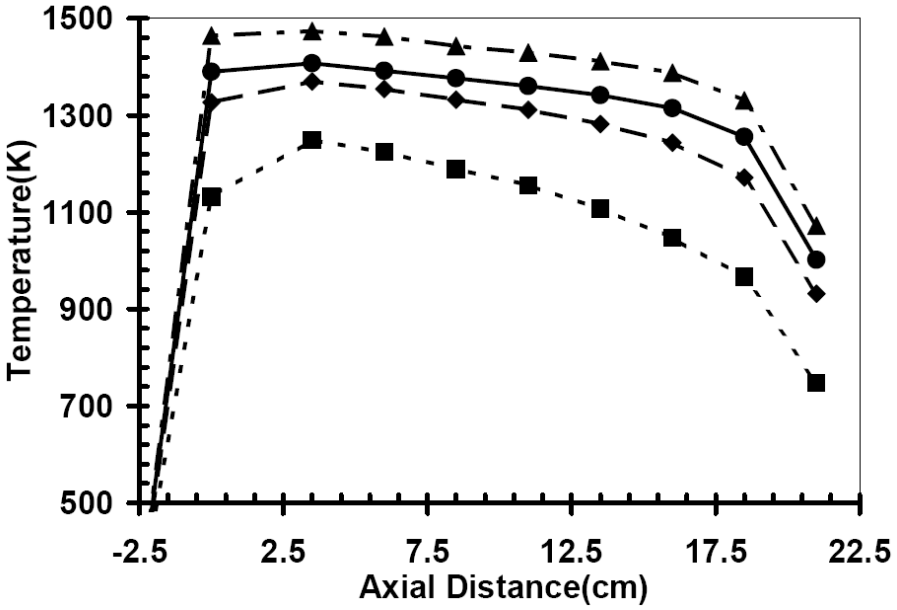

Figure 5.15: Measured axial temperature profiles for different air flow rates and for an equivalence ratio of 1.1. (Dotted line,■), (Dashed line,◆), (solid line,●) and (Dashed-Dotted line,▲) represent air flow rates of 50 slpm, 100 slpm, 150 slpm and 200 slpm, respectively.

It is now well established that the increase in the mixture flow rate affects the residence time in three ways:

1. Increasing the superficial velocity and actual velocity inside the bed leads to a shorter residence time, as seen in Figure 5.16;
2. Moving the flame location further downstream decreases the burner effective length, *(L-f)*, in the following equation and with it the effective residence time. The effective residence time (τ_{eff}) in porous burners is defined as the time during which the gas mixture is exposed to temperatures where chemical reactions can happen. The equation below calculates the effective residence time under different operating conditions of the burner.

$$\tau_{eff} = \frac{T_{in}(L-f)A_{up}\varepsilon}{T_{(x)}\dot{Q}_{up}} + \int_{x_0}^{x} \frac{A_{up}\varepsilon dx}{\dot{Q}_{up} + A_{up}\ln(\frac{T(x)}{T_{in}})} \quad (5.2)$$

The first term on the right hand side represents the gas residence time after the flame front and the second term represents the gas residence time between the inlet and the flame front (the preheating stage).

Applying boundary conditions $x = x_0 = 0$, $T_{(x)} = T_{max}$ and no preheating results in:

$$\tau_{eff} = \frac{T_{in}(L-f)A_{up}\varepsilon}{T_{\max}\dot{Q}_{up}} \quad (5.3)$$

In the above equations, T_{in}, T_{max}, L, f, A_{up} and ε are the gas mixture inlet temperature, flame temperature, porous bed length, flame location, upstream cross sectional area of the burner and the porosity, respectively. $\dot{Q}_{up}$ is the inlet volume flow rate;

3. Increasing the firing rate and the heat exchange between the solid and the gas phases simultaneously increases the flame temperature, T_{max}, in the above equation and hence decreases the density and residence time, as indicated in Figure 5.15.

In summary, by increasing the flow rate, $\dot{Q}_{up}$, the flame temperature, T_{max}, and the flame location (the distance between the flame front and the heat exchanger), f, also increases. This will decrease the residence time and, as a consequence, the conversion efficiency, as can be seen in Figure 5.16. It should also be noted that in the temperature range from 1000 K to 1500 K, increasing the flame temperature for the same residence time could result in better NO_X to N_2 conversion efficiency.

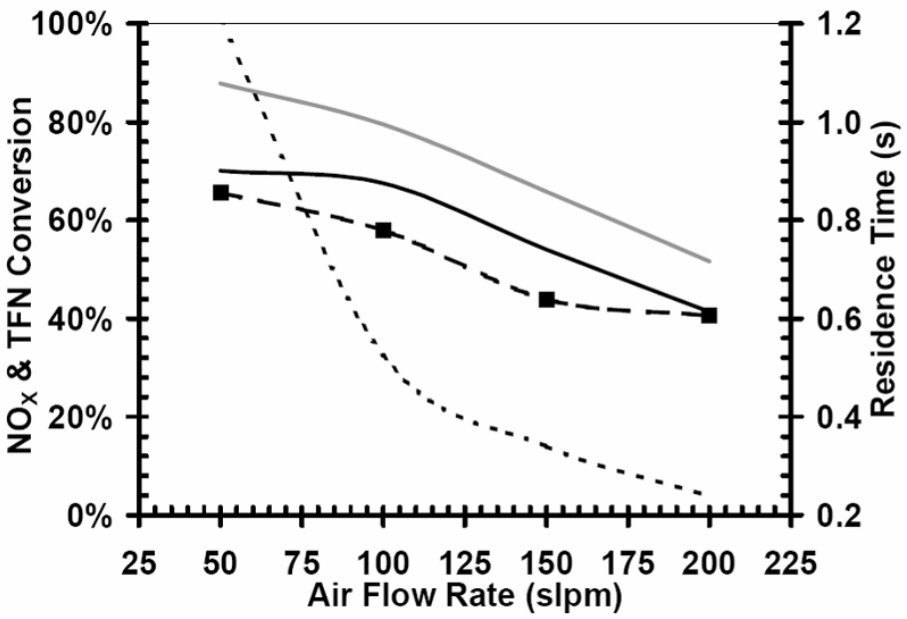

Figure 5.16: Measured and calculated NO_X conversion ratios plotted versus air flow rates for an input NO level of 100 ml and φ = 1.1. Black solid line, grey solid line and (dashed line,■) represent the calculated TFN conversion, calculated NO_X conversion and experimental NO_X conversion, respectively. The dotted line represents the residence time for different cases.

It is worth noting, that increasing the total flow rate (by adding more fuel) results in a reduced residence time and higher temperatures along the burner. If the temperature is within the desirable range of 1000 - 1500 K, there would be a competition between the two effects of production and destruction of NO. For temperatures above 1500 K, both 'temperature increase' and 'residence time decrease' degrade the NO_X and TFN conversion efficiency.

Figure 5.16 shows a comparison between the numerical and experimental conversion results for different air flow rates and for φ=1.1. Also plotted in Figure 5.16 is the change of residence time with the air flow rate. It is clear that the numerical NO_X and TFN modelling results show fairly similar trends to that measured experimentally (for the NO_X conversion only), albeit with a difference in the absolute values. This difference is larger at lower flow rates and lower equivalence ratios. This discrepancy is again believed to be a product of the experimental setup where the maximum flame temperature happens closer to the heat exchangers and is not captured by the existing thermocouples.

It is worth noting that the above mixture strength range can vary slightly from one system to another. This range gets narrower when the flow rate is increased, as the

flame moves further downstream. As a result, the discrepancy between the experimental and numerical results was smaller for higher air flow rates (e.g. 200 slpm in Figure 5.16) or higher equivalence ratios where the flame stabilises further downstream.

It is clear from Figure 5.16 that increasing the flow rate from 50 slpm to 200 slpm increases the rate of consumption by a factor of 3.7, while the residence time decreases by a factor of 4.75. This eventually results in a decrease in NO consumption and hence NO_X and TFN conversion efficiency.

5.4.5 Effect of Initial NO_X Mole Fraction

Figure 5.17 shows the NO_X and TFN conversion efficiency plotted versus the inlet NO concentration for an air flow rate of 100 slpm and $\varphi = 1.1$. It was found that the NO concentration in the inlet mixture may change the conversion efficiency by up to 20%. In general, the higher the NO level in the reactant stream, the better the conversion efficiency. However, this trend is only sustained up to a certain level. The desirable NOx reduction was found to be a function of the flow rate and almost independent of the equivalence ratio. In other words, for any flow rate there is an optimum inlet NO_X/air ratio (or more accurately a narrow range of ratios), which gives the best conversion efficiency. This ratio seemed to be almost the same for different equivalence ratios and decreases as the flow rate increases.

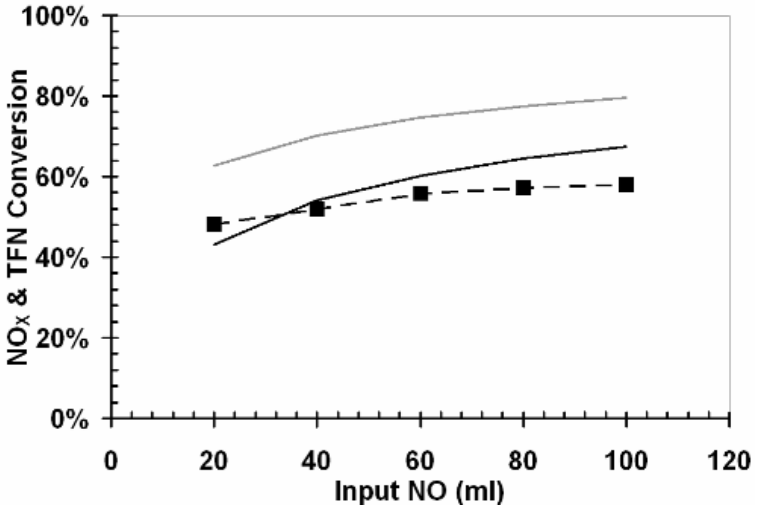

Figure 5.17: Measured and calculated NO_X conversion ratios plotted versus the input NO levels for air flow rates of 100 slpm and $\varphi = 1.1$. The black solid line, grey solid line and (dashed line,■) represent the calculated TFN conversion, calculated NO_X conversion and experimental NO_X conversion, respectively.

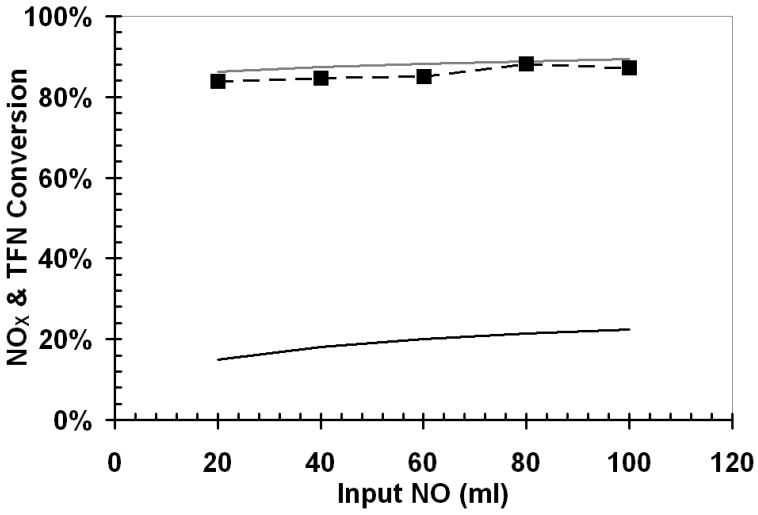

Figure 5.18: Measured and calculated NOx conversion ratios plotted versus the input NO levels for air flow rates of 100 slpm, and φ = 1.7. The black solid line, grey solid line and (dashed line,■) represent the calculated TFN conversion, calculated NOx conversion and experimental NOx conversion, respectively.

From Figure 5.17, it is clear that for the φ = 1.1 case there is a clearly increasing trend in NO conversion in line with the increase in the initial level of NO. For example, increasing the initial NO level from 20 ml to 100 ml for an equivalence ratio of 1.1 increases the conversion efficiency by 20%. While for richer fuel conditions (φ = 1.7) as shown in Figure 5.18, the conversion efficiency increases just by 4% for the same range of input NO level.

5.4.6 Effect of CO_2 in the inlet mixture on NOx and TFN

The motivation of this particular part of the project is to reduce NOx from the exhaust gases of any combustion system. All of the work reported above shows a mixture of fuel and air doped with NO. In this section, the effect of CO_2 in the inlet mixture on the NOx and TFN conversion is considered. In doing so, the composition of the exhaust stream, say of an engine or a furnace, will be simulated.

Figure 5.19, below, presents the NOx reburning efficiency plotted versus the equivalence ratio for two cases. One with no CO_2 added to the mixture at the inlet and the second with 7.8% CO_2 by volume added to the mixture. It is clear that the addition of CO_2 has no effect on the trend, which implies that there are no changes to the chemical kinetics. This is expected, as CO_2 at these temperatures is chemically inert and does not influence the chemical pathways. The small difference (< 4%) in

the magnitude of the efficiency is related to the slight reduction in temperature due to the dilution effect, which also shifted the flame slightly downstream, as compared with the flame with no added CO_2. These results indicate that the concept of NOx reburning inside the porous bed is not affected by the amount of CO_2 (or other inert substance including N_2) in the mixture, as long as the temperature of the flame can be maintained.

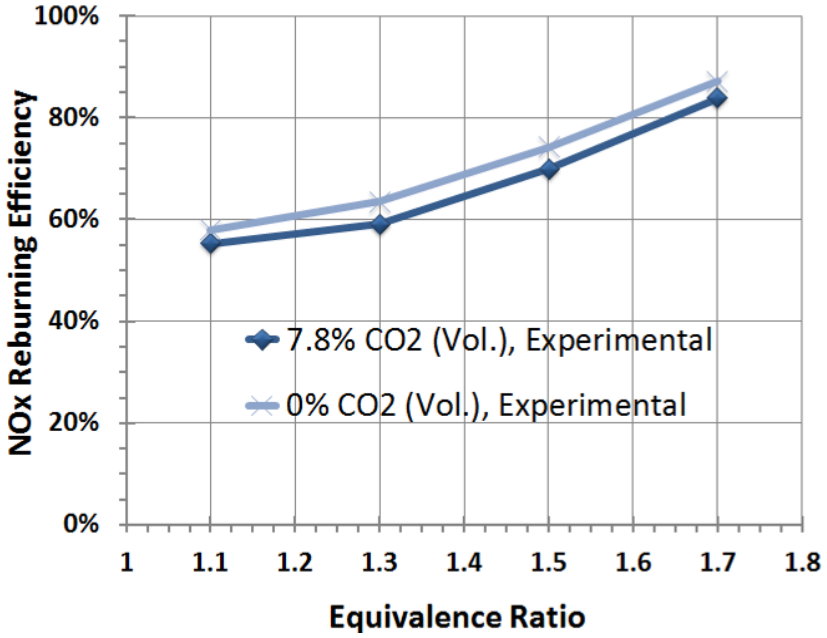

Figure 5.19: The effect of CO_2 addition on the measured NO_X conversion efficiency at different equivalence ratios, for 100slpm and an input NO of 100 ml.

5.5 Summary and Conclusions

A laboratory-scale porous burner was designed and constructed to examine the parameters controlling the NO_X and TFN conversion inside a porous medium. The experimental porous burner showed consistent, reliable and stable behaviour for a wide range of conditions. Results from the experiments were compared with those calculated using the PLUG simulator of the CHEMKIN package and with the GRI-Mech 3.0 chemical kinetic mechanism.

It was found that porous burners are a suitable medium for NO_X conversion because of the ease by which temperature, equivalence ratios and residence time can be

controlled. This feature allows for maximum optimisation to improve the conversion efficiency under varied inlet conditions.

It was also found that the best conversion was achieved for a maximum bed temperature below 1500 K and that NO_X conversion of 90% is possible. It was also found that for the slightly rich equivalence ratios $\varphi < 1.3$ conditions, most of the NO converts into N_2, while for higher equivalence ratio cases, more intermediate species are formed, in particular NH_3. The best TFN conversion efficiency (65%) was found at $\varphi = 1.1$, T = 1370 K and a total air flow rate of 100 slpm.

For similar equivalence ratios, it was also found that lower flow rates or flow velocities result in better conversions by increasing the residence time and decreasing the temperature to the desirable temperature range. While residence time was the most important parameter in the conversion process, lower temperatures (for lower flow rates) were also found to improve both NO_X and TFN conversion. In addition, lower mixture flow rates were found to have a wider range of flame stability.

Analysis of the chemical pathways for low and high equivalence ratio cases showed that the formation of nitrogen-containing species in the very rich conditions is due to the increased importance of the HCNO, as compared with the HNO, path. The latter is the dominant path at low equivalence ratios and leads to the formation of N_2.

The NO concentration in the initial mixture can change the conversion by up to 20% at low equivalence ratios ($\varphi \leq 1.3$) and have a negligible effect at higher equivalence ratios.

Adding CO_2 to the mixture had a negligible effect on the NOx conversion efficiency. This is believed to be due to the non-reactive nature of CO_2 at such low temperatures.

SURFACE REACTION IN POROUS BURNERS

6.1 Introduction

In the previous chapter, detailed measurements and modelling of the NOx and TFN conversion in a premixed mixture of CNG/air flames were presented and discussed. These flames were stabilized inside a porous burner and the effects of different controlling parameters were investigated. This chapter expands on the modelling study and, in particular, assesses the role of surface kinetics on the results under different operating conditions.

Many studies have modelled porous burners, treating the non-catalytic porous media as being chemically inert [23-25, 54, 61, 64, 78, 91, 92, 118-122]. However, it is known that the presence of surfaces can strongly influence gas-phase reaction systems (e.g. the oxidation of hydrogen and carbon monoxide [123]) due to the termination of reactive radicals at the surface. The rate of radical termination at a surface is strongly influenced by both the nature of the surface and the conditions, if any, under which the surface has been pre-treated. Given the large surface-to-volume ratios that are characteristic of porous burners, it is imperative that surface reactions leading to the termination of gas-phase radicals be considered when modelling

combustion and, in particular, the formation of minor species in porous burners. Despite an extensive search in the literature, no previous studies have specifically considered the impact of radical recombination at the surfaces in the predictions of NO_X conversion in porous burners.

Despite the absence of detailed information about the nature of the surface or a detailed elementary heterogeneous gas-solid reaction mechanism, it is still possible to estimate the impact of surface reactions in a gas-phase system. One approach is to assume that the rate of radical termination at the burner surface occurs at the mass-transfer-limited rate [124-126]. The diffusion-limited reaction rate may be calculated following the method of Thomas et al. [124], based on a cylindrical channel model, assuming laminar flow. This approach estimates the maximum possible rate of radical termination and hence the maximum possible effect of surface reactions on the model predictions. A comparison of these predictions with those for which surface reactions are neglected provides an upper and lower limit of the likely effects of surface reactions on the model predictions. Under conditions where the upper and lower limits coincide, it is appropriate to neglect the influence of radical termination at the burner surface. Otherwise, an effective rate of radical recombination (with a value intermediate between these limiting cases) may be assumed.

In this chapter, the impact of radical termination at the surfaces on the kinetic model predictions of NO reburning in a porous burner is examined and the effect is compared with our previous experimental measurements of NO_X/TFN conversion in a porous burner, as presented in Chapter 5.

6.2 Numerical Modelling

The PLUG simulator from the CHEMKIN 3.6 [158] package, which is designed to model the non-dispersive and one-dimensional chemically reacting ideal gas mixture flowing in a channel of arbitrary geometry, is used in this study.

As discussed earlier in the thesis, the pressure drop, ΔP, across the porous media is calculated [160-162] as:

$$\Delta P = L V_{bed} \left(\frac{\mu_f}{K} + \frac{\rho F}{\sqrt{K}} V_{bed} \right) \tag{6.1}$$

In this equation, V_{bed} (m/sec), μ_f (kg.sec/m), K (m^2), ρ (kg/m^3), F (m^{-1}) and L (m) are the cross-sectional mean velocity (also called the Darcian or seepage velocity [161]), dynamic viscosity, permeability, gas density, inertia coefficient and bed length, respectively.

For the conditions used in the experiments, the maximum calculated pressure drop along the porous foam is less than 250 Pa and hence atmospheric pressure and isobaric conditions are assumed in the model.

The fuel used in the experiments is Compressed Natural Gas (CNG) which comprises methane, ethane, propane, butane, nitrogen and carbon dioxide, with volumetric fractions as detailed earlier in Table 3.2.

As discussed earlier, the GRI-Mech 3.0 mechanism is used here, however it does not include C_4H_{10}, which has a mole fraction of 0.3%. Instead, the C_4H_{10} in the CNG is substituted for the same amount of C_3H_8 when specifying the inlet composition for the model.

As discussed in Chapter 5, the burner is designed to have a uniform radial temperature profile. In addition, the tubular burner shape, very high porosity of the foams, and the relatively large burner diameter result in the flow being similar to that of a plug flow reactor. In the modelling calculations, the reactor temperatures are set to values equal to those measured experimentally. Other assumptions include having fully mixed inlet gases and a uniform gas concentration across the burner.

Unless otherwise indicated, kinetic modelling predictions were determined using the GRI-Mech 3.0 chemical kinetic mechanism [159] and the Sandia thermodynamic database [163]. In some limited cases, the Konnov chemical kinetic mechanism [164] has also been used for comparison. In both mechanisms, surface reactions are incorporated by considering the termination of key radicals at the reactor surfaces. The key radicals for the CH_4-H_2-O_2 system, *viz.* H, O, OH, HO_2, CH_3, and CH_3O, are assumed to react to stable species according to the irreversible pseudo-reactions shown in Table 6.1. The pseudo-species, “H_W”, “O_W”, etc., denote radicals which are converted to stable species and hence are removed from the radical pool. This is an approximation since, in the experimental system, radicals that are lost at the wall would actually be converted to stable species. However, the rates of production of pseudo-species in the simulations presented are relatively small and so this

assumption does not impact on the predicted concentrations of stable species under any of the conditions investigated.

NO.	Reaction	*A (S-1)*	*n*	*E/R*
326	H=>H_W	4.18E-01	1.75	0
327	O=>O_W	1.01E-01	1.75	0
328	OH=>OH_W	9.06E-02	1.75	0
329	HO_2=>HO_2_W	6.42E-02	1.75	0
330	CH_3=>CH_3_W	6.66E-02	1.75	0
331	CH_3O=>CH_3O_W	5.03E-02	1.75	0

Table 6.1: Arrhenius parameters for reactions added to GRI-Mech 3.0 and Konnov mechanisms that account for surface reactions.

The forward rate constant, k_j, for these pseudo-reactions is estimated according to three different conditions, as detailed in the cases below:

Case 1: Negligible surface reactions ($k_j = 0$)

The surface reactions are assumed to be negligible and therefore each of the kinetic mechanisms is unchanged.

Case 2: Very fast surface reactions ($k_j = k_{ci}$)

The surface reactions are assumed to occur at the mass-transfer limited rate, k_{ci}, which is estimated based on a cylindrical channel model, assuming a laminar flow [124]. Thus,

$$k_j = 1.5\eta\theta^2 D_i \tag{6.2}$$

and D_i is estimated using the Chapman-Enskog model [165] as applied by Fuller et al. [166]:

$$D_{i,N_2} = \frac{1.00*10^{-3}*T^{1.75}(1/M_A + 1/M_{N2})^{1/2}}{P[(\sum_i \nu_k)^{1/3} + (\sum_{N_2} \nu_k)^{1/3}]^2} \tag{6.3}$$

Fuller et al. [166] define a procedure for calculating $\sum_i \nu_k$ for simple molecules using empirically determined data. Note the temperature dependence, $T^{1.75}$, which is determined empirically by Fuller et al. [166].

The forward rate constants for the surface pseudo-reactions are then expressed in Arrhenius form as:

$$k_j = AT^n.\exp(-E/RT) = 1.5\eta\theta^2.\frac{1.00\times10^{-3}\left(1/M_i + 1/M_{N_2}\right)^{1/2}}{P[(\sum_i \nu_k)^{1/3} + (\sum_{N_2} \nu_k)^{1/3}]^2} T^{1.75} \qquad (6.4)$$

where A, n and E are the 3-parameter Arrhenius coefficients. Thus, using Eqn. (4), the 3-parameter Arrhenius coefficients for the surface reactions (R326 – R331) are calculated, as shown in Table 6.1. Note that the temperature exponent, n = 1.75, occurs due to the temperature dependence of the diffusivity, D_i, as determined by Fuller et al. [166].

Case 3: Intermediate case ($0 < k_j < k_{ci}$)

In this case, the effective rate of surface reaction, k_{eff}, is assumed to be intermediate between the two limiting cases (Cases 1 and 2), such that $k_j = k_{eff}$, where $0 < k_{eff} < k_{ci}$. Here we define a parameter, η, so that $\eta = k_{eff} / k_{ci}$, such that $k_j = \eta k_{ci}$.

Thus, the maximum rate of radical termination at the reactor surfaces occurs for Case 2 when the forward rate constant, k_j, corresponds to the mass-transfer-limited rate k_{ci}, or, in terms of the effective reaction rate, when $k_{eff} = k_{ci}$ (i.e. when η = 1.0). The minimum rate of radical termination occurs when the surface reactions are neglected, which corresponds to η = 0.

6.3 Results and Discussion

This work utilizes experimental data that were presented in Chapter 5. A short description of the setup and data collected are provided here, as a quick reminder. The insulated porous bed is 150 mm in diameter and is 210 mm long. The bed is made of 4 SiC disks with a porosity of ~ 90%, and 10 pores per inch (ppi). A premixed mixture of CNG, Air and NO is introduced uniformly at the inlet of the

burner. The temperature inside the bed and the exhaust composition are measured for different total flow rates, equivalence ratios and NO initial concentrations.

In Figure 6.1, the measured NO_X conversion efficiency versus equivalence ratio, for an air flowrate of 100 slpm (standard litres per minute) and 100 ml of input NO, are reproduced. Also plotted in Figure 6.1, are the modelling predictions (black solid line) using the GRI-Mech 3.0 mechanism, without surface reactions (i.e. $\eta = 0$), and modelling predictions (dash-dot line) from the present study assuming that key radicals are consumed on the surfaces at the mass-transfer limited rate (i.e. $\eta = 1.0$). It is clear from the Figure that this assumption produces results which are not in agreement with the experimental data, particularly for $\varphi = 1.1$. Further assessment of the effect of surface reactions ($\eta > 0$) on the NO_X conversion rate shows that values in the range $\eta = 8 \times 10^{-4}$ to 10×10^{-4} give better overall agreement with the experimental results.

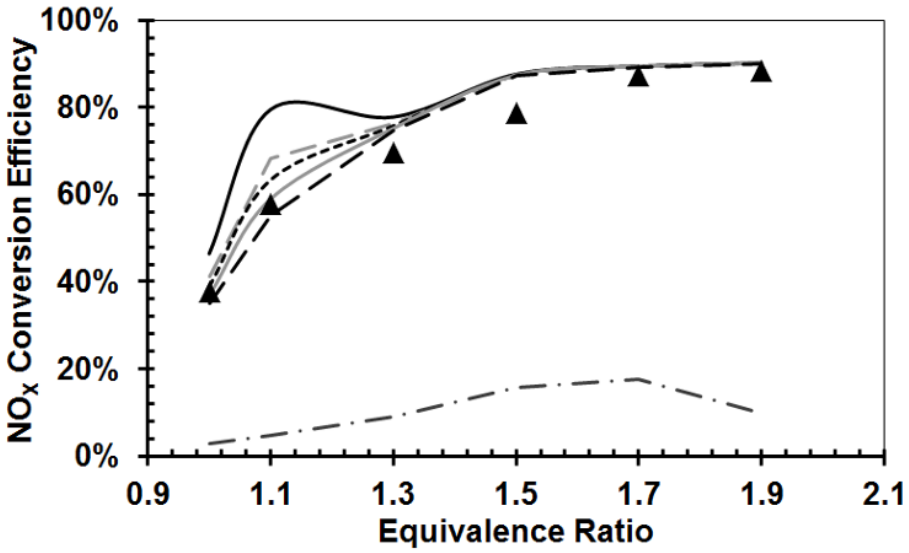

Figure 6.1: Measured NO_X conversion ratios and calculated NO_X plotted versus equivalence ratio for an air flow rate of 100 slpm and initial NO level of 100 ml. Lines (from top to bottom) represent $\eta = 0$, $\eta = 4\times10^{-4}$, $\eta = 6\times10^{-4}$, $\eta = 8\times10^{-4}$, $\eta = 10\times10^{-4}$ and $\eta = 1$ (100% collision probability), respectively. Also, ▲ represents the experimental NO_X conversion efficiency.

Thus, values of the collision probability which are $\eta << 1$ are more suitable, suggesting that radical loss at the burner surface occurs at an effective rate that is finite and much lower than the mass-transfer-limited rate.

For the case where the effective rate of radical loss is much lower than the mass-transfer-limited rate, the overall reaction will be kinetically controlled. Accordingly, it is more relevant to compare the assumed rate of radical loss with the theoretical collision rate of radicals with the burner surface. The surface collision rate constant for species *i*, $k_{coll,i}$, may be estimated [167] as:

$$k_{coll,i} = \frac{\bar{c}_i \theta}{4} \tag{6.5}$$

where the mean speed, $\bar{c}_i$, is the average magnitude of the velocity of gaseous molecules, which can be determined from the kinetic theory of gases as:

$$\bar{c}_i = \sqrt{\frac{8RT}{\pi M_i}} \tag{6.6}$$

For the case of H atoms, $\bar{c}$ = 5.4 × 10^3 m/s at 1400 K, corresponding to a typical burner temperature for these experiments. Thus, the collision rate of H atoms at the burner surface may be estimated as k_{coll} = 8.7 × 10^6 s^{-1}. This collision rate is approximately five orders of magnitude larger than the effective reaction rate, k_{eff}, implied by the predictions (η = 8 × 10^{-4}) plotted in Figure 6.1. This implies a recombination efficiency, defined as: $\gamma = k_{eff} / k_{coll}$, in the order of $\gamma = 1 \times 10^{-5}$.

The role of surfaces in the recombination of radicals is well known, e.g. [168], and depends on many factors, including the nature of the surface and any surface pre-treatment. More recently, Grubbs and George [169] have measured the rate of H atom recombination on Pyrex and quartz surfaces with a recombination efficiency of $\gamma = 0.94 \times 10^{-5}$ and $\gamma = 0.75 \times 10^{-5}$, respectively, which is in good agreement with the values estimated by the present work.

The effect on NO_X conversion, at different equivalence ratios, of different η is also shown in Figure 6.1. It is clear that for higher equivalence ratios ($\phi \geq 1.3$), radical termination at the surface has a minimal effect on the NO_X conversion efficiency. On the other hand, for slightly fuel rich conditions ($\phi < 1.3$), surface reactions play an important role in the prediction of NO_X conversion efficiency.

In Figure 6.2, the measured NO_X conversion efficiency versus the equivalence ratio, for an air flowrate of 100 slpm (standard litres per minute) and 100 ml of input NO,

are compared with the modelling predictions obtained using the Konnov mechanism [164]. While the predictions of NO_X conversion using the Konnov mechanism differ substantially from those obtained with GRI-Mech 3.0, it is clear that the assumption of surface reactions, even at very low η, also has a significant effect on model predictions using the Konnov mechanism and that this effect is also only observed for $\phi < 1.3$.

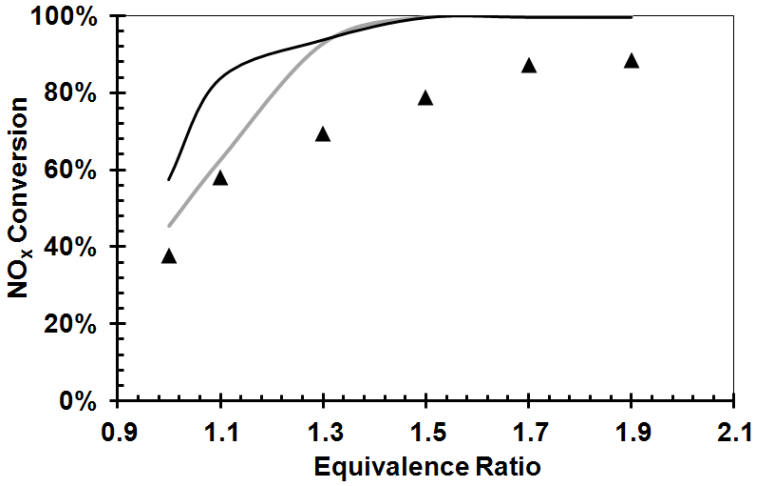

Figure 6.2: Measured NO_X conversion ratio and calculated NO_X (using Konnov mechanism) plotted versus the equivalence ratio for an air flow rate of 100slpm and initial NO level of 100ml. Lines (from top to bottom) represent η = 0 and $\eta = 8\times10^{-4}$. Also, ▲ represents experimental NO_X conversion efficiency.

In Figure 6.3 and Figure 6.4, the calculated concentrations of N-containing species along the burner for η = 0 (left) and $\eta = 8\times10^{-4}$ (right) are shown, using GRI-Mech 3.0 and Konnov mechanism. Both graphs are plotted for an air flow rate of 100 slpm, φ = 1.1 and input NO of 100 ml. It is clear that the different rates of production of the species change the concentration of those species along the burner. Studying the chemical paths at different locations also confirms that NO conversion follows different paths at different points. Hence, as a first order approximation, the net average reaction rate is calculated for different conditions as:

$$\bar{\sigma} = \frac{\int_0^L \sigma(x)dx}{L} \tag{6.7}$$

where $\bar{\sigma}$ (mole/s), $\sigma(x)$ (mole/cm^3.s) and L (cm) are the average and net reaction rates along the burner, and the bed length, respectively. Considering the uniformity

of the radial heat distribution for this burner [48], it can be concluded that the local reaction rate, $\sigma(x)$, is one dimensional.

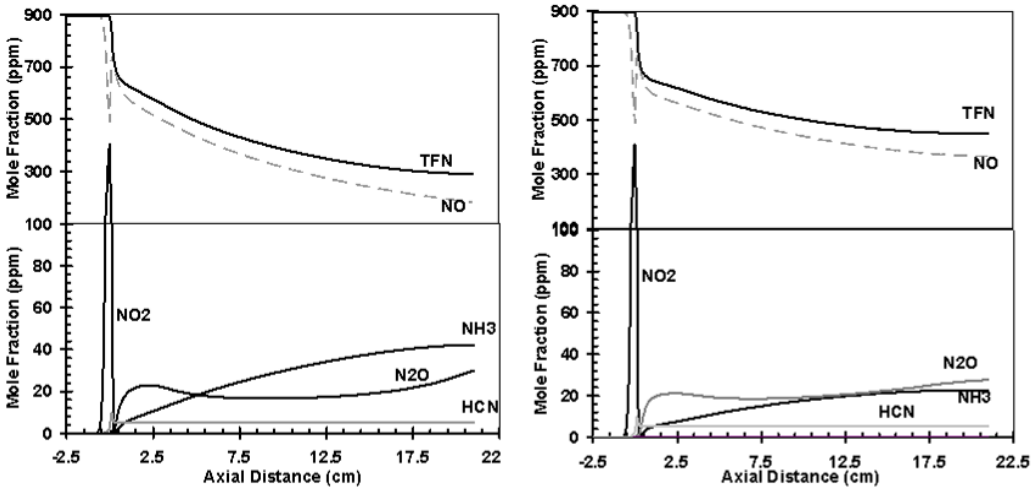

Figure 6.3: Comparison of N-containing species calculated using GRI-Mech 3.0. Left figure show predictions for no surface reactions (η = 0) and the right plot show predictions with surface reactions for η = 8×10^{-4}. All predictions are for flow rates of 100 slpm, φ = 1.1 and input NO of 100 ml.

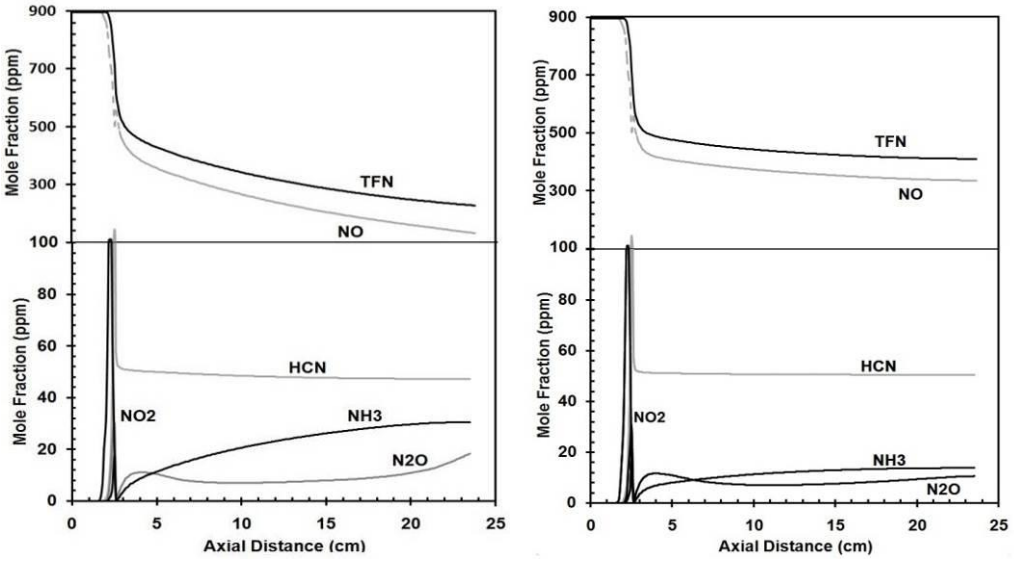

Figure 6.4: Comparison of N-containing species calculated using Konnov mechanism; Left plot show predictions for no surface reactions (η = 0) and the plot in the right show predictions with surface reactions for η = 8×10^{-4}. All predictions are for flow rates of 100 slpm, φ=1.1 and input NO of 100 ml.

Figure 6.8 shows the indicative chemical paths for an air flow rate of 100 slpm, φ = 1.1, input NO of 100 ml for the cases η = 0 (left) and η = 8×10^{-4} (right). The chemical pathways are qualitatively similar for both cases. Table 6.2 summarises the

major reactions involved in the conversion of NO to N_2 or other N-containing species. Analysis of the two chemical paths revealed that incorporating surface reactions had little effect on the majority of the reaction rates, however a few reaction rates decreased significantly, mainly due to the effect of H ⇒ H_W. Amongst those reactions, R212 and -R214 had the maximum effect on decreasing the NO conversion rate to N_2 through NO => HNO => NH => N_2. This is attributed to the importance of H concentration in the net reduction of NO to HNO, via reactions R212 and -R214. This effect is also observed when the Konnov mechanism is used.

			GRI-Mech 3.0 Mechanism						**Konnov**	
Rxn # GRI-Mech 3.0	Rxn # Konnov	Reaction	**Case 1**	**Case 2**	**Case 3**	**Case 4**	**Case 5**	**Case 6**	**Case 7**	**Case 8**
			Φ = 1.1		Φ = 1.7		Φ = 1.1		Φ = 1.1	
			Input NO = 100 ml				Input NO = 20 ml		Input NO = 100 ml	
			η=0	η=8×10^{-4}	η=0	η=8×10^{-4}	η=0	η=8×10^{-4}	η=0	η=8×10^{-4}
178	29	N+NO<=>N2+O	75.9	68.0	5.1	5.1	16.5	12.5	109.6	95.4
179	30	N+O2<=>NO+O	-	-	-	-	-	-	-7.7	-8.0
180	106	N+OH<=>NO+H	26.7	26.9	0.0	0.0	16.0	15.5	26.3	25.8
183	107	N2O+H<=>N2+OH	238.5	121.5	61.3	61.1	29.9	8.6	215.6	102.0
185	33	N2O(+M)<=>N2+O(+M)	61.3	64.5	22.3	22.3	7.3	5.5	30.4	31.2
186	126	HO2+NO<=>NO2+OH	16891.7	16840.6	22851.6	22865.2	3816.6	3788.2	40410.1	40400.0
187	38	NO+O+M<=>NO2+M	91.6	95.8	-8.0	-8.1	33.4	34.9	42.1	42.2
188	40	NO2+O<=>NO+O2	135.5	135.4	110.0	110.1	30.1	29.9	81.9	81.8
---	1058	CH3+NO2<=>CH3O+N	-	-	-	-	-	-	27611.0	27603.2
189	125	NO2+H<=>NO+OH	17055.4	17000.8	22774.8	22796.9	3866.9	3839.4	11525.6	11500.4
---	127	NO2+HO2<=>HONO+O	-	-	-	-	-	-	623.6	623.1
---	150	NO+OH(+M)<=>HONO(	-	-	-	-	-	-	-517.0	-518.5
---	153	HONO+H<=>HNO+OH	-	-	-	-	-	-	158.1	156.3
---	1192	NO2+HCO<=>OH+NO+	-	-	-	-	-	-	356.2	356.3
191	58	NH+H<=>N+H2	112.5	101.3	6.7	6.7	46.2	37.4	161.8	141.7
192	187	NH+OH<=>HNO+H	-20.7	-20.4	0.4	0.4	-6.0	-5.8	-15.2	-14.0
193	188	NH+OH<=>N+H2O	5.6	5.1	0.4	0.4	2.2	1.8	8.8	8.0
194	191	NH+O2<=>HNO+O	9.1	9.0	23.9	23.9	2.5	2.4	47.9	48.3
197	193	NH+H2O<=>HNO+H2	-529.9	-368.0	-84.1	-83.7	-116.9	-54.8	-564.4	-396.2
198	196	NH+NO<=>N2+OH	108.7	73.4	24.5	24.5	15.0	5.1	49.3	31.8
199	108	NH+NO<=>N2O+H	369.3	250.5	82.4	82.2	51.1	17.4	355.6	230.1
---	192	NH+O2<=>NO+OH	-	-	-	-	-	-	113.1	110.6

280	1196	NH+CO2<=>HNO+H2	-148.8	-102.4	-135.9	-135.2	-36.8	-14.7	-251	-192.4
202	64	NH2+H<=>NH+H2	-75.3	-39.7	-60.2	-59.4	-37.3	-9.8	-71.2	-23.5
203	174	NH2+OH<=>NH+H2O	-3.8	-2.0	-0.9	-0.9	-1.9	-0.5	-3.9	-0.2
212	137	H+NO+M<=>HNO+M	4629.5	4278.8	213.6	212.2	1439.9	1247.4	2226.8	1860
213	140	HNO+O<=>NO+OH	12.1	12.6	0.5	0.5	4.1	4.3	3.7	3.7
214	138	HNO+H<=>H2+NO	3886.5	3738.0	37.0	36.9	1262.7	1155.5	1836.8	1703.4
215	139	HNO+OH<=>NO+H2O	62.7	61.7	0.9	0.9	19.9	18.7	56.1	53.2
216	142	HNO+O2<=>HO2+NO	-15.3	-15.2	-17.2	-17.2	-3.0	-2.9	9.9	9.9
237	1097	H+HCN(+M)<=>H2CN(+	-4.6	-4.6	-14.8	-14.7	-0.7	-0.7	-2.3	-20.9
249	1108	CH2+NO<=>H+HNCO	38.3	37.2	87.9	87.9	5.7	5.6	1.8	1.8
250	998	CH2+NO<=>OH+HCN	6.2	6.0	14.3	14.3	0.9	0.9	0.0	1.2
251	1109	CH2+NO<=>H+HCNO	8.7	8.5	10.2	10.2	1.3	1.3	8.6	8.6
252	---	CH2(S)+NO<=>H+HNC	4.0	3.9	2.7	2.7	0.7	0.7	-	-
253	---	CH2(S)+NO<=>OH+HC	0.6	0.6	0.4	0.4	0.1	0.1	-	-
254	---	CH2(S)+NO<=>H+HCN	1.0	0.9	0.5	0.5	0.2	0.2	-	-
255	1112	CH3+NO<=>HCN+H2O	28.9	28.7	81.4	81.2	4.5	4.4	94.9	94.8
256	1113	CH3+NO<=>H2CN+OH	4.4	4.4	12.1	12.0	0.7	0.7	7.0	7.1
265	1159	HNCO+H<=>NH2+CO	12.3	9.9	981.7	980.9	2.8	1.3	100.1	91.5
268	1165	HNCO+OH<=>NH2+CO	0.2	0.2	3.7	3.7	0.0	0.0	0.0	0.0
270	1119	HCNO+H<=>H+HNCO	49.8	46.8	904.8	905.0	4.0	3.7	233.1	232.2
271	1118	HCNO+H<=>OH+HCN	4.4	4.1	80.0	80.0	0.4	0.3	47.7	47.5
272	1121	HCNO+H<=>NH2+CO	2.6	2.4	46.8	46.9	0.2	0.2	12.1	12.9
274	1114	HCCO+NO<=>HCNO+C	161.1	155.1	1022.2	1021.7	17.8	16.9	943.3	938.4
---	1122	HCNO+O<=>NCO+NO	-	-	-	-	-	-	584.4	589.2
---	1117	HCNO<=>HCN+O	-	-	-	-	-	-	35.8	36.4
277	73	NH3+H<=>NH2+H2	-50.3	-29.8	-904.9	-905.0	-22.3	-6.4	-91.9	-75.7
278	168	NH3+OH<=>NH2+H2O	-43.0	-23.5	-233.7	-232.1	-19.8	-5.4	-20.5	-4.4
279	167	NH3+O<=>NH2+OH	0.1	0.1	49.6	49.7	0.0	0.0	3.1	3.1
283	1127	N+CO2<=>NO+CO	13.5	9.8	-5.8	-5.8	15.1	10.3	26.9	19.4
---	242	HNO+NH2<=>NO+NH3	-	-	-	-	-	-	0.1	0.1
---	1032	CH4+NH2<=>NH3+CH3	-	-	-	-	-	-	17.9	17.9
---	1115	HCCO+NO<=>HCN+CO	-	-	-	-	-	-	281.8	281.2
---	1184	NO+HCO<=>CO+HNO	-	-	-	-	-	-	183.2	179.5
---	1188	CH3O+NO<=>CH2O+H	-	-	-	-	-	-	120.2	124.0

Table 6.2: Net average reaction rates (1×10^{10}) of reactions affecting NO reduction for cases 1 to 8.

Also, the differences between the concentrations of N_2O and NH_3 in Figure 6.4 (left and right) are due to the different branching ratios of NH between N_2O, N_2, NO and NH_3, compared with the total NH produced by the reactions R197, -R192, -R194 and -R280. This is quantitatively shown in Table 6.3. Again, it is observed that these differences are due to the assumed termination of H atoms at the surface (H $\Rightarrow$ H_W).

NH=>	$\eta = 0$	$\eta = 8 \times 10^{-4}$
N_2	70.2%	68%
N_2O	10%	13.4%
NH_3	11.3%	8.4%
NO	5.8%	7.6%

Table 6.3: Branching ratios of NH between N_2O, N_2, NO and NH_3 compared with the total NH produced.

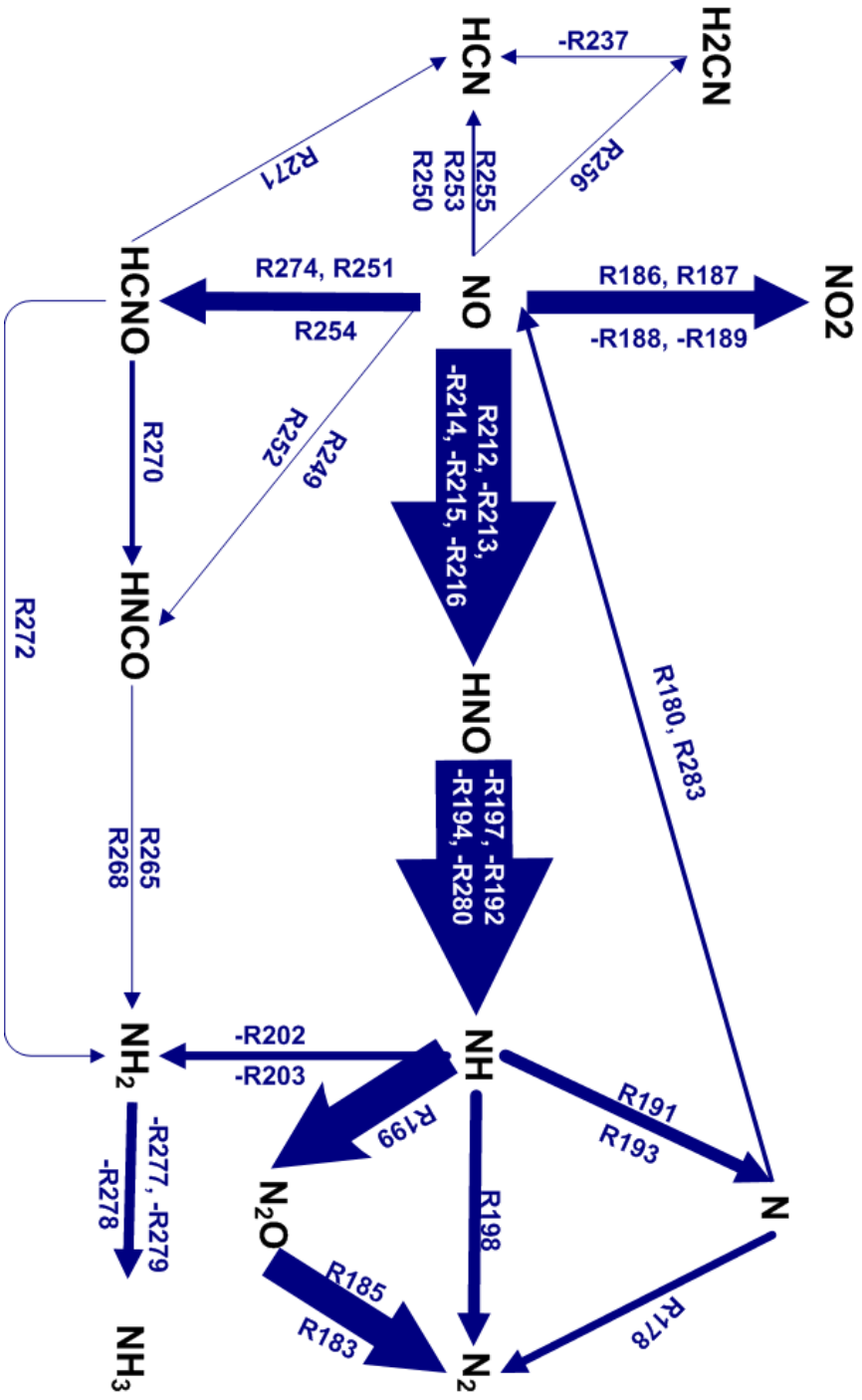

Figure 6.5: Integrated chemical path for a flow rate of 100 slpm using GRI-Mech 3.0, φ = 1.1, input NO of 100ml and η = 0. Arrow thicknesses are scaled based on the reaction rates for different reactions.

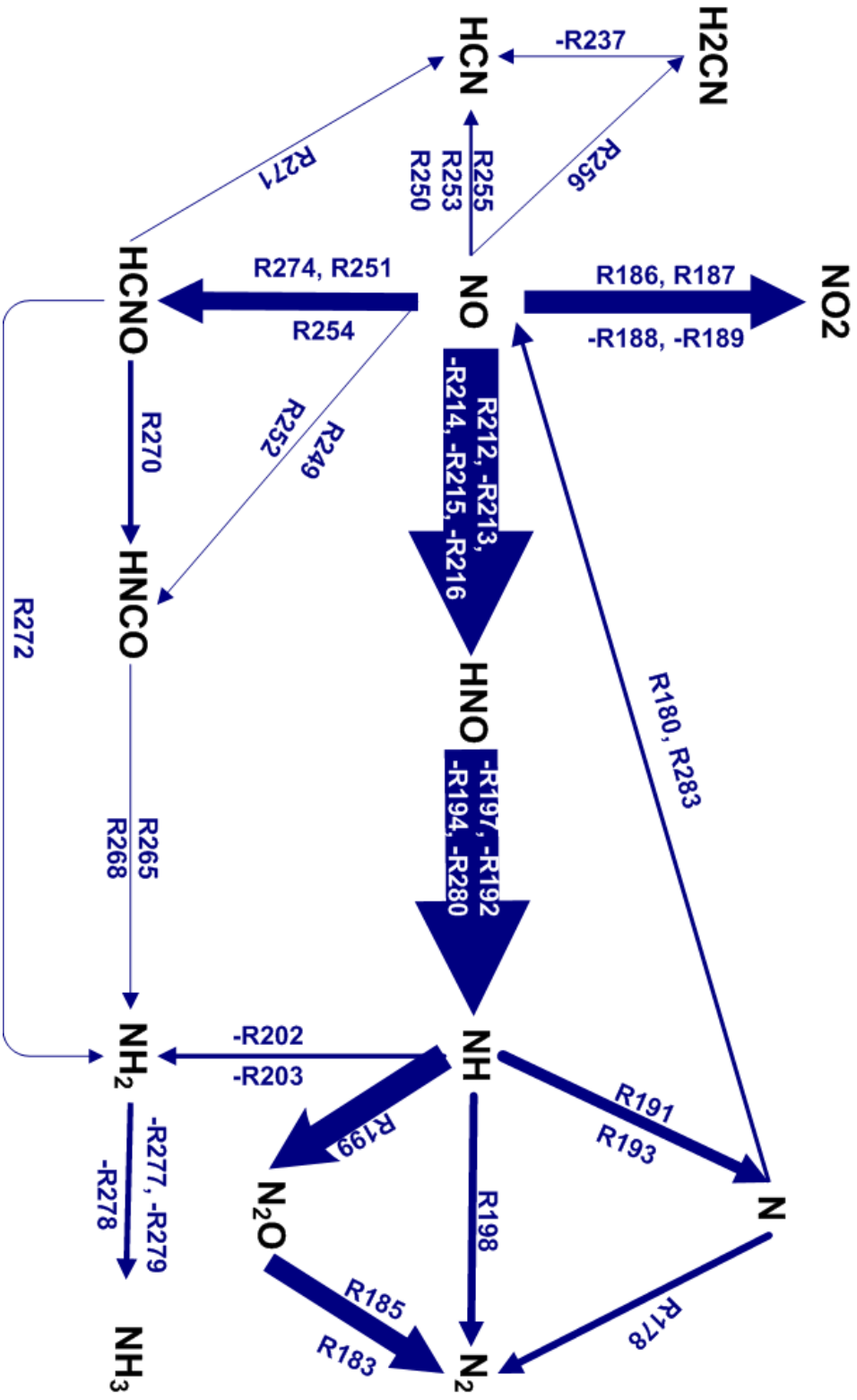

Figure 6.6: Integrated chemical path for a flow rate of 100 slpm using GRI-Mech 3.0, φ = 1.1, input NO of 100ml and η = 8×10^{-4}. Arrow thicknesses are scaled based on the reaction rates for different reactions.

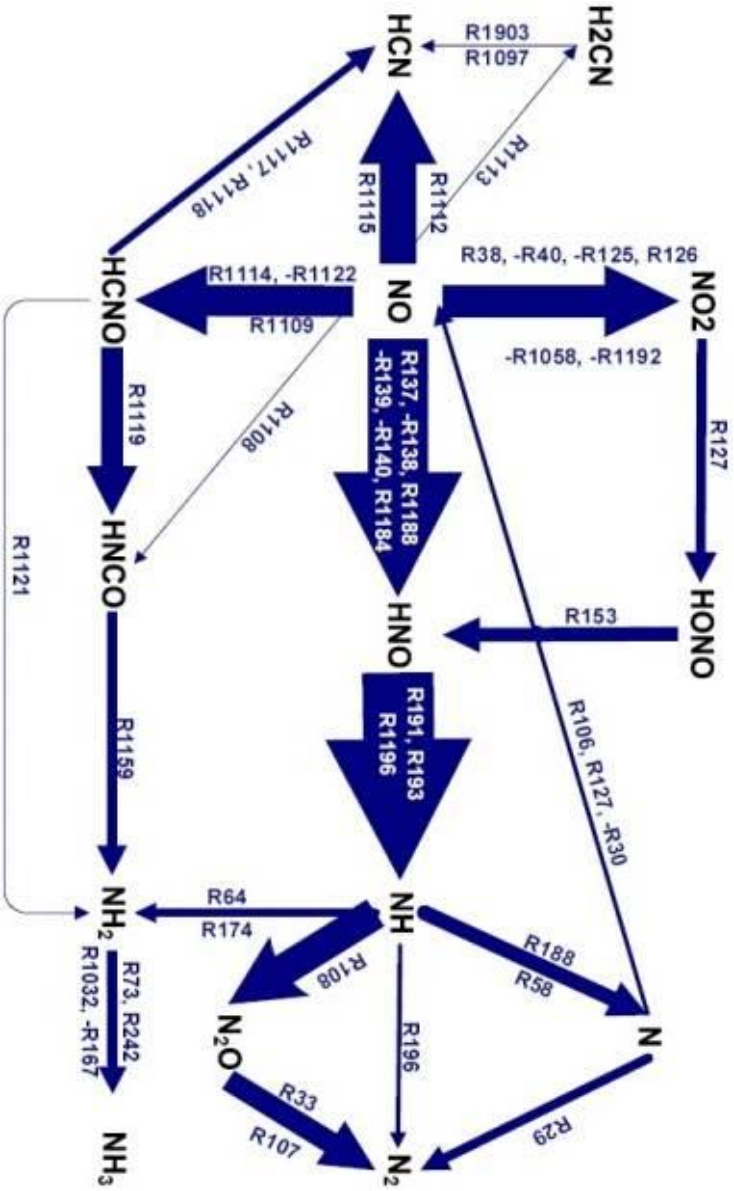

Figure 6.7: Integrated chemical path for a flow rate of 100 slpm using the Konnov mechanism, φ = 1.1, input NO of 100 ml and η = 0. Arrow thicknesses are scaled based on the reaction rates for different reactions.

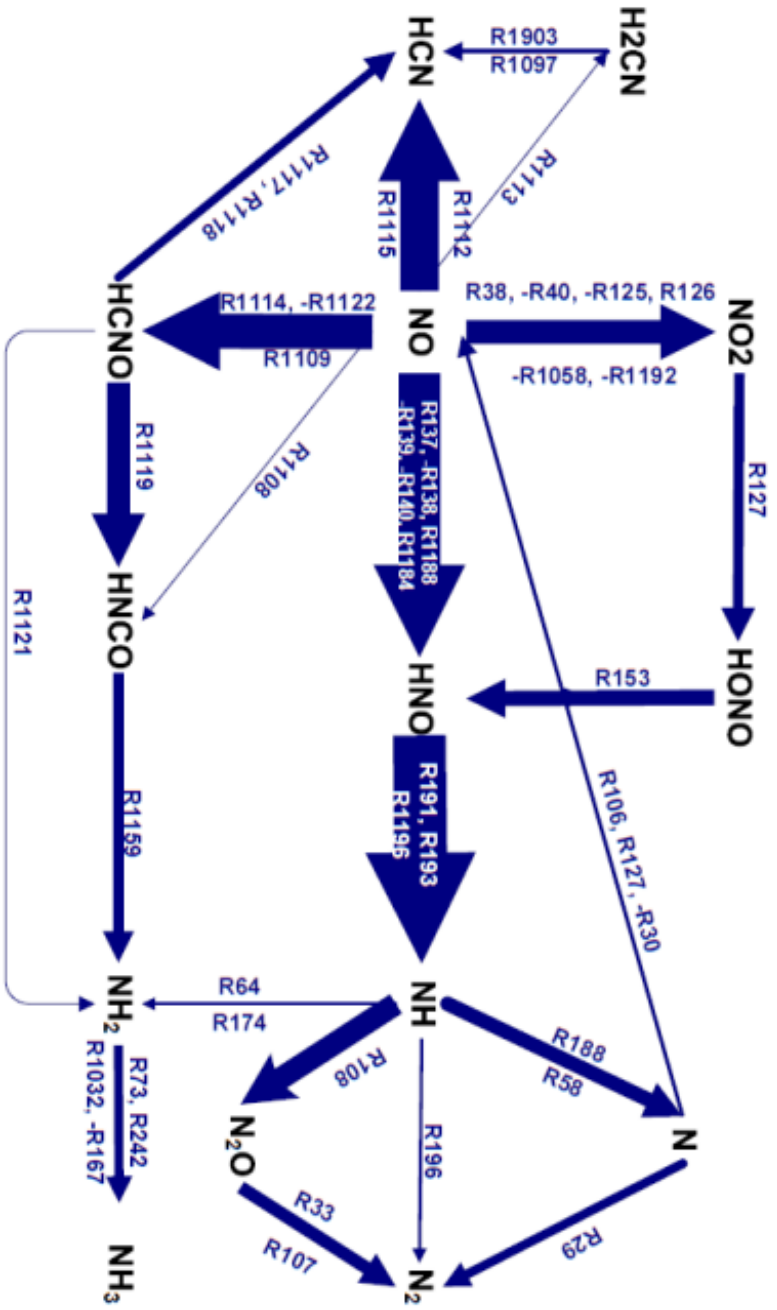

Figure 6.8: Integrated chemical path for a flow rate of 100 slpm using the Konnov mechanism, φ = 1.1, input NO of 100ml and η = 8×10^{-4}. Arrow thicknesses are scaled based on the reaction rates for different reactions.

The importance of reactions R212 and –R214 is confirmed by the sensitivity analysis. At the conditions corresponding to Case 1 in Table 6.2 (GRI-Mech 3.0; φ = 1.1, input NO of 100 ml; η = 0) the predicted NO concentration is most sensitive to reactions R212 and R214 (relative sensitivity coefficient = -0.89 and 0.82, respectively). Due to the high sensitivity to these two reactions, it is possible to explore the possibility of accounting for the discrepancy between the model

predictions and the experiments at φ = 1.1 by adjusting these two rate constants. Figure 6.9 plots the measured NO_x conversion efficiency, for the conditions of Figure 6.1, over the range of φ = 1.1 to φ = 1.3.

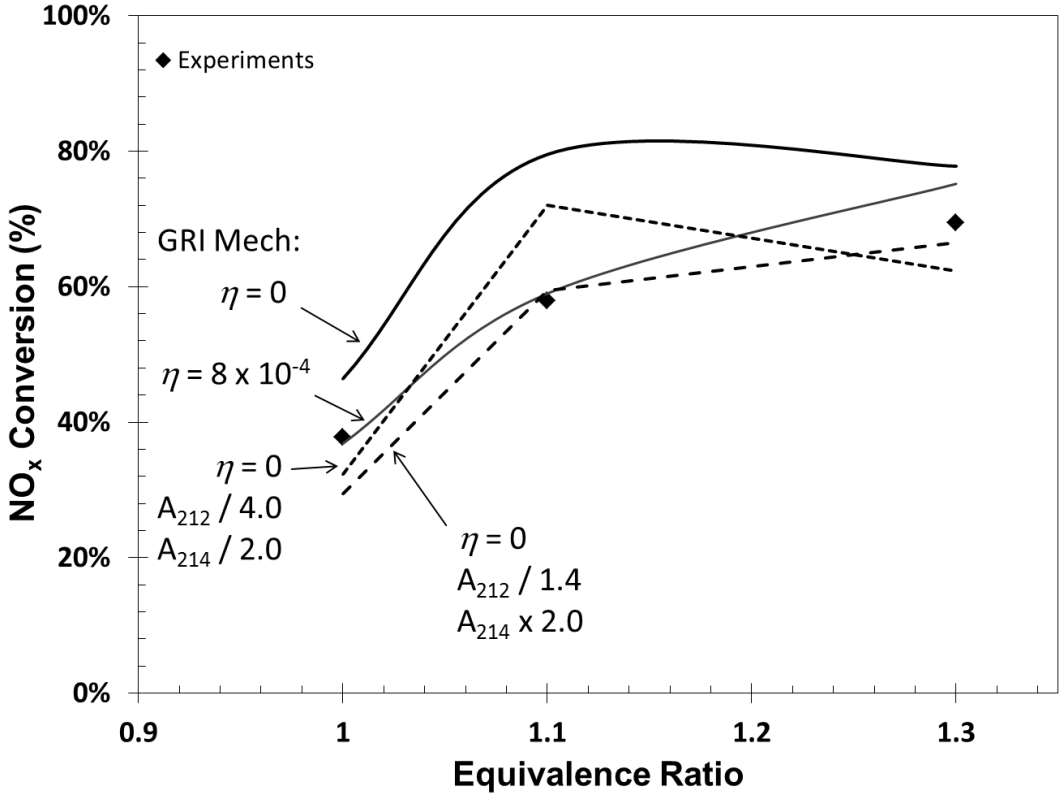

Figure 6.9: Measured NOx conversion ratio and predicted NOx (using GRI-Mech 3.0 mechanism) plotted versus the equivalence ratio for an air flow rate of 100 slpm and initial NO level of 100 ml. Data and predictions are shown for φ = 1.0 to φ = 1.3. Lines (as labeled) show the model predictions using the GRI-Mech 3.0 mechanism for the following cases: (i) No surface reactions (η = 0); (ii) Surface reactions ($\eta = 8\times10^{-4}$); (iii) No surface reactions, A_{212} decreased by a factor of 4.0 and A_{214} decreased by a factor 2.0; and (iv) No surface reactions, A_{212} decreased by a factor of 1.4 and A_{214} increased by a factor of 2.0.

Figure 6.9 presents the model predictions using GRI-Mech 3.0, also shown in Figure 6.1, for the case without surface reactions (η = 0) and with surface reactions ($\eta = 8\times10^{-4}$). While the model predictions using GRI-Mech 3.0 with surface reactions ($\eta = 8\times10^{-4}$) provide reasonable agreement to the measured data, it is also possible to obtain good agreement using GRI-Mech 3.0 without surface reactions (η = 0) by manipulating the rate constants for reactions R212 and R214. Shown in Figure 6.9 are two instances: (a) R212 decreased by a factor of 4.0 with R214 decreased by a factor of 2.0, or (b) R212 decreased by a factor of 1.4 with R214 increased by a

factor of 2.0. However, manipulation of these rate constants to such an extent is inconsistent with currently accepted values for these reactions.

Tsang and Herron [113] have evaluated previous data for these two reactions and recommend rate constants for each reaction over a temperature range which includes that of the present experiments. These recommendations are plotted in Figure 6.10 and Figure 6.11 for reactions R212 and R214, respectively. More recently, however, Skreiberg et al. [112] have recommended the experimental determination of Riley et al. [116] for R212 and the *ab initio* calculations of Soto and Page [114] for R214. Also plotted in Figure 6.10 is a recommendation for R212 by Glarborg et al. [115], which is based on their flow reactor experiments. At 1000 K, the rate constant for R212 used in GRI-Mech 3.0 is 15% larger than that of Soto and Page [114] and 70% larger than that of Glarborg et al. [115]. Figure 6.11 also plots recommendations based on the more recent *ab initio* calculations of Nguyen et al. [170], which are both consistent with the Soto and Page [114] calculations. At 1000 K, the rate constant for R214 used in GRI-Mech 3.0 is 75% larger than the Soto and Page recommendation.

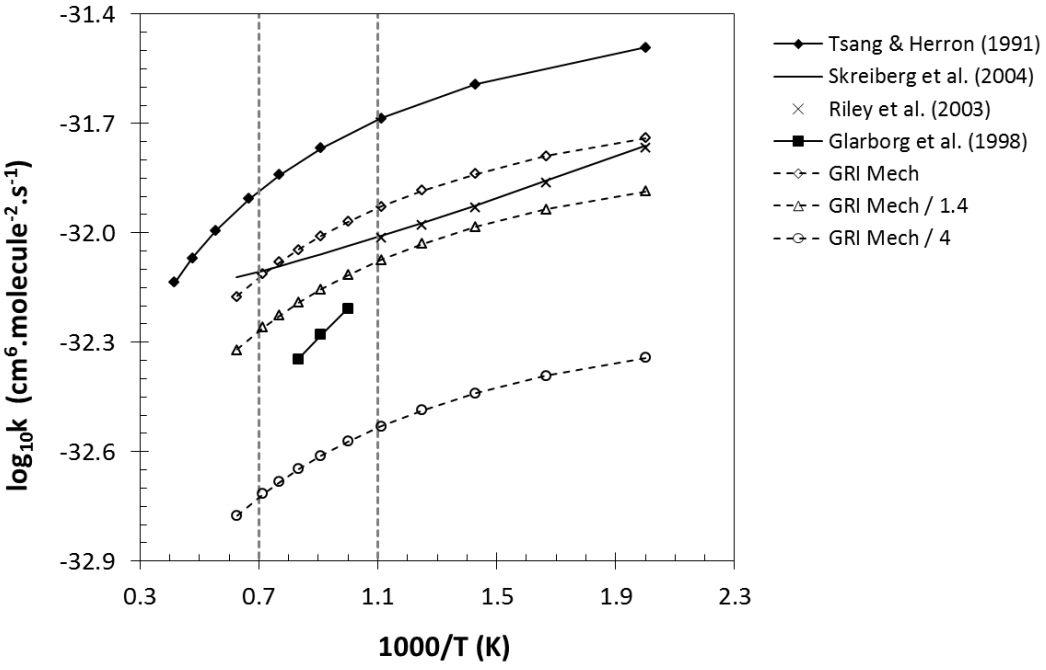

Figure 6.10: Arrhenius plot of recommended rate constants for reaction R212: H + NO + M → HNO + M (M = N2). The vertical dashed lines indicate the approximate temperature range of interest for this work.

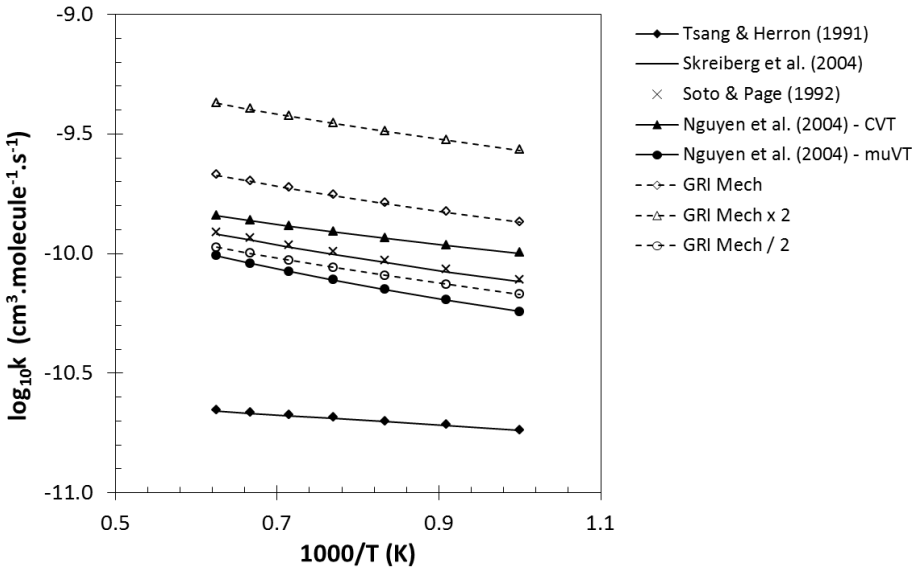

Figure 6.11: Arrhenius plot of recommended rate constants for reaction R214: HNO + H → H2 + NO in the temperature range 1000 - 1600 K.

Figure 6.9 shows two instances in which the rate constants for R212 and R214 have been manipulated to allow reasonable agreement between the experiments and the model predictions using GRI-Mech 3.0 without surface reactions. It is clear that neither of these predictions is consistent with the accepted rate constants for these two reactions. In the first instance, R212 is decreased by a factor of 4.0 and is assigned a value which, at 1000 K, is a factor of 3.4 less than the recent recommendation by Skreiberg et al. [112]. In the second instance, R214 is increased by a factor of 2.0 and is assigned a value which, at 1000 K, is 250% higher than the Skreiberg et al. [112] recommendation. In both cases, model predictions that are in good agreement with the experiments can only be obtained using GRI-Mech 3.0 and without surface reactions, if rate constants are chosen for R212 or R214 which are significantly outside of the accepted range for these reactions.

The experimental conditions for the data shown in Figure 6.12 are similar to those for Figure 6.4 except that the equivalence ratio is increased to φ = 1.7. It is clear from Figure 6.12 that the effect of the surface reactions on the model predictions at φ = 1.7 is quite small and that, despite removing a considerable number of radicals from the gaseous mixture via surface reactions, for both conditions (η = 0 and η = 8×10^{-4}) the concentrations of all N-containing components are predicted to remain almost identical along the burner.

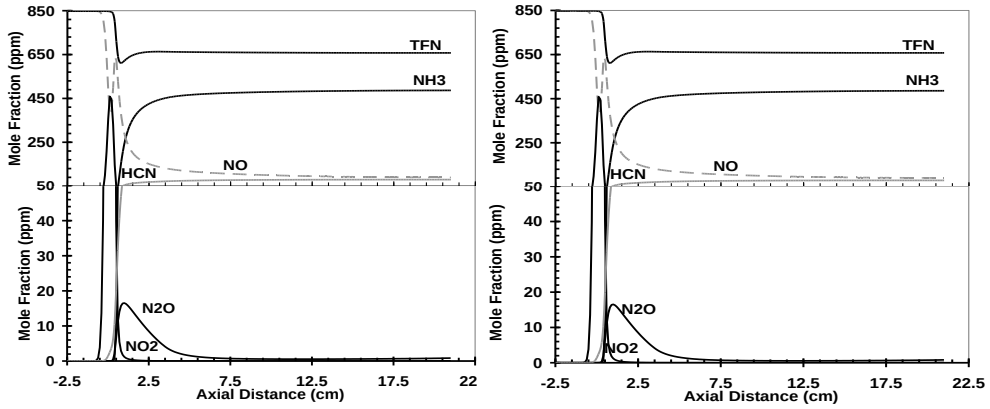

Figure 6.12: A comparison of N-containing components; no surface reactions (left) and applying surface reactions with η = 8e-4 (right). Both graphs are plotted based on a flow rate of 100 slpm, φ = 1.7 and input NO of 100 ml.

Figure 6.13 shows the indicative chemical pathways for the average reaction rates along the burner for φ = 1.7 and with η = 8×10^{-4}. It can be seen from Table 6.2 (Case 3 cf. Case 4), that the chemical pathways for η = 0 and η = 8×10^{-4} are practically identical. Thus, the inclusion of surface reactions in the chemical mechanism did not affect the chemical pathways either qualitatively or quantitatively for these experimental conditions. This is also consistent with the prediction of similar NO_X conversion rates at φ = 1.7 in Figure 6.1.

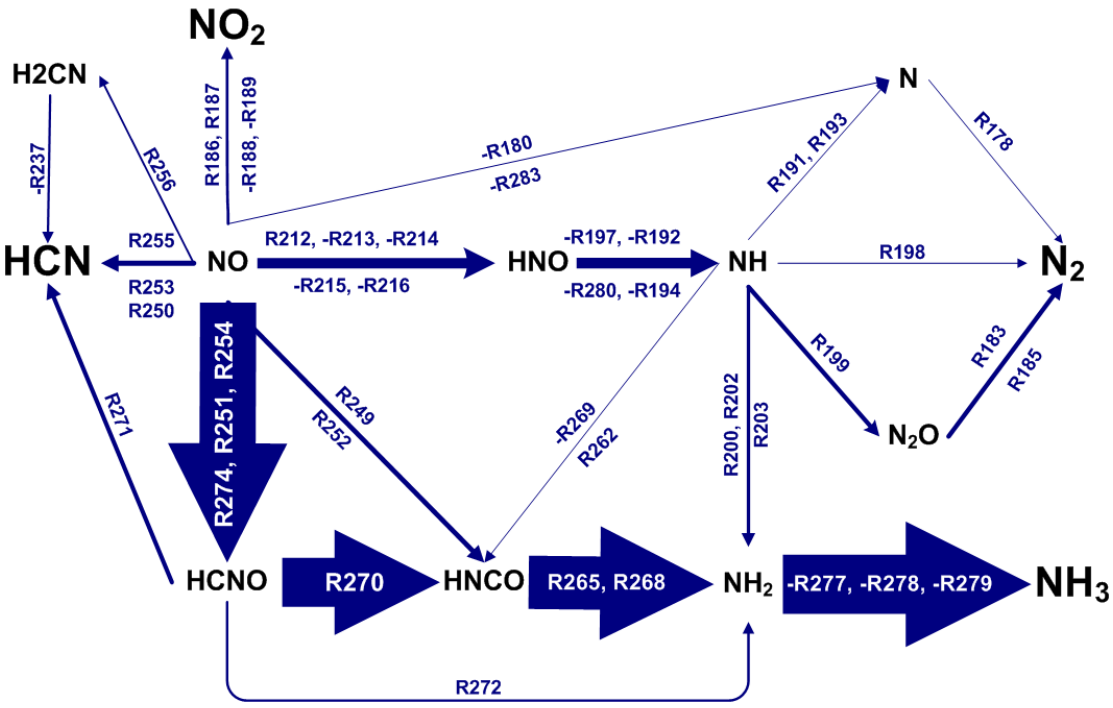

Figure 6.13: Integrated chemical paths for a flow rate of 100 slpm, η=8×10^{-4}, an equivalence ratio of 1.7 and input NO of 100 ml.

As shown in Figure 6.13, this could be explained by the insignificant rate of reactions R212, -R213, -R214, -R215 and -R216 (mostly R212 and –R214) when compared with the rates of reactions R251, R254 and R274 in a chemical path without considering wall reactions. Quantitatively, only l6.5% of the NO destruction follows the NO => HNO => NH => N_2 path, compared with 80% for φ = 1.1.

In Chapter 5 it was shown that the NO_X conversion efficiency in a porous burner firing CNG was also dependent on the input NO level in addition to the equivalence ratio, temperature and firing rate. The NO conversion efficiency was found to change significantly with the NO input level for ($\varphi \leq 1.3$) but had no significant effect on higher equivalence ratios.

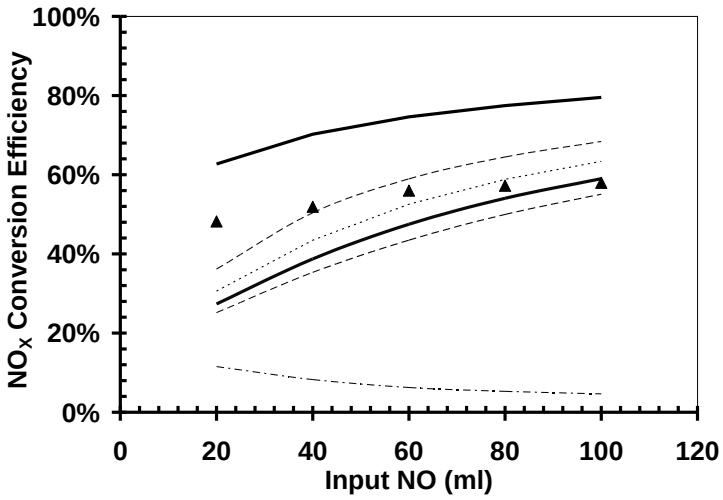

Figure 6.14: Measured NO_x conversion ratios and calculated NO_x plotted versus input NO for an air flow rate of 100 slpm and an equivalence ratio of φ = 1.1. Lines (from top to bottom) represent η = 0, $\eta = 4\times10^{-4}$, $\eta = 6\times10^{-4}$, $\eta = 8\times10^{-4}$, $\eta = 10\times10^{-4}$ and η = 1, respectively.

The measured NO_X conversion efficiency versus input NO for an air flow rate of 100 slpm and φ = 1.1 is shown in Figure 6.14. The conversion efficiencies for various input NO levels (20 ml to 100 ml) and extents of radical loss (η = 0 to $\eta = 8\times10^{-4}$) are plotted in Figure 6.14. The NO_X conversion efficiency at η = 0 is overpredicted by more than 20%. The trend over the range of NO input levels follows that of the experimental data. When surface reactions are included ($\eta = 8\times10^{-4}$), the trend is the same but the discrepancies increase at lower NO levels. This phenomenon is further explored in Figure 6.15 and in Table 6.2 where Cases 1, 2, 5 and 6 are compared for the same air flow rate of 100 slpm.

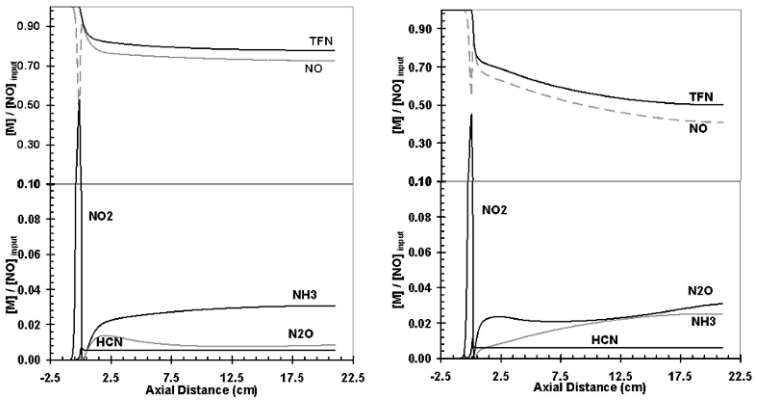

Figure 6.15: Comparison of normalised N-containing components for an air flow rate of 100 slpm, equivalence ratio of 1.1 and input NO of 20 ml (left) and 100 ml (right) considering $\eta = 8\times10^{-4}$. Note the different scales in the upper and lower graphs.

The normalised concentrations of N-containing species, for an air flow rate of 100 slpm, equivalence ratio of 1.1 and input NO level of 20 ml (left) and 100 ml (right) for $\eta = 8\times10^{-4}$, are shown in Figure 6.15. It is clear that for lower concentrations of input NO, the $[NO]/[NO]_{in}$ ratio decreases or NO_X conversion efficiency decreases. This could be analysed further by studying the reaction rates and chemical paths for Cases 1 and 5. As shown earlier, applying surface reactions has a significant effect on reactions R212, -R213, -R214, -R215 and -R216 (mostly R212 and –R214). In other words, for cases in which the NO conversion mostly follows the NO => HNO => NH => N_2 path, surface reactions have a significant effect. In Case 1, the NO => HNO => NH => N_2 path contributes to 80% of the NO conversion mechanism, while a similar path for Case 5 is responsible for 89% of the NO conversion mechanism. Thus, applying surface reactions will have a higher impact on the NO_X conversion efficiency at lower input NO levels.

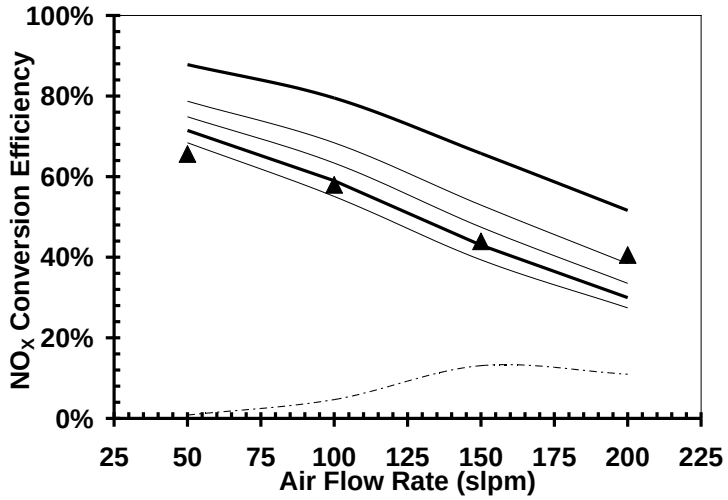

Figure 6.16: Measured NO_X conversion efficiency and calculated NO_X plotted versus the air flow rate for an equivalence ratio of 1.1 and initial NO level of 100ml. Lines (from top to bottom) represent $\eta = 0$, $\eta = 4\times10^{-4}$, $\eta = 6\times10^{-4}$, $\eta = 8\times10^{-4}$, $\eta = 10\times10^{-4}$ and $\eta = 1$, respectively.

The effect of the air flow rate on NO_X conversion efficiency at $\varphi = 1.1$ and an initial NO level of 100 ml for different extents of radical loss is shown in Figure 6.16. The model with $\eta = 8\times10^{-4}$ gives the best agreement with the experimental data. For the same equivalence ratio (i.e. $\varphi = 1.1$ in Figure 6.16) a lower air flowrate results in a higher NO_X conversion efficiency and is less affected by surface reactions. For example, with $\eta = 8\times10^{-4}$, and for an air flow rate of 50 slpm, the NO_X conversion

efficiency drops by 19% while for an air flow rate of 200 slpm it drops by 42%. This is believed to be caused by the higher concentrations of NO in the mixture (Figure 6.14) and also because of the lower temperatures (Figure 6.17), which give a better NO_X conversion efficiency, before and after applying surface reactions.

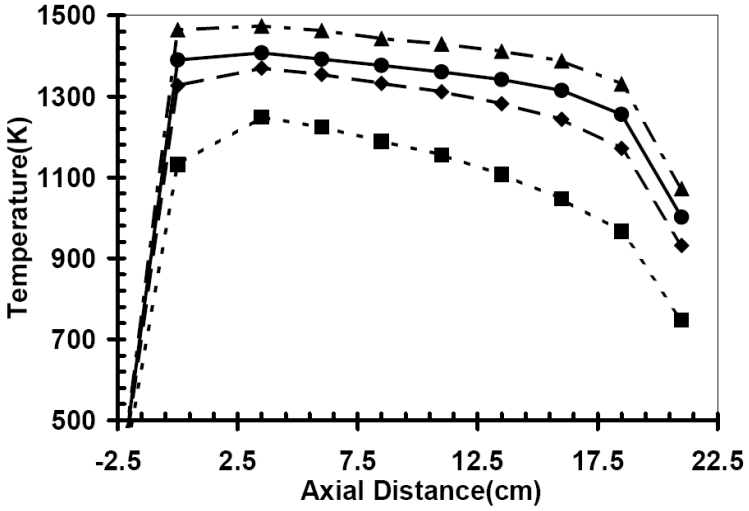

Figure 6.17: Measured axial temperature profiles for different air flow rates and for an equivalence ratio of 1.1. (Dotted line, ■), (Dashed line, ◆), (solid line, ●) and (Dashed-Dotted line, ▲) represent air flow rates of 50 slpm, 100 slpm, 150 slpm and 200 slpm, respectively.

6.4 Summary and Conclusions

Predictions of NO_x conversion efficiency in a porous burner which ignore the effect of radical loss at the burner surface disagree with the previous experimental measurements and this discrepancy cannot be accounted for within the uncertainty of the assumed gas-phase rate constants.

It is well known that the NO_X conversion efficiency of a porous burner is highly dependent on the equivalence ratio. The presented results in this chapter show that the effect of considering surface reactions on the prediction of NO_X conversion efficiency also strongly depends on the equivalence ratio. Under slightly fuel-rich conditions ($\varphi \leq 1.3$), the conversion of NO_X is strongly influenced by the concentration of H radicals. Thus, the inclusion of reactions in the gas-phase mechanism, which account for the radical termination at the burner surface, strongly influences the model predictions for $\varphi \leq 1.3$, whereas for higher equivalence ratios ($\varphi > 1.3$) the inclusion of surface reactions has minimal or no effect. The magnitude of

the assumed rate of radical loss at the burner surface that is necessary to match the experimental results is consistent with a recombination efficiency, $\gamma = 1 \times 10^{-5}$, which is in good agreement with recent measurements for H atoms on glassy surfaces. The inclusion of surface reactions has a significant impact on the NO_X reduction efficiency results for mixtures with lower concentrations of NO. It is found that these effects are due to different NO conversion paths under different conditions. The dominant path for NO conversion is found to be $NO \Rightarrow HNO \Rightarrow NH \Rightarrow N_2$; for cases that mainly follow this path, surface reactions have the maximum effect. In other words, these effects are minimal when the NO conversion follows the alternative NO conversion path ($NO \Rightarrow HCNO \Rightarrow HNCO \Rightarrow NH_2 \Rightarrow NH_3$).

Furthermore, for a certain input NO level and equivalence ratio, including surface reactions in the calculations has different effects for different flow rates. The significant changes in NO_X conversion efficiency under such conditions are related to the different temperature range and initial NO concentrations at various flow rates.

SUMMARY, CONCLUSIONS AND FUTURE WORK

For many decades, porous media have been used in industrial applications to stabilise flames, mostly for heating and drying processes. Porous burners have been investigated in depth by many groups from around the world due to their favourable characteristics of low emissions, high energy density and extended flammability limits resulting from the excess enthalpy phenomenon. While porous burners have been classified as low NOx burners, as a stand-alone combustion system, little is known about the use of these burners as a post combustion NOx conversion system. This thesis is focused on exploring the interdependent parameters that control the conversion of NOx fed externally into the porous bed. Both experimental and numerical techniques are utilised in this work.

The thesis reports on two distinct, but interlinked studies. The first study includes a series of experimental and computational campaigns that investigated important design and operating parameters that affect flames' stability under the very lean

condition inside a porous burner and the resulting emission of pollutants. The parametric study included: fuel injection approaches, equivalence ratios, flow velocities and a range of types of fuels. These studies informed the choice of burners for the second part of the work and revealed many of the principal operations of porous burners. In particular, the studies provided an insight into pollutant formation mechanisms in these burners.

The second part of the study is focused on the NOx and other nitrogen containing species conversions inside a porous bed, as a function of the operating conditions. Both experimental and detailed modelling studies are utilised in this study, including the surface reactions.

7.1 Porous Burner as a Combustion Medium

7.1.1 The Effect of Fuel Mixing

In this section, different approaches to injecting fuel into the porous bed have been explored. The aim of this study was to find an alternative approach to fuel air premixing, in order to minimize the risk of flashback and increase the safe operating range of the porous burner.

7.1.1.1 Porous Burner with Bed Fuel Injection

There are known difficulties associated with the stabilisation of a flame using bed injection in a porous burner. Different ways to introduce the fuel into the air stream were trialled and their impacts on flame uniformity, flame stability and pollutant emissions levels were investigated. Bed fuel injection studies were conducted in a 600 mm tall ceramic cylinder with a 154 mm diameter, filled with 6 mm (nominal size) Alumina beads forming a packed porous bed. Fuel then was injected into the porous bed using different fuel distributors, while air was introduced uniformly through the bed inlet. Where the fuel bed injection method was used in this study, the total fuel to air ratio was defined as the Global Equivalence Ratio (GER) and was presented as $\overline{\Phi}$. Temperatures across the porous bed were measured using N-type thermocouples inserted in the ceramic cylinder circumferentially, spaced at 25 mm in height and staggered at 90º.

Three different designs were experimented with, including a single-tube with 0.6 mm holes drilled in two rows, a spiral-tube design, 150 mm in diameter, with similar small holes drilled along the tube and a multi-tube design with small holes drilled on it to cover the whole cross section of the burner.

While the uniformity and stability of the flames have improved with a more elaborate multi-tube design, the laminar nature of the flow and the porous bed itself made it extremely hard to achieve perfectly uniform flames that are highly stable, especially at low equivalence ratios, close to blow-off. It was also found that minor non-uniformity in the mixture strength had major effects on the flame stability, especially for ultra-lean mixtures.

7.1.1.2 Porous Burner with premixed Fuel Injection

In this design, the fuel and air are premixed *a priori* before they are fed uniformly into the inlet of the burner. As expected, a premixed air/fuel mixture resulted in a more stable flame along with temperature gradients that were radially uniform.

This burner was also fitted with a 75 mm layer of fine calcined flint clay, stacked upstream of the porous bed, to prevent flashback and arrest the flame before it could propagate further upstream to the supply line. In addition the air and fuel streams were injected into a mixing chamber upstream of the calcined flint clay layer to ensure that a well-mixed mixture enters the burner.

Both Compressed Natural Gas (CNG, mostly methane) and Liquefied Petroleum Gas (LPG, mostly propane) were used in this burner.

7.2 Porous Burner as a Post Process Combustion Medium

Based on the knowledge and experience gained from the above study, a different porous burner was designed and built which could work at higher equivalence ratios ≥ 1.0. In the burner, the porous bed consisted of 4 silicon carbide disks stacked on top of each other to form a 200 mm high porous bed. Each disk was 150 mm in diameter, had a porosity of ~ 90 % and 10 pores per inch (ppi). The stack was wrapped with insulation sheets (Kaowool paper -2600 grade) followed by a layer of

pumpable Kaofil to minimise the radial heat loss to the surrounding. As the porous burner was working at higher temperatures (especially when close to stoichiometric conditions), R-type thermocouples were inserted at 25 mm intervals (staggered at 90°). Thermocouples were inserted in the porous bed, measuring the temperature at the centre of the disks.

In order to avoid any flashback, a heat exchanger was designed and installed upstream of the porous bed. The heat exchanger consisted of a series of ¼" copper coils arrayed (longitudinally and laterally) in a copper enclosure (150 mm x 150 mm x 100 mm) with a water inlet and outlet. The heat exchanger was filled with fine calcined flint clay (less than 2 mm in size) with low thermal conductivity (K = 0.03 $Wm^{-1}K^{-1}$) in order to extract as much heat as possible from the flint clay layer, should the temperature rise and approach auto-ignition temperature. The exhaust gas was sampled using a suction probe and the samples were analysed using gas chromatography to reveal the concentration of NO, NOx, CH_4, CO and CO_2.

Air, fuel and NOx were injected into a mixing chamber upstream of the heat exchanger using two T-piece fittings. The mixing chamber assured complete mixing of all the input gases.

7.2.1 NOx reduction in Porous Media

It is known well known from the literature that moderately low temperatures, fuel rich conditions and sufficiently high residence times are suitable conditions to achieve reductions of NO_X using hydrocarbon fuels. In this study, NO_X conversion (or NOx reduction) is defined as the ratio of the burner outlet NO_X concentration to the burner inlet NO_X concentration. The literature has also shown that well-controlled conditions are essential for achieving these conditions and optimising the reduction efficiency. These conditions are readily achievable through the use of porous burners, which can be designed to give a uniform temperature and long residence time.

The parameters affecting the NOx reduction inside the porous burner were studied including the equivalence ratio, flow velocity (and hence residence time) and initial NOx levels in the mixture.

These findings were also modelled using a PLUG simulator, which is part of the CHEMKIN package. The GRI-Mech 3.0 chemical kinetics mechanism was used to represent the gaseous chemical reaction inside the bed while the surface reactions are incorporated through consideration of the termination of key radicals at the reactor surfaces. The key radicals for the CH_4-H_2-O_2 system (H_2 O, OH, HO_2, CH_3, and CH_3O, are assumed to react to the stable species, according to the irreversible pseudo-reactions.

The pressure drop across the porous burner was calculated to be less than 250 Pa and hence atmospheric pressure was assumed for all the calculations.

Both the experiments and the modelling were performed for air flow rates ranging from 50 slpm to 200 slpm, equivalence ratios of 1.0 to 2.0 and different inlet NO mole fractions (up to 1800 ppm). CNG was used for the experiments and the same composition, with minor modifications, of fuel was also used in the numerical calculations.

To simulate the mixture from an exhaust stream of a typical combustion system, different amounts of CO_2 were added to the inlet mixtures to examine their impact on NOx conversion and flame stability. It was found that under these conditions, especially low bed temperatures, CO_2 was not chemically active and had negligible impact on the NOx reduction, other than a minor reduction of the flame temperature due to dilution effects. Thus, none of the other experiments included CO_2 in the mixture.

With such rich mixtures, $1.0 < \varphi < 2.0$, the mole fraction of CO in the exhaust was substantial. Through a simple chamber, mounted on top of the porous burner and equipped with external air jets, it was possible to show that for such a mixture, with a temperature of ~1000 K, all the CO emitted from the porous burner can be burned into CO_2.

7.2.1.1 Effects of equivalence ratio on NOx conversion efficiency

For a fixed mixture velocity (or fixed flow rate) and also fixed input NO level, the equivalence ratio was changed between $\varphi = 0.93$ and $\varphi = 1.9$. Both the NOx concentrations and NOx reductions were measured. Repetitions of the results were

also examined for other selected flow rates (to be translated to mixture velocities) such as 50 slpm, 150 slpm and 200 slpm.

7.2.1.2 Effects of Flow Velocity on NOx conversion efficiency

For similar equivalence ratio and fixed input NO, increasing the flow velocity results in higher flame temperatures and also decreases in the residence time. This directly affected the NOx conversion efficiency. Increasing the flow velocity was found to shorten the residence time in a non-linear way. The residence time was found to be affected by three distinct parameters:

1. Increasing superficial velocity and actual velocity inside the porous bed;
2. Moving the flame further downstream and hence shortening the time that the inlet gases are exposed to high temperatures;
3. Increasing the peak temperature and hence further increasing the hot gases downstream of the flame.

Thus, a series of tests were conducted using a fixed input NO, fixed equivalence ratio and the flow velocities were changed between 5 cm/sec and 20 cm/sec (or between 50 slpm and 200 slpm). Similar experiments were repeated for different equivalence ratios and input NO to verify that all cases followed the same trend.

7.2.1.3 Effects of Input NO on NOx conversion efficiency

For a fixed flow velocity and equivalence ratio, the input NO was changed between 20 ml and 100 ml and the NOx concentrations at the porous burner outlet were measured and, from that, the NOx reductions were deduced. The repeatability of the results was also examined for other selected flow rates (to be translated to mixture velocities) such as 50 slpm, 150 slpm and 200 slpm along with equivalence ratios falling between $\varphi = 1$ and $\varphi = 1.9$.

7.2.2 TFN Reduction in Porous Burners

Extensive and detailed study of the intermediate radicals and final combustion products (using modelling techniques) showed that NOx conversion follows different chemical paths under different conditions. A better measure to indicate the accurate

conversion of NOx to N_2 was found to be the concentration of Total Fixed Nitrogen (TFN).

The TFN conversion ratio is calculated as: TFN conversion ratio = 1- [TFN] / [NO_{in}] × 100 where; [TFN] = [NO] + [NO_2] + [HCN] + [NH_3] + 2 × [N_2O].

It was concluded that the NO_X and TFN conversion profiles exhibit different behaviours at different equivalence ratios, flow velocities and also input NO levels. The analysis showed that NO does not necessarily convert to N_2 for all conditions.

7.2.3 Effect of Surface Reaction on NOx/TFN Reduction

Predictions of NO_x conversion efficiency in a porous burner that ignore the effect of radical loss at the burner surface, disagree with the previous experimental measurements at equivalence ratios close to stoichiometric and this discrepancy cannot be accounted for within the uncertainty of the assumed gas-phase rate constants.

The PLUG simulator from the CHEMKIN 3.6 package was used for the numerical calculations. PLUG is designed to model the non-dispersive and one-dimensional chemically reacting ideal gas mixture flowing in a channel of arbitrary geometry. Kinetic modelling predictions were determined using the GRI-Mech 3.0 chemical kinetic mechanism. The Sandia thermodynamic database was used to model the CNG reaction in this study. The Konnov chemical kinetics mechanism was used for comparison purposes and only for some of the cases.

In a series of extensive numerical calculations, the impact of radical termination at the surfaces on the kinetic model predictions was examined. These effects were compared with the experimental measurements of NO_X/TFN conversion in the porous burner.

7.3 Conclusions

The following conclusions can be drawn from the research conducted in this thesis:

1. Flame stabilisation inside a porous burner requires careful consideration of the way that the fuel and air are fed into the bed and strategies are needed to

prevent the flame from flashing back, such as a low porosity bed (Pe < 65) or embedded cooling tubes to extract any heat transferred upstream of the porous bed. Injecting fuel directly into the bed did not produce the required mixture uniformity and flame stability needed to stabilize flames close to blow-off limits.

2. Premixed compressed natural gas, CNG-air flames, at very low equivalence ratios, were stabilised inside the porous bed. The relationship between the volume flow rate of the mixture and the minimum equivalence ratio achieved was established. It was found that flames with $\varphi = 0.35$ can stabilise at flow rates of 96 to 312 slpm or a heat capacity of 2 to 6.2 kW, while flames with $\varphi = 0.40$ can be sustained up to 618 slpm or 12.3 kW. The maximum temperature was also above that calculated at equilibrium by ~250 K, consistent with the super-adiabatic temperatures measured, previously, in such burners. Flames with rich mixtures were only stable up to $\varphi \leq 2.1$ and low flow rates. As the mixture flow rate increased, the equivalence ratio required for stable flames decreased. Modelling was conducted using the PBM and it showed trends consistent with the experimental data. The difference in maximum flame temperatures between the calculated and experimental results was observed to be less than 10%. The model also predicted the extinction limit and preheat region quite effectively.

3. Premixed liquefied petroleum gas, LPG-air flames, at low equivalence ratios, were also stabilised in the porous burner. Similar trends and observations were made for LPG as for CNG, with some minor differences. It was found that LPG-air flames were stable over a narrower range of flow rates, from 96 to 203 slpm for the same mixture strength of $\varphi = 0.35$. It is worthy of note that, as with CNG-air flames, these flames produced very few pollutants, with the maximum measured NO_X and CO mole fractions at the burner exit recorded to be lower than 2 ppm and 7 ppm, respectively. Also, the maximum measured temperature at an equivalence ratio of 0.35 was higher than the equilibrium temperature by 209 K.

4. The conversion of NOx was assessed in a specially designed porous burner. A mixture of CNG-air doped with NO was introduced into the burner and the

effect of the operating parameters on NOx reduction, from the resulting flames, was assessed. It was found that NOx reduction (conversion) started at $\varphi = 0.93$ and that the conversion rate increased as a function of the equivalence ratio, the NO mole fraction and the inlet and total flow rates (or residence time). Higher flow rates led to an increase in the conversion rates at higher equivalence ratios, due to shorter residence times and hence the need for more radicals in the flame.

5. A simulated exhaust gas stream, via the addition of CO_2 to the mixture, showed very similar results to the mixture without CO_2, mostly because CO_2 is very stable at these temperatures. The CO emissions, due to the rich mixtures, were found to be substantial and can easily be burned using an additional chamber mounted at the end of the porous burner where jets of air are introduced.

6. The maximum bed temperature (and hence gas temperature) was found to play an important role in conversion efficiency. The best conversion was achieved when the maximum temperature was kept at 1500 K or lower. If such conditions were achieved, NOx conversions of up to 90% were also achieved.

7. A numerical study using a Plug flow reactor, with a pre-set temperature profile obtained from the experiments, revealed that different chemical pathways dominated at different equivalence ratios, which led to the production of other intermediates and stable radicals, e.g. NH_3. Hence instead of NOx, the Total Fixed Nitrogen (TFN) was investigated, where TFN = $[NO] + [NO_2] + [HCN] + [NH_3] + 2 \times [N_2O]$. The study showed that TFN reduction followed a similar trend to NOx reduction for moderately fuel-rich conditions ($\varphi \leq 1.2$) and opposite trends for higher equivalence ratios. For $\varphi > 1.2$, most of the NO is converted to N-containing species such as N_2O, NH_3 and HCN and not to N_2. Analysis of the chemical pathways showed that the formation of nitrogen-containing species in the very rich conditions is due to the increased importance of the HCNO path, rather than the HNO path. The latter is the dominant path at low equivalence ratios and leads to the

formation of N_2. The best TFN conversion efficiency of 65% was found at $\varphi = 1.1$, T = 1370 K and a flow rate of 106 slpm.

8. The concentration of NO in the initial mixture was also found to affect both NOx and TFN conversion for $\varphi \leq 1.3$. Increasing the NO in the inlet mixture increased the TFN conversion by up to 20%. For $\varphi > 1.3$ this effect was reduced and was negligible after $\varphi = 1.7$ or higher.
9. The numerical study also revealed that, while the bed is treated as an inert surface in most studies, the porous bed surface played an important role in scavenging flame radicals, especially for mixtures close to stoichiometric conditions. For moderately fuel-rich conditions, ($\varphi \leq 1.3$), the conversion of NO_X is strongly influenced by the concentration of H radicals. This influence becomes less important for higher equivalence ratios. A collision probability of $\eta = 8\times10^{-4}$ was found to represent this effect of radical loss and to help predict the destruction and production of intermediate terminals with a good level of accuracy.
10. This study found that NOx reduction using porous burners is technically feasible and that the resulting CO in the exhaust from the rich mixtures can be burned outside the porous bed.

7.4 Future Work

This study has resulted in the development of an experimental porous burner and a numerical model, which provided a good understanding of the mechanisms that influence NOx/TFN reduction in porous burners. However, more can be done in order to improve the current setup and also explore further opportunities for this technology.

Based on the findings of this study, the following future studies are recommended.

7.4.1 Porous Bed Material and Geometry

While there was no direct comparison of porous bed material in this study, two different materials (Aluminium Oxide beads and Silicon Carbide foams) were used.

These two porous bed materials exhibited different behaviours regarding the lead-time for flame stabilisation in the bed and the peak temperature and temperature gradient along the porous bed.

Furthermore, the study on the surface reaction and the effect of termination and production of the radicals, suggests that different porous materials (including the shape. i.e. saddles, beads or foams), porosity and pores per inch (ppi) will behave differently.

It is also interesting to investigate the effect of the porous bed length on the NOx and CO levels. Longer porous beds simply lead to a longer residence time, which should be beneficial for CO reduction with a positive or no effect on NOx reduction. This was observed numerically and needs further exploration to achieve the optimum porous bed length.

7.4.2 Effects of actual exhaust gases on TFN conversion

In order to extend the above findings into the real world, experiments need to be conducted where the exhaust gases from a combustion system are fed into a specially designed porous burner and the conversion efficiency is measured and modelled. This study will take into account the effect of other minor species in the exhaust stream, as well as the presence of water and unburned hydrocarbons. The experiments will also test the dynamic response of the porous burner to variations in the exhaust stream composition, due to variations in the operating conditions.

REFERENCES

1. Seinfeld, J.H., *Atmospheric Chemistry and Physics of Air Pollution*. 1986, New York: John Wiley & Sons.

2. Gauss, M., I.S.A. Isaksen, D.S. Lee, and O.A. Søvde, *Impact of aircraft NOx emissions on the atmosphere – tradeoffs to reduce the impact.* Atmos. Chem. Phys., 2006(6): p. 1529-1548.

3. Turns, S.R., *An Introduction to Combustion*. 2000: McGraw-Hill International Editions.

4. Prather, M.J. and J.A. Logan. *Combustion's Impact on the Global Atmosphere*. in *Twenty-Fifth Symposium (International) on Combustion*. 1994. Pittsburgh: The Combustion Institute.

5. Koshland, C.P. *Impacts and Control of Air Toxic from Combustion*. in *Twenty-sixth Symposium (International) on Combustion*. 1996. Pittsburgh: The Combustion Institute.

6. Kennedy, L.A., A.A. Fridman, and A.V. Saveliev, *Superadiabatic Combustion in Porous Media: Wave Propagation, Instabilities, New Type of Chemical Reactor.* Int. J. Fluid Mechanics Research, 1996. **22**(2).

7. Kennedy, L.A., A.V. Saveliev, and A.A. Fridman. *Transient Filtration Combustion*. in *Mediterranean Combustion Symposium*. 1999. Antalya, Turkey.

8. Min, D.K. and H.D. Shin, *Laminar Premixed Flame Stabilized Inside a Honeycomb Ceramic.* Int. J. of Heat and Mass Transfer, 1991. **34**(2): p. 341-356.

9. Aldushin, A.P. and R.I. E., *Maximal Energy Accumulation in a Superadiabatic Filtration Combustion Wave.* Combustion and Flame, 1999. **118**: p. 76-90.

10. Lammers, F.A. and L.P.H. De Goey, *The Influence of Gas Radiation on The Temperature Decrease Above A Burner With A Flat Porous Inert Surface.* Combustion and Flame, 2003. **136**(4): p. 533-547.

11. Christo, F., S.D. Joseph, J. Lynch, and B.S. Haynes. *Porous Radiant Burner Technology in Lean Combustion Systems*. in *Fifth European Conference on Industrial Furnaces and Boilers(IN-FUB5)*. 2000. Esphino-Porto, Portugal.

12. Rumminger, M.D. and R.W. Dibble. *Gas Temperature Above a Porous Radiant Burner: Comparison of Measurements and Model Predictions*. in *Twenty-Sixth Symposium (International) on Combustion*. 1996. The Combustion Institute, Pittsburgh.

13. Rumminger, M.D., R.D. Hamlin, and R.W. Dibble, *Numerical Analysis of a Catalytic Radiant Burner: Effect of Catalyst on Radiant Efficiency and Operability.* Catalysis Today, 1999. **47**: p. 253-262.

14. Rumminger, M.D., R.W. Dibble, and J. Warantz, *Interactions between Radiant Burners and Inserts: Implications for Pollutant Formation and Radiant Output,Modelling of Chemical Reaction Systems. IWR/SFB 359,*, 1996: Heidelberg.

15. Mital, R., J.P. Gore, and R. Viskanta, *A Study of the Structure of Submerged Reaction Zone in Porous Ceramic Radiant Burners.* Combustion and Flame, 1997. **111**: p. 175-184.

16. Vandadi, V., C. Park, and M. Kaviany, *Superadiabatic radiant porous burner with preheater and radiation corridors.* International Journal of Heat and Mass Transfer, 2013. **64**: p. 680-688.

17. Wu, H., Y.J. Kim, V. Vandadi, C. Park, M. Kaviany, and O.C. Kwon, *Experiment on superadiabatic radiant burner with augmented preheating.* Applied Energy, 2015. **156**: p. 390-397.

18. Bone, *Surface Combustion.* The Journal of the Franklin Institute, 1912. **173**(2): p. 101-131.

19. Lucke, C.E., *Design of surface combustion appliances.* The Journal of Industrial and Engineering Chemistry, 1913. **5**(10): p. 801-824.

20. Hanamura, K. and R. Echigo, *An analysis of flame stabilization mechanism in radiation burners.* Wfirme- und Stoffiibertragung, 1991. **26**: p. 377-383.

21. Williams, A., R. Woolley, and M. Lawes, *The formation of NOx in surface burners.* Combustion and Flame, 1992. **89**: p. 157-166.

22. Xiong, T.-y., *Ultra-Low Pollutant Emissions Radiant Gas Burner with Stabilised Porous-Phase Combustion*, in *United States Patent No. 51472011*990, Institute of Gas Technology (Chicago, IL): United States.

23. Martynenko, V.V., R. Echigo, and Yoshida, *Mathematical Model of Self-Sustaining Combustion in Inert Porous Medium With Phase Change Under Complex Heat Transfer.* Int. J. of Heat and Mass Transfer, 1998. **41**(1): p. 117-126.

24. Ziauddin, M., A. Balkarishna, D.G. Vlachos, and L.D. Schmidt, *Ignition of Methane Flames in Oxygen Near Inert Surfaces: Effect of Composition, Pressure, Preheat, and Residence Time.* Combustion and Flame, 1997. **110**: p. 377-391.

25. Marbach, T.L. and A.K. Agrawal. *Combustion Characteristics of a Natural Gas Burner Using Inert Porous Media*. in *Proc. of the 2002 Spring Technical Meeting of the Central States Section of the Combustion Institute, Paper A5.5*. 2002.

26. Cerri, I., G. Saracco, V. Specchia, and D. Trimis, *Improved-Performance Knitted Fibre mats as Supports for Pre-mixed Natural Gas Catalytic Combustion.* Chemical Engineering Journal, 2001. **82**: p. 73-85.

27. Montanaro, L. and G. Saracco, *Influence of Some Precursors on the Phsio-Chemical Characteristics of Transition Aluminas for the Preparation of Ceramic Catalytic Filters.* Ceramics International, 1995. **21**(1): p. 43-49.

28. Cerri, I., G. Saracco, and V. Specchia, *Methane Combustion Over Low-Emission Catalytic Foam Burners.* Catalysis Today, 2000. **60**: p. 21-32.

29. Maruko, S., T. Naoi, and M. Onodera, *Multistage Catalytic Combustion Systems and High Temperature Combustion systems using SiC.* Catalysis Today, 1995. **26**: p. 309-317.

30. Afsharvahid, S., *Upgrade from Master to PhD (Long Report)*, 2003, School of Mechanical Engineering, Adelaide University: Adelaide.

31. Christo, F., *An Experimental and Numerical Study of Infrared (IR) Emission from a Porous Radiant Burner*, 2001, Defence science and technology organisation, Report no. DSTO-TR-1154, Australia.

32. Trimis, D. *Stabilized Combustion in Porous Media Applications of the Porous Burner Technology in Energy- and Heat-Engineering*. in *Fluids 2000 Conference and Exhibit*. 2000. Denver, Colorado: American Institute of Aeronautics and Astronautics.

33. Hanamura, K., K. Bohda, and Y. Miyairi, *A Study of Super-Adiabatic Combustion Engine.* Energy Convers. Mgmt., 1997. **38**(10-13): p. 1259-1266.

34. Mujeebu, M.A., M.Z. Abdullah, M.Z. Abu Bakar, A.A. Mohamad, and M.K. Abdullah, *Application of Porous Media Combustion Technology - A Review.* Applied Energy, 2009. **86**: p. 1365-1375.

35. Mößbauer, S., O. Pickenäcker, K. Pickenäcker, and D. Trimis. *Application of the porous Burner Technology in Energy- and Heat-Engineering*. in *Fifth International Conference on Technologies and Combustion for a Clean Environment (Clean Air V)*. 1999. Lisbon (Portugal).

36. Rumminger, M.D., *Numerical and Experimental Investigation of Heat Transfer and Pollutant Formation in Porous Direct-Fired Radiant Burners; PhD thesis*, in *Department of Mechanical Engineering*1996, University of California, Berkeley.

37. Durst, F. and M. Weclas. *A New Type of Internal Combustion Engine Based on the porous-Medium Combustion Technique*. in *Proc Instn Mech Engrs*. 2001.

38. Weclas, M., *Strategy for intelligent internal combustion engine with homogeneous combustion in cylinder*. Vol. 26. 2004: Sonderdruck Schriftenreihe University of Applied Sciences in Nuernberg.

39. Weclas, M., *Potential of Porous Medium Combustion Technology as Applied to Internal Combustion Engines.* Vol. 32. 2005: Sonderdruck Schriftenreihe University of Applied Sciences in Nuernberg.

40. Weclas, M., *Porous Media in Internal Combustion Engines*, in *Cellular ceramics-structure, manufacturing, properties and applications.*, M. Scheffler and P. Colombo, Editors. 2005, Wiley-VCH Publication.

41. Advic, F., M. Adzic, and F. Durst, *Small scale porousnext term medium combustion system for heat production in households.* Applied Energy, 2010. **87**(7): p. 2148-2155.

42. Trimis, D., K. wawrzinek, Hatzfeld, and e. al. *High Modulation burner for liquid fuels based on Porous Media Combustion and Cool Flame Vaporization*. in *Sixth International Conference on technologies and combustion for a clean environment. Vol.2 Paper 23.1*. 2001. Porto, Portugal.

43. Xiong, T.-y., *Gas-Fired, Porous Matrix, Combustor-Steam Generator*, in *United States Patent No. 55446241994*, Institute of Gas Technology (Chicago, IL): United States.

44. Keramiotis, C. and M.A. Founti, *An experimental investigation of stability and operation of a biogas fueled porous burner.* Fuel, 2013. **103**: p. 278-284.

45. Wood, S. and A.T. Harris, *Porous burners for lean-burn applications.* Progress in Energy and Combustion Science, 2008. **34**: p. 667-684.

46. Wood, S., D.F. Fletcher, S.D. Joseph, A. Dawson, and A.T. Harris, *Design and Evaluation of a Porous Burner for the Mitigation of Anthropogenic Methane Emissions.* Environ. Sci. Tech, 2009. **43**: p. 9329-9334.

47. Zheng, C., L. Cheng, T. Li, Z.Y. Luo, and K.F. Cen, *Filtration combustion characteristics of low calorific gas in SiC foams.* Fuel, 2010. **89**(9): p. 2331-2337.

48. Afsharvahid, S., P.J. Ashman, and B. Dally, *Investigation of NO_X Conversion Characteristics in a porous Medium.* Combustion and Flame, 2008. **152**: p. 604-615.

49. Afsharvahid, S. and B. Dally. *Investigation of NO_X Reburning Inside a Porous Burner*. in *5th Asia-Pacific Conference on Combustion*. 2005,18-20 July. Adelaide, Australia.

50. Slimane, R.B., F.S. Lau, and J. Abbasian, *Hydrogen Production by Superadiabatic Combustio n of Hydrogen Sulfide*, 2000, Proceeding of the 2000 Hydrogen program Review, NREL/CP-570-28890.

51. Binguea, J.P., A.A. Savaliev, A.A. Fridman, and L.A. Kennedy, *Hydrogen Production in Ultra-rich Filtration Combustion of Methane and Hydrogen Sulfide.* Int. J. Hydrogen Energy, 2002. **27**: p. 643-649.

52. Al-Hamamre, Z., A. Al-Zoubi, and D. Trimis, *Numerical investigation of the partial oxidation process in porous media based reformer.* Combustion Theory and Modelling, 2010. **14**(1): p. 91-103.

53. Pastore, A. and E. Mastorakos, *Syngas production from liquid fuels in a non-catalytic porous burner.* Fuel, 2011. **90**(1): p. 64-76.

54. Howell, J.R., M.J. Hall, and J.L. Ellzey, *Combustion of Hydrocarbon Fuels Within Porous Inert Media.* Progress in Energy and Combustion Science, 1996. **22**: p. 121-145.

55. McCausland, D., L. Shirvill, and K. Coles, *Surface-combustion radiant burner*, in *United States Patent*, U.S. Patent, Editor 1986, 4,597,734.

56. Oliveira, A.A.M. and M. Kaviany, *Nonequilibrium in the Transport of Heat and Reactants in Comnbustion in Porous Media.* Progress in Energy and Combustion Science, 2001. **27**: p. 523-545.

57. Zepter, K. and J.E. Hustad. *1st Biennial meeting of the Scandinavian-Nordic Section of the Combustion Institute*. 2001.

58. Durst, F. and D. Trimis. *Combustion by Free Flames Versus Combustion Ractors*. in *4th International Conference on Technologies and Combustion for a Clean Environment*. 1997.

59. Yoksenakul, W. and S. Jugjai, *Design and Development of a SPMB (Self Aspirating, Porous Medium Burner) With a Submerged Flame.* Energy, 2011. **36**: p. 3092-3100.

60. Babkin, V.S., A.A. Korzhavin, and V.A. Bunev, *Propagation of Premixed Gaseous Explosion Flames in Porous Media.* Combustion and Flame, 1991. **87**: p. 182-190.

61. Lyamin, G.A. and A.V. Pinaev, *Combustion Regimes in an Inert Porous Material.* Combustion Explosion and Shock Waves USSR, 1986. **22**(5): p. 553-558.

62. Kulkarni, M.R. and R.E. Peck, *Analysis of a Bilayered Porous Radiant Burner.* Numerical Heat Transfer, 1996. **30**(3): p. 219-232.

63. Trimis, D., F. Durst, O. Pickenäcker, and K. Pickenäcker. *Porous Medium Combustor Versus Combustion Systems with Free Flames*. in *2nd International Symposium on Heat Transfer Enhancement and Energy Conservation*. 1997. Guanzhou, China.

64. Korzhavin, A.A., V.A. Bunev, R.K. Abdullin, and V.S. Babkin, *Flame Zones in Gas combustion in an Inert Porous Medium.* Combustion Expolsion and Shock Waves USSR, 1982. **18**(6): p. 628-631.

65. Pantangi, V.K. and C.M. Subbash, *Combustion of gaseous hydrocarbon fuels within porous media – a review.* Adv. Energy. Res. (AER), 2006: p. 455-461.

66. Cerri, I., G. Saracco, F. Geobaldo, and V. Specchia, *Development of a Methane Premixed Catalytic Burner for Houshold Applications.* Industrial & Engineering Chemistry Research, 2000. **39**: p. 24-33.

67. Gao, H.B., Z.G. Qu, X.B. Feng, and W.Q. Tao, *Methane/air premixed combustion in a two-layer porous burner with different foam materials.* Fuel, 2014. **115**: p. 154-161.

68. Saggio-Woyansky, J., C.E. Scott, and W.P. Minnear, 1992, American Ceram. Soc. Bull. 71.

69. Gomez, S.Y., J.A. Escobar, O.A. Alvarez, C.R. Rambo, A.P. Novaes de Oliveria, and D. Hotza, *ZrO2 foams for porous radiant burners.* Journal of Materials Science, 2009. **44**(13): p. 3466-3471.

70. Nield, D.A. and A. Bejan, *Convection in Porous Media*. 1992, New York: Springer.

71. Tien, C. and B.V. Ramarao, *Can filter cake porosity be estimated based on the Kozeny–Carman equation?* Powder Technology, 2013. **237**: p. 233-240.

72. Kaviany, M., *Principles of Heat Transfer in Porous Media*. 1991, New York: Springer.

73. Kennedy, L.A., Saveliev, A.V. and Fridman A.A. *Superadiabatic Partial Oxidation of Methane in Reciprocal and Counterflow Porous Burners*. in *Heat Transfer, Proceedings of 11th IHTC*. 1998. Kyongju, Korea.

74. Lammers, F.A. and L.P.H. De Goey, *A numerical study of flash back of laminar premixed flames in ceramic-foam surface burners.* Combustion and Flame, 2003. **133**(1-2): p. 47-61.

75. Akbari, M.H., P. Riahi, and R. Roohi, *Lean flammability limits for stable performance with a porous burner.* Applied Energy, 2009. **86**(12): p. 2635-2643.

76. Weinberg, F.J., "*Combustion temperatures: the future?*". Nature, 1971. **233**: p. 239-241.

77. Hardesty, D.R. and F.J. Weinberg, *Burners producing large excess enthalpies.* Combustion Science and Technology, 1974. **8**: p. 201-214.

78. Chaffin, C., *Reduction of NO_X emissions Using the Technique of Two-Stage Combustion Within Porous Inert Media, M.S. Thesis*, in *Dept. of Mechanical Engineering*1991, The university of Texas, Austin, TX.

79. Bell, R.D., W.C. Gardiner, J.R. Howell, R.D. Matthews, S.P. Nicholas, and S. P., *Aparatus and Method for Combustion Within Porous Matrix*

Elements, in *United States Patent No. 51602541*991, Institute of Gas Technology (Chicago, IL): United States.

80. Bell, R.D., W.C. Gardiner, J.R. Howell, R.D. Matthews, and S.P. Nicholas, *Combustion Method and Apparatus for Staged Combustion within Porous Matrix Elements*, in *United States Patent No. 50805771*991, Institute of Gas Technology (Chicago, IL): United States.

81. Bell, R.D., C. Chaffin, and M. Koeroghlian, *Experimental Investigation of a Staged Porous Ceramic Burner.* Fossil Fuels Combustion, ASME, 1992. **PD-vol.29**: p. 41-46.

82. Khinkis, M.J., H.A. Abbasi, and T.D. Briselden, *Staged Combustion in a Porous-Matrix Surface Combustor to Promote Ultra-Low NOx Emissions*, in *United States Patent No. 54763751*994, Institute of Gas Technology (Chicago, IL)I: United States.

83. Zhao, Z. and X. Maozhao, *Numerical simulation about interaction between pressure swirl spray and hot porous medium.* Energy Convers. Mgmt., 2008. **49**(5): p. 1047-1055.

84. Fuse, T., N. Kobayashi, and M. Hasatani, *Combustion Characteristics of Ethanol in a Porous Ceramic Burner and Ignition Improved by Enhancement of Liquid-Fuel Intrusion in the Pore With Ultrasonic Irradiation.* Experimental Thermal and Fluid Science, 2004. **29**: p. 467-476.

85. Jugjai, S. and N. Polmart, *Enhancement of evaporation and combustion of liquid fuels through porous media.* Experimental Thermal and Fluid Science, 2003. **27**: p. 901-909.

86. Jugjai, S. and C. Pongsai, *Liquid fuels-fired porous burner.* Combustion Science and Technology, 2007. **179**: p. 1823-1840.

87. Jugjai, S., N. Wongpanit, T. Laoketkan, and S. Nokkaew, *The Combustion of Liquid Fuels Using a Porous Medium.* Experimental Thermal and Fluid Science, 2002. **26**(1): p. 15-23.

88. Tseng, C.J. and J.R. Howell, *The Combustion of Liquid Fuels in a Porous Radiant Burner.* Combustion Science and Technology, 1996. **112**: p. 141-161.

89. Mujeebu, M.A., M.Z. Abdullah, M.Z. Abu Bakar, A.A. Mohamad, and M.K. Abdullah, *A review of investigations on liquid fuel combustion in porous inert media* Progress in Energy and Combustion Science, 2009. **35**(2): p. 216-230.

90. Takami, H., T. Suzuki, Y. Itaya, and M. Hasatani, *Performance of Flammability of Kerosene and NOX Emission in the Porous Burner.* Fuel, 1998. **77**(3): p. 165-171.

91. Korzhavin, A.A., V.A. Bunev, and V.S. Babkin, *Flame Propagation in Closed Vessels with Inert Porous Medium Wetted with Fuel.* Combustion Expolsion and Shock Waves USSR, 1997. **33**(3): p. 306-314.

92. Binguea, J.P., A.A. Savaliev, A.A. Fridman, and L.A. Kennedy, *NOx and CO Emissions of Lean and Ultra-lean Filtration Combustion of Methane/Air mixture in an Inert Porous Media.* Clean Air, 1999. **3**: p. 199-210.

93. Bouma, P.H., R.L.G.M. Eggels, L.P.H. De Goey, J.K. Nieuwenhuizen, and A. Van Der DRIFT, *A Numerical and Experimental Study of the No-Emission of Ceramic Foam Surface Burners.* Combustion Science and Technology, 1995. **108**(1): p. 193-203.

94. Makansi, J., W. Bartok, and B.A. Folsom, *Special Report: Reducing NO_X Emissions from Today's Powerplants.* Power, 1993, May: p. 11-28.

95. Boardman, R.D. and L.D. Smoot, *Pollutant formation and control*, in *Fundamentals of Coal Combustion*, L.D. Smoot, Editor. 1993, Elsevier: The Netherlands.

96. Wendt, J.O.L., C.V. Sternling, and M.A. Matovich, *Reduction of sulfur trioxide and nitrogen oxides by secondary fuel injection.* Proc. Combust. Inst. , 1973. **14**: p. 897-904.

97. Bertran, C.A. and C.S.T. Marques, *Study of the Particulate Matter Emitted from Residual Oil Combustion and Natural Gas Reburning.* Braz. Chem. Soc, 2004. **15**(4): p. 548-555.

98. Bertran, C.A., C.S.T. Marques, and R.V. Filho, *Reburning and Burnout Simulations of Natural Gas for Heavy Oil Combustion.* Fuel, 2004. **83**: p. 109-121.

99. Dagaut, P., J. Luche, and M. Cathonnet, *The Kinetics of C_1 to C_4 Hydrocarbons/NO Interactions in Relation with Reburning.* Proc. Combust. Inst., 2000. **28**: p. 2459-2465.

100. Kilpinen, P., P. Glarborg, and M. Hupa, Industrial & Engineering Chemistry Research, 1992. **31**: p. 1477.

101. Shi, C., A.B. Walters, and M.A. Vannice, *NO Reduction by CH_4 in the Presense of O_2 over La_2O_3 supported on Al_2O_3.* Applied Catalysis, 1997. **14**: p. 175-188.

102. Zamansky, V., P.M. Maly, and V. Lissianski, *Second Generation Advanced Reburning for High Efficiency NO_X Control*, 1999, Energy and Environmental Research Corporation: Irvine.

103. Babcock and Wilcox, *Demonstration of Coal Reburning for Cyclone Boiler NO_X Control.*, 1990, Comprehensive Report to Congress Clean Coal Technology Program.

104. Glarborg, P., M.U. Alzueta, and K. Dam-Johansen, *Kinetic Modeling of Hydrocarbon/Nitric Oxide Interactions in a Flow Reactor.* Combustion and Flame, 1998. **115**: p. 1-27.

105. Dagaut, P., J. Luche, and M. Cathonnet, *Experimental and Kinetic Modeling of Reduction of NO by Propene at 1 Atm.* Combustion and Flame, 2000. **121**: p. 651-661.

106. Dagaut, P., J. Luche, and M. Cathonnet, *Reduction of NO by Propane in a JSR at 1 Atm: Experimental and Kinetic Modeling.* Fuel, 2001. **80**: p. 979-986.

107. Kolb, T., P. Jansohn, and W. Leuckel, *Reduction of NO_X Emission in Turbulent Combustion by Fuel-Staging.* Proc. Combust. Inst., 1988. **22**: p. 1193.

108. Cha, C.M. and J.C. Kramlich, *Modeling Finite-Rate Mixing Effects in Reburning Using a Simple Mixing Model.* Combustion and Flame, 2000. **122**: p. 151-164.

109. Bilbao, R., A. Milleria, M.U. Alzueta, and L. Prada, *Evaluation of the Use of Different Hydrocarbon Fuels for Gas Reburning.* Fuel, 1997. **76**(14/15): p. 1401-1407.

110. Dagaut, P. and K. Hadj Ali, *Kinetics of Oxidation of a LPG Blend Mixture in a JSR: Experimental and Modeling Study.* Fuel, 2003. **82**: p. 475-480.

111. Williams, A.B. and L. Pasternack, *The Effect of Nitric Oxide on Premixed Flames of CH_4, C_2H_6, C_2H_4, and C_2H_2.* Combustion and Flame, 1997. **111**: p. 87-110.

112. Skreiberg, Ø., P. Kilpainen, and P. Glarborg, *Ammonia chemistry below 1400 K under fuel-rich conditions in a flow reactor.* Combustion and Flame, 2004. **136**(4): p. 501-518.

113. Tsang, W. and J.T. Herron, *Chemical kinetic data base for propellant combustion. I. Reactions involving NO, NO2, HNO, HNO2, HCN and N2O.* J. Phys. Chem., 1991. **20**: p. 609-633.

114. Soto, M.R. and M. Page, *Ab initio variational transition-state-theory reaction-rate calculations for the gas-phase reaction H + HNO → H2 + NO.* J. Phys. Chem., 1992. **97**: p. 7287-7296.

115. Glarborg, P., M. Østberg, M.U. Alzueta, and K. Dam-Johansen, *The recombination of hydrogen atoms with nitric oxide at high temperatures.* Proc. Combust. Inst., 1998. **27**: p. 219-226.

116. Riley, P.S., B. Cosic, and A. Fontijn, *The H+NO recombination reaction over a wide temperature range.* J. Chem. Kinet., 2003. **35**: p. 374-380.

117. Barra, A.J. and J.L. Ellzey, *Heat Recirculation and Heat Transfer in Porous Burners.* Combustion and Flame, 2004. **137**(1-2): p. 230-241.

118. Brenner, G., Pickenacker, K., Pickenacker, O., Trimis, D., Wawrzinek, K., and Weber, T., *Numerical and Experimental Investigation of Matrix-Stabilized Methane/Air Combustion in Porous Inert Burner.* Combustion and Flame, 2000. **123**: p. 201-213.

119. Kayal, T.K. and M. Chakravarty, *Modeling of trickle flow liquid fuel combustion in inert porous medium.* International Journal of Heat and Mass Transfer, 2006. **49**: p. 975-983.

120. Neef, M., P. Knabner, and G. Summ, *Numerical Bifurcation Analysis of Premixed Combustion in porous Inert Media*, in *Computational Science and Engineering 8*1999. p. 39-50.

121. Pickenäcker, O., A. Kesting, and D. Trimis. *Novel low NOX Burner Designs for Boilers and Furnaces by Using Staged Combustion in Inert Porous Media*. in *5th European Conference on Industrial Furnaces and Boilers*. 2000. Espinho-Porto, Portugal.

122. Pickenäcker, O. and D. Trimis, *Experimental Study of a Staged Methane/Air Burner Based on Combustion in a Porous Inert Medium.* Journal of Porous Media, 2001. **4**(3): p. 197-213.

123. Dixon-Lewis, G. and D.J. Williams, *The Oxidation of Hudrogen and Carbon Monoxide.* Comprehensive chemical Kinetics, Elsevier Scientific Publishing Company 1977. **17**(Gas-Phase Combustion).

124. Thomas, D.J., R. Willi, and A. Baiker, *Partial Oxidation of Methane: The Role of Surface Reactions.* Industrial & Engineering Chemistry Research, 1992. **31**: p. 2272-2278.

125. Ashman, P.J. and B.S. Haynes, *Rate Coefficient of $H + O_2 + M$ => $HO_2 + M$ (M=H_2O, N_2, Ar, CO_2).* Twenty-Seventh symposium (International) on Combustion, 1998: p. 185-191.

126. Ashman, P.J., *Aspects of Homogeneous and Heterogeneous Reactions leading to the Emission of Oxides of Nitrogen from Combustion Processes* in *Department of Chemical Engineering*1999, University of Sydney.

127. Sathe, S.B., M.R. Kulkarni, R.E. Peck, and T.W. Tong, *An Experimental and Theoretical Study of Porous Radiant Burner Performance.* Twenty-Third Symposium (International) on Combustion, 1990: p. 1011-1018.

128. Sathe, S.B., R.E. Peck, and T.W. Tong, *Anumerical Analysis of Heat Transfer and Combustion in Porous Radiant Burner.* Int. J. of Heat and Mass Transfer, 1990. **33**(6): p. 1331-1338.

129. Hackert, C.L., J.L. Ellzey, and O.A. Ezekoye, *Combustion and Heat Transfer in Model Two-Dimensional Porous Burners.* Combustion and Flame, 1999. **116**: p. 177-191.

130. Mishra, S.C., M. Steven, S. Nemoda, P. Talukdar, D. Trimis, and F. Durst, *Heat Transfer Analysis of a Two-Dimensional Rectangular Porous*

Radiant Burner. international Communications in Heat and Mass Transfer, 2006. **33**: p. 467-474.

131. Hsu, P.-F. and R.D. Matthews, *The Necessity of Using Detailed Kinetics in Models for Premixed Combustion within Porous Media.* Combustion and Flame, 1993. **93**: p. 457-466.

132. Kee, R.J., J.F. Grcar, M.D. Smooke, and J.A. Miller, *A Fortran Computer Program for Modeling Steady Laminar One-Dimensional Premixed Flames, Report SAND 85-8240*, 1985, Sandia NAtional Laboratories, CA.

133. Shardlow, P.J., *Master Thesis; A One Dimensional Model for Catalysed Combustion in a Porous Burner*, in *The Department of Chemical Engineering*1999, The University of Sydney: Sydney.

134. Yoshizawa, Y., Sasaki, K. and Echigo, R., *Analytical Study of the Structure of Radiation Controlled Flame.* Int. J. of Heat and Mass Transfer, 1988. **31**: p. 311-319.

135. Trimis, D. and F. Durst, *Combustion in a Porous Medium - Advances and Applications.* Combustion Science and Technology, 1996. **121**: p. 153-168.

136. Tong, T.W., S.B. Sathe, and R.E. Peck, *Improving the Performance of Porous Radiant Burners Through Use of Sub-Micron Size Fibers.* Int. J. of Heat and Mass Transfer, 1990. **33**(6): p. 1339-1346.

137. Meng, W.H., C. McCordic, J.P. Gore, and K.E. Herold. *A study of effects of porous inserts on heat transfer and combustion in a fired heat exchanger.* in *Proceedings of the ASME/JSME Thermal Engineering Joint Conference*. 1991. The Japanese Society of Mechanical Engineers, Japan.

138. McCarthy, T.A., *Measurements of Infrared Radiative Transfer for Porous Ceramic Materials, M. Sc Thesis*, 1989, University of Illinois, Urbana-Champaign.

139. Hall, M.J. *A Porous Ceramic Radiant Burner Utilizing Non-Premixed Combustion of Gaseous Fuels*. in *Proceedings of the Joint Technical Meeting on Combustion fundamentals and applications, Central/Eastern States Sections Meeting of the Combustion Institute*. 1993. Madison, Wisconsin, USA

140. Kamal, M.M. and A.A. Mohamad, *Enhanced radiation output from foam burners operating with a nonpremixed flame.* Combustion and Flame, 2005. **140**(3): p. 233-248.

141. Barra, A.J. and J.L. Ellzey, *Heat recirculation and heat transfer in porous burners.* Combustion and Flame, 2004. **137**: p. 230-241.

142. Zheng, C., L. Cheng, A.A. Savaliev, Z.Y. Luo, and K. Cen. *Gas and solid phase temperature measurements of porous media combustion*. in *Proc. Combust. Inst.* 2011.

143. Henríquez-Vargas, L., M. Valeria, and V. Bubnovich, *Numerical study of lean combustibility limits extension in a reciprocal flow porous media burner for ethanol/air mixtures.* International Journal of Heat and Mass Transfer, 2015. **89**: p. 1155-1163.

144. Keramiotis, C., M. Katoufa, G. Vourliotakis, A. Hatziapostolou, and M.A. Founti, *Experimental investigation of a radiant porous burner performance with simulated natural gas, biogas and synthesis gas fuel blends.* Fuel, 2015. **158**: p. 835-842.

145. Chen, X., X.-L. Xia, C. Sun, and Y. Li, *Numerical analysis on the transient measurement of gas temperature in porous material using thermocouples at high temperatures.* International Journal of Heat and Mass Transfer, 2015. **91**: p. 1060-1068.

146. Kee, R.J., F.M. Rupley, and J.A. Miller, *CHEMKIN II: A Fortran Chemical Kinetics Package for the Analysis of Gas-Phase Chemical Kinetics, Report SAND 89-8009*, 1989, Sandia National Laboratories, CA.

147. Kee, R.J., G. Dixon-Lewis, and J. Warantz, *A Fortran Computer Code Package for the Evaluation of Gas-Phase Multicomponenet Transport Properties, Report SAND 86-8246*, 1986, Sania NAtional Laboratories, CA.

148. Coltrin, M.E., R.J. Kee, and F.M. Rupley, *SURFACE CHEMKIN: a Fortran Package for Analysing Heterogeneous Chemical Kinetics at a Solid-Surface - Gas-Phase Interface, Report SAND 90-8003B*, 1991, Sandia National LAboratories, CA.

149. Christo, F., *A Parametric Analysis of a Coupled Chemistry-Radiation Model in Porous Media*, 2000, Defence science and technology organisation, Report no. DSTO-RR-0188, Australia.

150. Vagelopoulos, C.M. and F.N. Egolfopoulos, *Direct experimental determination of laminar flame speeds.* Symposium (International) on Combustion, 1998. **27**(1): p. 513-519.

151. Vagelopoulos, C.M., F.N. Egolfopoulos, and C.K. Law, *Twenty-Fifth Symposium (International) on CombustionFurther considerations on the determination of laminar flame speeds with the counterflow twin-flame technique.* Symposium (International) on Combustion, 1994. **25**(1): p. 1341-1347.

152. Morley, C., *Gaseq; Chemical equilibria in perfect gases; Ver. 0.71*, HTTP://www.c.morley.ukgateway.net.

153. Zabetakis, M.G., *Flammability characteristics of combustible gases and vapors.*, in *No. BULL-627. Bureau of Mines* 1965: Washington DC.

154. Comparato, J.R. *NO_X Control Technologies: Focus SNCR*. in *Western Coal Council, Burning PRB Coal Seminar*. 2001. Birmingham, Alabama.

155. Binguea, J.P., A.A. Savaliev, and L.A. Kennedy, *NO Reburning in Ultrarich Filtration Combustion of Methane.* Proc. Combust. Inst., 2007. **31**: p. 3417-3424.

156. Fursenko, R., A. Maznoy, E. Odintsov, A. Kirdyashkin, S. Minaev, and K. Sudarshan, *Temperature and radiative characteristics of cylindrical porous Ni–Al burners.* International Journal of Heat and Mass Transfer, 2016. **98**: p. 277-284.

157. Szekely, J., J.W. Evans, and H.Y. Sohn, *Gas-Solid Reactions*. 1976, New York: Academic Press.

158. Kee, R.J., F.M. Rupley, J.A. Miller, M.E. Coltrin, J.F. Grcar, E. Meeks, H.K. Moffat, A.E. Lutz, G. Dixon-Lewis, M.D. Smooke, and J. Warantz, *CHEMKIN Collection, Release 3.6, Reaction Design, Inc.*,, 2001: San Diego, CA.

159. Gregory, P.S., D.M. golden, M. Frenklach, N.W. Moriarty, Eiteneer, B. Eiteneer, M. Goldenberg, C.T. Bowman, R.K. Hanson, S. Song, W.C. Gardiner, V.V. Lissianski, and Z. Qin. *GRI - MECH 3.0*. 10/07/2005].

160. Leong, K.C. and L.W. Jin, *Characteristics of Oscillating Flow Through a Channel Filled with Open-Cell Metal Foam.* International Journal of Heat and Fluid Flow, 2005. **27**: p. 144-153.

161. Dukhan, N., *Correlations for the Pressure Drop for Flow Through Metal Foam.* Experiments in Fluids, 2006. **41**: p. 665-672.

162. Philips, A.P. and H.L. Schram, *Non-Darcian Airflow Through Ceramic Foams.* American Ceramic Society Bulletin, 1991. **74**: p. 728-732.

163. Kee, R.J., F.M. Rupley, and J.A. Miller, *The Chemkin Thermodynamic Database*, in *SAND87-8215*1991, Sandia National Laboratories.

164. Konnov, A.A., *Implementation of the NCN pathway of prompt-NO formation in the detailed reaction mechanism.* Combustion and Flame, 2009. **156**: p. 2093-2105.

165. Chapman, S. and T.G. Cowling, *The Mathematical Theory of Nonuniform Gases.* Cambridge University Press, 1952. **2**: p. 245.

166. Fuller, E.N., P.D. Schettler, and J.C. Giddings, *A New Method For Prediction Of Binary Gas-Phase Diffusion Coefficients.* Industrial and Engineering Chemistry, 1996. **58**(5): p. 19-27.

167. Bird, R.B., W.E. Stewart, and E.N. Lightfoot, *Transport Phenomena (2nd Edition)*. 2002: John Wiley & Sons.

168. Lewis, B. and G. Von Elbe, *Combustion, Flames and Explosions of Gases. (2nd Edition)*. 1961: Academic Press.

169. Grubbs, R.K. and S.M. George, *Attenuation of hydrogen radicals travelling under flowing gas conditions through tubes of different materials.* JVST A – Vacuum, Surfaces, and Films, 2006. **24**(3): p. 486-496.

170. Nguyen, H.M., S.W. Zhang, J. Peeters, and M.T. Truong, *Direct ab initio dynamics studies of the reactions of HNO with H and OH radicals.* Chem. Phys. Lett., 2004. **388**: p. 94-99.

171. NIST. *Species Data* *http://www.cstl.nist.gov/div386/ckmech/SpeciesData.html*. 20/10/2006].

172. McBride, B.J., *Database of Coefficients for Calculating Thermodynamic and Transport Properties*, 1993, NASA TM-4513.

173. Burcat, A. and B.J. McBride, *1997 Ideal Thermodynamics Data for Combustion and Air-Pollution Use*, 1997, Technion Aerospace Report TAE804, ftp://ftp.technion.ae.il/pub/supported/aetdd/thermodynamics.

APPENDICES

A. Publications originating from this study

- **S. Afsharvahid**, Pedro N. Alvarado, Peter J. Ashman and Bassam B. Dally, The effect of surface reactions on the prediction of NO_X conversion efficiency in a porous burner, in *the Journal of Combustion and Flame,* October 2013
- **S. Afsharvahid***,* Peter J. Ashman and B. Dally, Investigation of NO_X Conversion Behaviour in a Porous Medium, in *the Journal of Combustion and Flame,* March 2007.
- **S. Afsharvahid** and B. Dally, Investigation of NO_X Reburning Inside a Porous Burner. The *5th Asia-Pacific Conference on Combustion*. 2005, Adelaide, Australia.
- **S. Afsharvahid**, B. Dally, and F. Christo, NO_X Reburning Technology In Porous Media, work-in-progress at the *30th International symposium on combustion*, Chicago, Illinois, USA, 2004.
- **S. Afsharvahid**, B. Dally, and F. Christo, Numerical Study of Flame Stabilisation Inside Porous Burner**,** *2003 Australian Symposium on Combustion and The 8th Australian Flame Days*, Monash university, Melbourne, Australia 2003
- **S. Afsharvahid**, B. Dally, and F. Christo, On the stabilisation of ultra-lean methane and propane flames in porous media, *The Fourth Asia-Pacific Conference on Combustion*, 2003, Nanjing, P.R.China,
- F. Christo, B. Dally, P.V. Lanspeary, and **S. Afsharvahid**, Development of Porous Burner Technology for Ultra-Lean Combustion Systems, *Technical Report No. GC-FR–F-220202.*
- **S. Afsharvahid**, P.V. Lanspeary, B. Dally, and F. Christo, Development of porous burner technology for Ultra-lean combustion systems, work-in-

progress at the *29th International symposium on combustion*, Sapporo, Japan, 2002.

- F. Christo, B. Dally, **S. Afsharvahid** and P.V. Lanspeary, Burning Lean and Green with Porous Burner Technology, Technical presentation in the *2002 SENRAC Conference*, Adelaide, July 2002.
- **S. Afsharvahid**, P.V. Lanspeary, B. Dally, and F. Christo, On the Design of an Ultra Lean Porous Burner**,** *2002 Australian Symposium on Combustion and The Seventh Australian Flame Days*, Adelaide, 2002.

B. Calculating holes distances in multi-tube fuel distributor

```
'********************************************************************************
'Calculate optimum distance between tubes and holes for multi-fuel distributor to create uniform concentration of the fuel inside porous bed
'********************************************************************************
'Define Assumptions, Constants, Variables
'********************************************************************************
CLS
CLEAR
DIM x0(100)
DIM y0(100)
Eqconstant = 18
Concentration = 0
ConcentrationMax = 0
ConcentrationMin = 100
DIM TotalConcentration(127, 127)
COLOR 4, 0, 8
INPUT "Please input the MINIMUM Distance you need to scan"; ScanDistance
INPUT "Please input the HORIZONTAL Distance BETWEEN the Holes"; HorHolesDistance
INPUT "Please input the VERTICAL Distance BETWEEN the Holes"; VerHolesDistance
CLS
COLOR 15, 0
'********************************************************************************
'Calculations
'********************************************************************************
FOR i = -77 TO 77 STEP ScanDistance
    FOR j = -77 TO 77 STEP ScanDistance
     Concentration = 0
     x = i
     y = j
        'FOR k = -(INT(77 / HorHolesDistance) + 1) * HorHolesDistance TO -(INT(77 / HorHolesDistance) + 1) * HorHolesDistance STEP
HorHolesDistance
          FOR k = -80 TO 80 STEP HorHolesDistance
          absk = ABS(k)
          x0(absk) = k
             'FOR l = -(INT(77 / VerHolesDistance) + 1) * VerHolesDistance TO -(INT(77 / VerHolesDistance) + 1) * VerHolesDistance STEP
VerHolesDistance
               FOR l = -80 TO 80 STEP 18
                absl = ABS(l)
                y0(absl) = l
                Radius = SQR((x - x0(absk)) ^ 2 + (y - y0(absl)) ^ 2)
                Concentration = Concentration + EXP(-(Radius ^ 2 / Eqconstant ^ 2))
               NEXT l
         NEXT k
     absi = ABS(i)
     absj = ABS(j)
     TotalConcentration(absi, absj) = Concentration
          IF absi >= 70 OR absj >= 70 GOTO 10
          IF ConcentrationMax < Concentration THEN ConcentrationMax = Concentration: iimax = i: jjmax = j
          IF ConcentrationMin > Concentration THEN ConcentrationMin = Concentration: iimin = i: jjmin = j
     PRINT "TotalConcentration"; "("; i; ","; j; ")"; "="; INT(TotalConcentration(absi, absj) * 1000) / 1000
10 NEXT j
NEXT i
'Results
PRINT : PRINT "The MAXIMUM Concentration is:"; INT(ConcentrationMax * 10000) / 10000; "and occurs at"; "("; iimax; ","; jjmax; ")"
PRINT "The MINIMUM Concentration is:"; INT(ConcentrationMin * 10000) / 10000; "and occurs at"; "("; iimin; ","; jjmin; ")"
COLOR 14, 2
PRINT : PRINT "    WARNING: THE DATA IN POINTS MORE THAN 70 mm FROM THE CENTRE IS IGNORED    "
COLOR 15, 0
PRINT : PRINT "Maximum Error"; "="; INT((ConcentrationMax / ConcentrationMin - 1) * 1000) / 1000 * 100; "%"
PRINT : INPUT "do you need a GRAPHICAL view of Concentration (1=Yes, Any Key=End)"; YesOrNo
IF YesOrNo = 1 GOTO 20 ELSE END
20 SCREEN 12
CLS
FOR i = -77 TO 77 STEP ScanDistance
    FOR j = -77 TO 77 STEP ScanDistance
absi = ABS(i)
absj = ABS(j)
'IF TotalConcentration(absi, absj) > .5 * ((ConcentrationMax + ConcentrationMin) / 2) THEN LINE (i + 77, j + 77)-(i + 77, j + 77), 2 ELSE LINE (i + 77, j +
77)-(i + 77, j + 77), 4
CIRCLE (177, 177), 77, 3
IF TotalConcentration(absi, absj) > .95 * (ConcentrationMax) THEN LINE (i + 177, j + 177)-(i + 177, j + 177), 2 ELSE LINE (i + 177, j + 177)-(i + 177, j +
177), 4
'LINE (absi, TotalConcentration(absi, absj))-(absi + ScanDistance, TotalConcentration(absi, absj)), 2
      NEXT
NEXT
END
```

C. Modelling porous burner using PBM

C.1 Governing equations

The governing equations for mass, species, and energy conservation are described next. In these equations, ρ is the gas density, u is the gas velocity, ϕ is the porosity of the solid (ϕ=1 in the gas region), Y_k , V_k , W_k and ω_k are the mass fraction, diffusive velocity, molecular weight, and the production rate of the k^{th} species, respectively. It should be mentioned here that the porous matrix in this study is inert and does not contribute chemically to the combustion process. Hence, the governing equations presented below are not including the surface reaction terms. A comprehensive description of the governing equations, including the terms for surface chemistry can be found in Shardlow [133].

C.1.1 Mass continuity equation

$$m'' = \rho u \phi \tag{7.1}$$

where m'' , is the mass flow rate per unit area.

C.1.2 Gas species conservation equation

$$\rho u \phi \frac{dY_k}{dx} + \frac{d}{dx}\left(\rho u Y_k V_k\right) = \omega_k \; W_k \phi \ldots k = 1, kk \tag{7.2}$$

where kk, is the total number of gaseous species.

C.1.3 Gas-phase energy equation

$$\rho u \phi c_{pg} \frac{dT_g}{dx} - \frac{d}{dx}\left(k_{g,e} \frac{dT_g}{dx}\right) + \sum_{k=1}^{kk} \rho \phi Y_k V_k c_{pg} \frac{dT_g}{dx} + h_v (T_g - T_s) = -\sum_{k=1}^{kk} \omega_k \; h_k W_k \phi \tag{7.3}$$

where c_{pg} is the specific heat of the k^{th} gaseous species, T_g , T_s are the gas and solid temperatures, respectively, h_v is the volumetric heat transfer coefficient, h_k is the

enthalpy of the k^{th} species and $k_{g,e}$ is the effective thermal conductivity of the gas ($\approx \phi k_g$).

The production rate term (ω_k) is calculated using the kinetic mechanism that describes the chemistry of the fuel. A general form for representing the chemistry of kk^{th} chemical species is:

$$\sum_{k=1}^{kk} \upsilon_{ki}^{'} \Lambda_k \Leftrightarrow \sum_{k=1}^{kk} \upsilon_{ki}^{''} \Lambda_k \cdots (i = 1,..., I) \qquad 7.4$$

where ν_{ki} are the stoichiometric coefficients, 'I' is the total number of reactions, and Λ_k is the chemical symbol of the k^{th} species. The superscripts ` and `` refer to the forward and backward stoichiometric coefficients, respectively. Accordingly, the term for the production rate for the set of chemical reactions described by Equation 7.4, is given as:

$$\omega_k = \sum_{i=1}^{I} \upsilon_{ki} \left[k_{fi} \prod_{k=1}^{kk} [X_k]^{\upsilon_{ki}^{'}} - k_{bi} \prod_{k=1}^{kk} [X_k]^{\upsilon_{ki}^{''}} \right] \cdots (k = 1,..., kk) \qquad 7.5$$

where X_k is the molar concentration of the k^{th} species, and k_{fi} , k_{bi} are the forward and backward rate constants of the i^{th} species, respectively. The forward rate constant, k_f is calculated using the Arrhenius temperature dependence formula:

$$k_{fi} = A_i T^{\beta_i} \exp\left(\frac{-E_i}{RT} \right). \qquad 7.6$$

In Equation 7.6 the pre-exponential factor A_i, the temperature exponent β_i, and the activation energy E_i, are specified by the kinetic mechanism. The backward rate constant k_{bi}, is calculated indirectly from the equilibrium rate constant k_{ei}:

$$k_{bi} = \frac{k_{fi}}{k_{ei}}, \qquad 7.7$$

where the equilibrium constants k_{ei} is given by:

$$\ln(k_{ei}) = \sum_{i=1}^{I} (\upsilon_{ki}^{'} - \upsilon_{ki}^{''}) \Delta G^{*}_{ki} - (\upsilon_{ki}^{'} - \upsilon_{ki}^{''}) \ln(\frac{P}{RT}) \qquad 7.8$$

The Gibbs free energy ΔG_{ki}^{*} (normalised by RT, R being the universal gas constant) is calculated from the changes in the system's normalised enthalpy ΔH_{ki}^{*} and entropy ΔS_{ki}^{*}. These terms are correlated in the relationship:

$$\Delta G^{*}_{ki} = \Delta H^{*}_{ki} - T\Delta S^{*}_{ki} \qquad 7.9$$

The normalised enthalpy and entropy terms are calculated using the polynomial formulation:

$$\Delta H^{*}_{ki} = \sum_{n=1}^{N} \frac{a_{nk} T_k^{(n-1)}}{n} + \frac{a_{N+1,k}}{T_k} \qquad 7.10$$

$$\Delta S^{*}_{ki} = \sum_{n=2}^{N} \frac{a_{nk} T_k^{(n-1)}}{(n-1)} + a_{1k} \ln(T_k) + a_{N+2,k} \qquad 7.11$$

where the polynomial coefficients, a_n, are obtainable from a number of databases [171-173].

C.1.4 Solid-phase energy equation

$$\frac{d}{dx}\left[k_{e,s} \frac{dT_s}{dx} \right] + h_v (T_g - T_s) = \frac{dq_r}{dx} \qquad 7.12$$

The terms in Equation 7.12 represent conduction, convection and radiation heat transfer, respectively. An empirical correlation has been used to determine the convective heat transfer coefficient h_v, for the porous medium.

C.1.5 Heat convection coefficient

As the characteristic pore size or particle diameter is typically in the order of millimetres and the gas velocity for combustion is restricted within a range limited by the flame velocity, it turns out that for most porous burners, the Reynolds number of the flow is well within the laminar region. The Nusselt number within the various porous solids will be different and very low as well. In the current model of the packed bed, the Nusselt number has been estimated using the following correlation:

$$Nu_d = 0.012\,\mathrm{Re}^{1.6}\,\mathrm{Pr}^{1/3} \qquad 7.13$$

where the Nu_d and *Re* are the Nusselt number based on the average particle diameter of the packed bed and *Re* and *Pr* are the Reynolds and the Prandtl numbers.

C.2 Radiation model

A two-flux radiation model, also known as the Schuster-Schwarzchild approximation has been used to calculate the net radiative flux q_r, in equation 7.12. The model is valid for radiative transfer in absorbing, emitting and scattering media. The main limiting assumption of the model is that the medium properties are such as to yield homogenous absorbing, emitting and scattering of electromagnetic radiation in a forward scattering hemisphere and in a backward scattering hemisphere, separately.

The net radiative flux q_r, is then calculated as the difference between the forward radiation flux q^+, and the backward radiation flux q^-, ($q_r = q^+ - q^-$). These radiative transfer fluxes are obtained by solving the following equations:

$$\frac{dq^+}{dx} = -2\sigma_e q^+ + 2\sigma_e\omega_0(fq^+ + bq^-) + 2\sigma_e(1-\omega_0)\sigma T_s^4 \qquad 7.14$$

and,

$$-\frac{dq^-}{dx} = -2\sigma_e q^- + 2\sigma_e\omega_0(fq^- + bq^+) + 2\sigma_e(1-\omega_0)\sigma T_s^4 \qquad 7.15$$

Here ω_0 is the single scattering albedo, which represents the fraction of attenuated energy that is the result of scattering. For a non-scattering medium $\omega_0=0$, while for pure scattering $\omega_0 = 1$, σ_e is the extinction coefficient that represents the fraction of attenuated energy that is the result of absorption and scattering, and *f* & *b* are the forward- and backward-radiation scattering fractions, respectively and σ is the Stefan-Boltzmann constant.

C.3 Boundary conditions

The boundary conditions required for solving the governing equations consist of user specified inlet conditions and a set of conditions dictated from energy balance considerations. At the inlet ($x=x_{in}$) the gas temperature and the mass fraction of the reactants are known quantities: $T_g=T_{g,in}$, $Y_k=Y_{k,in}$. The boundary condition at the

upstream surface of the first porous layer $x=x_0$, is established from the energy balance equation:

$$-(1-\phi)k_s \frac{dT_s}{dx}|_{x=x_0} = (1-\phi)h_0(T_g - T_s) - [q^-(x_0) - q^+(x_0)] \quad 7.16$$

where h_0, is the convective heat transfer coefficient per unit area and k_s, is the thermal conductivity of the solid. The radiative heat transfer components are calculated using:

$$q^+(x_0) = \varepsilon\sigma T_-^4 + \chi_0 q^-(x_0) \quad 7.17$$

where T_- is the upstream temperature of the environment to which the upstream boundary of the porous medium is exposed, i.e. the burner housing. χ_0, is the reflectivity of the porous medium, and ε, is the average emissivity of the burner surface. $q^-(x_0)$ in Equation 7.17 is the backward radiation fraction at x_0.

The boundary condition at the downstream surface of the burner ($x=x_{L1}$):

$$q^-(x_{L1}) = \varepsilon\sigma T_+^4 + \chi_0 q^+(x_{L1}) \quad 7.18$$

and

$$q^-(x_{L2}) = \varepsilon\sigma T_+^4 + \chi_0 q^+(x_{L2}) \quad 7.19$$

T_+ being the downstream temperature of the environment to which the downstream boundary of the porous medium is exposed i.e. the ambient temperature.

At the outlet $x=x_{out}$, the boundary conditions are:

$dT_g/dx = 0$ and $dY_k/dx = 0$. These conditions imply that the process is adiabatic and the chemical reactions are completed.

C.4 Numerical solver

The method for solving Equations 7.1 to 7.19 is to discretise the conservation equations establishing a set of simultaneous algebraic equations that are applied on discrete mesh points within a predetermined computational domain. The core solver is based on Sandia's PREMIX module [132], and makes use of the well-known CHEMKIN

package [132, 146-148]. It uses a combined time-dependent and steady state method. That is, a modified damped Newton method is initially used to solve the non-linear algebraic equations by an iterative process. If the Newton method fails to achieve the required level of convergence, then a time-stepping algorithm is used. The idea is to determine the steady-state solution by solving the transient equations. For each of the conservation equations (mass, species, etc.), an additional time-dependent component is added. For example, an extra term dY_k/dt is added in the left-hand side of Equation 7.2. The combination of Newton and time-stepping methods utilises the advantage of the rapid convergence of Newton's method, and the robustness of the time-stepping algorithm for handling the stiffness problem.

An adaptive meshing placement is a powerful tool to alleviate convergence difficulties and reduce the user intervention in influencing the convergence of the solution. The iterative process commences with a coarse mesh, which is easy to converge and provides an improved guess over that specified by the user. The refinement of the mesh is then done automatically, allowing more mesh points to be inserted in regions with high gradients and/or curvatures in the concentration profiles. The gradient (GRAD) and curvature (CURV) parameters have a strong effect on the convergence rate (but not on the solution's accuracy). The parameter GRAD determines the number of additional mesh point to be inserted in regions with high gradients of concentrations, while CURV controls the number of additional points to be added in regions with high curvature in the concentration profiles. Lower numbers for GRAD and CURV mean more mesh points will be inserted each time the adaptive mesh routine is called. The default values for GRAD and CURV are 0.1 and 0.5, respectively. However, it has been found that in some cases a GRAD value of 0.1 could be too restrictive for achieving a fully converged solution. This is especially true near a flame front where sharp changes in the radicals' concentration create large gradients and curvatures in the concentration profiles of radical species. Furthermore, inserting more mesh points does not necessarily improve the accuracy of the solution, but it definitely demands more computing resources. Since the Newton algorithm is more likely to converge on a coarse mesh, the strategy used was to start the computations with a coarse grid and relax the GRAD parameter, to say 0.8. Once a solution has been achieved, the value of GRAD is then reduced and the computations are repeated, restarting from the previously converged solution. This

cycle is continued until the required accuracy is achieved. Typically, GRAD and CURV values of 0.3 and 0.5, respectively, have been used.

Convergence of the solution is achieved when the residuals of the discretised conservation equations for mass and energy are reduced to a pre-selected tolerance and when the mesh is sufficiently refined to meet specified gradient and curvature criteria of the solution profiles. Details of the numerical schemes, the adaptive mesh algorithm and convergence criteria can be found in Refs [132, 146-148].

D. Appendix C: Modified GRI-Mech 3.0 Chemical Kinetic Mechanism Used in Surface Reaction Calculations

```
! GRI-Mech Version 3.0 3/12/99  CHEMKIN-II format
! See README30 file at anonymous FTP site unix.sri.com, directory gri;
! WorldWideWeb home page http://www.me.berkeley.edu/gri_mech/ or
! through http://www.gri.org , under 'Basic  Research',
! for additional information, contacts, and disclaimer
ELEMENTS
O  H  C  N  AR
END
SPECIES
H2     H      O      O2     OH     H2O    HO2    H2O2
C      CH     CH2    CH2(S) CH3    CH4    CO     CO2
HCO    CH2O   CH2OH  CH3O   CH3OH  C2H    C2H2   C2H3
C2H4   C2H5   C2H6   HCCO   CH2CO  HCCOH  N      NH
NH2    NH3    NNH    NO     NO2    N2O    HNO    CN
HCN    H2CN   HCNN   HCNO   HOCN   HNCO   NCO    N2
AR     C3H7   C3H8   CH2CHO CH3CHO H_W    O_W    OH_W
CH3_W  CH3O_W
END
THERMO ALL
300.000  1000.000  5000.000
O               L 1/90O   1   00   00   00G   200.000  3500.000  1000.000    1
2.56942078E+00-8.59741137E-05 4.19484589E-08-1.00177799E-11 1.22833691E-15    2
2.92175791E+04 4.78433864E+00 3.16826710E+00-3.27931884E-03 6.64306396E-06    3
-6.12806624E-09 2.11265971E-12 2.91222592E+04 2.05193346E+00                  4
O_W             L 1/90O   1   00   00   00G   200.000  3500.000  1000.000    1
2.56942078E+00-8.59741137E-05 4.19484589E-08-1.00177799E-11 1.22833691E-15    2
2.92175791E+04 4.78433864E+00 3.16826710E+00-3.27931884E-03 6.64306396E-06    3
-6.12806624E-09 2.11265971E-12 2.91222592E+04 2.05193346E+00                  4
O2              TPIS89O   2   00   00   00G   200.000  3500.000  1000.000    1
3.28253784E+00 1.48308754E-03-7.57966669E-07 2.09470555E-10-2.16717794E-14    2
-1.08845772E+03 5.45323129E+00 3.78245636E+00-2.99673416E-03 9.84730201E-06    3
-9.68129509E-09 3.24372837E-12-1.06394356E+03 3.65767573E+00                  4
H               L 7/88H   1   00   00   00G   200.000  3500.000  1000.000    1
2.50000001E+00-2.30842973E-11 1.61561948E-14-4.73515235E-18 4.98197357E-22    2
2.54736599E+04-4.46682914E-01 2.50000000E+00 7.05332819E-13-1.99591964E-15    3
2.30081632E-18-9.27732332E-22 2.54736599E+04-4.46682853E-01                   4
H_W             L 7/88H   1   00   00   00G   200.000  3500.000  1000.000    1
2.50000001E+00-2.30842973E-11 1.61561948E-14-4.73515235E-18 4.98197357E-22    2
                2.54736599E+04-4.46682914E-01 2.50000000E+00 7.05332819E-13-1.99591964E-15    3
                2.30081632E-18-9.27732332E-22 2.54736599E+04-4.46682853E-01                   4
H2              TPIS78H   2   00   00   00G   200.000  3500.000  1000.000    1
                3.33727920E+00-4.94024731E-05 4.99456778E-07-1.79566394E-10 2.00255376E-14    2
-9.50158922E+02-3.20502331E+00 2.34433112E+00 7.98052075E-03-1.94781510E-05    3
                2.01572094E-08-7.37611761E-12-9.17935173E+02 6.83010238E-01                   4
OH              RUS 78O   1H   1   00   00G   200.000  3500.000  1000.000    1
                3.09288767E+00 5.48429716E-04 1.26505228E-07-8.79461556E-11 1.17412376E-14    2
                3.85865700E+03 4.47669610E+00 3.99201543E+00-2.40131752E-03 4.61793841E-06    3
-3.88113333E-09 1.36411470E-12 3.61508056E+03-1.03925458E-01                   4
OH_W            RUS 78O   1H   1   00   00G   200.000  3500.000  1000.000    1
                3.09288767E+00 5.48429716E-04 1.26505228E-07-8.79461556E-11 1.17412376E-14    2
                3.85865700E+03 4.47669610E+00 3.99201543E+00-2.40131752E-03 4.61793841E-06    3
-3.88113333E-09 1.36411470E-12 3.61508056E+03-1.03925458E-01                   4
H2O             L 8/89H   2O   1   00   00G   200.000  3500.000  1000.000    1
                3.03399249E+00 2.17691804E-03-1.64072518E-07-9.70419870E-11 1.68200992E-14    2
-3.00042971E+04 4.96677010E+00 4.19864056E+00-2.03643410E-03 6.52040211E-06    3
-5.48797062E-09 1.77197817E-12-3.02937267E+04-8.49032208E-01                   4
HO2             L 5/89H   1O   2   00   00G   200.000  3500.000  1000.000    1
                4.01721090E+00 2.23982013E-03-6.33658150E-07 1.14246370E-10-1.07908535E-14    2
                1.11856713E+02 3.78510215E+00 4.30179801E+00-4.74912051E-03 2.11582891E-05    3
-2.42763894E-08 9.29225124E-12 2.94808040E+02 3.71666245E+00                   4
HO2_W           L 5/89H   1O   2   00   00G   200.000  3500.000  1000.000    1
                4.01721090E+00 2.23982013E-03-6.33658150E-07 1.14246370E-10-1.07908535E-14    2
                1.11856713E+02 3.78510215E+00 4.30179801E+00-4.74912051E-03 2.11582891E-05    3
-2.42763894E-08 9.29225124E-12 2.94808040E+02 3.71666245E+00                   4
H2O2            L 7/88H   2O   2   00   00G   200.000  3500.000  1000.000    1
                4.16500285E+00 4.90831694E-03-1.90139225E-06 3.71185986E-10-2.87908305E-14    2
-1.78617877E+04 2.91615662E+00 4.27611269E+00-5.42822417E-04 1.67335701E-05    3
-2.15770813E-08 8.62454363E-12-1.77025821E+04 3.43505074E+00                   4
C               L11/88C   1   00   00   00G   200.000  3500.000  1000.000    1
                2.49266888E+00 4.79889284E-05-7.24335020E-08 3.74291029E-11-4.87277893E-15    2
                8.54512953E+04 4.80150373E+00 2.55423955E+00-3.21537724E-04 7.33792245E-07    3
-7.32234889E-10 2.66521446E-13 8.54438832E+04 4.53130848E+00                   4
CH              TPIS79C   1H   1   00   00G   200.000  3500.000  1000.000    1
```

```
              2.87846473E+00 9.70913681E-04 1.44445655E-07-1.30687849E-10 1.76079383E-14    2
              7.10124364E+04 5.48497999E+00 3.48981665E+00 3.23835541E-04-1.68899065E-06    3
              3.16217327E-09-1.40609067E-12 7.07972934E+04 2.08401108E+00                   4
CH2           L S/93C   1H   2   00   00G   200.000  3500.000  1000.000    1
              2.87410113E+00 3.65639292E-03-1.40894597E-06 2.60179549E-10-1.87727567E-14    2
              4.62636040E+04 6.17119324E+00 3.76267867E+00 9.68872143E-04 2.79489841E-06    3
-3.85091153E-09 1.68741719E-12 4.60040401E+04 1.56253185E+00                   4
CH2(S)        L S/93C   1H   2   00   00G   200.000  3500.000  1000.000    1
              2.29203842E+00 4.65588637E-03-2.01191947E-06 4.17906000E-10-3.39716365E-14    2
              5.09259997E+04 8.62650169E+00 4.19860411E+00-2.36661419E-03 8.23296220E-06    3
-6.68815981E-09 1.94314737E-12 5.04968163E+04-7.69118967E-01                   4
CH3           L11/89C   1H   3   00   00G   200.000  3500.000  1000.000    1
              2.28571772E+00 7.23990037E-03-2.98714348E-06 5.95684644E-10-4.67154394E-14    2
              1.67755843E+04 8.48007179E+00 3.67359040E+00 2.01095175E-03 5.73021856E-06    3
-6.87117425E-09 2.54385734E-12 1.64449988E+04 1.60456433E+00                   4
CH3_W         L11/89C   1H   3   00   00G   200.000  3500.000  1000.000    1
              2.28571772E+00 7.23990037E-03-2.98714348E-06 5.95684644E-10-4.67154394E-14    2
              1.67755843E+04 8.48007179E+00 3.67359040E+00 2.01095175E-03 5.73021856E-06    3
-6.87117425E-09 2.54385734E-12 1.64449988E+04 1.60456433E+00                   4
CH4           L 8/88C   1H   4   00   00G   200.000  3500.000  1000.000    1
              7.48514950E-02 1.33909467E-02-5.73285809E-06 1.22292535E-09-1.01815230E-13    2
-9.46834459E+03 1.84373180E+01 5.14987613E+00-1.36709788E-02 4.91800599E-05    3
-4.84743026E-08 1.66693956E-11-1.02466476E+04-4.64130376E+00                   4
CO            TPIS79C   1O   1   00   00G   200.000  3500.000  1000.000    1
              2.71518561E+00 2.06252743E-03-9.98825771E-07 2.30053008E-10-2.03647716E-14    2
-1.41518724E+04 7.81868772E+00 3.57953347E+00-6.10353680E-04 1.01681433E-06    3
              9.07005884E-10-9.04424499E-13-1.43440860E+04 3.50840928E+00                   4
CO2           L 7/88C   1O   2   00   00G   200.000  3500.000  1000.000    1
              3.85746029E+00 4.41437026E-03-2.21481404E-06 5.23490188E-10-4.72084164E-14    2
-4.87591660E+04 2.27163806E+00 2.35677352E+00 8.98459677E-03-7.12356269E-06    3
              2.45919022E-09-1.43699548E-13-4.83719697E+04 9.90105222E+00                   4
HCO          L12/89H   1C   1O   1   00G   200.000  3500.000  1000.000    1
              2.77217438E+00 4.95695526E-03-2.48445613E-06 5.89161778E-10-5.33508711E-14    2
              4.01191815E+03 9.79834492E+00 4.22118584E+00-3.24392532E-03 1.37799446E-05    3
-1.33144093E-08 4.33768865E-12 3.83956496E+03 3.39437243E+00                   4
CH2O          L 8/88H   2C   1O   1   00G   200.000  3500.000  1000.000    1
              1.76069008E+00 9.20000082E-03-4.42258813E-06 1.00641212E-09-8.83855640E-14    2
-1.39958323E+04 1.36563230E+01 4.79372315E+00-9.90833369E-03 3.73220008E-05    3
-3.79285261E-08 1.31772652E-11-1.43089567E+04 6.02812900E-01                   4
CH2OH          GUNL93C   1H   3O   1   00G   200.000  3500.000  1000.000    1
              3.69266569E+00 8.64576797E-03-3.75101120E-06 7.87234636E-10-6.48554201E-14    2
-3.24250627E+03 5.81043215E+00 3.86388918E+00 5.59672304E-03 5.93271791E-06    3
-1.04532012E-08 4.36967278E-12-3.19391367E+03 5.47302243E+00                   4
CH3O           121686C   1H   3O   1    G 0300.00   3000.00   1000.000    1
              0.03770799E+02 0.07871497E-01-0.02656384E-04 0.03944431E-08-0.02112616E-12    2
              0.12783252E+03 0.02929575E+02 0.02106204E+02 0.07216595E-01 0.05338472E-04    3
-0.07377636E-07 0.02075610E-10 0.09786011E+04 0.13152177E+02                   4
CH3O_W         121686C   1H   3O   1    G 0300.00   3000.00   1000.000    1
              0.03770799E+02 0.07871497E-01-0.02656384E-04 0.03944431E-08-0.02112616E-12    2
              0.12783252E+03 0.02929575E+02 0.02106204E+02 0.07216595E-01 0.05338472E-04    3
-0.07377636E-07 0.02075610E-10 0.09786011E+04 0.13152177E+02                   4
CH3OH          L 8/88C   1H   4O   1   00G   200.000  3500.000  1000.000    1
              1.78970791E+00 1.40938292E-02-6.36500835E-06 1.38171085E-09-1.17060220E-13    2
-2.53748747E+04 1.45023623E+01 5.71539582E+00-1.52309129E-02 6.52441155E-05    3
-7.10806889E-08 2.61352698E-11-2.56427656E+04-1.50409823E+00                   4
C2H           L 1/91C   2H   1   00   00G   200.000  3500.000  1000.000    1
              3.16780652E+00 4.75221902E-03-1.83787077E-06 3.04190252E-10-1.77232770E-14    2
              6.71210650E+04 6.63589475E+00 2.88965733E+00 1.34099611E-02-2.84769501E-05    3
              2.94791045E-08-1.09331511E-11 6.68393932E+04 6.22296438E+00                   4
C2H2          L 1/91C   2H   2   00   00G   200.000  3500.000  1000.000    1
              4.14756964E+00 5.96166664E-03-2.37294852E-06 4.67412171E-10-3.61235213E-14    2
              2.59359992E+04-1.23028121E+00 8.08681094E-01 2.33615629E-02-3.55171815E-05    3
              2.80152437E-08-8.50072974E-12 2.64289807E+04 1.39397051E+01                   4
C2H3          L 2/92C   2H   3   00   00G   200.000  3500.000  1000.000    1
              3.01672400E+00 1.03302292E-02-4.68082349E-06 1.01763288E-09-8.62607041E-14    2
              3.46128739E+04 7.78732378E+00 3.21246645E+00 1.51479162E-03 2.59209412E-05    3
-3.57657847E-08 1.47150873E-11 3.48598468E+04 8.51054025E+00                   4
C2H4          L 1/91C   2H   4   00   00G   200.000  3500.000  1000.000    1
              2.03611116E+00 1.46454151E-02-6.71077915E-06 1.47222923E-09-1.25706061E-13    2
              4.93988614E+03 1.03053693E+01 3.95920148E+00-7.57052247E-03 5.70990292E-05    3
-6.91588753E-08 2.69884373E-11 5.08977593E+03 4.09733096E+00                   4
C2H5          L12/92C   2H   5   00   00G   200.000  3500.000  1000.000    1
              1.95465642E+00 1.73972722E-02-7.98206668E-06 1.75217689E-09-1.49641576E-13    2
              1.28575200E+04 1.34624343E+01 4.30646568E+00-4.18658892E-03 4.97142807E-05    3
-5.99126606E-08 2.30509004E-11 1.28416265E+04 4.70720924E+00                   4
C2H6          L 8/88C   2H   6   00   00G   200.000  3500.000  1000.000    1
              1.07188150E+00 2.16852677E-02-1.00256067E-05 2.21412001E-09-1.90002890E-13    2
-1.14263932E+04 1.51156107E+01 4.29142492E+00-5.50154270E-03 5.99438288E-05    3
-7.08466285E-08 2.68685771E-11-1.15222055E+04 2.66682316E+00                   4
CH2CO         L 5/90C   2H   2O   1   00G   200.000  3500.000  1000.000    1
              4.51129732E+00 9.00359745E-03-4.16939635E-06 9.23345882E-10-7.94838201E-14    2
-7.55105311E+03 6.32247205E-01 2.13583630E+00 1.81188721E-02-1.73947474E-05    3
              9.34397568E-09-2.01457615E-12-7.04291804E+03 1.22156480E+01                   4
HCCO          SRIC91H   1C   2O   1    G 0300.00   4000.00   1000.000    1
              0.56282058E+01 0.40853401E-02-0.15934547E-05 0.28626052E-09-0.19407832E-13    2
              0.19327215E+05-0.39302595E+01 0.22517214E+01 0.17655021E-01-0.23729101E-04    3
              0.17275759E-07-0.50664811E-11 0.20059449E+05 0.12490417E+02                   4
```

```
HCCOH            SRI91C  2O  1H  20  0G  300.000 5000.000 1000.000    1
              0.59238291E+01 0.67923600E-02-0.25658564E-05 0.44987841E-09-0.29940101E-13    2
              0.72646260E+04-0.76017742E+01 0.12423733E+01 0.31072201E-01-0.50866864E-04    3
              0.43137131E-07-0.14014594E-10 0.80316143E+04 0.13874319E+02                   4
H2CN             41687H  2C  1N  1    G 0300.00  4000.000 1000.000    1
              0.52097030E+01 0.29692911E-02-0.28555891E-06-0.16355500E-09 0.30432589E-13    2
              0.27677109E+05-0.44444780E+01 0.28516610E+01 0.56952331E-02 0.10711400E-05    3
-0.16226120E-08-0.23511081E-12 0.28637820E+05 0.89927511E+01                   4
HCN              GRI/98H  1C  1N  1   0G  200.000 6000.000 1000.000    1
              0.38022392E+01 0.31464228E-02-0.10632185E-05 0.16619757E-09-0.97997570E-14    2
              0.14407292E+05 0.15754601E+01 0.22589886E+01 0.10051170E-01-0.13351763E-04    3
              0.10092349E-07-0.30089028E-11 0.14712633E+05 0.89164419E+01                   4
HNO              And93 H  1N  1O  1   0G  200.000 6000.000 1000.000    1
              0.29792509E+01 0.34944059E-02-0.78549778E-06 0.57479594E-10-0.19335916E-15    2
              0.11750582E+05 0.86063728E+01 0.45334916E+01-0.56696171E-02 0.18473207E-04    3
-0.17137094E-07 0.55454573E-11 0.11548297E+05 0.17498417E+01                   4
N              L 6/88N  1   0   0   0G  200.000 6000.000 1000.000    1
              0.24159429E+01 0.17489065E-03-0.11902369E-06 0.30226245E-10-0.20360982E-14    2
              0.56133773E+05 0.46496096E+01 0.25000000E+01 0.00000000E+00 0.00000000E+00    3
              0.00000000E+00 0.00000000E+00 0.56104637E+05 0.41939087E+01                   4
NNH              T07/93N  2H  1  00  00G  200.000 6000.000 1000.000    1
              0.37667544E+01 0.28915082E-02-0.10416620E-05 0.16842594E-09-0.10091896E-13    2
              0.28650697E+05 0.44705067E+01 0.43446927E+01-0.48497072E-02 0.20059459E-04    3
-0.21726464E-07 0.79469539E-11 0.28791973E+05 0.29779410E+01                   4
N2O              L 7/88N  2O  1   0   0G  200.000 6000.000 1000.000    1
              0.48230729E+01 0.26270251E-02-0.95850874E-06 0.16000712E-09-0.97752303E-14    2
              0.80734048E+04-0.22017207E+01 0.22571502E+01 0.11304728E-01-0.13671319E-04    3
              0.96819806E-08-0.29307182E-11 0.87417744E+04 0.10757992E+02                   4
NH               And94 N  1H  1   0   0G  200.000 6000.000 1000.000    1
              0.27836928E+01 0.13298430E-02-0.42478047E-06 0.78348501E-10-0.55044470E-14    2
              0.42120848E+05 0.57407799E+01 0.34929085E+01 0.31179198E-03-0.14890484E-05    3
              0.24816442E-08-0.10356967E-11 0.41880629E+05 0.18483278E+01                   4
NH2              And89 N  1H  2   0   0G  200.000 6000.000 1000.000    1
              0.28347421E+01 0.32073082E-02-0.93390804E-06 0.13702953E-09-0.79206144E-14    2
              0.22171957E+05 0.65204163E+01 0.42040029E+01-0.21061385E-02 0.71068348E-05    3
-0.56115197E-08 0.16440717E-11 0.21885910E+05-0.14184248E+00                   4
NH3              J 6/77N  1H  3   0   0G  200.000 6000.000 1000.000    1
              0.26344521E+01 0.56662560E-02-0.17278676E-05 0.23867161E-09-0.12578786E-13    2
-0.65446958E+04 0.65662928E+01 0.42860274E+01-0.46605230E-02 0.21718513E-04    3
-0.22808887E-07 0.82638046E-11-0.67417285E+04-0.62537277E+00                   4
NO               RUS 78N  1O  1   0   0G  200.000 6000.000 1000.000    1
              0.32606056E+01 0.11911043E-02-0.42917048E-06 0.69457669E-10-0.40336099E-14    2
              0.99209746E+04 0.63693027E+01 0.42184763E+01-0.46389760E-02 0.11041022E-04    3
-0.93361354E-08 0.28035770E-11 0.98446230E+04 0.22808464E+01                   4
NO2              L 7/88N  1O  2   0   0G  200.000 6000.000 1000.000    1
              0.48847542E+01 0.21723956E-02-0.82806906E-06 0.15747510E-09-0.10510895E-13    2
              0.23164983E+04-0.11741695E+00 0.39440312E+01-0.15854290E-02 0.16657812E-04    3
-0.20475426E-07 0.78350564E-11 0.28966179E+04 0.63119917E+01                   4
HCNO             BDEA94H  1N  1C  1O  1G  300.000 5000.000 1382.000    1
              6.59860456E+00 3.02778626E-03-1.07704346E-06 1.71666528E-10-1.01439391E-14    2
              1.79661339E+04-1.03306599E+01 2.64727989E+00 1.27505342E-02-1.04794236E-05    3
              4.41432836E-09-7.57521466E-13 1.92990252E+04 1.07332972E+01                   4
HOCN             BDEA94H  1N  1C  1O  1G  300.000 5000.000 1368.000    1
              5.89784885E+00 3.16789393E-03-1.11801064E-06 1.77243144E-10-1.04339177E-14    2
-3.70653331E+03-6.18167825E+00 3.78604952E+00 6.88667922E-03-3.21487864E-06    3
              5.17195767E-10 1.19360788E-14-2.82698400E+03 5.63292162E+00                   4
HNCO             BDEA94H  1N  1C  1O  1G  300.000 5000.000 1478.000    1
              6.22395134E+00 3.17864004E-03-1.09378755E-06 1.70735163E-10-9.95021955E-15    2
-1.66599344E+04-8.38224741E+00 3.63096317E+00 7.30282357E-03-2.28050003E-06    3
-6.61271298E-10 3.62235752E-13-1.55873636E+04 6.19457727E+00                   4
NCO              EA 93 N  1C  1O  1   0G  200.000 6000.000 1000.000    1
              0.51521845E+01 0.23051761E-02-0.88033153E-06 0.14789098E-09-0.90977996E-14    2
              0.14004123E+05-0.25442660E+01 0.28269308E+01 0.88051688E-02-0.83866134E-05    3
              0.48016964E-08-0.13313595E-11 0.14682477E+05 0.95504646E+01                   4
CN               HBH92 C  1N  1   0   0G  200.000 6000.000 1000.000    1
              0.37459805E+01 0.43450775E-04 0.29705984E-06-0.68651806E-10 0.44134173E-14    2
              0.51536188E+05 0.27867601E+01 0.36129351E+01-0.95551327E-03 0.21442977E-05    3
-0.31516323E-09-0.46430356E-12 0.51708340E+05 0.39804995E+01                   4
HCNN             SRI/94C  1N  2H  10  0G  300.000 5000.000 1000.000    1
              0.58946362E+01 0.39895959E-02-0.15982380E-05 0.29249395E-09-0.20094686E-13    2
              0.53452941E+05-0.51030502E+01 0.25243194E+01 0.15960619E-01-0.18816354E-04    3
              0.12125540E-07-0.32357378E-11 0.54261984E+05 0.11675870E+02                   4
N2              121286N  2            G  300.000 5000.000 1000.000    1
              0.02926640E+02 0.14879768E-02-0.05684760E-05 0.10097038E-09-0.06753351E-13    2
-0.09227977E+04 0.05980528E+02 0.03298677E+02 0.14082404E-02-0.03963222E-04    3
0.05641515E-07-0.02444854E-10-0.10208999E+04 0.03950372E+02                   4
AR               120186AR 1            G  300.000 5000.000 1000.000    1
              0.02500000E+02 0.00000000E+00 0.00000000E+00 0.00000000E+00 0.00000000E+00    2
-0.07453750E+04 0.04366000E+02 0.02500000E+02 0.00000000E+00 0.00000000E+00    3
              0.00000000E+00 0.00000000E+00-0.07453750E+04 0.04366000E+02                   4
C3H8             L 4/85C  3H  8   0   0G  300.000 5000.000 1000.00     1
              0.75341368E+01 0.18872239E-01-0.62718491E-05 0.91475649E-09-0.47838069E-13    2
-0.16467516E+05-0.17892349E+02 0.93355381E+00 0.26424579E-01 0.61059727E-05    3
-0.21977499E-07 0.95149253E-11-0.13958520E+05 0.19201691E+02                   4
C3H7             L 9/84C  3H  7   0   0G  300.000 5000.000 1000.00     1
              0.77026987E+01 0.16044203E-01-0.52833220E-05 0.76298590E-09-0.39392284E-13    2
              0.82984336E+04-0.15480180E+02 0.10515518E+01 0.25991980E-01 0.23800540E-05    3
```

```
-0.19609569E-07 0.93732470E-11 0.10631863E+05 0.21122559E+02                4
CH3CHO          L 8/88C   2H   4O   1    0G   200.000  6000.000  1000.00     1
                0.54041108E+01 0.11723059E-01-0.42263137E-05 0.68372451E-09-0.40984863E-13    2
-0.22593122E+05-0.34807917E+01 0.47294595E+01-0.31932858E-02 0.47534921E-04    3
-0.57458611E-07 0.21931112E-10-0.21572878E+05 0.41030159E+01                 4
CH2CHO          SAND86O   1H   3C   2    G   300.00   5000.00   1000.00     1
                0.05975670E+02 0.08130591E-01-0.02743624E-04 0.04070304E-08-0.02176017E-12    2
                0.04903218E+04-0.05045251E+02 0.03409062E+02 0.10738574E-01 0.01891492E-04    3
-0.07158583E-07 0.02867385E-10 0.15214766E+04 0.09558290E+02                 4
END
REACTIONS
2O+M<=>O2+M                                       1.200E+17  -1.000       .00
H2/ 2.40/ H2O/15.40/ CH4/ 2.00/ CO/ 1.75/ CO2/ 3.60/ C2H6/ 3.00/ AR/  .83/
O+H+M<=>OH+M                                      5.000E+17  -1.000       .00
H2/2.00/ H2O/6.00/ CH4/2.00/ CO/1.50/ CO2/2.00/ C2H6/3.00/ AR/ .70/
O+H2<=>H+OH                                       3.870E+04   2.700    6260.00
O+HO2<=>OH+O2                                     2.000E+13    .000       .00
O+H2O2<=>OH+HO2                                   9.630E+06   2.000    4000.00
O+CH<=>H+CO                                       5.700E+13    .000       .00
O+CH2<=>H+HCO                                     8.000E+13    .000       .00
O+CH2(S)<=>H2+CO                                  1.500E+13    .000       .00
O+CH2(S)<=>H+HCO                                  1.500E+13    .000       .00
O+CH3<=>H+CH2O                                    5.060E+13    .000       .00
O+CH4<=>OH+CH3                                    1.020E+09   1.500    8600.00
O+CO(+M)<=>CO2(+M)                                1.800E+10    .000    2385.00
                LOW/ 6.020E+14     .000    3000.00/
H2/2.00/ O2/6.00/ H2O/6.00/ CH4/2.00/ CO/1.50/ CO2/3.50/ C2H6/3.00/ AR/ .50/
O+HCO<=>OH+CO                                     3.000E+13    .000       .00
O+HCO<=>H+CO2                                     3.000E+13    .000       .00
O+CH2O<=>OH+HCO                                   3.900E+13    .000    3540.00
O+CH2OH<=>OH+CH2O                                             1.000E+13    .000       .00
O+CH3O<=>OH+CH2O                                  1.000E+13    .000       .00
O+CH3OH<=>OH+CH2OH                                            3.880E+05   2.500    3100.00
O+CH3OH<=>OH+CH3O                                             1.300E+05   2.500    5000.00
O+C2H<=>CH+CO                                     5.000E+13    .000       .00
O+C2H2<=>H+HCCO                                   1.350E+07   2.000    1900.00
O+C2H2<=>OH+C2H                                   4.600E+19  -1.410   28950.00
O+C2H2<=>CO+CH2                                   .940E+06   2.000    1900.00
O+C2H3<=>H+CH2CO                                  3.000E+13    .000       .00
O+C2H4<=>CH3+HCO                                  1.250E+07   1.830     220.00
O+C2H5<=>CH3+CH2O                                 2.240E+13    .000       .00
O+C2H6<=>OH+C2H5                                  8.980E+07   1.920    5690.00
O+HCCO<=>H+2CO                                    1.000E+14    .000       .00
O+CH2CO<=>OH+HCCO                                             1.000E+13    .000    8000.00
O+CH2CO<=>CH2+CO2                                 1.750E+12    .000    1350.00
O2+CO<=>O+CO2                                     2.500E+12    .000   47800.00
O2+CH2O<=>HO2+HCO                                 1.000E+14    .000   40000.00
H+O2+M<=>HO2+M                                    2.800E+18   -.860       .00
O2/ .00/ H2O/ .00/ CO/ .75/ CO2/1.50/ C2H6/1.50/ N2/ .00/ AR/ .00/
H+2O2<=>HO2+O2                                    2.080E+19  -1.240       .00
H+O2+H2O<=>HO2+H2O                                            11.26E+18   -.760       .00
H+O2+N2<=>HO2+N2                                  2.600E+19  -1.240       .00
H+O2+AR<=>HO2+AR                                  7.000E+17   -.800       .00
H+O2<=>O+OH                                       2.650E+16   -.6707  17041.00
2H+M<=>H2+M                                       1.000E+18  -1.000       .00
H2/ .00/ H2O/ .00/ CH4/2.00/ CO2/ .00/ C2H6/3.00/ AR/ .63/
2H+H2<=>2H2                                                   9.000E+16   -.600       .00
2H+H2O<=>H2+H2O                                   6.000E+19  -1.250       .00
2H+CO2<=>H2+CO2                                   5.500E+20  -2.000       .00
H+OH+M<=>H2O+M                                    2.200E+22  -2.000       .00
H2/ .73/ H2O/3.65/ CH4/2.00/ C2H6/3.00/ AR/ .38/
H+HO2<=>O+H2O                                     3.970E+12    .000     671.00
H+HO2<=>O2+H2                                     4.480E+13    .000    1068.00
H+HO2<=>2OH                                       0.840E+14    .000     635.00
H+H2O2<=>HO2+H2                                   1.210E+07   2.000    5200.00
H+H2O2<=>OH+H2O                                   1.000E+13    .000    3600.00
H+CH<=>C+H2                                                   1.650E+14    .000       .00
H+CH2(+M)<=>CH3(+M)                               6.000E+14    .000       .00
                LOW  /  1.040E+26   -2.760   1600.00/
                TROE/   .5620  91.00  5836.00  8552.00/
H2/2.00/ H2O/6.00/ CH4/2.00/ CO/1.50/ CO2/2.00/ C2H6/3.00/ AR/ .70/
H+CH2(S)<=>CH+H2                                  3.000E+13    .000       .00
H+CH3(+M)<=>CH4(+M)                               13.90E+15   -.534     536.00
                LOW  /  2.620E+33   -4.760   2440.00/
                TROE/   .7830   74.00  2941.00  6964.00 /
H2/2.00/ H2O/6.00/ CH4/3.00/ CO/1.50/ CO2/2.00/ C2H6/3.00/ AR/ .70/
H+CH4<=>CH3+H2                                    6.600E+08   1.620   10840.00
H+HCO(+M)<=>CH2O(+M)                                          1.090E+12    .480    -260.00
                LOW  /  2.470E+24   -2.570    425.00/
                TROE/   .7824  271.00  2755.00  6570.00 /
H2/2.00/ H2O/6.00/ CH4/2.00/ CO/1.50/ CO2/2.00/ C2H6/3.00/ AR/ .70/
H+HCO<=>H2+CO                                     7.340E+13    .000       .00
H+CH2O(+M)<=>CH2OH(+M)                                        5.400E+11    .454    3600.00
                LOW  /  1.270E+32   -4.820   6530.00/
                TROE/   .7187  103.00  1291.00  4160.00 /
H2/2.00/ H2O/6.00/ CH4/2.00/ CO/1.50/ CO2/2.00/ C2H6/3.00/ AR/ .70/
H+CH2O(+M)<=>CH3O(+M)                                         5.400E+11    .454    2600.00
```

```
              LOW  /  2.200E+30   -4.800   5560.00/
              TROE/   .7580   94.00  1555.00  4200.00 /
H2/2.00/ H2O/6.00/ CH4/2.00/ CO/1.50/ CO2/2.00/ C2H6/3.00/
H+CH2O<=>HCO+H2                          5.740E+07   1.900    2742.00
H+CH2OH(+M)<=>CH3OH(+M)                                1.055E+12    .500     86.00
              LOW  /  4.360E+31   -4.650   5080.00/
              TROE/   .600  100.00  90000.0  10000.0 /
H2/2.00/ H2O/6.00/ CH4/2.00/ CO/1.50/ CO2/2.00/ C2H6/3.00/
H+CH2OH<=>H2+CH2O                        2.000E+13    .000      .00
H+CH2OH<=>OH+CH3                         1.650E+11    .650   -284.00
H+CH2OH<=>CH2(S)+H2O                                   3.280E+13   -.090    610.00
H+CH3O(+M)<=>CH3OH(+M)                                 2.430E+12    .515     50.00
              LOW  /  4.660E+41   -7.440   14080.0/
              TROE/   .700  100.00  90000.0 10000.00 /
H2/2.00/ H2O/6.00/ CH4/2.00/ CO/1.50/ CO2/2.00/ C2H6/3.00/
H+CH3O<=>H+CH2OH                         4.150E+07   1.630   1924.00
H+CH3O<=>H2+CH2O                         2.000E+13    .000      .00
H+CH3O<=>OH+CH3                          1.500E+12    .500   -110.00
H+CH3O<=>CH2(S)+H2O                      2.620E+14   -.230   1070.00
H+CH3OH<=>CH2OH+H2                                     1.700E+07   2.100   4870.00
H+CH3OH<=>CH3O+H2                        4.200E+06   2.100   4870.00
H+C2H(+M)<=>C2H2(+M)                     1.000E+17  -1.000      .00
              LOW  /  3.750E+33   -4.800   1900.00/
              TROE/   .6464  132.00  1315.00  5566.00 /
H2/2.00/ H2O/6.00/ CH4/2.00/ CO/1.50/ CO2/2.00/ C2H6/3.00/ AR/ .70/
H+C2H2(+M)<=>C2H3(+M)                    5.600E+12    .000   2400.00
              LOW  /  3.800E+40   -7.270   7220.00/
              TROE/   .7507   98.50  1302.00  4167.00 /
H2/2.00/ H2O/6.00/ CH4/2.00/ CO/1.50/ CO2/2.00/ C2H6/3.00/ AR/ .70/
H+C2H3(+M)<=>C2H4(+M)                    6.080E+12    .270    280.00
              LOW  /  1.400E+30   -3.860   3320.00/
              TROE/   .7820  207.50  2663.00  6095.00 /
H2/2.00/ H2O/6.00/ CH4/2.00/ CO/1.50/ CO2/2.00/ C2H6/3.00/ AR/ .70/
H+C2H3<=>H2+C2H2                         3.000E+13    .000      .00
H+C2H4(+M)<=>C2H5(+M)                    0.540E+12    .454   1820.00
              LOW  /  0.600E+42   -7.620   6970.00/
              TROE/   .9753  210.00   984.00  4374.00 /
H2/2.00/ H2O/6.00/ CH4/2.00/ CO/1.50/ CO2/2.00/ C2H6/3.00/ AR/ .70/
H+C2H4<=>C2H3+H2                         1.325E+06   2.530  12240.00
H+C2H5(+M)<=>C2H6(+M)                    5.210E+17   -.990   1580.00
              LOW  /  1.990E+41   -7.080   6685.00/
              TROE/   .8422  125.00  2219.00  6882.00 /
H2/2.00/ H2O/6.00/ CH4/2.00/ CO/1.50/ CO2/2.00/ C2H6/3.00/ AR/ .70/
H+C2H5<=>H2+C2H4                         2.000E+12    .000      .00
H+C2H6<=>C2H5+H2                         1.150E+08   1.900   7530.00
H+HCCO<=>CH2(S)+CO                       1.000E+14    .000      .00
H+CH2CO<=>HCCO+H2                                      5.000E+13    .000   8000.00
H+CH2CO<=>CH3+CO                         1.130E+13    .000   3428.00
H+HCCOH<=>H+CH2CO                                      1.000E+13    .000      .00
H2+CO(+M)<=>CH2O(+M)                     4.300E+07   1.500  79600.00
              LOW  /  5.070E+27   -3.420  84350.00/
              TROE/   .9320  197.00  1540.00 10300.00 /
H2/2.00/ H2O/6.00/ CH4/2.00/ CO/1.50/ CO2/2.00/ C2H6/3.00/ AR/ .70/
OH+H2<=>H+H2O                            2.160E+08   1.510   3430.00
2OH(+M)<=>H2O2(+M)                       7.400E+13   -.370      .00
              LOW  /  2.300E+18   -.900  -1700.00/
              TROE/   .7346   94.00  1756.00  5182.00 /
H2/2.00/ H2O/6.00/ CH4/2.00/ CO/1.50/ CO2/2.00/ C2H6/3.00/ AR/ .70/
2OH<=>O+H2O                              3.570E+04   2.400  -2110.00
OH+HO2<=>O2+H2O                          1.450E+13    .000   -500.00
 DUPLICATE
OH+H2O2<=>HO2+H2O                        2.000E+12    .000    427.00
 DUPLICATE
OH+H2O2<=>HO2+H2O                        1.700E+18    .000  29410.00
 DUPLICATE
OH+C<=>H+CO                              5.000E+13    .000      .00
OH+CH<=>H+HCO                            3.000E+13    .000      .00
OH+CH2<=>H+CH2O                          2.000E+13    .000      .00
OH+CH2<=>CH+H2O                          1.130E+07   2.000   3000.00
OH+CH2(S)<=>H+CH2O                       3.000E+13    .000      .00
OH+CH3(+M)<=>CH3OH(+M)                                 2.790E+18  -1.430   1330.00
              LOW  /  4.000E+36   -5.920   3140.00/
              TROE/   .4120  195.0  5900.00  6394.00/
H2/2.00/ H2O/6.00/ CH4/2.00/ CO/1.50/ CO2/2.00/ C2H6/3.00/
OH+CH3<=>CH2+H2O                         5.600E+07   1.600   5420.00
OH+CH3<=>CH2(S)+H2O                      6.440E+17  -1.340   1417.00
OH+CH4<=>CH3+H2O                         1.000E+08   1.600   3120.00
OH+CO<=>H+CO2                            4.760E+07   1.228     70.00
OH+HCO<=>H2O+CO                          5.000E+13    .000      .00
OH+CH2O<=>HCO+H2O                                      3.430E+09   1.180   -447.00
OH+CH2OH<=>H2O+CH2O                                    5.000E+12    .000      .00
OH+CH3O<=>H2O+CH2O                                     5.000E+12    .000      .00
OH+CH3OH<=>CH2OH+H2O                                   1.440E+06   2.000   -840.00
OH+CH3OH<=>CH3O+H2O                                    6.300E+06   2.000   1500.00
OH+C2H<=>H+HCCO                          2.000E+13    .000      .00
OH+C2H2<=>H+CH2CO                        2.180E-04   4.500  -1000.00
OH+C2H2<=>H+HCCOH                                      5.040E+05   2.300  13500.00
```

```
OH+C2H2<=>C2H+H2O                                 3.370E+07   2.000   14000.00
OH+C2H2<=>CH3+CO                                  4.830E-04   4.000   -2000.00
OH+C2H3<=>H2O+C2H2                                5.000E+12    .000       .00
OH+C2H4<=>C2H3+H2O                                3.600E+06   2.000    2500.00
OH+C2H6<=>C2H5+H2O                                3.540E+06   2.120     870.00
OH+CH2CO<=>HCCO+H2O                                           7.500E+12    .000    2000.00
2HO2<=>O2+H2O2                                    1.300E+11    .000   -1630.00
 DUPLICATE
2HO2<=>O2+H2O2                                    4.200E+14    .000   12000.00
 DUPLICATE
HO2+CH2<=>OH+CH2O                                 2.000E+13    .000       .00
HO2+CH3<=>O2+CH4                                  1.000E+12    .000       .00
HO2+CH3<=>OH+CH3O                                 3.780E+13    .000       .00
HO2+CO<=>OH+CO2                                   1.500E+14    .000   23600.00
HO2+CH2O<=>HCO+H2O2                                           5.600E+06   2.000   12000.00
C+O2<=>O+CO                                       5.800E+13    .000     576.00
C+CH2<=>H+C2H                                     5.000E+13    .000       .00
C+CH3<=>H+C2H2                                    5.000E+13    .000       .00
CH+O2<=>O+HCO                                     6.710E+13    .000       .00
CH+H2<=>H+CH2                                     1.080E+14    .000    3110.00
CH+H2O<=>H+CH2O                                   5.710E+12    .000    -755.00
CH+CH2<=>H+C2H2                                   4.000E+13    .000       .00
CH+CH3<=>H+C2H3                                   3.000E+13    .000       .00
CH+CH4<=>H+C2H4                                   6.000E+13    .000       .00
CH+CO(+M)<=>HCCO(+M)                                          5.000E+13    .000       .00
            LOW  / 2.690E+28   -3.740   1936.00/
            TROE/   .5757  237.00  1652.00  5069.00 /
H2/2.00/ H2O/6.00/ CH4/2.00/ CO/1.50/ CO2/2.00/ C2H6/3.00/ AR/ .70/
CH+CO2<=>HCO+CO                                   1.900E+14    .000   15792.00
CH+CH2O<=>H+CH2CO                                             9.460E+13    .000    -515.00
CH+HCCO<=>CO+C2H2                                             5.000E+13    .000       .00
CH2+O2=>OH+H+CO                                   5.000E+12    .000    1500.00
CH2+H2<=>H+CH3                                    5.000E+05   2.000    7230.00
2CH2<=>H2+C2H2                                    1.600E+15    .000   11944.00
CH2+CH3<=>H+C2H4                                  4.000E+13    .000       .00
CH2+CH4<=>2CH3                                    2.460E+06   2.000    8270.00
CH2+CO(+M)<=>CH2CO(+M)                                        8.100E+11    .500    4510.00
            LOW  / 2.690E+33   -5.110   7095.00/
            TROE/   .5907  275.00  1226.00  5185.00 /
H2/2.00/ H2O/6.00/ CH4/2.00/ CO/1.50/ CO2/2.00/ C2H6/3.00/ AR/ .70/
CH2+HCCO<=>C2H3+CO                                            3.000E+13    .000       .00
CH2(S)+N2<=>CH2+N2                                1.500E+13    .000     600.00
CH2(S)+AR<=>CH2+AR                                9.000E+12    .000     600.00
CH2(S)+O2<=>H+OH+CO                                           2.800E+13    .000       .00
CH2(S)+O2<=>CO+H2O                                1.200E+13    .000       .00
CH2(S)+H2<=>CH3+H                                 7.000E+13    .000       .00
CH2(S)+H2O(+M)<=>CH3OH(+M)                                    4.820E+17   -1.160    1145.00
            LOW  / 1.880E+38   -6.360   5040.00/
            TROE/   .6027  208.00  3922.00  10180.0 /
H2/2.00/ H2O/6.00/ CH4/2.00/ CO/1.50/ CO2/2.00/ C2H6/3.00/
CH2(S)+H2O<=>CH2+H2O                                          3.000E+13    .000       .00
CH2(S)+CH3<=>H+C2H4                               1.200E+13    .000    -570.00
CH2(S)+CH4<=>2CH3                                 1.600E+13    .000    -570.00
CH2(S)+CO<=>CH2+CO                                9.000E+12    .000       .00
CH2(S)+CO2<=>CH2+CO2                                          7.000E+12    .000       .00
CH2(S)+CO2<=>CO+CH2O                                          1.400E+13    .000       .00
CH2(S)+C2H6<=>CH3+C2H5                                        4.000E+13    .000    -550.00
CH3+O2<=>O+CH3O                                   3.560E+13    .000   30480.00
CH3+O2<=>OH+CH2O                                  2.310E+12    .000   20315.00
CH3+H2O2<=>HO2+CH4                                2.450E+04   2.470    5180.00
2CH3(+M)<=>C2H6(+M)                               6.770E+16   -1.180     654.00
            LOW  / 3.400E+41   -7.030   2762.00/
            TROE/   .6190  73.20  1180.00  9999.00 /
H2/2.00/ H2O/6.00/ CH4/2.00/ CO/1.50/ CO2/2.00/ C2H6/3.00/ AR/ .70/
2CH3<=>H+C2H5                                     6.840E+12    .100   10600.00
CH3+HCO<=>CH4+CO                                  2.648E+13    .000       .00
CH3+CH2O<=>HCO+CH4                                            3.320E+03   2.810    5860.00
CH3+CH3OH<=>CH2OH+CH4                                         3.000E+07   1.500    9940.00
CH3+CH3OH<=>CH3O+CH4                                          1.000E+07   1.500    9940.00
CH3+C2H4<=>C2H3+CH4                                           2.270E+05   2.000    9200.00
CH3+C2H6<=>C2H5+CH4                                           6.140E+06   1.740   10450.00
HCO+H2O<=>H+CO+H2O                                            1.500E+18  -1.000   17000.00
HCO+M<=>H+CO+M                                    1.870E+17   -1.000   17000.00
H2/2.00/ H2O/ .00/ CH4/2.00/ CO/1.50/ CO2/2.00/ C2H6/3.00/
HCO+O2<=>HO2+CO                                   13.45E+12    .000     400.00
CH2OH+O2<=>HO2+CH2O                                           1.800E+13    .000     900.00
CH3O+O2<=>HO2+CH2O                                            4.280E-13   7.600   -3530.00
C2H+O2<=>HCO+CO                                   1.000E+13    .000    -755.00
C2H+H2<=>H+C2H2                                   5.680E+10   0.900    1993.00
C2H3+O2<=>HCO+CH2O                                            4.580E+16   -1.390    1015.00
C2H4(+M)<=>H2+C2H2(+M)                                        8.000E+12    .440   86770.00
            LOW  / 1.580E+51   -9.300   97800.00/
            TROE/   .7345  180.00  1035.00  5417.00 /
H2/2.00/ H2O/6.00/ CH4/2.00/ CO/1.50/ CO2/2.00/ C2H6/3.00/ AR/ .70/
C2H5+O2<=>HO2+C2H4                                8.400E+11    .000    3875.00
HCCO+O2<=>OH+2CO                                  3.200E+12    .000     854.00
2HCCO<=>2CO+C2H2                                  1.000E+13    .000       .00
```

```
N+NO<=>N2+O                                 2.700E+13   .000    355.00
N+O2<=>NO+O                                 9.000E+09  1.000   6500.00
N+OH<=>NO+H                                 3.360E+13   .000    385.00
N2O+O<=>N2+O2                               1.400E+12   .000  10810.00
N2O+O<=>2NO                                 2.900E+13   .000  23150.00
N2O+H<=>N2+OH                               3.870E+14   .000  18880.00
N2O+OH<=>N2+HO2                             2.000E+12   .000  21060.00
N2O(+M)<=>N2+O(+M)                          7.910E+10   .000  56020.00
              LOW  /  6.370E+14     .000  56640.00/
H2/2.00/ H2O/6.00/ CH4/2.00/ CO/1.50/ CO2/2.00/ C2H6/3.00/ AR/ .625/
HO2+NO<=>NO2+OH                             2.110E+12   .000   -480.00
NO+O+M<=>NO2+M                              1.060E+20 -1.410     .00
H2/2.00/ H2O/6.00/ CH4/2.00/ CO/1.50/ CO2/2.00/ C2H6/3.00/ AR/ .70/
NO2+O<=>NO+O2                               3.900E+12   .000   -240.00
NO2+H<=>NO+OH                               1.320E+14   .000    360.00
NH+O<=>NO+H                                 4.000E+13   .000     .00
NH+H<=>N+H2                                 3.200E+13   .000    330.00
NH+OH<=>HNO+H                               2.000E+13   .000     .00
NH+OH<=>N+H2O                               2.000E+09  1.200     .00
NH+O2<=>HNO+O                               4.610E+05  2.000   6500.00
NH+O2<=>NO+OH                               1.280E+06  1.500    100.00
NH+N<=>N2+H                                 1.500E+13   .000     .00
NH+H2O<=>HNO+H2                             2.000E+13   .000  13850.00
NH+NO<=>N2+OH                               2.160E+13  -.230     .00
NH+NO<=>N2O+H                               3.650E+14  -.450     .00
NH2+O<=>OH+NH                               3.000E+12   .000     .00
NH2+O<=>H+HNO                               3.900E+13   .000     .00
NH2+H<=>NH+H2                               4.000E+13   .000   3650.00
NH2+OH<=>NH+H2O                             9.000E+07  1.500   -460.00
NNH<=>N2+H                                  3.300E+08   .000     .00
NNH+M<=>N2+H+M                              1.300E+14  -.110   4980.00
H2/2.00/ H2O/6.00/ CH4/2.00/ CO/1.50/ CO2/2.00/ C2H6/3.00/ AR/ .70/
NNH+O2<=>HO2+N2                             5.000E+12   .000     .00
NNH+O<=>OH+N2                               2.500E+13   .000     .00
NNH+O<=>NH+NO                               7.000E+13   .000     .00
NNH+H<=>H2+N2                               5.000E+13   .000     .00
NNH+OH<=>H2O+N2                             2.000E+13   .000     .00
NNH+CH3<=>CH4+N2                            2.500E+13   .000     .00
H+NO+M<=>HNO+M                              4.480E+19 -1.320    740.00
H2/2.00/ H2O/6.00/ CH4/2.00/ CO/1.50/ CO2/2.00/ C2H6/3.00/ AR/ .70/
HNO+O<=>NO+OH                               2.500E+13   .000     .00
HNO+H<=>H2+NO                               9.000E+11   .720    660.00
HNO+OH<=>NO+H2O                             1.300E+07  1.900   -950.00
HNO+O2<=>HO2+NO                             1.000E+13   .000  13000.00
CN+O<=>CO+N                                 7.700E+13   .000     .00
CN+OH<=>NCO+H                               4.000E+13   .000     .00
CN+H2O<=>HCN+OH                             8.000E+12   .000   7460.00
CN+O2<=>NCO+O                               6.140E+12   .000   -440.00
CN+H2<=>HCN+H                               2.950E+05  2.450   2240.00
NCO+O<=>NO+CO                               2.350E+13   .000     .00
NCO+H<=>NH+CO                               5.400E+13   .000     .00
NCO+OH<=>NO+H+CO                            0.250E+13   .000     .00
NCO+N<=>N2+CO                               2.000E+13   .000     .00
NCO+O2<=>NO+CO2                             2.000E+12   .000  20000.00
NCO+M<=>N+CO+M                              3.100E+14   .000  54050.00
H2/2.00/ H2O/6.00/ CH4/2.00/ CO/1.50/ CO2/2.00/ C2H6/3.00/ AR/ .70/
NCO+NO<=>N2O+CO                             1.900E+17 -1.520    740.00
NCO+NO<=>N2+CO2                             3.800E+18 -2.000    800.00
HCN+M<=>H+CN+M                              1.040E+29 -3.300 126600.00
H2/2.00/ H2O/6.00/ CH4/2.00/ CO/1.50/ CO2/2.00/ C2H6/3.00/ AR/ .70/
HCN+O<=>NCO+H                               2.030E+04  2.640   4980.00
HCN+O<=>NH+CO                               5.070E+03  2.640   4980.00
HCN+O<=>CN+OH                               3.910E+09  1.580  26600.00
HCN+OH<=>HOCN+H                             1.100E+06  2.030  13370.00
HCN+OH<=>HNCO+H                             4.400E+03  2.260   6400.00
HCN+OH<=>NH2+CO                             1.600E+02  2.560   9000.00
H+HCN(+M)<=>H2CN(+M)                        3.300E+13   .000     .00
    LOW /  1.400E+26   -3.400    1900.00/
H2/2.00/ H2O/6.00/ CH4/2.00/ CO/1.50/ CO2/2.00/ C2H6/3.00/ AR/ .70/
H2CN+N<=>N2+CH2                             6.000E+13   .000    400.00
C+N2<=>CN+N                                 6.300E+13   .000  46020.00
CH+N2<=>HCN+N                               3.120E+09  0.880  20130.00
CH+N2(+M)<=>HCNN(+M)                        3.100E+12   .150     .00
              LOW  /  1.300E+25   -3.160    740.00/
              TROE/   .6670  235.00  2117.00  4536.00 /
H2/2.00/ H2O/6.00/ CH4/2.00/ CO/1.50/ CO2/2.00/ C2H6/3.00/ AR/ 1.0/
CH2+N2<=>HCN+NH                             1.000E+13   .000  74000.00
CH2(S)+N2<=>NH+HCN                          1.000E+11   .000  65000.00
C+NO<=>CN+O                                 1.900E+13   .000     .00
C+NO<=>CO+N                                 2.900E+13   .000     .00
CH+NO<=>HCN+O                               4.100E+13   .000     .00
CH+NO<=>H+NCO                               1.620E+13   .000     .00
CH+NO<=>N+HCO                               2.460E+13   .000     .00
CH2+NO<=>H+HNCO                             3.100E+17 -1.380   1270.00
CH2+NO<=>OH+HCN                             2.900E+14  -.690    760.00
CH2+NO<=>H+HCNO                             3.800E+13  -.360    580.00
CH2(S)+NO<=>H+HNCO                          3.100E+17 -1.380   1270.00
```

```
CH2(S)+NO<=>OH+HCN                      2.900E+14  -.690    760.00
CH2(S)+NO<=>H+HCNO                      3.800E+13  -.360    580.00
CH3+NO<=>HCN+H2O                        9.600E+13   .000  28800.00
CH3+NO<=>H2CN+OH                        1.000E+12   .000  21750.00
HCNN+O<=>CO+H+N2                        2.200E+13   .000      .00
HCNN+O<=>HCN+NO                         2.000E+12   .000      .00
HCNN+O2<=>O+HCO+N2                                  1.200E+13   .000      .00
HCNN+OH<=>H+HCO+N2                                  1.200E+13   .000      .00
HCNN+H<=>CH2+N2                         1.000E+14   .000      .00
HNCO+O<=>NH+CO2                         9.800E+07  1.410   8500.00
HNCO+O<=>HNO+CO                         1.500E+08  1.570  44000.00
HNCO+O<=>NCO+OH                         2.200E+06  2.110  11400.00
HNCO+H<=>NH2+CO                         2.250E+07  1.700   3800.00
HNCO+H<=>H2+NCO                         1.050E+05  2.500  13300.00
HNCO+OH<=>NCO+H2O                                   3.300E+07   1.500   3600.00
HNCO+OH<=>NH2+CO2                                   3.300E+06   1.500   3600.00
HNCO+M<=>NH+CO+M                                    1.180E+16   .000  84720.00
H2/2.00/ H2O/6.00/ CH4/2.00/ CO/1.50/ CO2/2.00/ C2H6/3.00/ AR/ .70/
HCNO+H<=>H+HNCO                         2.100E+15  -.690   2850.00
HCNO+H<=>OH+HCN                         2.700E+11   .180   2120.00
HCNO+H<=>NH2+CO                         1.700E+14  -.750   2890.00
HOCN+H<=>H+HNCO                         2.000E+07  2.000   2000.00
HCCO+NO<=>HCNO+CO                                   0.900E+13   .000      .00
CH3+N<=>H2CN+H                          6.100E+14  -.310    290.00
CH3+N<=>HCN+H2                          3.700E+12   .150    -90.00
NH3+H<=>NH2+H2                          5.400E+05  2.400   9915.00
NH3+OH<=>NH2+H2O                        5.000E+07  1.600    955.00
NH3+O<=>NH2+OH                          9.400E+06  1.940   6460.00
NH+CO2<=>HNO+CO                         1.000E+13   .000  14350.00
CN+NO2<=>NCO+NO                         6.160E+15 -0.752    345.00
NCO+NO2<=>N2O+CO2                       3.250E+12   .000   -705.00
N+CO2<=>NO+CO                           3.000E+12   .000  11300.00
O+CH3=>H+H2+CO                          3.370E+13   .000      .00
O+C2H4<=>H+CH2CHO                       6.700E+06  1.830    220.00
O+C2H5<=>H+CH3CHO                       1.096E+14   .000      .00
OH+HO2<=>O2+H2O                         0.500E+16   .000  17330.00
 DUPLICATE
OH+CH3=>H2+CH2O                         8.000E+09   .500  -1755.00
CH+H2(+M)<=>CH3(+M)                     1.970E+12   .430   -370.00
            LOW/ 4.820E+25  -2.80  590.0 /
            TROE/ .578  122.0  2535.0  9365.0 /
H2/2.00/ H2O/6.00/ CH4/2.00/ CO/1.50/ CO2/2.00/ C2H6/3.00/ AR/ .70/
CH2+O2=>2H+CO2                          5.800E+12   .000   1500.00
CH2+O2<=>O+CH2O                         2.400E+12   .000   1500.00
CH2+CH2=>2H+C2H2                        2.000E+14   .000  10989.00
CH2(S)+H2O=>H2+CH2O                     6.820E+10   .250   -935.00
C2H3+O2<=>O+CH2CHO                                  3.030E+11   .290     11.00
C2H3+O2<=>HO2+C2H2                      1.337E+06  1.610   -384.00
O+CH3CHO<=>OH+CH2CHO                                5.840E+12   .000   1808.00
O+CH3CHO=>OH+CH3+CO                                 5.840E+12   .000   1808.00
O2+CH3CHO=>HO2+CH3+CO                               3.010E+13   .000  39150.00
H+CH3CHO<=>CH2CHO+H2                                2.050E+09  1.160   2405.00
H+CH3CHO=>CH3+H2+CO                                 2.050E+09  1.160   2405.00
OH+CH3CHO=>CH3+H2O+CO                               2.343E+10  0.730  -1113.00
HO2+CH3CHO=>CH3+H2O2+CO                             3.010E+12   .000  11923.00
CH3+CH3CHO=>CH3+CH4+CO                              2.720E+06  1.770   5920.00
H+CH2CO(+M)<=>CH2CHO(+M)                            4.865E+11  0.422  -1755.00
            LOW/ 1.012E+42  -7.63  3854.0/
            TROE/ 0.465  201.0  1773.0  5333.0 /
H2/2.00/ H2O/6.00/ CH4/2.00/ CO/1.50/ CO2/2.00/ C2H6/3.00/ AR/ .70/
O+CH2CHO=>H+CH2+CO2                                 1.500E+14   .000      .00
O2+CH2CHO=>OH+CO+CH2O                               1.810E+10   .000      .00
O2+CH2CHO=>OH+2HCO                                  2.350E+10   .000      .00
H+CH2CHO<=>CH3+HCO                                  2.200E+13   .000      .00
H+CH2CHO<=>CH2CO+H2                                 1.100E+13   .000      .00
OH+CH2CHO<=>H2O+CH2CO                               1.200E+13   .000      .00
OH+CH2CHO<=>HCO+CH2OH                               3.010E+13   .000      .00
CH3+C2H5(+M)<=>C3H8(+M)                             .9430E+13   .000      .00
LOW/ 2.710E+74  -16.82  13065.0 /
            TROE/ .1527  291.0  2742.0  7748.0 /
H2/2.00/ H2O/6.00/ CH4/2.00/ CO/1.50/ CO2/2.00/ C2H6/3.00/ AR/ .70/
O+C3H8<=>OH+C3H7                        1.930E+05  2.680   3716.00
H+C3H8<=>C3H7+H2                        1.320E+06  2.540   6756.00
OH+C3H8<=>C3H7+H2O                      3.160E+07  1.800    934.00
C3H7+H2O2<=>HO2+C3H8                                3.780E+02   2.720   1500.00
CH3+C3H8<=>C3H7+CH4                                 0.903E+00   3.650   7154.00
CH3+C2H4(+M)<=>C3H7(+M)                             2.550E+06   1.600   5700.00
LOW/ 3.00E+63  -14.6  18170./
TROE/ .1894  277.0  8748.0  7891.0 /
H2/2.00/ H2O/6.00/ CH4/2.00/ CO/1.50/ CO2/2.00/ C2H6/3.00/ AR/ .70/
O+C3H7<=>C2H5+CH2O                      9.640E+13   .000      .00
H+C3H7(+M)<=>C3H8(+M)                   3.613E+13   .000      .00
LOW/ 4.420E+61  -13.545  11357.0/
TROE/ .315  369.0  3285.0  6667.0 /
H2/2.00/ H2O/6.00/ CH4/2.00/ CO/1.50/ CO2/2.00/ C2H6/3.00/ AR/ .70/
H+C3H7<=>CH3+C2H5                       4.060E+06   2.190    890.00
OH+C3H7<=>C2H5+CH2OH                                2.410E+13   .000      .00
```

```
HO2+C3H7<=>O2+C3H8                  2.550E+10    0.255   -943.00
HO2+C3H7=>OH+C2H5+CH2O                           2.410E+13     .000      .00
CH3+C3H7<=>2C2H5                    1.927E+13   -0.320       .00
H=>H_W                                           4.180E-01    1.750     0.00
O=>O_W                                           1.010E-01    1.750     0.00
OH=>OH_W                             9.060E-02    1.750      0.00
HO2=>HO2_W                                       6.420E-02    1.750     0.00
CH3=>CH3_W                                       6.660E-02    1.750     0.00
CH3O2=>CH3O2_W                                   4.320E-02    1.750     0.00
CH3O=>CH3O_W                                     5.030E-02    1.750     0.00
END
```

E. Conversion of Selected Flow Rates and Equivalence Ratios to Flow Velocities and Power

E.1 CNG/Air Mixtures

Flow Rate (slpm)	Velocity & Power	Equivalence Ratio							
		0.35	0.4	0.6	1.1	1.3	1.5	1.7	1.9
50	Flow Velocity (cm/sec)	4.64	4.66	4.76	4.99	5.09	5.18	5.27	5.37
	Power (kW)	1.00	1.15	1.72	3.15	3.72	4.30	4.87	5.44
100	Flow Velocity (cm/sec)	9.28	9.32	9.51	9.98	10.17	10.36	10.55	10.73
	Power (kW)	2.00	2.29	3.44	6.30	7.44	8.59	9.74	10.88
150	Flow Velocity (cm/sec)	13.92	13.98	14.27	14.97	15.26	15.54	15.82	16.10
	Power (kW)	3.00	3.44	5.15	9.45	11.17	12.89	14.60	16.32
200	Flow Velocity (cm/sec)	18.56	18.64	19.02	19.96	20.34	20.72	21.09	21.47
	Power (kW)	4.00	4.58	6.87	12.60	14.89	17.18	19.47	21.76
300	Flow Velocity (cm/sec)	27.84	27.96	28.54	29.94	30.51	31.07	31.64	32.20
	Power (kW)	6.00	6.87	10.31	18.90	22.33	25.77	29.21	32.64
600	Flow Velocity (cm/sec)	55.68	55.92	57.07	59.88	61.02	62.15	63.28	64.40
	Power (kW)	12.00	13.74	20.62	37.80	44.66	51.54	58.42	65.28

Table 7.1: Conversion of selected flow rates and equivalence ratios to flow velocities and power for CNG/air mixtures

E.2 LPG/Air Mixtures

Flow Rate (slpm)	Velocity & Power	Equivalence Ratio							
		0.35	0.4	0.6	1.1	1.3	1.5	1.7	1.9
50	Flow Velocity (cm/sec)	4.54	4.55	4.59	4.68	4.72	4.76	4.79	4.83
	Power (kW)	1.02	1.17	1.75	3.21	3.79	4.38	4.96	5.54
100	Flow Velocity (cm/sec)	9.08	9.10	9.17	9.36	9.44	9.51	9.59	9.66
	Power (kW)	2.04	2.33	3.50	6.42	7.59	8.75	9.92	11.09
150	Flow Velocity (cm/sec)	13.62	13.65	13.76	14.04	14.15	14.27	14.38	14.49
	Power (kW)	3.06	3.50	5.25	9.63	11.38	13.13	14.88	16.63
200	Flow Velocity (cm/sec)	18.16	18.20	18.35	18.72	18.87	19.02	19.17	19.32
	Power (kW)	4.08	4.67	7.00	12.84	15.17	17.51	19.84	22.17
300	Flow Velocity (cm/sec)	27.24	27.30	27.52	28.08	28.31	28.54	28.76	28.98
	Power (kW)	6.13	7.00	10.50	19.26	22.76	26.26	29.76	33.26
600	Flow Velocity (cm/sec)	54.48	54.60	55.04	56.16	56.62	57.07	57.52	57.96
	Power (kW)	12.25	14.00	21.00	38.52	45.52	52.52	59.52	66.52

Table 7.2: Conversion of selected flow rates and equivalence ratios to flow velocities and power for LPG/air mixtures